

12

AD A113594

RADC-TR-81-382
Final Technical Report
January 1982



MICROCIRCUIT PACKAGE STRESS ANALYSIS

Syracuse University

Charles Libove
Richard W. Perkins
Klod Kokini

APPROVED FOR PUBLIC RELEASE; DISTRIBUTION UNLIMITED

DTIC FILE COPY

ROME AIR DEVELOPMENT CENTER
Air Force Systems Command
Griffiss Air Force Base, New York 13441

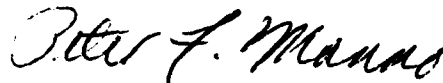
DTIC
ELECT
APR 19 1982
S
E

82 04 19 003

This report has been reviewed by the RADC Public Affairs Office (PA) and is releasable to the National Technical Information Service (NTIS). At NTIS it will be releasable to the general public, including foreign nations.

RADC-TR-81-382 has been reviewed and is approved for publication.

APPROVED:



PETER F. MANNO
Project Engineer

APPROVED:



EDMUND J. WESTCOTT
Technical Director
Reliability and Compatibility Division

FOR THE COMMANDER:



JOHN P. HUSS
Acting Chief, Plans Office

If your address has changed or if you wish to be removed from the RADC mailing list, or if the addressee is no longer employed by your organization, please notify RADC (RBRA) Griffiss AFB NY 13441. This will assist us in maintaining a current mailing list.

Do not return copies of this report unless contractual obligations or notices on a specific document requires that it be returned.

UNCLASSIFIED

SECURITY CLASSIFICATION OF THIS PAGE (When Data Entered)

REPORT DOCUMENTATION PAGE		READ INSTRUCTIONS BEFORE COMPLETING FORM
1. REPORT NUMBER RADC-TR-81-382	2. GOVT ACCESSION NO. AD-A113594	3. RECIPIENT'S CATALOG NUMBER
4. TITLE (and Subtitle) MICROCIRCUIT PACKAGE STRESS ANALYSIS		5. TYPE OF REPORT & PERIOD COVERED Final Technical Report 10 Apr 80 - 9 Aug 81
		6. PERFORMING ORG. REPORT NUMBER MAE-1237-F1
7. AUTHOR(s) Charles Libove Richard W. Perkins Klod Kokini		8. CONTRACT OR GRANT NUMBER(s) F30602-80-C-0155
9. PERFORMING ORGANIZATION NAME AND ADDRESS Syracuse University Syracuse NY 13210		10. PROGRAM ELEMENT PROJECT, TASK AREA & WORK UNIT NUMBERS 61102F 2306J408
11. CONTROLLING OFFICE NAME AND ADDRESS Rome Air Development Center (RBRA) Griffiss AFB NY 13441		12. REPORT DATE January 1982
		13. NUMBER OF PAGES 357
14. MONITORING AGENCY NAME & ADDRESS (if different from Controlling Office) Same		15. SECURITY CLASS. (of this report) UNCLASSIFIED
		15a. DECLASSIFICATION/DOWNGRADING SCHEDULE N/A
16. DISTRIBUTION STATEMENT (of this Report) Approved for public release; distribution unlimited.		
17. DISTRIBUTION STATEMENT (of the abstract entered in Block 20, if different from Report) Same		
18. SUPPLEMENTARY NOTES RADC Project Engineer: Peter F. Manno (RBRA). Appendix D author: R.W. Perkins, Appendix E co-author: K. Kokini, Chapter 8 of this report supersedes Appendices A through C of RADC-TR-79-201.		
19. KEY WORDS (Continue on reverse side if necessary and identify by block number) Design Reliability External pressure Vibration Stresses Transistors Constant acceleration Seals Stress analysis Thermal stress Drop test Materials Screening Thermal shock Impact		
20. ABSTRACT (Continue on reverse side if necessary and identify by block number) The response of various package components to various stressful environ- ments is studied. The environments selected are among those that the package might experience in the course of mechanical screening by the methods of MIL-STD-883 ("Test Methods and Procedures for Microelec- tronics") or they are approximations and idealizations of conditions that the package might encounter in the field. Specifically, the following environments are considered: external pressure, constant acceleration,		

DD FORM 1473 1 JAN 73 EDITION OF 1 NOV 65 IS OBSOLETE

UNCLASSIFIED

SECURITY CLASSIFICATION OF THIS PAGE (When Data Entered)

UNCLASSIFIED

SECURITY CLASSIFICATION OF THIS PAGE(When Data Entered)

impact, sinusoidal vibration, and thermal shock. One or more chapters of the present report are devoted to each environment.

The package types that are addressed in this study are generally those that can be described as flat and rectangular (which includes square). Thus, flatpacks and dual-in-line packages are included. The newer package types now under development, with names such as hermetic chip carriers, leadless chip carriers, or ceramic chip carriers, are also included, for an investigation into the construction of these packages has shown that, as far as the stress analyst is concerned, they are very similar to the traditional flatpacks. The specific package components considered include lids, bases, glass side-walls, lid-to-wall seals, annular glass lead-through seals, internal wires and their bonds, and chip and substrate attachments.

The broad objective of this work is to direct attention, for each environment, to those package areas that are most directly affected by that environment, and to show, by means of analysis, what the major effects might be, in terms of stress and deformation. Thus, the information provided should be of interest mainly to two groups of people: (a) The package screeners, who wish to know what screening techniques might or might not be effective in attacking an area of anticipated mechanical weakness, and what the severity level of an effective screening technique should be in order that sound packages will not be damaged by it. (b) The package designers who, knowing what field or screening environments will be applied to their packages, wish to design them strong enough to survive those environments. The information in this report may also be of interest to any one involved in the diagnosis of mechanical damage to packages.

There are five appendices in the report. Appendix A contains a compilation of useful material property data. Appendices B and C contain some analytical derivations that are of too detailed a nature to warrant inclusion in the main body of the report. Appendix D is a preliminary study of transistor thermal stresses due to internal heat generation, a subject not treated elsewhere in the report. Appendix E describes proposed additional work, of an experimental and theoretical nature, related to the stress and strength analysis of annular glass seals in thermal shock.

Accession For	
NTIS GRA&I	<input checked="" type="checkbox"/>
DTIC TAB	<input type="checkbox"/>
Unannounced	<input type="checkbox"/>
Justification	
By _____	
Distribution/	
Availability Codes	
Dist	Avail and/or Special
A	

UNCLASSIFIED

SECURITY CLASSIFICATION OF THIS PAGE(When Data Entered)

DTIC
COPY
INSPECTED
2

CONTENTS

	Page
Introduction.....	1
<u>Chapter 1 - EXTERNAL PRESSURE.....</u>	<u>4</u>
I. DESCRIPTION OF PACKAGES.....	5
II. ELASTIC RESTRAINT FURNISHED BY THE WALLS.....	10
III. FORMULAS FOR MAXIMUM TENSILE STRESS IN THE SEAL.....	14
A. Linearly Elastic Lid.....	14
B. Inelastic Lid.....	20
C. Summary of Formulas for S_{max}	24
D. Application to Design.....	24
E. Application to Screening.....	27
IV. LID COLLAPSING PRESSURE.....	30
A. Brittle-Material Lids.....	30
B. Ductile-Material Lids.....	37
V. BASE COLLAPSING PRESSURE.....	39
VI. LID DEFLECTION.....	42
A. Brittle-Material Lids.....	42
B. Ductile-Material Lids.....	46
VII. FLATPACKS IN A CENTRIFUGE.....	51
VIII. NUMERICAL EXAMPLES.....	53
IX. EXPERIMENTAL CONFIRMATION AND INFERRED GLASS STRENGTH.....	69
X. REMARKS.....	73
<u>Chapter 2 - CONSTANT ACCELERATION.....</u>	<u>74</u>
I. WIRE AND WIRE BOND TENSIONS.....	75
A. Nomenclature and Physical Constants.....	75
B. Wire Stress in a Centrifuge Test.....	78
C. Wire Stress in a Pull Test.....	82
D. Comparison of Centrifuge and Pull Test.....	84
II. CHIP AND SUBSTRATE ATTACHMENT STRESSES.....	87
A. Conventional Bonding.....	87
B. Face-Down Bonding.....	90
III. LIDS AND BASES OF RECTANGULAR FLATPACKS.....	92
IV. WIRE FLEXURE.....	94
V. REMARKS.....	97

	Page
<u>Chapter 3 - FLATWISE IMPACT</u>	99
I. WIRE STRESSES.....	100
A. Upper Bound Estimate.....	100
B. More Accurate Analyses.....	103
C. Numerical Examples.....	108
II. BASE STRESSES.....	111
A. Equivalent Lateral Pressure.....	111
B. Numerical Examples.....	113
C. Incorporation of Elastic Large Deflection Effects: A Simple Expedient.....	118
D. Incorporation of Elastic Large Deflection Effects: A More Rigorous Approach.....	118
III. LID RESPONSE.....	119
A. Plasticity Considerations.....	119
B. Maximum Deflection of a Constant-Thickness Ductile Lid.....	124
C. Maximum Deflection of a Ductile Lid with Thinned Edges.....	125
D. Numerical Examples.....	126
IV. FEASIBILITY OF THE DROP TEST AS A SCREEN.....	127
<u>Chapter 4 - EDGEWISE IMPACT</u>	131
I. SINGLE COMPONENT LID OR BASE.....	131
A. Elastic.....	131
B. Inelastic.....	136
C. Lid with Thinned Edges.....	140
II. TWO-COMPONENT BASE.....	140
A. Elastic.....	141
B. Inelastic.....	142
<u>Chapter 5 - SINUSOIDAL VIBRATION</u>	143
<u>Chapter 6 - THERMAL SHOCK: FLEXURAL STRESS IN FLATPACK LID SEALS</u>	150
I. SYMBOLS.....	151
II. THERMAL ANALYSIS.....	155
A. Case (a): $d_c < t$	156
B. Case (b): Temperature Perturbation Extends Through Entire Thickness of Lid.....	159
C. Time-Temperature Equation for Case (a).....	160
D. Time-Temperature Relation for Case (b).....	162
III. STRESS ANALYSIS.....	164
A. Maximum Bending Moment.....	166
B. Flexural Stresses in the Seal.....	170

	Page
IV. NUMERICAL EXAMPLE.....	173
A. Problem.....	173
B. Solution.....	174
V. FLEXURAL STRESSES PRODUCED IN SCREENING.....	176
VI. APPLICATION TO PACKAGE OR SCREEN DESIGN.....	180
VII. INCLUSION OF BOILING.....	180
VIII. REMARKS.....	184
<u>Chapter 7 - THERMAL SHOCK: BIAXIAL SURFACE TENSION IN DIP SEALS.....</u>	<u>186</u>
I. EVALUATION OF SURFACE TENSION.....	187
II. APPLICATIONS.....	188
<u>Chapter 8 - THERMAL SHOCK: ANNULAR GLASS SEALS.....</u>	<u>192</u>
I. MODELLING.....	195
A. Modelling for Temperature Analysis.....	196
B. Modelling for Stress Analysis.....	199
II. TEMPERATURE ANALYSIS.....	201
A. Basic Equations.....	201
B. Finite-Difference Formulation.....	203
C. Solution of the Finite-Difference Equations.....	206
III. STRESS ANALYSIS.....	209
A. Basic Equations.....	210
B. Glass Stress Equations in Dimensionless Form.....	214
C. The Limiting Case $c \rightarrow \infty$	216
D. Numerical Evaluation of Stresses in the Glass.....	217
IV. COMPUTER PROGRAM.....	219
V. ILLUSTRATIVE APPLICATION.....	230
APPENDIX A: MATERIAL PROPERTIES.....	236
1. Adhesives.....	238
2. Ceramics.....	243
3. Fluids.....	253
4. Glasses.....	260
5. Nickel-Iron Alloys.....	279
6. Solders.....	282
7. Wires.....	297
APPENDIX B: FLEXURAL ANALYSIS OF A TWO-COMPONENT COMPOSITE PLATE...	300
1. Notation.....	302
2. Moment-Curvature Relations.....	302
3. Stresses.....	306
4. Use of Existing Data.....	308

	Page
APPENDIX C: APPROXIMATE RESPONSE OF AN ELASTIC FLAT PLATE TO A PRESCRIBED MOTION OF ITS BOUNDARY.....	313
1. Notation.....	313
2. Analysis.....	314
3. Illustrative Application.....	317
APPENDIX D: TRANSISTOR THERMAL STRESSES DUE TO INTERNAL HEAT GENERATION (By R.W. Perkins).....	323
1. Introduction.....	323
2. Thermal Stress Analysis.....	326
3. Temperature Analysis.....	328
4. Discussion.....	331
APPENDIX E: PROPOSED ANALYSIS AND EXPERIMENTS FOR FURTHER EVALUA- TION OF THE EFFECTS OF THERMAL SHOCK ON THE STRESSES AND STRENGTH OF ANNULAR GLASS SEALS (By K. Kokini and C. Libove).....	334
1. Introduction.....	334
2. Improved Temperature Analysis.....	335
3. Improved Stress Analysis.....	338
4. Experimental Program.....	345
REFERENCES.....	351

EVALUATION

MICROCIRCUIT PACKAGE STRESS ANALYSIS

The objective of this effort was to refine and summarize the past research on the stress analysis of microcircuit packages and to compile a listing of material properties for use in performing mechanical stress predictions. Included in this study was the mechanical evaluation of leadless chip carrier packages. This investigation showed that the formulas for traditional flatpacks are applicable to leadless chip carrier packages. The following are some of the important results:

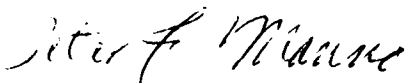
1. Formulas were developed to predict the maximum tensile stress in the lid-to-wall seal; the central deflection of the lid, including the pressure required to crack or collapse the lid or the base; and the equivalence of external pressure resulting from centrifuge acceleration testing applicable to lid behavior and seal stress resistance.
2. Centrifuge testing was determined to be less effective than the pull test in stressing aluminum wires and wire bonds. However the centrifuge test can produce significant flexural stressing of gold wires if the centrifugal force acts parallel to the base of the package and perpendicular to the plane of the wire loop.
3. Theoretical analysis of the feasibility to perform drop test as a mechanical reliability screen indicates that the concept is promising enough to warrant development of a prototype test fixture.

4. Equations were developed to predict the damaging effects that edgewise shock impact has on the lids and bases of microcircuit packages.

5. Sinusoidal vibration shows little promise as a mechanical screen for detecting defective wires or weak wire bonds in microcircuit packages.

6. Formulas were developed to predict the maximum flexural stresses produced in the lid-to-wall seal of a microelectronic flatpack under conditions of thermal-shock screening.

In addition, five detailed appendices to this report were prepared. Appendix A contains a compilation on the following microcircuit material properties: adhesives, ceramics, fluids, glasses, nickel-iron alloys, solders, and wires. Appendix B contains the flexural analysis of a two-component composite plate. Appendix C contains an analysis of the approximate response of an elastic flat plate to a prescribed motion of its boundary. Appendix D is a preliminary study of transistor thermal stresses due to internal heat generation. Finally Appendix E describes proposed additional work, of an experimental and theoretical nature, related to the stress and strength analysis of annular glass seals in thermal shock.



PETER F. MANNO

Project Engineer

INTRODUCTION

This report summarizes several years' research on the stress analysis of microcircuit packaging performed at Syracuse University under the sponsorship of the Rome Air Development Center and monitored by Mr. Peter Manno of the Reliability branch of that agency.

In this research we have studied the response of various package components to various stressful environments. The environments selected are among those that the package might experience in the course of mechanical screening by the methods of MIL-STD-883 ("Test Methods and Procedures for Microelectronics") or they are approximations and idealizations of conditions that the package might encounter in the field. Specifically, the following environments are considered: external pressure, constant acceleration, impact, sinusoidal vibration, and thermal shock. One or more chapters of the present report are devoted to each environment.

The package types that are addressed in this study are generally those that can be described as flat and rectangular (which includes square). Thus, flatpacks and dual-in-line packages are included. The newer package types now under development, with names such as hermetic chip carriers, leadless chip carriers, or ceramic chip carriers, are also included, for an investigation into the construction of these packages has shown that, as far as the stress analyst is concerned, they are very similar to the traditional flatpacks. The specific package components considered include lids, bases, glass side-walls, lid-to-wall seals, annular glass lead-through seals, internal wires and their bonds, and chip and substrate attachments.

The broad objective of this work is to direct attention, for each environment, to those package areas that are most directly affected by

that environment, and to show, by means of analysis, what the major effects might be, in terms of stress and deformation. Thus, the information provided should be of interest mainly to two groups of people: (a) The package screeners, who wish to know what screening techniques might or might not be effective in attacking an area of anticipated mechanical weakness, and what the severity level of an effective screening technique should be in order that sound packages will not be damaged by it. (b) The package designers who, knowing what field or screening environments will be applied to their packages, wish to design them strong enough to survive those environments. The information in this report may also be of interest to any one involved in the diagnosis of mechanical damage to packages.

It will be seen that the analyses in this report rely heavily on approximations, simplifying assumptions, and idealized models wherever it appears that such techniques can reduce a complex problem to a simple one without loss of the essential aspects of the phenomenon being studied. This, the time-honored approach of applied mechanics, has a number of advantages over the usually more accurate detailed numerical analysis by the finite element method, which is so popular at the present time. First, it often yields a closed form solution from which the important dimensionless parameters become evident. A knowledge of those parameters is very helpful if one wishes to know, for example, whether or not a stressful situation can be relieved by changing certain dimensions or geometrical form or by substituting one material for another. Such insights may be more difficult to obtain from the finite element methods. Secondly, the approximate solutions often give "answers" more quickly and cheaply than the finite element analyses, especially if one is not experienced in using the latter on a routine basis. And thirdly, the environmental conditions,

material properties, and package construction details are often not known well enough to justify the cost and time expenditure required for a more precise analysis. Thus it is felt that the analysis techniques and formulas presented in this report can be of considerable value. Their ultimate justification will, of course, depend on the reasonableness of the results that they give and on their usefulness in leading to successful package designs and screening procedures.

There are five appendices in the present report. Appendix A contains a compilation of useful or conceivably useful material property data, Appendices B and C some analytical derivations that were considered to be of too detailed a nature to include in the main body. Appendix D is a preliminary study of transistor thermal stresses due to internal heat generation (the subject of internal heat generation is not treated elsewhere in the report). And Appendix E described proposed additional work, experimental and theoretical, related to the stress and strength analysis of annular glass seals in thermal shock.

Within each chapter or appendix the numbering of tables, equations and figures starts from 1. If it is necessary to refer to an item in another chapter or appendix, the location of the item will be specified.

Chapter 1 - EXTERNAL PRESSURE

External pressure is employed in the MIL-STD-883 seal hermeticity test (test method 1014.2 of Reference 1). This environment tends to produce inward bending of the lid and base of rectangular flatpacks, which can be especially pronounced in the larger size packages. If sufficiently high, the external pressure can cause cracking of ceramic lids or bases and excessive deflection or collapse of metal lids. The relatively short stubby sidewalls provide a considerable amount of elastic restraint against rotation of the edges of the lid and base. Thus, there is also a transfer of bending moments through the lid-to-wall and base-to-wall seals into the walls. If the bending moments are sufficiently high, they can damage the seals, or, if the walls are mainly of glass, they can fracture the glass. The metal lids of some packages have their edges thinned down to a small fraction of the main lid thickness.* In that case the transfer of bending moment from the lid to the wall is not likely to be a problem. The thinness of the edge, in conjunction with plastic yielding of the lid material, will severely limit the maximum developable bending moment in the edge of the lid -- in effect, providing a barrier against the transmission of excessive bending moment across the lid-to-wall seal.

All of the above-mentioned effects of external pressure are assessed quantitatively in this chapter, which is based largely on Reference 2. For simplicity, the discussion will generally be in terms of the lid; it should be understood, however, that much of what is said will apply with obvious modifications to the base as well. Usually, the base-to-wall connection is

* The increased flexibility achieved thereby makes the lid edges conform better to any unevenness in the mating wall surface, thus promoting seal tightness.

much sturdier than the lid-to-wall connection (in fact, the base and wall are integral in some packages). Therefore, when discussing seal stresses due to the transmission of edge bending moments, it is appropriate for the discussion to be in terms of the lid, rather than the base.

I. DESCRIPTION OF PACKAGES

The package is rectangular, as shown in Figure 1, with the cavity having width a , length b , and height h . The dimensions a and b are measured at the top of the cavity, and a is the shorter of the two if they are unequal. The dimension h is assumed to be small compared to b .

If ceramic, the lid is assumed to have a constant thickness t in the region above the cavity and to be no thinner than t in the edge regions above the walls, (Fig. 2). If metallic, the lid is assumed to have a constant thickness t in the region above the cavity and is allowed to have a smaller thickness t_e in the edge strips above the walls; if the lid does not have thinned edges, t_e should be replaced by t in the formulas to be developed.

The Young's modulus E (modulus of elasticity) and the Poisson's ratio ν of the lid material are assumed to be known. For most metals ν can be taken as 0.3 with little error. For ceramics a ν of 0.22 is reasonable. Knowing E , t and ν , one can compute the elastic "plate flexural stiffness" D of the lid as follows:

$$D = Et^3/[12(1-\nu^2)] \quad (1)$$

The basic flexural strength of the lid is assumed to be known in terms of its ultimate bending moment per unit width, which will be designated as m in the interior and m_e in the edge regions, with the latter designation

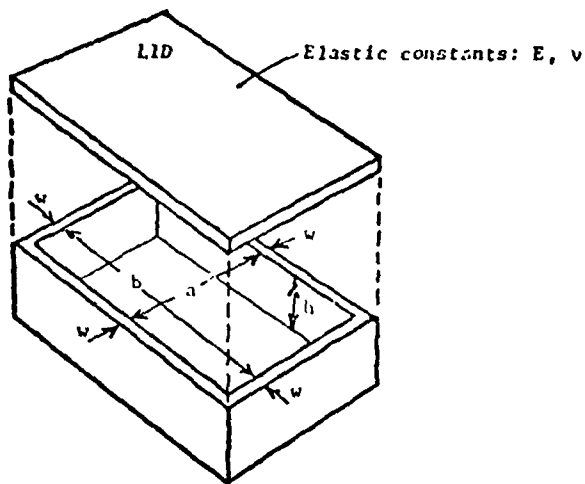


Figure 1.- Package configuration.

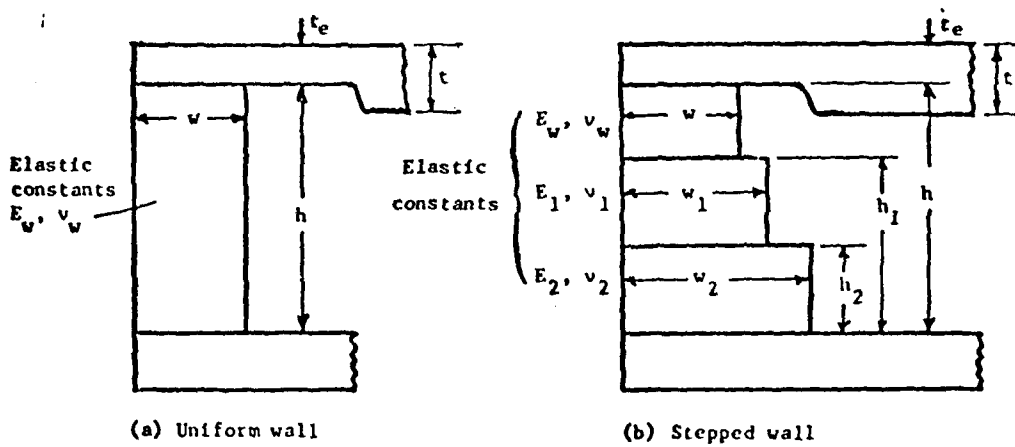


Figure 2.- Wall configurations.

being pertinent only to metallic lids with edge zone thickness t_e smaller than the main thickness t . These ultimate bending moments per unit width can be computed from the bending modulus of rupture σ_b of the material via the formulas

$$m = \sigma_b t^2/6 \quad m_e = \sigma_b t_e^2/6 \quad (2)$$

By means of tests on cantilever strips cut from commercially available Kovar lids (see Appendix A, Section 5), the writer has estimated σ_b for such lids to be 107 ksi, with a coefficient of variation of 8 percent. For ceramic lids σ_b can be obtained from the manufacturer's literature, where it is sometimes referred to as the "flexural strength."

There are different physical actions associated with the development of the ultimate bending moment, depending upon whether the lid is a ductile metal, like Kovar, or a brittle ceramic. In the former case, m and m_e are equal to the fully plastic bending moments per unit width, and they are associated with the development of very high curvatures without any fracture of the material. In the latter case, m is the bending moment per unit width at which fracture occurs, and there is little or no plastic deformation preceding the fracture.

Two kinds of wall construction will be assumed, namely "uniform" and "stepped," as illustrated in Figures 2(a) and (b). In the former, which is typical of an all metal package, the material and the thickness w are constant along the entire height of the wall. In this case E_w and ν_w will denote the Young's modulus and Poisson's ratio of the wall material and

$$D_w \equiv E_w w^3/[12(1-\nu_w^2)] \quad (3a)$$

will denote its plate flexural stiffness. In the 3-segment stepped wall illustrated in Figure 2(b), the material and/or the thickness are only piece-wise constant. In such a wall, w , w_1 , w_2 will denote the thicknesses of the three segments, starting from the top. E_w , E_1 , E_2 will denote their respective Young's moduli; ν_w , ν_1 , ν_2 their Poisson's ratios; and D_w , D_1 , D_2 , their plate flexural stiffnesses, defined as follows:

$$D_w \equiv \frac{E_w w^3}{12(1-\nu_w^2)}, \quad D_1 \equiv \frac{E_1 w_1^3}{12(1-\nu_1^2)}, \quad D_2 \equiv \frac{E_2 w_2^3}{12(1-\nu_2^2)} \quad (3b)$$

The top of the top segment of the wall will have a height above the base that is equal to h , the depth of the cavity. The heights of the tops of the remaining segments above the base will be denoted by h_1 and h_2 , respectively, as indicated in Figure 2(b). In a typical three-segment stepped wall like the one shown in Figure 2(b), the top segment would be a metal seal frame and the other two segments would be of glass. All four walls are assumed to be identical in construction and cross section.

Two kinds of lid-to-wall seal will be considered: the "wide seal" and the "narrow seal," which are illustrated in Figure 3. In the former, the seal width w_s is essentially equal to the thickness w of the top of the wall. This kind of seal would result typically from the use of a solder preform. In the narrow seal, which might result from an electrical seam welding process, the seal width w_s is much smaller than w , and the seal is confined to the outer limits of the lid-wall interface. In such a seal, e will denote the distance from the inner edge of the wall top to the middle of the seal width (see Figure 3(b)).

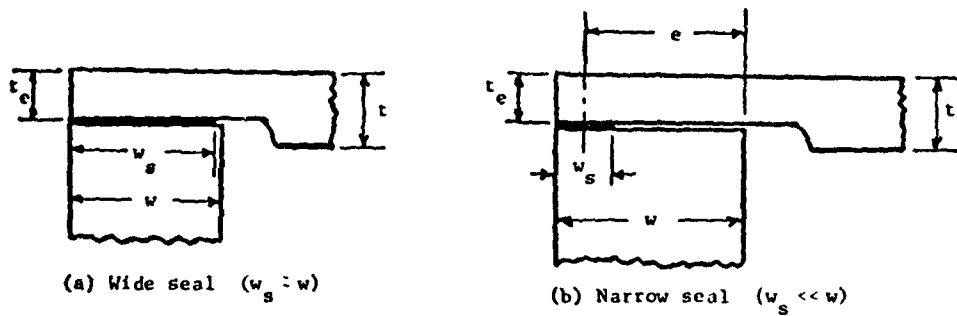


Figure 3.- Lid-to-wall seal geometries.

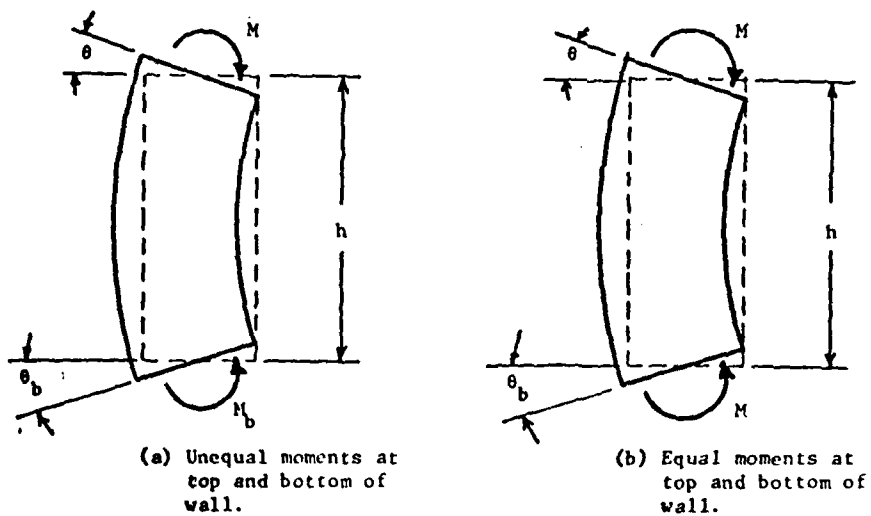


Figure 4.- Wall flexure due to bending moments applied at top and bottom by lid and base.

II. ELASTIC RESTRAINT FURNISHED BY THE WALLS

It will be assumed that under hydrostatic external pressure the lid may be regarded as a uniformly loaded rectangular plate, with width and length equal to the cavity dimensions a and b , and with edges elastically restrained against rotation by the walls of the package. Therefore it will be necessary to evaluate the degree of elastic restraint furnished by the walls to the edge of the lid, and to that end the walls will be regarded as wide vertical beams of length (i.e., height) h . At any location within a wall there will be a local rotation θ (in radians) and a local bending moment intensity M (in-lb/in) at the upper end, and correspondingly a local rotation θ_b and local bending moment intensity M_b at the lower end (see Figure 4), where M and M_b are furnished by the lid and base, respectively, to the wall. Thus the lid "sees" an elastic restraint against rotation of stiffness $k \equiv M/\theta$.

The simplifying assumption $M_b = M$ will often be appropriate as an approximation. Making this assumption and analyzing the wall as a wide beam of length h , we can solve for θ as a linear function of M and thus arrive at the following formula for k :

$$k = \alpha \frac{D_w}{h} \quad (4)$$

where α is a dimensionless constant whose value depends on the nature of the wall. If the wall is uniform, as in Figure 2(a),

$$\alpha = 2 \quad (5a)$$

If the wall is a three-segment stepped wall, as in Figure 2(b),

$$\alpha = \frac{2}{\frac{D_w}{h^2} \left(\frac{h^2 - h_1^2}{D_w} + \frac{h_1^2 - h_2^2}{D_1} + \frac{h_2^2}{D_2} \right)} \quad (5b)$$

Setting $D_1 = D_2$ in Eq. (5b) reduces it to (5a), as it should.

For later use we now introduce a dimensionless wall stiffness parameter, K , which is essentially a measure of the ratio of the wall flexural stiffness to the lid flexural stiffness. K is defined as follows:

$$K \equiv \frac{4}{\pi^2} \frac{k}{(D/a)} = \frac{4}{\pi^2} \frac{a}{h} \frac{D_w}{D} \alpha \quad (6a)$$

If the Poisson's ratios ν and ν_w are equal, this definition reduces to

$$K = \frac{4}{\pi^2} \frac{a}{h} \frac{E_w}{E} \left(\frac{w}{t} \right)^3 \alpha \quad (6b)$$

In graphs to be given later, certain quantities are plotted as functions of $\arctan K$, rather than as functions of K . Figure 5 will permit an easy conversion from K to $\arctan K$. For most packages $\arctan K$ will be fairly close to the upper limit of $\pi/2$, or 1.57, implying that the edges of the lid are very close to being clamped by the walls.

If the base, rather than the lid, is under consideration, the pertinent elastic restraint stiffness is $k_b \equiv M_b/\theta_b$ rather than k . When the assumption $M \approx M_b$ is appropriate, the following formulas are obtained for k_b from the analysis of the wall as a beam:

$$k_b = 2 \frac{D_w}{h} \quad (7a)$$

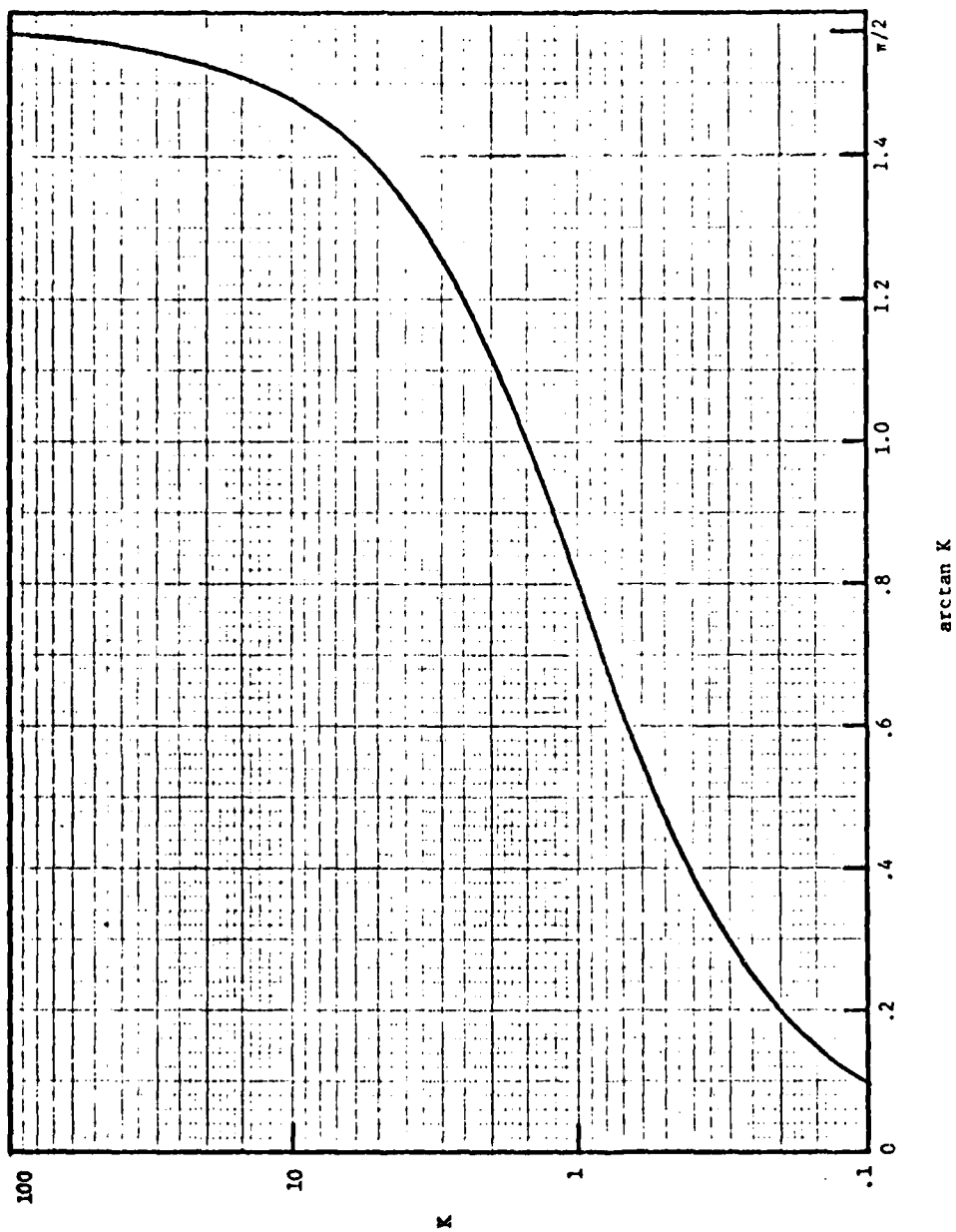


Figure 5.- Relationship between K and arctan K.

if the wall is uniform, as in Figure (2a); and if the wall is stepped, as in Figure 2(b),

$$k_b = \alpha_b \frac{D_2}{h} \quad (7b)$$

where

$$\alpha_b = \frac{2}{h^2 \left[\frac{h^2 - (h - h_2)^2}{D_2} + \frac{(h - h_2)^2 - (h - h_1)^2}{D_1} + \frac{(h - h_1)^2}{D_w} \right]} \quad (7c)$$

When studying the base, the assumption $M = 0$ will be more appropriate than $M = M_b$ if the lid has thinned edges which because of their thinness and plastic yielding cannot exert much moment. In that case, in place of (7a) and (7c) have, respectively,

$$k_b = 3 \frac{D_w}{h} \quad (7a)'$$

(7c)'

$$\alpha_b = \frac{3}{h^3 \left[\frac{h^3 - (h - h_2)^3}{D_2} + \frac{(h - h_2)^3 - (h - h_1)^3}{D_1} + \frac{(h - h_1)^3}{D_w} \right]}$$

And the dimensionless wall stiffness parameter K should then be computed from the formula

$$K = \frac{4}{\pi^2} \frac{k_b}{(D/a)} \quad (8)$$

instead of (6). When dealing with the base, the dimensions a and b should, of course, be based on the cavity dimensions at the bottom of the wall, rather than at the top of the wall, and D on the properties of the base.

III. FORMULAS FOR MAXIMUM TENSILE STRESS IN THE SEAL

A. Linearly Elastic Lid.- Under the action of a uniform gage pressure p (psi), reactions will develop along the edges of the lid, as depicted in Figure 6. These will include bending moments of varying intensity M (in.-lb per in.), due to the restraint against rotation furnished by the walls, and an effective vertical shear of varying intensity V (lb per in.). The maximum values of M and V occur at the middle of the long side and, as long as the lid is linearly elastic (i.e., obeys Hooke's Law), can be expressed as

$$M_{\max} = n_1 \cdot pa^2 \quad (9)$$

$$V_{\max} = n_2 \cdot pa \quad (10)$$

where n_1 and n_2 are functions of the elastic restraint parameter K and the aspect ratio b/a of the lid. The values of n_1 and n_2 associated with any given configuration can be obtained from Figures 7 and 8, respectively.*

The maximum tensile stress S_{\max} in the seal is most likely to occur at the middle of the long side, where the bending moment transmitted from the

*In Figure 7 the data for a clamped plate ($K = \infty$, $\arctan K = \pi/2$) are taken from Table 35 of Reference 3. All other data in this figure are based on the analysis in Appendix A of Reference 4. In Figure 8 the data for a simply supported plate ($\arctan K = 0$) are from Table 8 of Reference 3. The data for a clamped plate ($\arctan K = \pi/2$) are based on the analysis in Appendix B of Reference 4. The curves for elastically restrained plates ($\arctan K = .4, .8, 1.2$) were inserted by interpolation, assuming a linear variation of n_2 with respect to $\arctan K$, which is approximately the variation obtained for n_1 . In view of the small change in n_2 in going from simple support to clamping (around 6% at the most) and the small role that n_2 will play in the subsequent development, the linear interpolation employed in Figure 8 is considered acceptable.

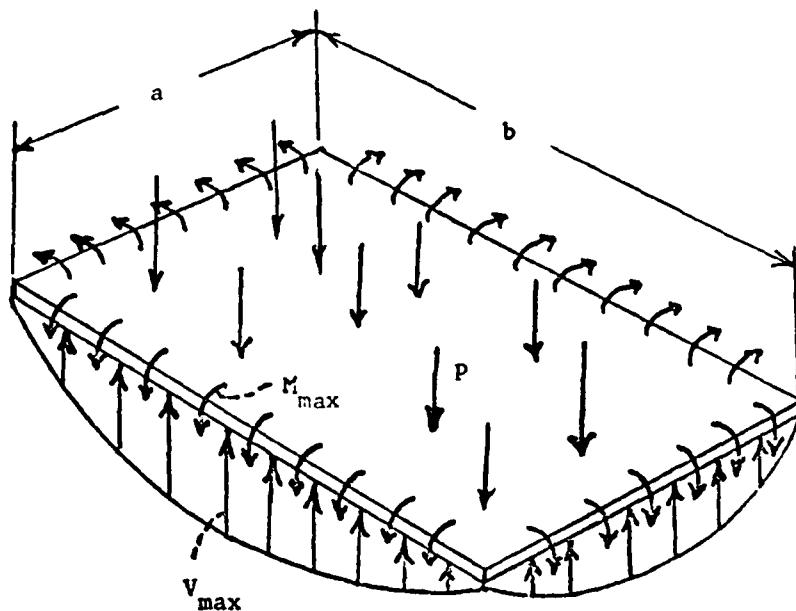


Figure 6.- Reactions on a uniformly loaded rectangular plate with edges elastically restrained against rotation.

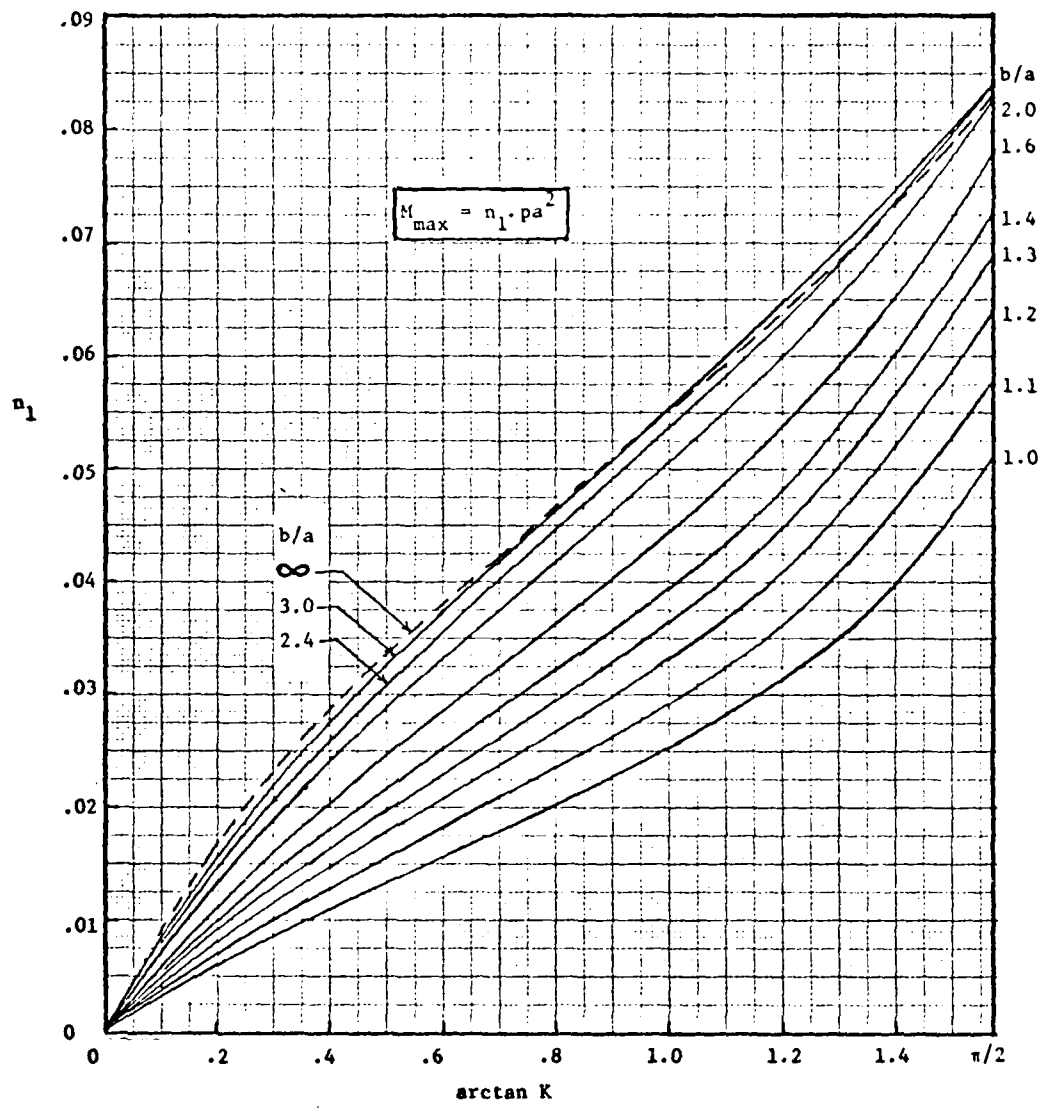


Figure 7.- Bending moment intensity at the middle of the long side for a uniformly loaded rectangular plate obeying Hooke's law with edges elastically restrained against rotation.

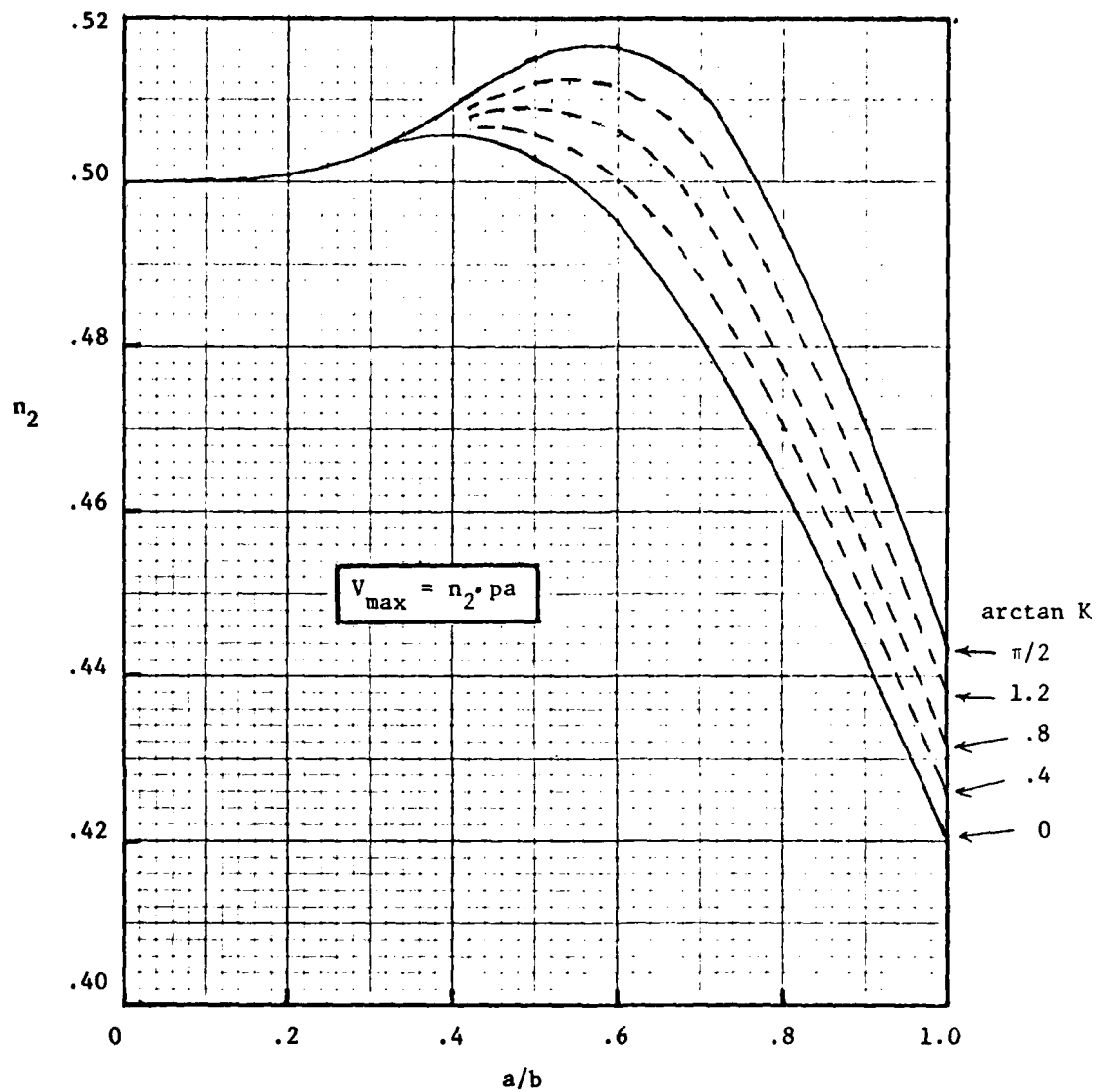


Figure 8.- Intensity of vertical reaction at the middle of the long side for a uniformly loaded rectangular plate obeying Hooke's law with edges elastically restrained against rotation ($\nu = 0.3$)

lid to the wall is a maximum. At this location the bending moment M_{\max} and vertical shear V_{\max} are transferred to the edge strip of the cover directly over the wall, as shown in Figure 9.* The edge strip transfers these in turn to the top of the wall, along with the force pw per unit length due to hydrostatic pressure p acting at the top of the edge strip. Thus, the edge strip is essentially a loading device to transfer the forces shown in Figure 9 to the wall below it.

The states of stress assumed to be developed at the top of the wall, as a result of the forces applied to it by the edge strip in the middle of the long side, are shown in Figure 10. In the case of a wide seal we are assuming a linear variation of normal stress across the thickness of the wall. In the case of a narrow seal we assume instead a uniform tensile stress in the seal area together with a concentrated compressive line load along the inner edge of the wall. In both cases the maximum tensile stress S_{\max} in the seal material occurs at the outside edge.

The stress distributions of Figure 10 must be statically equivalent to the loading of Figure 9. From this equivalence one can deduce the following expressions for the maximum tensile stress in the seal:

$$S_{\max} = \left(M_{\max} + V_{\max} \frac{w}{2} \right) \frac{6}{w^2} - \left(p + \frac{V_{\max}}{w} \right) \quad (11a)$$

in the case of a wide seal (Figure 10(a)), and

$$S_{\max} = \frac{M_{\max} - \frac{1}{2} pw^2}{w_s e} \quad (11b)$$

*Recall that for analytical purposes we are considering the lid to end at the inner edges of the wall.

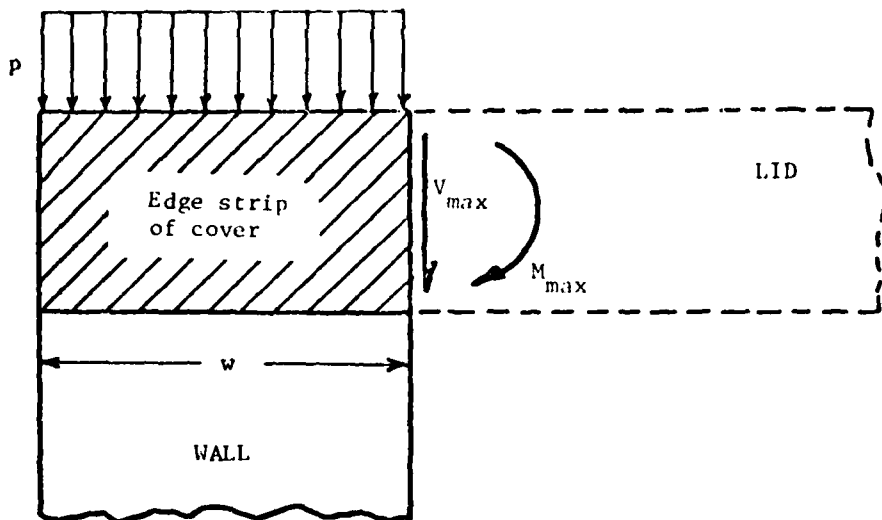
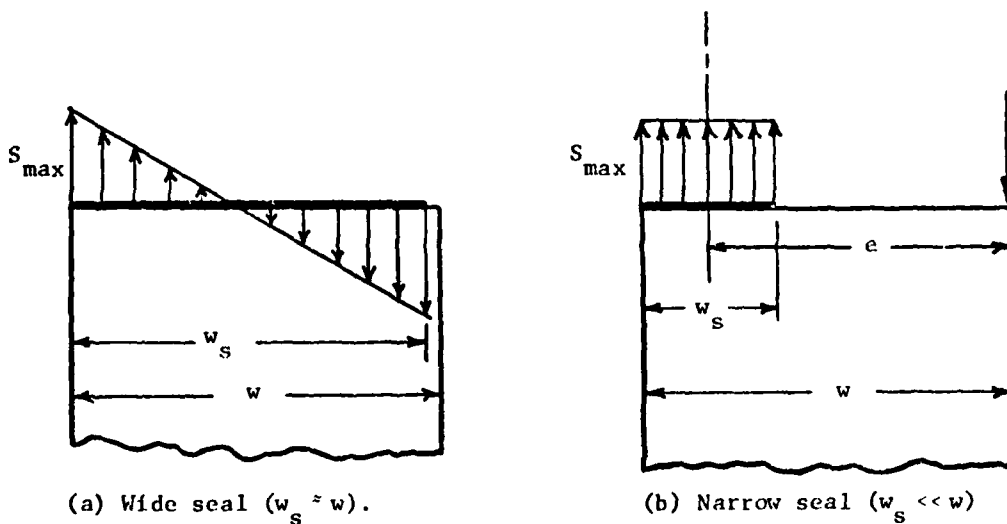


Figure 9.- Forces acting on edge strip of cover at middle of long side.



(a) Wide seal ($w_s \approx w$).

(b) Narrow seal ($w_s \ll w$)

Figure 10.- Stress distributions assumed across top of wall at middle of long side.

in the case of a narrow seal (Figure 10(b)). Substituting for M_{\max} and V_{\max} their known values from Equations (9) and (10), we obtain the following formula for computing S_{\max} :

$$S_{\max} = p \left(\frac{a}{w} \right)^2 n \quad (12)$$

where

$$n = 6n_1 + 2n_2 \frac{w}{a} - \left(\frac{w}{a} \right)^2 \quad (13a)$$

in the case of a wide seal, and

$$n = \left[n_1 - \frac{1}{2} \left(\frac{w}{a} \right)^2 \right] \frac{w^2}{cw_s} \quad (13b)$$

in the case of a narrow seal, (Fig. 10b). In extreme cases Equation (12) will give negative values of S_{\max} , implying that no amount of external pressure can produce tension in the seal.

Brittle materials, such as ceramics, obey Hooke's law reasonably well up to the point of fracture. Thus, Equation (12), which is based upon Hooke's law, may be assumed to be valid for ceramic lid packages as long as the pressure p is less than the lid collapsing pressure p_{ultimate} discussed in Section IV.

B. Inelastic Lid.- Equation (9) is based on Hooke's law and it therefore predicts a linear relationship between M_{\max} and p , which is represented by the line OBEA in Figure 11. In the case of a brittle material lid this line may be considered valid for all pressures up to the point of fracture. If the lid is of a ductile metal, however, at some point, represented by B in Figure 11, the pressure will become high enough to produce plastic

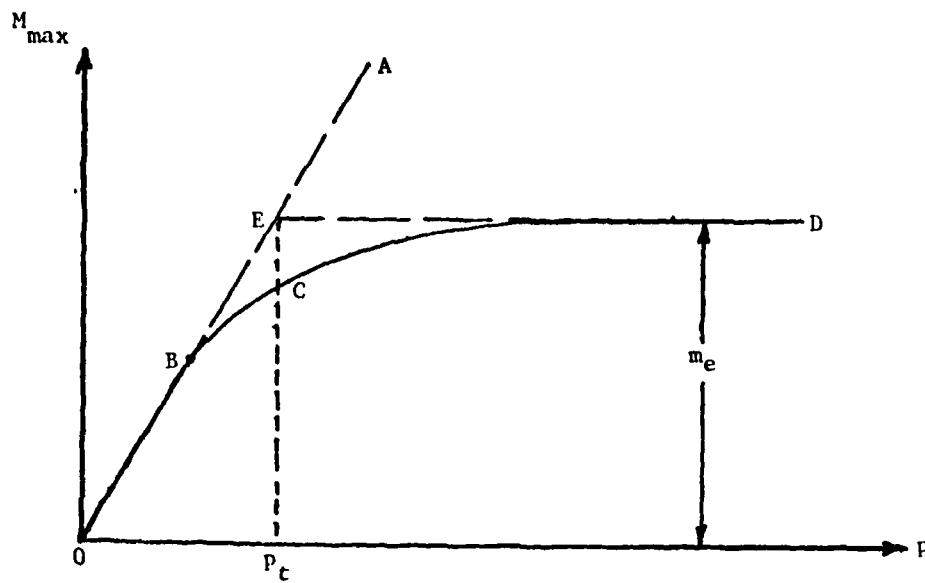


Figure 11.- Relationship between p and M_{\max} :

- OB~~E~~A - Hookean
- OB~~E~~C - Actual
- OB~~E~~D - Assumed

(i.e., inelastic) behavior. The lid will not fracture, but the graph of M_{\max} versus p will depart from the straight line, and M_{\max} will approach the fully plastic bending moment m_e asymptotically along a curve such as OBCD. The determination of this curve is a difficult problem in elasto-plastic plate analysis. We shall avoid this problem by simply approximating the curve OBCD by the two straight-line segments OE and ED. That is, Equation (9) will be considered valid as long as its right side, $n_1 p a^2$, is less than m_e , and Equation (9) will be replaced by

$$M_{\max} = m_e \quad (14)$$

if $n_1 p a^2$ equals or exceeds m_e . Equation (10) is also based on Hooke's law, and its validity will therefore also break down at the pressure associated with point B of Figure 11. We shall ignore this, however, and continue to use Equation (10) for all pressures, on the ground that V_{\max} generally plays a smaller role than M_{\max} in producing stress in the seal and we therefore do not need to know it as precisely. Thus, the sole effect of lid plasticity in our considerations will be to replace Equation (9) by (14) if $n_1 p a^2$ equals or exceeds m_e ; that is, if

$$p \geq m_e / n_1 a^2 \equiv p_t \quad (15)$$

We shall call the right side of this inequality the transition pressure and, as indicated, represent it by the symbol p_t . It is the pressure associated with point E in Figure 11. The corresponding value of S_{\max} we shall call the transition stress and represent it by S_{\max_t} . S_{\max_t} can be evaluated by substituting the transition pressure $p_t = m_e / n_1 a^2$ for p in Equation (12), with the result

$$S_{\max_t} = m_e n / w^2 n_1 \quad (16)$$

When the inequality (15) is satisfied, we may compute S_{\max} from Equations (11) by substituting m_e for M_{\max} and the right side of Equation (10) for V_{\max} . The result is

$$S_{\max} = \frac{6m_e}{w^2} + p(2n_2 \frac{a}{w} - 1) \quad (17)$$

for a wide seal, and

$$S_{\max} = \frac{m_e}{w_s e} - p(\frac{w^2}{2w_s e}) \quad (18)$$

for a narrow seal.

Equations (17) and (18) show that now the worst case (i.e., the largest positive S_{\max}) does not necessarily occur at the highest pressure. This is because the p term in Equation (18) is always negative and the p term in Equation (17) is negative if $2n_2 \frac{a}{w} - 1$ is negative. Thus, increasing p can cause a reduction in S_{\max} . To obtain "worst-case" formulas, we must replace p in Equation (18) by the lowest value it can have and still satisfy condition (15), that is, by the transition pressure p_t ; and we must make the same replacement in Equation (17) if $2n_2 \frac{a}{w} - 1$ is negative. Consequently, given any existing pressure p which satisfies (15), the maximum seal tension produced in the course of applying that pressure (not necessarily the seal tension at that pressure) is:

$$S_{\max} = \text{the larger of} \left\{ \begin{array}{l} \frac{6m_e}{w^2} + p \left(2n_2 \frac{a}{w} - 1 \right) \\ \frac{6m_e}{w^2} + \frac{m_e}{n_1 a^2} \left(2n_2 \frac{a}{w} - 1 \right) \end{array} \right. \quad (19a)$$

for a wide seal; and

$$S_{\max} = \frac{m_e}{w_s e} - \frac{m_e}{n_1 a^2} \left(\frac{w^2}{2w_s e} \right) = \frac{m_e}{w_s e} \left[1 - \frac{1}{2n_1} \left(\frac{w}{a} \right)^2 \right] \quad (19b)$$

for a narrow seal. Equations (19) can give negative values for S_{\max} , which means that the given pressure has produced no tension in the seal. Like Equation (12), they are limited to pressures below the lid collapsing pressure p_{ultimate} discussed in Section IV.

C. Summary of Formulas for S_{\max} .— The formulas for S_{\max} developed in the two preceding sections are summarized in Table 1.

D. Application to Design.— The formulas of Table 1 can be of use both to the designer, whose objective is to design a package that will remain hermetic under a specified screening pressure p , and the user, whose objective is to select an appropriate screening pressure p that will worsen or destroy the hermeticity of packages with poor quality seals.

Considering first the designer, let us suppose that he knows the sealing material to be used and has a value for the allowable tensile stress S_{all} of that material. Then his criterion for a satisfactory lid-to-wall seal design, from the point of view of retaining hermeticity under a given

Table 1.- Summary of Formulas for Maximum Seal Stress, S_{max}

	Linearly Elastic Lid		Inelastic Lid
	Brittle Material	Ductile Material and $p < m_e / n_1 a^2 \equiv p_t$	Ductile Material and $p > m_e / n_1 a^2 \equiv p_t$
Wide Seal	$S_{max} = p \left(\frac{a}{2}\right)^2 n$ $n = 6n_1 + 2n_2 \frac{w}{a} - \left(\frac{w}{a}\right)^2$ <p>(Eqs. 12 and 13(a))</p>	<p>where</p> $S_{max} = \text{the larger of}$ $\frac{6m_e}{w^2} + p \left(2n_2 \frac{a}{w} - 1\right) \quad \text{and}$ $\frac{6m_e}{w^2} + \frac{m_e}{n_1 a^2} \left(2n_2 \frac{a}{w} - 1\right)$ <p>[Eq. 19(a)]</p>	$S_{max} = \frac{m_e}{w_s e} \left[1 - \frac{1}{2n_1} \left(\frac{w}{a}\right)^2\right]$ <p>[Eq. 19(b)]</p>
Narrow Seal	$S_{max} = p \left(\frac{a}{w}\right)^2 n$ $n = \left[n_1 - \frac{1}{2} \left(\frac{w}{a}\right)^2\right] \frac{w^2}{e w_s}$ <p>(Eqs. 12 and 13(b))</p>	<p>where</p>	

external screening pressure p , should be that S_{\max} , as given by the appropriate box of Table 1, be less than S_{all} . That is,

$$S_{\max} \leq S_{\text{all}} \quad (20)$$

In selecting S_{all} the designer should of course be conservative. If S_{all} is taken as the median tensile strength of the sealing material, then packages designed on the basis of the equality sign in Equation (20) will have a failure rate of approximately 50% even if properly sealed. (The failure rate will be still higher for a mixture of properly and improperly sealed packages.) On the other hand, if the designer selects for S_{all} the lowest 1-percentile value of the material strength, then he should expect only a 1% failure rate for properly sealed packages designed on the basis of Equation (20) with the equality sign. The designer should also consider the possibility of the deposited sealing material or its interfacial compounds having a different tensile strength than the bulk sealing material. In the case of solder, the deposited sealing material may be stronger than the bulk sealing material because of the restraint against lateral contraction in a thin solder layer in tension (see Section 6 of Appendix A.)

There is one special precaution to be observed in applying Equation (20) to a stepped-wall package (Figure 2(b)). In such a package the uppermost wall segment is typically a metal seal frame, while the segment below it is of glass. In that case, the critical seal could be the glass-metal interface (or the glass itself) at the underside of the seal frame, rather than the metal-to-metal bond at the top of the seal frame. Therefore, the designer should be sure that the inequality in Equation (20) is satisfied for both seals - the usually wide (but possibly narrow) one at the top of

the seal frame, with S_{all} based on the tensile strength of the sealant there; and the wide seal of width w at the underside of the seal frame, with S_{all} based on the tensile strength of the glass.

It could happen that the designer has very little data on the distribution of tensile strength values for the sealing material, or even on the mean strength, but he does know that a certain previously designed similar package, designated as I, when properly sealed with the same material had an acceptable failure rate F under a screening pressure of p_I . Then in order for the new package, designated as II, to have a failure rate no greater than F when properly sealed and subjected to its screening pressure p_{II} , he should so design package II that its S_{max} is no greater than that of package I. Thus, his criterion for a satisfactory design of package II should be

$$(S_{max})_{II} \leq (S_{max})_I \quad (21)$$

where both S_{max} 's are taken from Table 1, but not necessarily from the same box of that table.

E. Application to Screening.— Turning now to the user of an already designed package, let us first suppose that he has a minimum acceptable value, S_{accept} , for the tensile strength of the seal, and he wants to be sure of rejecting all packages with seal strengths less than that. Then he should select a screening pressure p such that the S_{max} given by Table 1

is equal to or greater than S_{accept} , or, if that cannot be accomplished, a screening pressure p that will make S_{max} as large as possible.*

In the case of a ductile material lid, the procedure for accomplishing this depends upon whether S_{accept} is less than or greater than the transition stress S_{max_t} defined by Equation (16). If $S_{\text{accept}} < S_{\text{max}_t}$, the elastic formula (12) applies. Replacing S_{max} in this formula by S_{accept} , and solving for p , we obtain

$$p = S_{\text{accept}} \left[\left(\frac{a}{w} \right)^2 n \right]^{-1} \quad (22)$$

as the appropriate screening pressure. On the other hand, if $S_{\text{accept}} > S_{\text{max}_t}$, Equations (19) apply. Then for a wide seal with $2n_2 \frac{a}{w} - 1$ positive, we may equate the top expression of (19a) to S_{accept} and solve for p to obtain the following formula for the appropriate screening pressure:

$$p = \left(S_{\text{accept}} - \frac{6m_e}{w^2} \right) \left(2n_2 \frac{a}{w} - 1 \right)^{-1} \quad (23)$$

In the case of a narrow seal, or a wide seal with $2n_2 \frac{a}{w} - 1$ negative, it is not possible to achieve $S_{\text{max}} = S_{\text{accept}}$ when $S_{\text{accept}} > S_{\text{max}_t}$, for in those cases S_{max_t} is also the largest achievable value of S_{max} . Then we must settle for a screening pressure that will give S_{max} as large a value as possible; since that value is S_{max_t} , the required pressure is

*We are assuming here that whether good or poor the seal quality is uniform around the periphery of the seal, so that during screening seal stresses of damaging magnitude need not be present along the engine periphery, but may be localized at the middle of the longer sides.

$$p = p_t = m_e / n_1 a^2 \quad (24)$$

In the case of a ceramic lid, linearly elastic behavior will be assumed in the lid up to fracture. Thus, Equation (22) may be used in such a case as long as the screening pressure it provides is less than the lid collapsing pressure $p_{ultimate}$ discussed in Section IV.

The screening pressure formulas developed in this section are summarized in Table 2. The pressures therein should be regarded as minimums. Larger pressure, applied through stepwise increments, can be used as long as they are below $p_{ultimate}$ and do not cause undesirably large lid deflections. The effect of using a pressure that is higher than the one specified in the table is to enlarge the portion of the lid periphery in which the extreme-fiber seal stress exceeds S_{accept} or has equalled S_{max_t} . The use of larger pressures may be particularly advisable when the lid is ductile, in view of the fact that the simplified curve OBED of Figure 11, on which the tabulated formulas are based, tends to over-estimate M_{max} .

Table 2.- Summary of Formulas for Appropriate Screening Pressure

Brittle Lid	Ductile Lid			
	$S_{accept} \leq S_{max_t}$	$S_{accept} > S_{max_t}$		
		Wide Seal		Narrow Seal
		$2n_2 \frac{a}{w} - 1 \geq 0$	$2n_2 \frac{a}{w} - 1 < 0$	
$p = \frac{S_{accept}}{\left(\frac{a}{w}\right)^2 n}$ [Eq. (22)]	$p = \frac{S_{accept} - \frac{6m_e}{w^2}}{2n_2 \frac{a}{w} - 1}$ [Eq. (23)]	$p = \frac{m_e}{n_1 a^2}$ [Eq. (24)]		

In order to use the formulas in Table 2, one must decide on a value of the minimum acceptable seal strength, S_{accept} . It is conceivable that the screener of a package will not have enough information about the sealing material to be able to specify a value for S_{accept} , but he might know that in the past a certain pressure p_I was considered suitable for screening a certain package, designated as package I, that employed the same sealing material as the package now under consideration, which will be designated as package II. Then the S_{max} produced in package I by its screening pressure p_I should be an acceptable maximum seal stress in package II. Thus, the following rule can be used to arrive at a value of S_{accept} for package II:

$$(S_{\text{accept}})_{\text{II}} = (S_{\text{max}})_{\text{I}} \text{ produced by } p_I \quad (25)$$

where the quantity on the right side is obtained from the appropriate formula of Table 1.

IV. LID COLLAPSING PRESSURE

It is important, in both screening and design, to be able to estimate the lid collapsing pressure p_{ultimate} , and in this section formulas are presented to facilitate making such an estimate. In presenting these formulas we consider separately lids of a brittle material, such as ceramic, and lids of a ductile material, such as Kovar, since the mechanism of collapse is different for both types.

A. Brittle-Material Lids.— For a lid made of perfectly brittle material it could be assumed that fracture will occur when the calculated maximum tensile stress σ_{max} in the lid equals the ultimate tensile strength σ_t of the material. Ceramics employed for microelectronic

packaging may not, however, be perfectly brittle in flexure. This is evidenced by the fact that quoted values of the bending modulus of rupture σ_b (also called "flexural strength") of such ceramics are somewhat higher than the quoted values of σ_t (see Section 2 of Appendix A). Therefore it may be somewhat more realistic to take the following as a criterion of fracture or collapse of supposedly brittle-material lids:

$$\sigma_{\max} = \sigma_b \quad (26)$$

In order to apply this criterion, one must have information on σ_{\max} as a function of the applied pressure p . Information of this kind is presented in Figure 12, which is based mainly on Reference 5 and which takes into account large-deflection effects. Figure 12 gives σ_{\max} through a dimensionless constant n_7 related to σ_{\max} as follows:

$$\sigma_{\max} = n_7 E \left(\frac{t}{a}\right)^2 \quad (27)$$

This relationship permits the collapse criterion (26) for brittle-material lids to be written as

$$n_7 = \frac{\sigma_b}{E} \left(\frac{a}{t}\right)^2 \quad (28)$$

The graphs of n_7 (Figure 12) require some discussion: Although data for n_1 are available for K values ranging from 0 to ∞ ($\arctan K$ ranging from 0 to $\pi/2$), data for n_7 are available only for the limiting cases of simple support ($K = \arctan K = 0$) and clamping ($K = \infty$, $\arctan K = \pi/2$). Therefore interpolation between a $K = \infty$ graph and a $K = 0$ graph of Figure 12 may sometimes be needed in estimating n_7 . A linear interpolation based on $\arctan K$, though non-rigorous, should be sufficiently accurate for

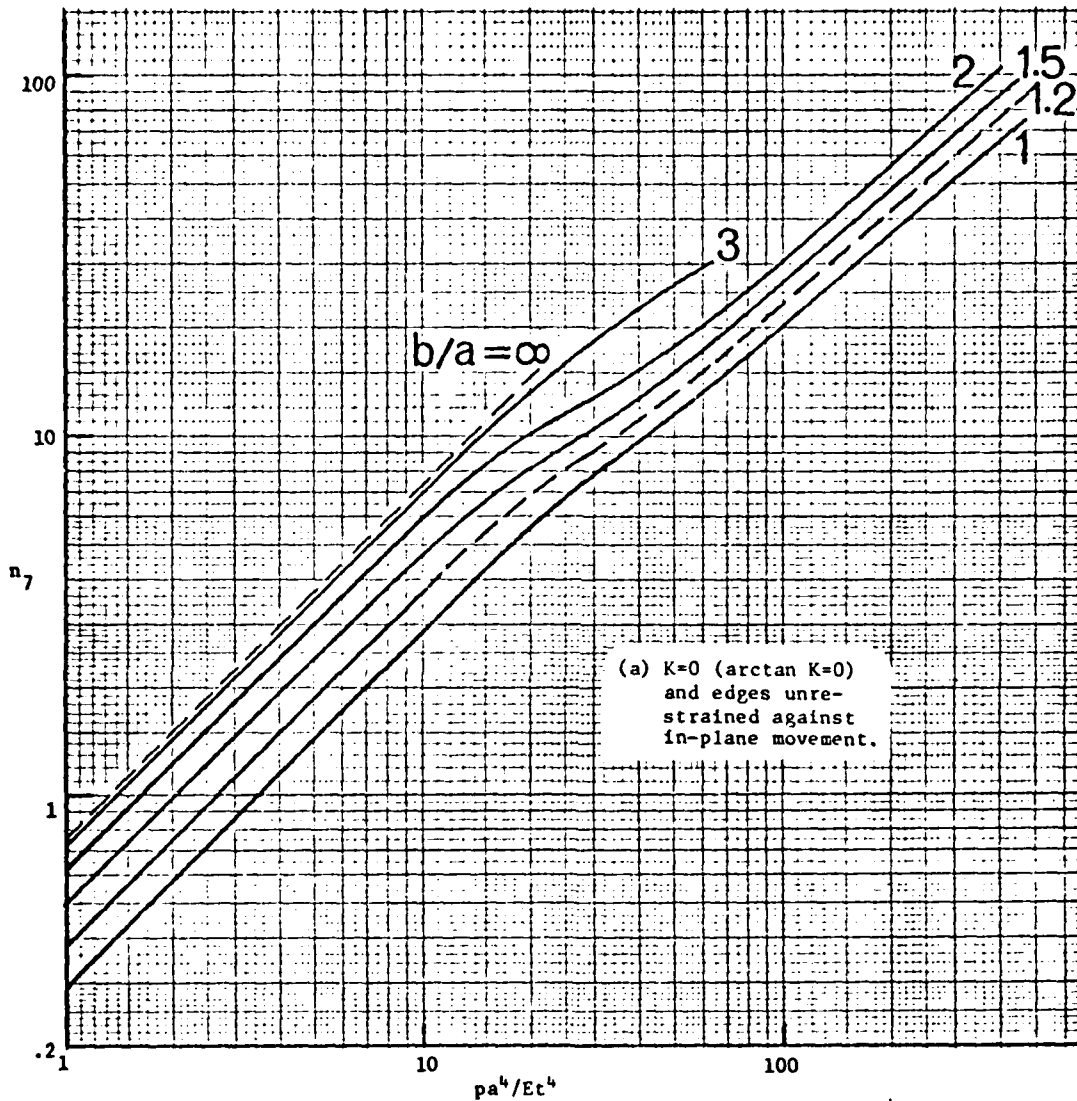


Figure 12.- Graphs for determining the maximum tensile stress σ_{\max} in uniformly loaded rectangular plates. Curves adapted from the following parts of Reference 5: (a) top graphs on p. 50, (b) middle graphs on p. 51, (c) middle graphs on p. 50, and (d) middle graphs on p. 52.

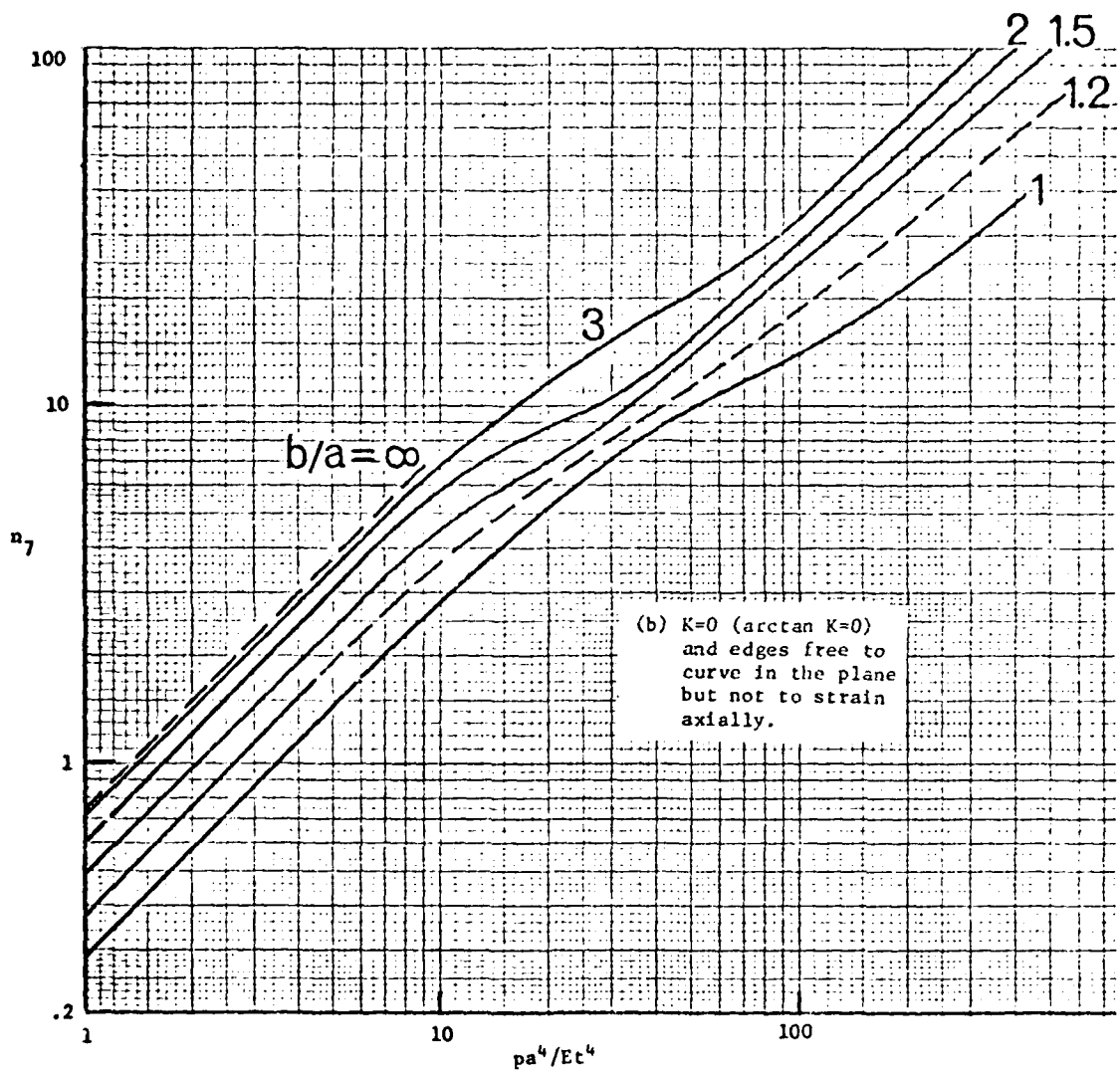


Figure 12.- Continued.

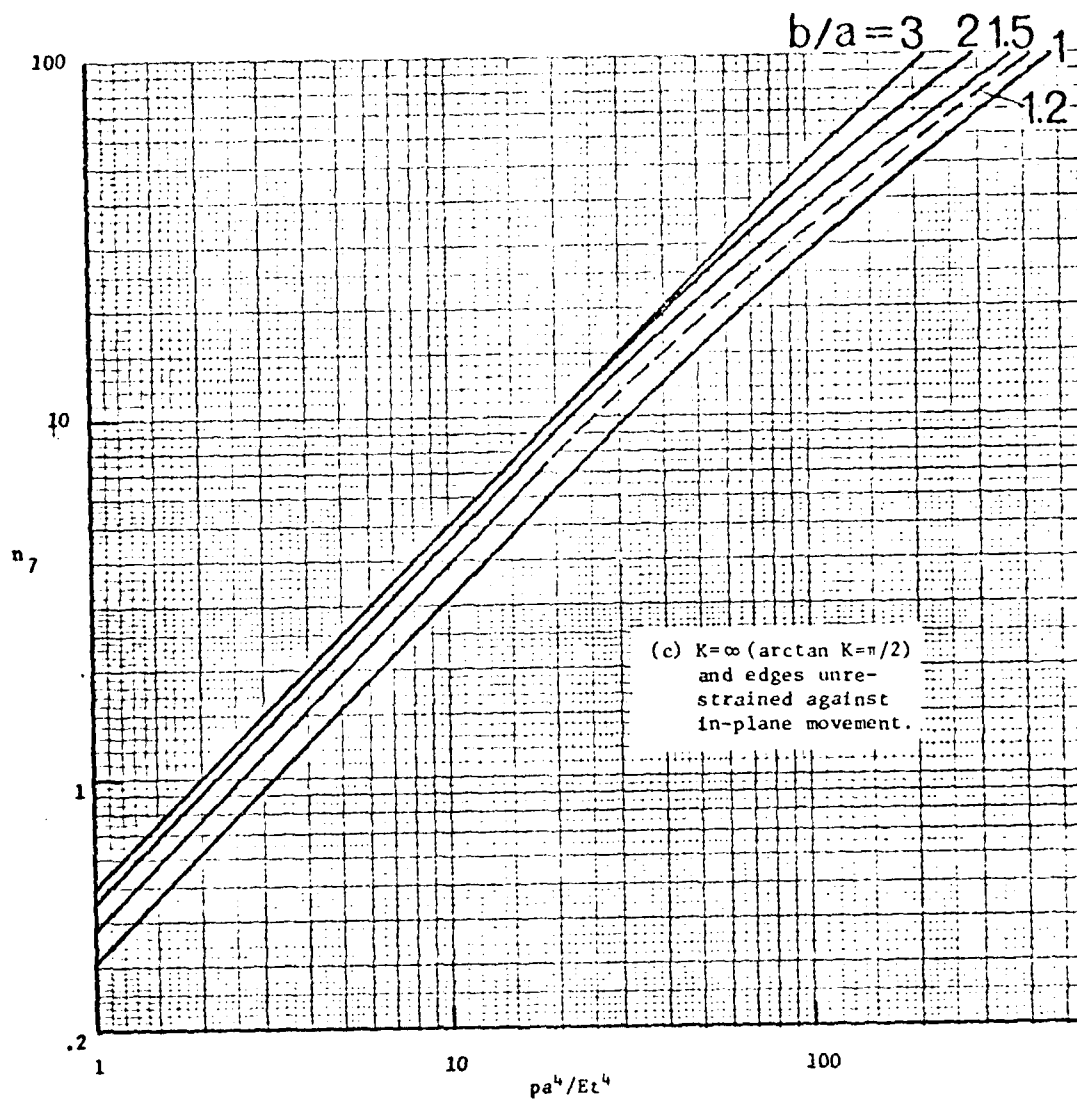


Figure 12.- Continued.

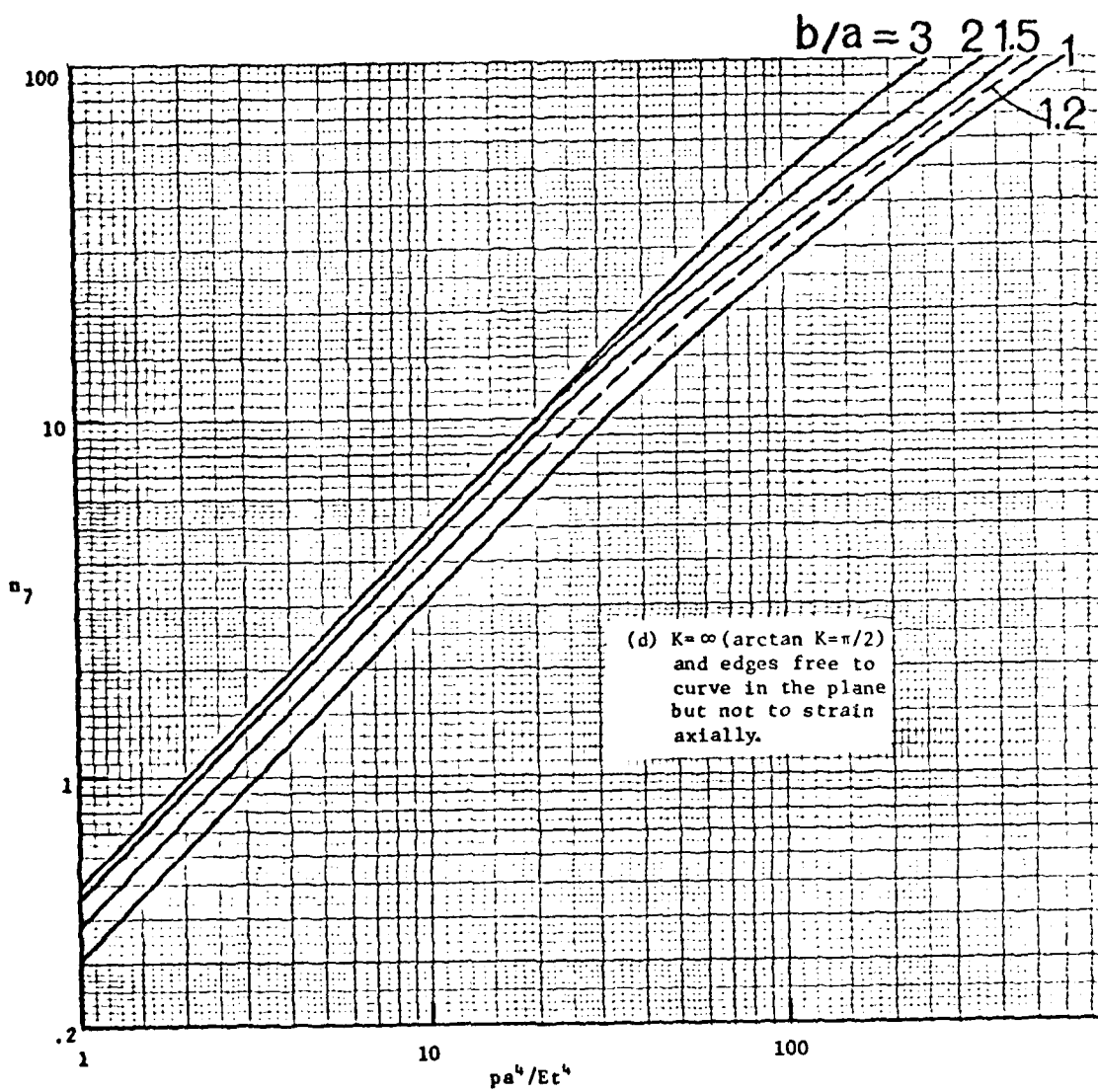


Figure 12.- Concluded.

practical purposes; for most large flat-packs the assumption $K = \infty$ would also be suitable. A second difficulty associated with the estimation of n_7 derives from the fact that the large-deflection behavior of a plate is sensitive to whatever restraint the plate edges are under, in regard to their movement in the plane of the plate. Graphs (a) and (c) of Figure 12 assume that such restraint is negligible; these graphs are felt to be appropriate when the wall stretching stiffness (e.g., $E_w h_w$ in the case of a uniform wall) is small compared to the lid stretching stiffness, $E_a t$. Graphs (b) and (d), on the other hand, assume that the edges are free to curve inward but not to strain along their length; these graphs are more appropriate for cases in which the wall stretching stiffness is large compared to the lid stretching stiffness. For most large flat-packs Figure 12(c) should be appropriate.

Let us denote by $p_{ultimate_1}$ the collapse pressure estimate obtained through the use of Equation (28) in conjunction with the graphs of Figure 12. Because of the above-discussed difficulties and uncertainties connected with the use of those graphs, there will always be some question as to the reliability of $p_{ultimate_1}$ as a true measure of the collapse pressure. It is therefore recommended that a second estimate, $p_{ultimate_2}$, be obtained by assuming σ_{max} to be the extreme-fiber stress at the edge of the lid in the middle of the long side, where, through Equation (9) and Figure 7, we have fairly accurate information about the bending moment as a function of both p and K in the small deflection régime. Accordingly, we write

$$\sigma_{max} = \frac{6M_{max}}{t^2} = \frac{6n_1 p a^2}{t^2} \quad (29)$$

then substitute this expression into Equation (26) and solve for p , to obtain

$$P_{ultimate_2} = \frac{\sigma_b}{6n_1} \left(\frac{t}{a}\right)^2 \quad (30)$$

as the second estimate of collapse pressure. Because it is based on a restricted search for σ_{max} (a search restricted to the middle of the long edge of the lid), $P_{ultimate_2}$ is likely to be an upper bound to the true collapse pressure. Therefore, it is advisable to select the smaller of $P_{ultimate_1}$ and $P_{ultimate_2}$ as the governing estimate of the collapse pressure of a brittle-material lid.

B. Ductile-Material Lids.- Collapse of ductile plates under lateral pressure is usually assumed to occur through the formation of plastic-hinge lines (yield lines). An analysis of a ductile lid on this basis (Reference 2) leads to the following collapse pressure:

$$P_{ultimate} = n_8 \frac{2(m_e + m)}{a^2} \quad (31)$$

where

$$n_8 = 4 + 3.2 \frac{a}{b} + 3.5 \left(\frac{a}{b}\right)^2 \quad (32)$$

and m_e and m are respectively the edge and interior fully plastic bending strengths of the lid. For a constant-thickness lid ($t_e = t$), m_e and m are equal. To facilitate the use of Equation (31) a graph of Equation (32) is plotted in Figure 13. Equation (31) is likely to be conservative, because the strengthening effect of membrane action was not considered in its derivation.

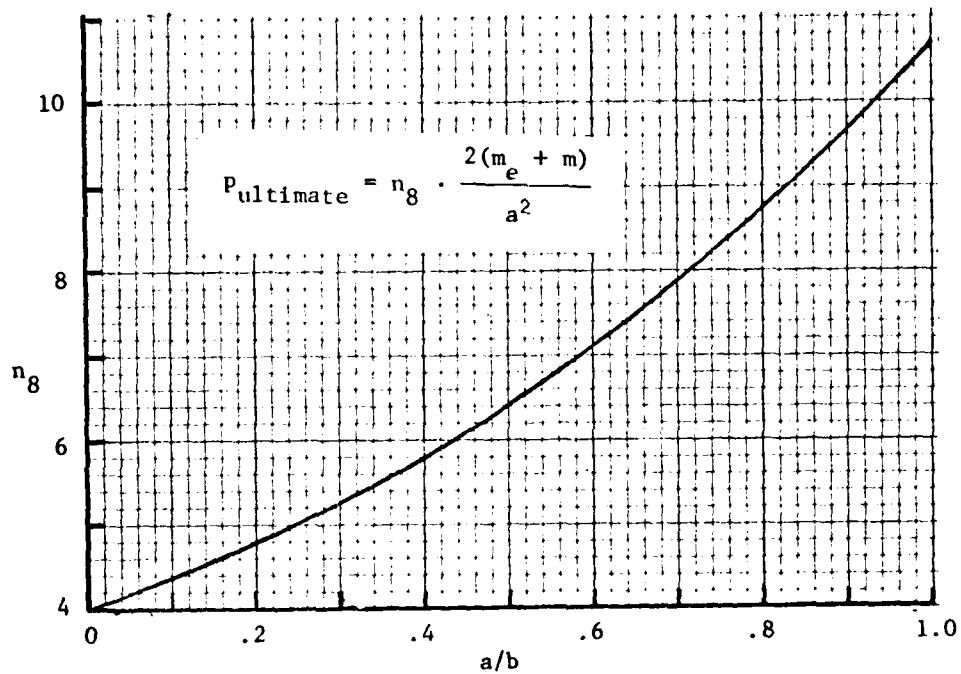


Figure 13.- Collapsing pressure $P_{ultimate}$ for ductile-material lids.

V. BASE COLLAPSING PRESSURE

If the base consists essentially of one component, say Kovar or ceramic, its collapsing pressure can be determined by the methods of the preceding section. It often happens, however, that in a metal package the original metal base will have a ceramic substrate bonded to it over most of its extent, thus, in effect, forming a new base which is a two-component composite like that shown in Figure 1 of Appendix B. It is this type of base whose $p_{ultimate}$ we will now estimate.

For the sake of concreteness we will take the upper component in Figure 1 of Appendix B to be the Kovar (or other metal) and the lower component to be the ceramic. The external pressure is therefore acting downward upon the upper component. As indicated in the figure, the Young's modulus, Poisson's ratio, and thickness of the upper component will be denoted by E_1 , ν_1 and t_1 , respectively; those of the lower component by E_2 , ν_2 and t_2 . The total thickness, $t_1 + t_2$, will be denoted by t .

Our basic assumptions will be that the base is a two-component clamped-edge plate obeying Hooke's law and undergoing small deflections, and that, in effect, collapse will occur due to cracking of the ceramic when the maximum tensile stress in the ceramic becomes equal to the flexural strength σ_b (i.e., modulus of rupture) of the ceramic.

The notation for the extreme-fiber stresses in the two components of the plate is shown in Figure 4 of Appendix B, where the stresses are denoted $\sigma_{x_{11}}$, $\sigma_{x_{12}}$, etc. (the logic behind the subscripts is self-evident). Visualizing the curvatures of the clamped plate under external pressure, we can anticipate that there are two candidates for the maximum tensile stress

in the ceramic. They are the stress $\sigma_{x_{21}}$ at the middle of the long sides (i.e., at $x=0$, $y=b/2$) and the stress $\sigma_{x_{22}}$ at the middle of the plate ($x=a/2$, $y=b/2$), (Under internal pressure, i.e., upward or negative pressure, the maximum tensile stress candidates would be $\sigma_{x_{22}}$ at the middle of the long sides and $\sigma_{x_{21}}$ at the center of the plate.) Both candidate maximum stresses have to be evaluated, and the larger governs.

The theory for evaluating these stresses is developed in Appendix B, where it is shown that existing data for homogeneous (single-component) plates can be used for this purpose. On the basis of this theory the stress calculation consists of the following main steps: First compute the plate flexural stiffness D and flexural Poisson's ratio ν through the sequence of equations (1) through (7) of Appendix B. Secondly, from the appropriate line of Table 1 of Appendix B, evaluate the bending moments M_x and M_y at two locations, the center of the plate and the middle of the longer edges. Those bending moments apply, strictly speaking, only to the case $\nu = 0.3$. The error will usually be very small if they are assumed to hold also for the value of ν obtained from Equation (5) of Appendix B. However, if desired, for each location one can readily compute corrected bending moments M'_x and M'_y from Equations (19) or (20) of Appendix B if the ν yielded by Equation (5) has a value other than 0.3. Finally, with the bending moments known for each location, Equations (17) of Appendix B are used to calculate the candidate ceramic tensions. Specifically, the third equation of the set (17), with M_x and M_y set equal to the bending moments or corrected bending moments for the middle of the longer sides, will give the $\sigma_{x_{21}}$ ceramic stress at that location; and the fourth equation

of the set, with M_x and M_y being those that apply to the center of the plate, will give the ceramic stress σ_{x22} at the center of the plate. The quantities \bar{v} and \bar{S} required in Equations (17) will already have been determined in the course of calculating D and v . If $M_x = M_y = M$, Equations (18) may be used instead of (17).

The calculation procedure just described will be demonstrated in Section VIII. In connection with that demonstration, a suggestion will also be made as to the handling of plastic hinges that might develop in the Kovar if there is a small gap between the periphery of the substrate and the walls of the package. The possibility of plastic hinges (at sufficiently high pressures) arises because in the region of this gap the Kovar must provide the edge bending moments of a clamped plate without any help from the ceramic.

VI. LID DEFLECTION

The maximum deflection δ_{\max} of the lid under any pressure p will occur at the center of the lid. Both the designer and the user must concern themselves with this deflection, in order to insure that during any screening the lid will not come in contact with the contents of the package. In this section we present formulas and graphs for estimating δ_{\max} . We consider separately the brittle-material and ductile-material lids. In the first case, plasticity (departure from Hooke's law) will play a negligible role; in the second case it will play a significant role.

A. Brittle-Material Lids.- An analysis based on the small-deflection theory of elastic plates is carried out in Appendix A of Reference 4 and leads to the following result:

$$\delta_{\max} = n_4 \frac{pa^4}{D} = 12(1 - \nu^2) \frac{p}{E} \left(\frac{a}{t}\right)^3 an_4 \quad (33)$$

where n_4 is the function of K and b/a plotted in Figure 14. With ν taken as 0.3, this formula reduces to

$$\delta_{\max} = 10.92 \frac{p}{E} \left(\frac{a}{t}\right)^3 an_4 \quad (34)$$

It is well known, however, that small-deflection theory tends to overestimate the deflection. Figure 15 therefore presents curves from which a correction factor n_5 , based on large-deflection theory, can be estimated. (The graphs of Figure 15 are for the same four boundary conditions as those of Figure 12, and the earlier discussion of those boundary conditions is pertinent here as well.) With this correction factor included, the above formulas now read

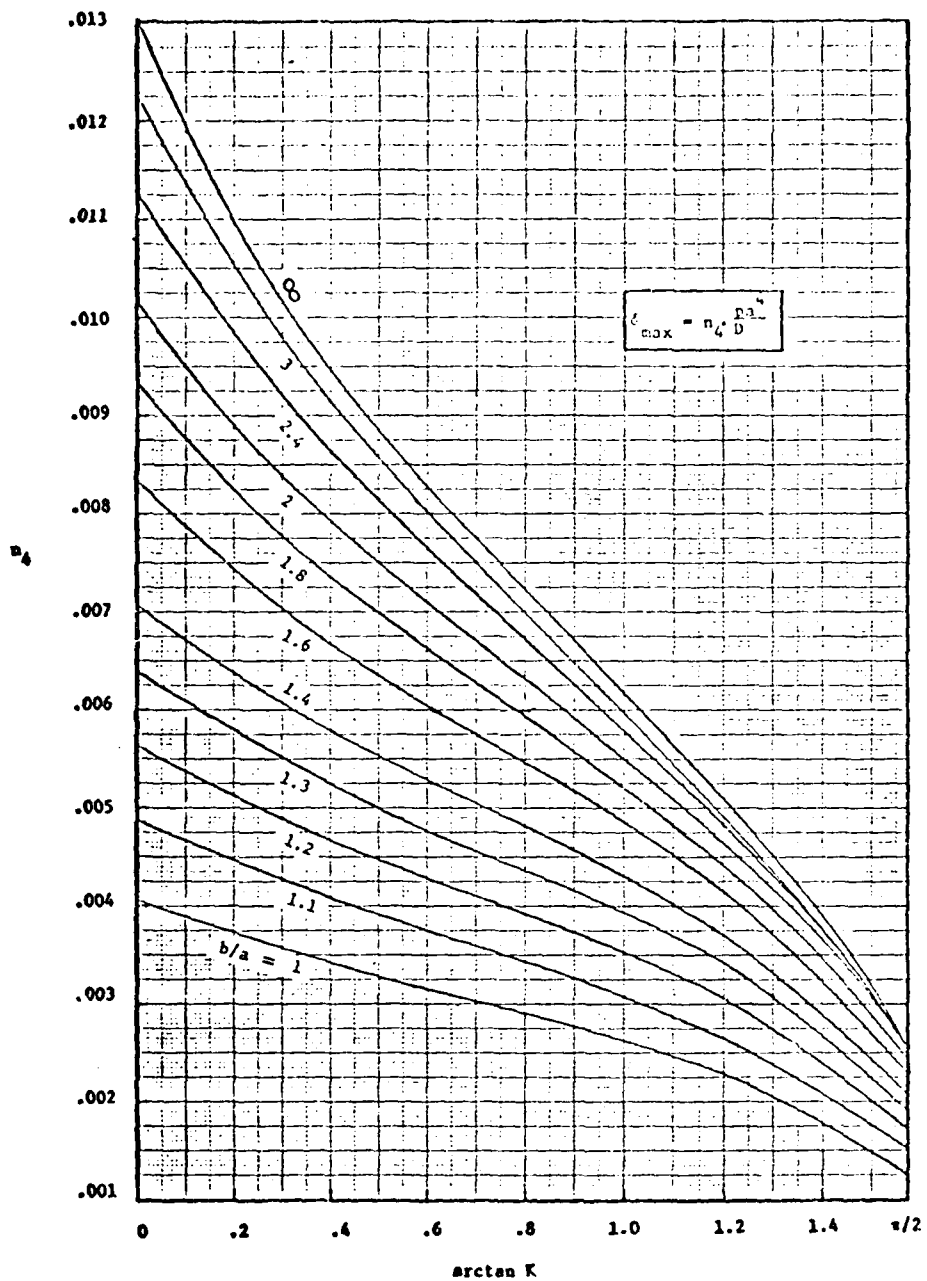


Figure 14.- Center deflection of a uniformly loaded rectangular plate that obeys Hooke's law with edges elastically restrained against rotation (small-deflection theory).

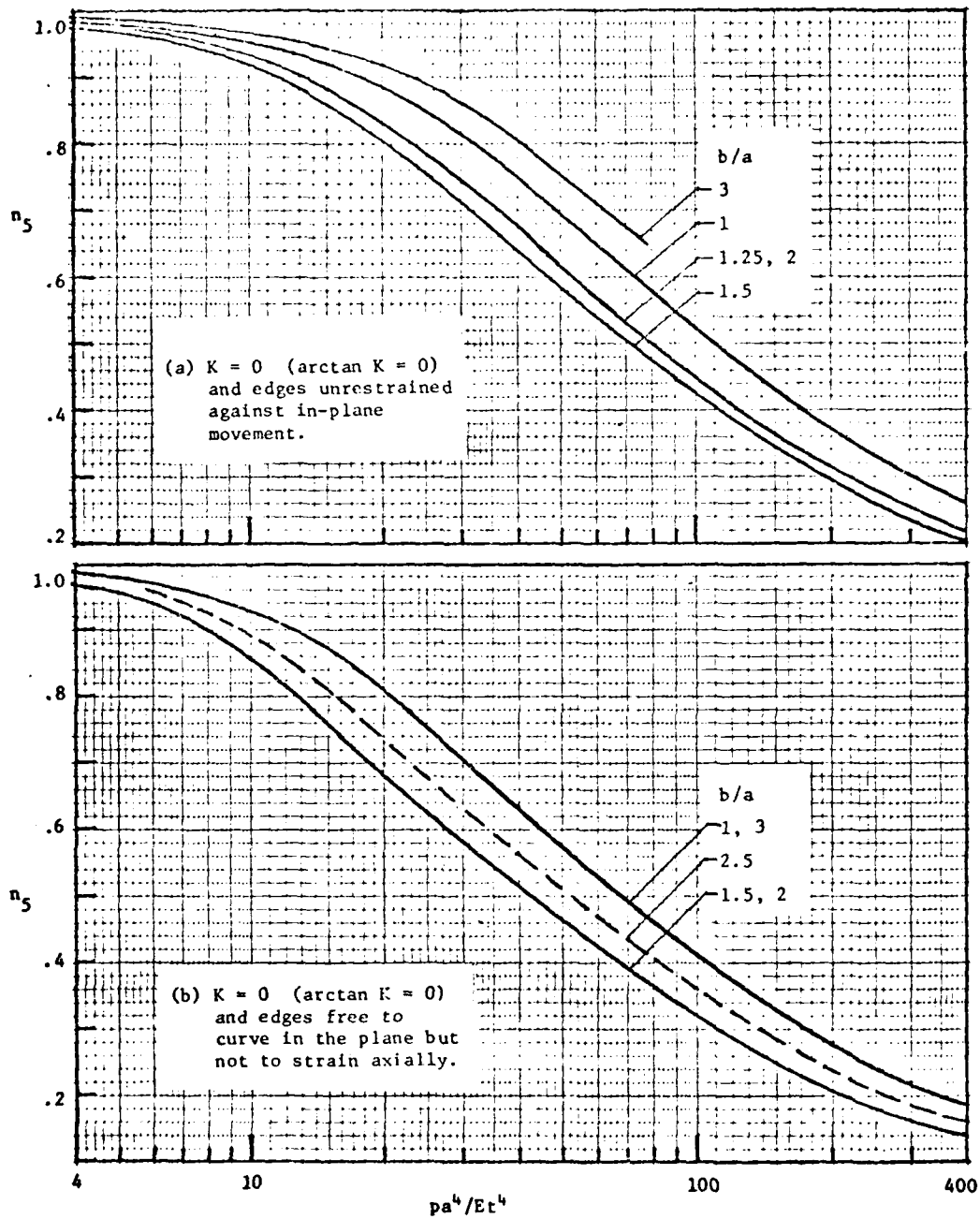


Figure 15.- Correction factors based on large-deflection theory to be applied to small-deflection theory value of center deflection of elastic lid ($\nu=0.3$). Data adapted from: (a) P. 181 of Ref. 6 and p. 150 of Ref. 5. (b) P. 152 of Ref. 5. (c) P. 190 of Ref. 6 and p. 154 of Ref. 5. (c) P. 156 of Ref. 5.

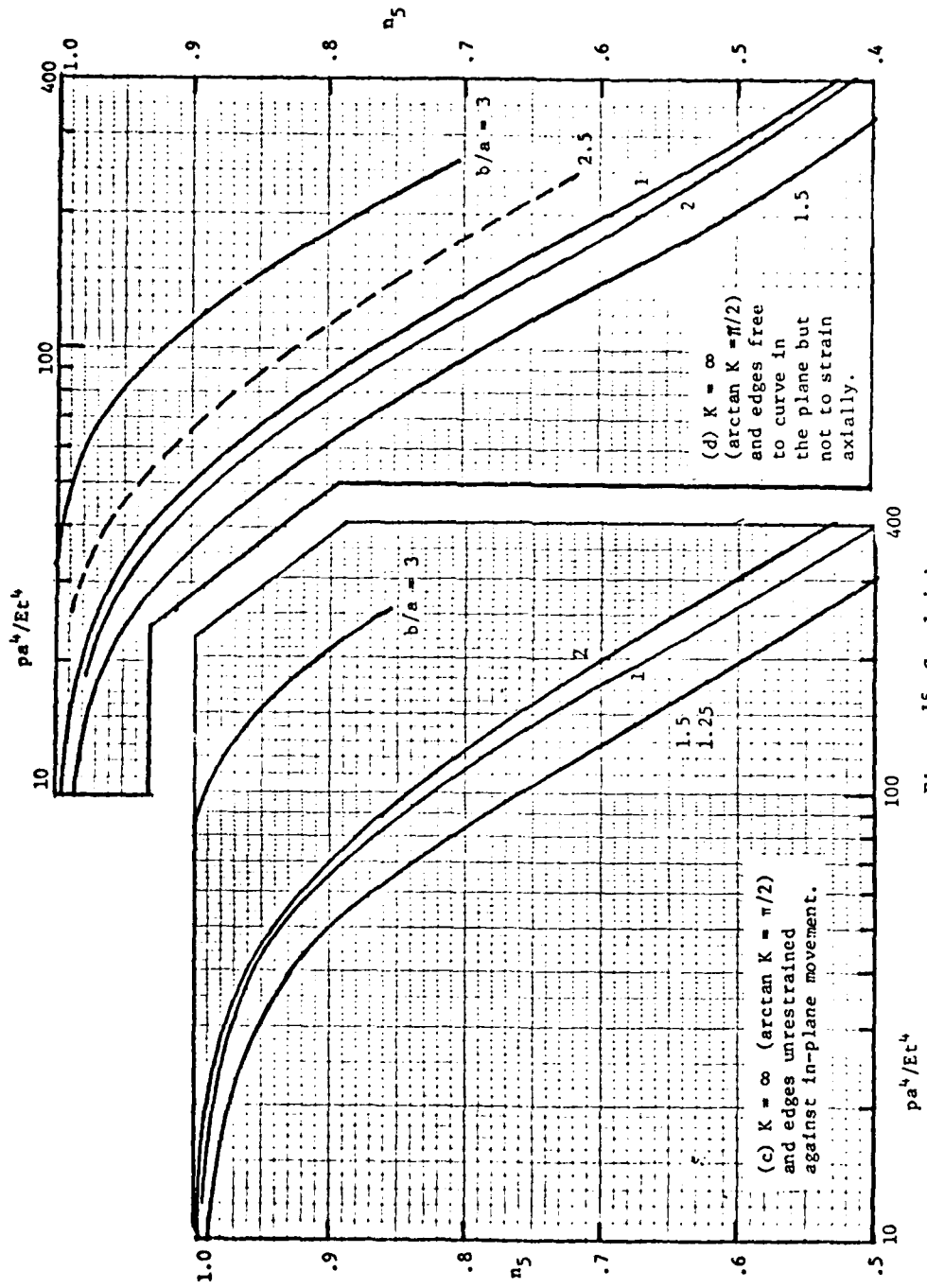


Figure 15.-Concluded.

$$\delta_{\max} = 12(1-\nu^2) \frac{P}{E} \left(\frac{a}{t}\right)^3 a n_4 n_5 \approx 10.92 \frac{P}{E} \left(\frac{a}{t}\right)^3 a n_4 n_5 \quad (35)$$

This equation can be considered valid for brittle-material lids at all pressures up to the lid-collapsing pressure p_{ultimate} .

B. Ductile-Material Lids.- For lids of a ductile material, like Kovar, Equation (35) will apply in the initial stages of pressure application. When the pressure becomes high enough, however, Hooke's law breaks down because of the initiation of plastic flow in the material. As the pressure is increased beyond this point, the regions of plastic deformation are enlarged and Equation (35) becomes increasingly in error on the low side. Finally, the collapse pressure p_{ultimate} is reached, at which the lid deflections increase virtually without limit.

The precise determination of lid deflections in a ductile lid beyond the range of validity of Hooke's law is a difficult computational task which will not be attempted here. Instead, a simplified model of the lid's behavior will be proposed which will lead to an approximate estimate of the central deflection with very little computational effort.

The proposed model breaks the entire load-central deflection history into three régimes which are represented by the curve segments OA, AB and BC of Figure 16. The first segment, OA, corresponds to linearly elastic material behavior and it is the initial portion of the load-deflection curve OG defined by Equation (35). The second segment, AB, is part of the curve DE, which is the pressure-versus-deflection curve of a simply supported linearly elastic plate subjected to increasing pressure p in conjunction with a constant and uniform restraining moment of m_e per unit width along its periphery. And the third segment, BE, represents the indeterminate deflections occurring under the collapse pressure p_{ultimate} .

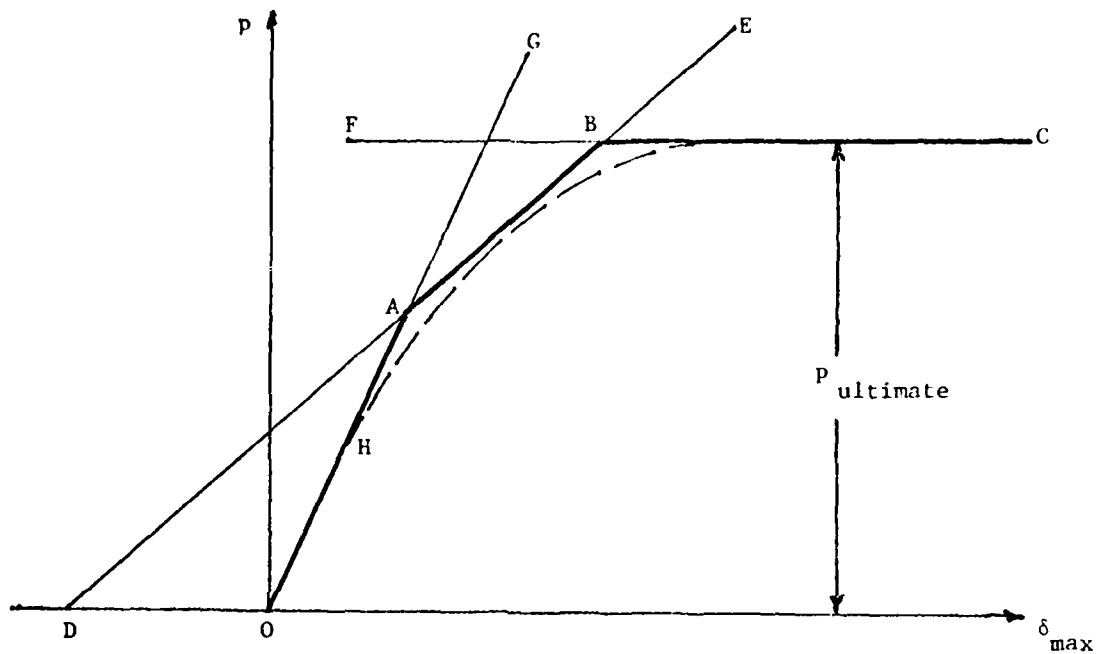


Figure 16.-Simplified graph (OABC) of central deflection of ductile lid as a function of pressure.

Thus, the model assumes an abrupt transition at A from a truly elastic behavior (OA) to a regime AB in which the fully plastic bending moment is developed all around the boundary while the interior of the lid still behaves elastically, then another abrupt transition at B to a regime BC of fully developed interior as well as exterior yield lines creating a collapse mechanism. In actuality, gradual transitions occur from one regime to the next, as suggested by the dashed curve, but such transitions are not included in the present model.

In order to make use of the proposed model, one must have an equation for the middle portion, AB, of the graph of pressure versus deflection. On the basis of linear elastic small-deflection plate theory (Figure 14 of the present paper and pp. 162-165 of Reference 3), the following equation can be derived for the line DE of which AB is a part:

$$\delta_{\max} = 12(1-\nu^2) \frac{p}{E} \left(\frac{a}{t}\right)^3 an_4(0) - \frac{m_e a^2}{D} n_9 \quad (36)$$

where $n_4(0)$ is the value of n_4 from Figure 14 for $K=0$, and n_9 is the following functions of b/a :

$$n_9 = \frac{4}{\pi^3} \sum_{m=1,3,5,\dots}^{\infty} \frac{\sin(m\pi/2)}{m^3} \left[1 - \operatorname{sech} \left(\frac{m\pi}{2} \frac{b}{a} \right) \right] \quad (37)$$

The first term on the right side of Equation (36) is the central deflection of a simply supported plate under a pressure p , and the second term is the diminution of that deflection due to the fully plastic restraining moment m_e along the boundary. Making use of Equation (1) we may rewrite Equation (36) as

$$\delta_{\max} = \frac{12(1-\nu^2)a^2}{Et^3} [pa^2n_4(0) - m_e n_9] \quad (38)$$

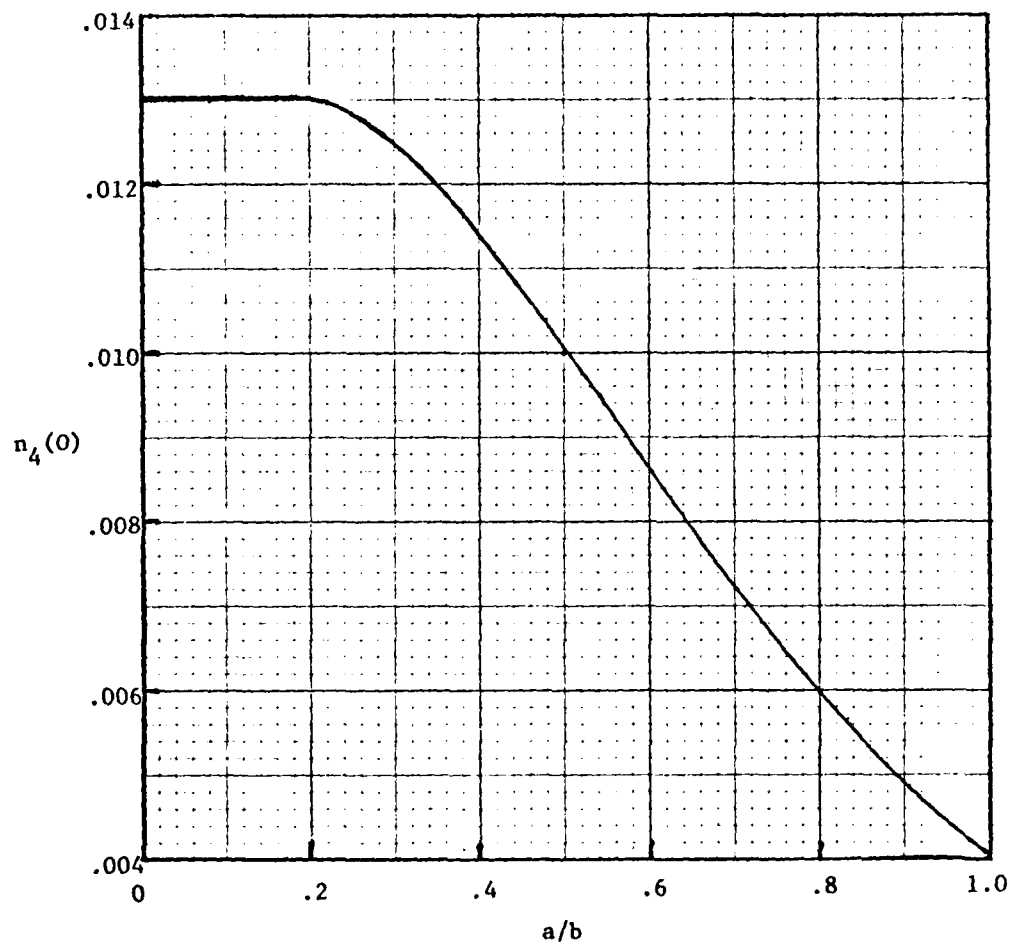


Figure 17.- Graph of $n_4(0)$ as a function of a/b .

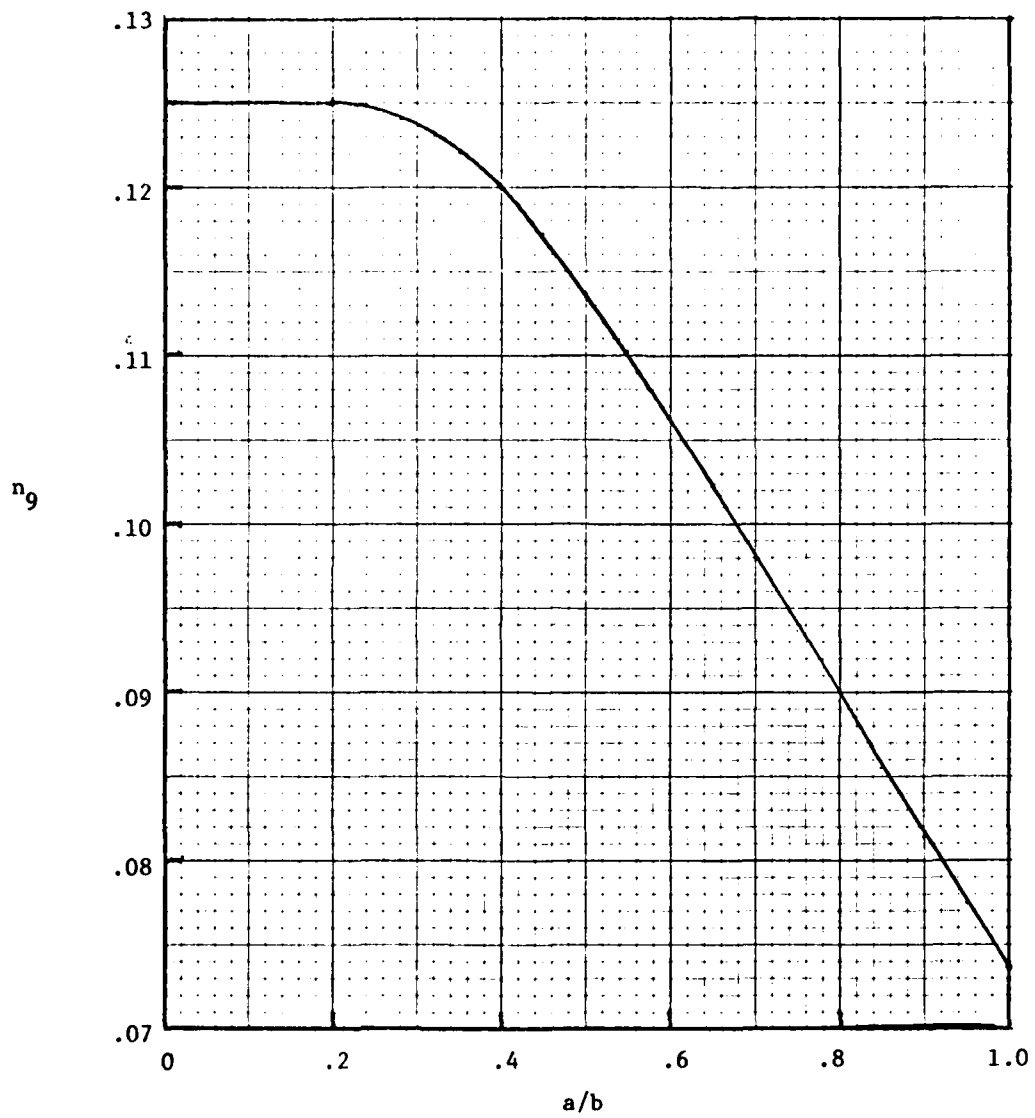


Figure 18.- Graph of n_g as a function of a/b .

and we note that for $\nu = 0.3$, $12(1-\nu^2)$ equals 10.92. To further facilitate the use of Equation (38), graphs of $n_4(0)$ and n_9 are given in Figures 17 and 18, respectively.

On the basis of the above discussion, we can now give the following rule for estimating the central deflection δ_{\max} of a ductile-material lid:

For $p \leq p_{\text{ultimate}}$, δ_{\max} is the larger of δ_{\max_1} }
 δ_{\max_2} , where δ_{\max_1} is the deflection computed } (39)
 from Equation (33) or (34) and δ_{\max_2} is the de-
 flection computed from Equation (38). For
 $p > p_{\text{ultimate}}$, δ_{\max} is arbitrarily large.

VII. FLATPACKS IN A CENTRIFUGE

As part of the total screening process, packages are frequently spun in a centrifuge in such a way that the centrifugal force tends to push the lid into the cavity. As far as the lid alone is concerned, this centrifugal force is equivalent to a lateral pressure of Gtd , where

d = specific weight (weight per unit volume) of the lid material

t = thickness of lid

G = centripetal acceleration in units of g (acceleration of gravity)

If t is in inches and d in lbs per cubic inch, the formula

$$P_{\text{equivalent}} = Gtd \quad (40)$$

will give the effective pressure in psi due to a centrifuge acceleration of G g 's. Alternatively, given any pressure p , we have from Equation (40) the following formula for the number of g 's of centrifuge acceleration

equivalent to that pressure:

$$G_{\text{equivalent}} = \frac{p}{td} \quad (41)$$

As an example of the use of this formula, let us consider a lid of .030 in. thickness and .302 lb/in.³ specific weight and ask how many g's of centrifuge acceleration are equivalent to a lateral pressure of 30 psi. From Equation (41) we obtain the following answer:

$$G_{\text{equivalent}} = \frac{30}{(.030)(.302)} = 3310 \text{ (g's)} \quad (42)$$

By virtue of the equivalence relation (40), all the formulas and graphs of the preceding sections can be made to apply to a package in a centrifuge simply by replacing the symbol p everywhere by Gtd . In this way, for example, the following formula is obtained from Equation (35) for the central deflection of a linearly elastic lid of a package in a centrifuge:

$$\sigma_{\text{max}} = 10.92 \frac{Gtd}{E} \left(\frac{a}{t}\right)^3 a n_4 n_5 \quad (43)$$

where n_5 is to be obtained from the graphs of Figure 15 with the abscissa labels therein changed to $Gtda^4/Et^4$. Similarly, Equation (12) gives the following formula for the maximum tensile stress in the seal when $Gtd < p_t$:

$$S_{\text{max}} = Gtd \left(\frac{a}{w}\right)^2 n \quad (44)$$

It should be noted that the interaction among the base, the walls, and the lid is slightly different for a package in a centrifuge than for the same package under hydrostatic pressure. Reference 2 discusses a refinement in the α computation to take this difference into account.

However, this refinement is omitted here, because the improvement will usually not be sufficient to justify the labor involved.

VIII. NUMERICAL EXAMPLES

Here we pose and solve a number of problems in order to demonstrate how the formulas and graphs of the preceding sections can be used.

Example 1.- A wide-seal uniform-wall constant-thickness-lid Kovar package of the type shown in Figure 1 has the following dimensions (in inches);

$$a=b=.92 \quad t=t_e=.015 \quad h=.125 \quad w=.040$$

and the following material properties:

$$E = E_w = 20 \times 10^6 \text{ psi} \quad \nu = \nu_w = .3 \quad \sigma_y = 50 \text{ ksi} \quad \sigma_b = 107 \text{ ksi}$$

We wish to find the maximum tensile stress S_{\max} in the seal and the central deflection δ_{\max} of the lid due to an external screening pressure p of 30 psi; also the pressure p_{ultimate} required to collapse the lid.

We first determine all the constants that will be needed to solve this problem. In accordance with Equation (5a) we take α to be 2, after which Equation (6b) and Figure 5 give

$$K = \frac{4}{\pi^2} \frac{.92}{.125} \left(\frac{.040}{.015} \right)^2 = 113 \quad \arctan K = 1.56$$

(The closeness of $\arctan K$ to $\pi/2$ indicates that in effect the walls are clamping the edges of the lid.) Entering Figures 7, 8, 13, 14, 17 and 18 with $b/a = 1$ and $\arctan K = 1.56$, we obtain

$$n_1 = .051 \quad n_2 = .443 \quad n_8 = 10.7 \quad n_4 = .00125$$

$$n_4(0) = .00406 \quad n_9 = .0737$$

Also, for $p = 30$ psi, we have

$$\frac{pa^4}{Et^4} = \frac{30}{20 \times 10^6} \left(\frac{.92}{.015} \right)^4 = 21.1$$

Since the wall cross-sectional area (wh) is only around one-third of the lid cross-sectional area (ta) and $\arctan K$ is very close to $\pi/2$, we shall use part (c) of Figure 15 to find

$$n_5 = .981$$

Equation (13a) gives

$$n = 6(.051) + 2(.443) \left(\frac{.04}{.92} \right) - \left(\frac{.04}{.92} \right)^2 = .343$$

Finally, from Equation (2),

$$m = m_e = (107,000)(.015)^2/6 = 4.0125 \text{ in.-lb/in.}$$

whence (Eq. (15))

$$p_t = \frac{m_e}{n_1 a^2} = \frac{4.0125}{(.051)(.92)^2} = 93 \text{ psi}$$

and the right sides of Equations (35) and (38) are, respectively,

$$\delta_{\max_1} = 10.92 \left(\frac{30}{20 \times 10^6} \right) \left(\frac{.92}{.015} \right)^3 (.92)(.00125)(.981) = .0043 \text{ in.}$$

$$\delta_{\max_2} = \frac{(10.92)(.92)^2}{(20 \times 10^6)(.015)^3} [30(.92)^2(.00406) - (4.0125)(.0737)]$$

$$= .1369 [.1031 - .2957] = -.026 \text{ in.}$$

We now have all the constants needed to determine the quantities we are looking for. We start with S_{\max} . Since Kovar is ductile and the screening pressure p (= 30 psi) is less than the transition pressure p_t (= 93 psi), the upper left hand box of Table 1 applies. It gives

$$S_{\max} = 30 \left(\frac{.92}{.04} \right)^2 (.343) = 5443 \text{ psi}$$

as the maximum tensile stress in the seal. This is a safe stress if the solder is one of the higher strength types, such as a gold-tin alloy, and probably still safe, but with less margin, if the solder is a lead-tin alloy.

To determine the central deflection of the lid we make use of rule (39) which states that δ_{\max} is the larger of δ_{\max_1} and δ_{\max_2} . Thus

$$\delta_{\max} = \delta_{\max_1} = .0043 \text{ in.}$$

This is 29% of the lid thickness but only 3% of the cavity depth. The fact that δ_{\max_1} governed indicates that the lid is still in the linearly elastic region OA of the simplified pressure-deflection curve of Figure 16.

The collapse pressure is given by Equation (31) as

$$p_{\text{ultimate}} = (10.7) \frac{2(4.0125 + 4.0125)}{(.92)^2} = 203 \text{ psi}$$

which is well above the screening pressure of 30 psi.

Example 2.- Suppose that 30 psi is considered a satisfactory screening pressure for the package of Example 1 (to be referred to as package I).

What screening pressure would be appropriate for a second package (package II) identical in all respects to package I except for the dimension b, which has been increased to 1.92 in.?

For package II we still have $\arctan K = 1.56$, but

$$\frac{b}{a} = \frac{1.92}{.92} = 2.1 \quad \frac{a}{b} = .48$$

Figures 7 and 8 now give

$$n_1 = .083 \quad n_2 = .513$$

and from Equation (13a) we obtain the following value of n for package II:

$$n = 6(.083) + 2(.513)\left(\frac{.04}{.92}\right) - \left(\frac{.04}{.92}\right)^2 = .541$$

Then, from Equation (16),

$$S_{\max_t} = \frac{(4.0125)(.541)}{(.083)(.040)^2} = 16,346 \text{ psi}$$

In accordance with the discussion preceding Equation (25), a suitable screening pressure for package II is one that will produce the same S_{\max} in its seal as 30 psi produced in the seal of package I, namely 5443 psi. Thus, in the formulas of Table 2 we may take S_{accept} to be 5443 psi. Since this is smaller than S_{\max_t} , the leftmost formula of Table 2 applies. It gives the following appropriate screening pressure for package II:

$$p = \frac{5443}{\left(\frac{.92}{.04}\right)^2 (.541)} = 19 \text{ psi}$$

Example 3.- Let us repeat Example 1, assuming now that the seal is a solderless electrically welded seal of the narrow type (Figure 3(b) with

$w_s = .010$ in., and that the edge of the lid is thinned to a thickness of $t_e = .004$ in. while the main thickness t remains .015 in.

The calculations of Example 1 up to, but not including, the evaluation of n are valid here. Since the seal is now of the narrow type, Equation (13b) must be used for determining n . With $w_s = .010$ in., we have $e = .035$ in., and Equation (13b) then gives

$$n = \left[.051 - \frac{1}{2} \left(\frac{.04}{.92} \right)^2 \right] \frac{(.04)^2}{(.035)(.010)} = .229$$

Furthermore, while the fully plastic bending strength m in the main part of the lid remains 4.0125 in.-lb/in., in the thinned edge it goes down to

$$m_e = (107,000)(.004)^2/6 = 0.2853 \text{ in.-lb/in.}$$

according to Equations (2), whence

$$p_t = \frac{m_e}{n_1 a^2} = \frac{0.2853}{(.051)(.92)^2} = 6.6 \text{ psi}$$

The right side of Equation (33) remains at the value $\delta_{\max_1} = .0043$ in., but the new m_e value changes the right side of Equation (38), so that now

$$\delta_{\max_2} = \frac{(10.92)(.92)^2}{(20 \times 10^6)(.015)^3} [30(.92)^2(.00406) - (.2853)(.0737)] = .0112 \text{ in.}$$

Proceeding as in Example 1, we note that the screening pressure p (= 30 psi) is now greater than p_t (= 6.6 psi) and that the seal is now a narrow one. Therefore the bottom right box of Table 1 applies, giving

$$S_{\max} = \frac{.2853}{(.01)(.035)} \left[1 - \frac{1}{2(.051)} \left(\frac{.04}{.92} \right)^2 \right] = 800 \text{ psi}$$

as the maximum seal stress produced in the course of applying p . Since the seal material in this case is Kovar with an ultimate tensile strength of at least 75,000 psi (See Section 5 of Appendix A), the 800 psi maximum seal stress can be considered harmless to the integrity of the seal. From the absence of p in the formula for S_{\max} , it can also be concluded that S_{\max} would be the same for all screening pressures greater than the transition pressure $p_t = 6.6$ psi. The effect of using screening pressures greater than 6.6 psi is simply to spread the length of seal periphery over which the S_{\max} of 800 psi is developed.

Turning to the deflections and again using rule (39), we obtain

$$\delta_{\max} = \delta_{\max_2} = .0112 \text{ in.}$$

This is 2.6 times larger than the δ_{\max} produced by the same screening pressure in the lid of Example 1, but still only a small percentage (9%) of the total cavity depth.

Finally, from Equation (31) we estimate the collapse pressure to be

$$p_{\text{ultimate}} = (10.7) \frac{2(.2853 + 4.0125)}{(.92)^2} = 109 \text{ psi}$$

which is approximately half that of the lid of Example 1.

The present example serves to show that a thinned edge and lid plasticity can combine to provide a barrier against severe stressing of the seal under external pressure, but at the same time tend to increase the lid central deflection and reduce the lid collapsing pressure.

Example 4.— Assume that the package of Example 1 has its base changed from Kovar to ceramic with a thickness of .025 in., a modulus of elasticity of 50×10^6 psi, and a flexural strength of 65 ksi. What external pressure p_{ultimate} will cause the base to crack?

We shall imagine the package turned upside down, so that the base becomes in effect a lid with

$$t = .025 \text{ in.} \quad E = 50 \times 10^6 \text{ psi} \quad \sigma_b = 65 \text{ ksi}$$

and, in accordance with the discussion in Section IV A, we shall make two estimates of p_{ultimate} , one based on Equation (28), the other on Equation (30), and select the smaller of the two.

We start with Equation (28), which gives

$$n_7 = \frac{65 \times 10^3}{50 \times 10^6} \left(\frac{.92}{.025} \right)^2 = 1.76$$

as the values of n_7 required to cause fracture. The extensional stiffness Eat of the ceramic base is much higher than the corresponding stiffness $E_w h_w$ of the wall. Therefore parts (a) and (c) of Figure 12 are the ones that apply. Assuming that the walls essentially clamp the edges of the base* (as they do the lid), we narrow the choice further to part (c) alone. It gives the following as the value of pa^4/Et^4 needed to achieve an n_7 of 1.76 with a b/a of 1.0:

$$\frac{pa^4}{Et^4} = 5.6$$

whence the pressure required to crack the base is

$$p_{\text{ultimate}_1} = \frac{5.6 Et^4}{a^4} = \frac{(5.6)(50 \times 10^6)(.025)^4}{(.92)^4} = 153 \text{ psi}$$

Proceeding now on the basis of Equation (30), we first compute (Eq. (8b))

*This assumption will be justified presently when arctan K is computed and found to be quite close to $\pi/2$.

$$K = \frac{4}{\pi^2} \frac{.92}{.125} \frac{50}{20} \left(\frac{.040}{.015} \right)^2 = 61 \quad \arctan K = 1.554$$

Then from Figure 7, $n_1 = .05$. Therefore Equation (30) gives

$$P_{\text{ultimate}_2} = \frac{65,000}{6(.05)} \left(\frac{.025}{.92} \right)^2 = 160 \text{ psi}$$

as the second estimate. This is slightly higher than the previous estimate and is therefore not the governing one. We are left with

$$P_{\text{ultimate}} = P_{\text{ultimate}_1} = 153 \text{ psi}$$

as the best estimate of the pressure required to fracture the ceramic base.

Example 5.- Suppose the package of Example 4 to be placed in a centrifuge in such a way that the centrifugal force tends to push the ceramic base into the cavity. Taking the specific gravity of the ceramic to be 3.85, determine how many g's of centrifuge acceleration are required to crack the base.

We first convert the specific gravity of 3.85 to a specific weight, d , by multiplying it by the specific weight of water, which is .0361 lbs/in³. The result is

$$d = .139 \text{ lbs/in}^3$$

The pressure required to crack the base is 153 psi, from Example 4. The equivalence relation (41) therefore gives

$$G = \frac{153 \text{ lb/in}^2}{(.025 \text{ in.})(.139 \text{ lb/in}^3)} = 44,000 \text{ g's}$$

of centrifuge acceleration required to crack the base.

Example 6.- A stepped-wall wide-seal package with a constant-thickness Kovar lid has the following dimensions (in inches):

$$\begin{array}{lll} a = .365 & b = .670 & t = t_e = .025 \\ h = .082 & h_1 = .060 & h_2 = .025 \\ w = .040 & w_1 = .049 & w_2 = .071 \end{array}$$

and the following mechanical properties:

$$\begin{array}{ll} E = E_w = 20 \times 10^6 \text{ psi (Kovar)} & E_1 = E_2 = 8.6 \times 10^6 \text{ psi (glass)} \\ \nu = \nu_w = 0.3 & \nu_1 = \nu_2 = 0.2 \\ \sigma_b = 107,000 \text{ psi for the Kovar lid} \end{array}$$

Determine the maximum tensile stress S_{\max} produced in the seal by a screening pressure p of 100 psi.

From Equations (1) and (3b) we have

$$D = \frac{(20 \times 10^6)(.025)^3}{12(.91)} = 28.6 \text{ in-lb}$$

$$D_w = \frac{(20 \times 10^6)(.040)^3}{12(.91)} = 117.5 \text{ in-lb}$$

$$D_1 = \frac{(8.6 \times 10^6)(.049)^3}{12(.96)} = 87.9 \text{ in-lb}$$

$$D_2 = \frac{(8.6 \times 10^6)(.071)^3}{12(.96)} = 267 \text{ in-lb}$$

Then Equation (5b) gives

$$\begin{aligned} \alpha &= \frac{2}{1 - \left(\frac{h_1}{h}\right)^2 + \frac{D_w}{D_1} \left[\left(\frac{h_1}{h}\right)^2 - \left(\frac{h_2}{h}\right)^2 \right] + \frac{D_w}{D_2} \left(\frac{h_2}{h}\right)^2} \\ &= \frac{2}{1 - \left(\frac{.060}{.082}\right)^2 + \frac{117.5}{87.9} \left[\left(\frac{.060}{.082}\right)^2 - \left(\frac{.025}{.082}\right)^2 \right] + \frac{117.5}{267} \left(\frac{.025}{.082}\right)^2} \\ &= 1.82 \end{aligned}$$

whence (Equation (6a) and Figure 5)

$$K = \frac{4}{\pi^2} \cdot \frac{.365}{.082} \cdot \frac{117.5}{28.6} (1.82) = 11.1 \quad \text{and } \arctan K = 1.48$$

From the given dimensions we have

$$\frac{a}{b} = \frac{.365}{.670} = .545 \quad \frac{b}{a} = 1.83$$

Entering these values, together with $\arctan K = 1.48$, into Figures 7 and 8, we find

$$n_1 = .074 \quad n_2 = .515$$

From Equation (2), $m = m_e = (107,000)(.025)^2/6 = 11.146$ psi, whence

$$P_t = \frac{m_e}{n_1 a^2} = \frac{11.146}{(.074)(.365)^2} = 1131 \text{ psi}$$

Since this is greater than the screening pressure of 100 psi, the upper left hand box of Table 1 applies, giving

$$n = 6(.074) + 2(.515)\left(\frac{.040}{.365}\right) - \left(\frac{.040}{.365}\right)^2 = .545$$

and

$$S_{\max} = (100)\left(\frac{.365}{.040}\right)^2 (.545) = 4540 \text{ psi}$$

Example 7.- Let us assume that a Kovar case has a ceramic substrate bonded to its base over virtually the entire extent of the base, creating, in effect, a two-component plate like that of Figure 1 of Appendix B. We shall consider the upper component to be Kovar with the properties

$$\begin{aligned} E_1 &= 20 \times 10^6 \text{ psi} & \nu_1 &= 0.3 \\ t_1 &= 0.015 \text{ in} & \sigma_b &= 107,000 \text{ psi} \end{aligned}$$

The lower component will be the ceramic with the following assumed properties:

$$\begin{aligned} E_2 &= 50 \times 10^6 \text{ psi} & \nu_2 &= 0.22 \\ t_2 &= 0.025 \text{ in.} & \sigma_b &= 65,000 \text{ psi} \end{aligned}$$

Assuming clamped edges and a square base of internal dimensions $a = b = 0.875$ in., and using the procedures described in Section V, let us calculate the maximum tensile stress produced in the ceramic by an external pressure of $p = 50$ psi and judge whether or not it is likely to crack under that pressure.

Visualizing the curvatures produced in the base by the external pressure, we can expect that there will be two candidates for the maximum tensile stress in the ceramic. They are the extreme-fiber stress $\sigma_{x_{22}}$ at the center of the base and the stress $\sigma_{x_{21}}$ near the interface at the middle of

the edges $x = 0$ and a . (Inasmuch as the base is square and clamped all around, σ_{y22} at the center and σ_{y21} at the middle of the edges $y = 0$ and b would be equally good candidates.) The calculations leading to these stresses must start with Equations (1) through (7) of Appendix B, from which we find that

$$D_1 = \frac{(20 \times 10^6)(.015)^3}{12[1 - (.3)^2]} = 6.1813$$

$$D_2 = \frac{(50 \times 10^6)(.025)^3}{12[1 - (.22)^2]} = 68.4155$$

$$\bar{S} = \frac{(20 \times 10^6)(.015)(50 \times 10^6)(.025)}{(20 \times 10^6)(.015) + (50 \times 10^6)(.125)} = 0.24194 \times 10^6$$

$$\bar{v} = \frac{.3(50 \times 10^6)(.025) + .22(20 \times 10^6)(.015)}{(50 \times 10^6)(.025) + (20 \times 10^6)(.015)} = 0.285$$

$$D_3 = \frac{(.015 + .025)^2}{4} \cdot \frac{.24194 \times 10^6}{1 - (.285)^2} = 105.332$$

$$D = 6.1813 + 68.4155 + 105.332 = 179.929$$

$$D' = (.30)(6.1813) + (.22)(68.4155) + (.285)(105.332) = 46.925$$

$$v = 46.925/179.929 = .261$$

We turn now to the calculation of σ_{x22} at the center of the base. For a square plate ($b/a = 1$), Table 1 of Appendix B gives the central bending moments

$$M_x = M_y = .0231 \text{ pa}^2$$

if $\nu = 0.3$. Inasmuch as ν was found to be actually 0.261, we will calculate corrected values M_x' and M_y' of these bending moments. We may use Equation (20) of Appendix B for that purpose, since $M_x = M_y$. It gives

$$M_x' = M_y' = \frac{1 + .261}{1.3} (.0231 \text{ pa}^2) = .0224 \text{ pa}^2$$

which, we note in passing, is only 3% different from the uncorrected value of $.0231 \text{ pa}^2$. Substituting $p = 50 \text{ psi}$ and $a = .875 \text{ in.}$, we obtain

$$M_x' = M_y' = .0224(50)(.875)^2 = .8575 \text{ in.-lb/in.}$$

for the bending moment intensities at the center of the base. Equations (18) of Appendix B are the stress equations that may be used when the bending moments M_x and M_y are equal. From the last equation in that group we find that

$$\begin{aligned} \sigma_{x_{22}} = \sigma_{y_{22}} &= \frac{.8575}{(179.929)(1 + .261)} \left[\frac{(.24194 \times 10^6)(.040)}{2(.025)(1 - .285)} + \frac{(50 \times 10^6)(.025)}{2(1 - .22)} \right] \\ &= 4050 \text{ psi} \end{aligned}$$

For the other candidate maximum stress, namely $\sigma_{x_{21}}$ at the middle of the edge $x = 0$, we start with the following data from Appendix B, Table 1, for $\nu = 0.3$:

$$M_x = -.0513 \text{ pa}^2 \qquad M_y = -.0154 \text{ pa}^2$$

To correct for the fact that $\nu = .0261$, not 0.3, we must now use Equations (19), inasmuch as M_x and M_y are not equal. They give

$$M_x' = \frac{1}{.91} \{ [1 - .3(.261)](-.0513) + (.261 - .3)(-.0154) \} \text{ pa}^2$$

$$= - .0513 \text{ pa}^2$$

$$M_y' = \frac{1}{.91} \{ [1 - .3(.261)](-.0154) + (.261 - .3)(-.0513) \} \text{ pa}^2$$

$$= - .0134 \text{ pa}^2$$

whence

$$M_x' = - .0513(50)(.875)^2 = - 1.9638 \text{ in.-lb/in.}$$

$$M_y' = - .0134(50)(.875)^2 = - 0.513 \text{ in.-lb/in.}$$

Substituting these values for M_x and M_y , respectively, in the third of Equations (17) of Appendix B, along with

$$1 - v\bar{v} = 1 - (.261)(.285) = .9256$$

$$1 - vv_2 = 1 - (.261)(.22) = .9426$$

$$\bar{v} - v = .285 - .261 = .024$$

$$v_2 - v = .22 - .261 = - .041$$

$$1 - v^2 = 1 - (.261)^2 = .9319$$

$$1 - \bar{v}^2 = 1 - (.285)^2 = .9188$$

$$1 - v_2^2 = 1 - (.22)^2 = .9516$$

we obtain

$$\begin{aligned} \sigma_{x_{21}} &= \frac{(.24194 \times 10^6)(.04)}{2(.025)} \cdot \frac{(-1.9638)(.9256) + (-.513)(.024)}{(179.929)(.9319)(.9188)} \\ &\quad - \frac{(50 \times 10^6)(.025)}{2} \cdot \frac{(-1.9638)(.9426) + (-.513)(-.041)}{(179.929)(.9319)(.9516)} \\ &= -2299 + 7168 \\ &= 4869 \text{ psi} \end{aligned}$$

Thus, the two candidate maximum tensions in the ceramic are 4050 psi and 4869 psi, and the governing one is the latter. It is well below the given breaking stress of 65,000 psi for that ceramic. We therefore tentatively conclude that there is no danger of the ceramic substrate cracking under the given external pressure of 50 psi.

Before accepting this conclusion as final, let us compute the center deflection of the base due to the 50 psi external pressure, in order to satisfy ourselves that the small-deflection assumption, on which all of the above calculations are based, is valid. From Table 1 of Appendix B we have, for $b/a = 1$,

$$\delta = .00126 \frac{pa^4}{D} = \frac{(.00126)(50)(.875)^4}{179.929} = .00021 \text{ in.}$$

and this is indeed very small compared to a , b and t .

A word of caution may be in order at this point: A ceramic substrate bonded to a package base would not ordinarily extend all the way to the walls of the package. Instead there would generally be a small gap between the periphery of the substrate and the package walls. This means that those edge bending moments in the base that are transmitted from the base to the wall must be borne by the Kovar alone, rather than by the Kovar-ceramic

composite, and there is therefore a possibility that the edge bending moments developed by a given pressure might exceed the fully plastic bending strength m_e of the Kovar. This would result in plastic hinges developing along portions of the edges of the base, which would invalidate the assumption of clamping.

In the present example, this possibility does not pose a serious problem: For the given modulus of rupture of $\sigma_b = 107,000$ psi for the Kovar, we obtain

$$m_e = \frac{\sigma_b t_1^2}{6} = \frac{(107,000)(.015)^2}{6} = 4.01 \frac{\text{in.-lb}}{\text{in.}}$$

as the fully plastic bending strength of the Kovar edge of the base, and this is much larger than the calculated actual edge bending moment of 1.9638 in.-lb/in. Therefore the edges of the base can still be considered to be clamped under the 50 psi external pressure, thus validating the calculation procedure that has been used. In fact, by scaling, we may conclude that the calculation procedure would be valid for pressures up to

$$p = \frac{4.01}{1.9638} \times 50 = 102 \text{ psi}$$

This is the pressure at which plastic hinges will first start to form in the Kovar at the midpoints of the sides of the base, if there is a gap between the periphery of the ceramic substrate and the walls of the package.

If the pressure is increased beyond 102 psi, the plastic hinges will gradually lengthen, and the base will depart more and more from the condition of a clamped plate. There will be no further increase in the values of M_x

and M_y at the middle of the edges $x = 0$ and a , inasmuch as M_x is at its maximum value of m_e and M_y at its maximum value of vm_e , but the bending moments at the center of the base will continue to increase.

There seems to be no easy way to estimate ceramic stresses once the Kovar plastic hinges have started to form in the gap between the edge of the substrate and the walls. However, a rather rough but conservative approach to this problem can be suggested: Assume that the base behaves as a simply supported plate with regard to any increments of pressure beyond the pressure p_0 at which plastic hingeing initiated (i.e., beyond 102 psi in the present example); therefore for any pressure $p > p_0$ find the stresses in the ceramic by superimposing the stresses at $p = p_0$ in the clamped plate and the stresses due to a pressure of $p - p_0$ in the simply supported plate. The latter stresses can be obtained using Table 2 of Appendix B, instead of Table 1. (They will, of course, be zero at the edges.) In adapting this approach to non-square plates, Table 3 will be more appropriate than Table 2 if plastic hinges have not yet formed along the short edges.

IX. EXPERIMENTAL CONFIRMATION AND INFERRED GLASS STRENGTH

According to Equation (22) the following relationship should exist between the pressure p_{cr} causing loss of hermeticity under a ductile lid and the ultimate tensile strength S_{ult} of the seal material, as long as $p_{cr} < p_t$:

$$p_{cr} = S_{ult} \left[\left(\frac{a}{w} \right)^2 n \right]^{-1} \quad (45)$$

Thus, given a family of different packages all having the same seal material and the same quality seals, the graph of p_{cr} versus $[(a/w)^2 n]^{-1}$ should theoretically be a straight line through the origin (admitting only p_{cr} 's that are less than p_t). In Reference 2 experimental data are presented which tend to confirm this theoretical conclusion.

The data were furnished by a package manufacturer. They involved 579 packages distributed among eighteen groups, with the packages nominally identical within each group. The packages had three-segment stepped-type walls, as in Figure 2(b). The top segment was a Kovar seal frame; the two lower segments were glass beads sandwiching a lead frame. The lids were Kovar and were sealed to the wall by means of a gold-tin solder preform.

Each group of packages was placed in a pressure bomb and subjected to external air pressure that was increased in increments of 5 psi or 10 psi. Each new pressure was held for approximately 10 minutes, after which the packages were tested for gross leaks by submerging them in a heated liquid and watching for bubbles emanating from the interior of the package. Consistently the bubbles were seen to emerge from under the lids in the middle of a longer side. The leakers were removed from the group and the rest of the group was then subjected to the next higher pressure. This process was continued until all the packages had been made to leak.

Thus, for each package an experimental value of p_{cr} was obtained. From the dimensions and elastic constants of the package components a value of the package parameter $[(a/w)^2 n]^{-1}$ was also computed for each package group, so that for each package group the mean p_{cr} of the group could be plotted against the package parameter. The plotted points fell reasonably close to a straight line through the origin, thus tending to confirm the validity of Equations (45) and (22).

From the slope of this straight line, the average tensile strength S_{ult} of the seal material could be inferred (see Eq. (45)) and was found to be 8450 psi. Inasmuch as the gold-tin solder between the lid and seal frame was undoubtedly stronger than the glass underneath the seal frame, this value of 8450 psi can be taken as an estimate of the mean tensile strength of the glass in the walls of these packages.

Using Equation (45) an inferred S_{ult} was computed for each of the 579 packages individually. The lowest inferred glass strength was 3400 psi, occurring in only one package. Only 14 packages (2.4%) had inferred glass strengths below 5000 psi. The highest inferred glass strength was 18,000 psi. These inferred strength values and their variability are consistent with the discussion of glass tensile strengths in Section 4 of Appendix A.

The cumulative distribution of inferred glass strengths for the individual packages is given in the following table:

S, psi	Percentage of packages having inferred $S_{ult} < S$
2,700	0
3,400	.17
4,000	.17
4,500	.62
5,000	2.4
5,500	6.7
6,000	12.8
7,000	26.8
8,000	47.1
9,000	62.5
10,000	79.1
11,000	89.7
12,000	95.1
13,000	96.4
14,000	96.9
15,000	97.6
16,000	98.3
17,000	99.4
18,000	100

X. REMARKS

In this chapter formulas have been presented, related to the mechanical behavior of microelectronic flatpacks under external pressure, that can assist in the design of such packages or in the selection of suitable screening pressures for testing their hermeticity.

The specific items covered by the formulas are: maximum tensile stress in the lid-to-wall seal (or seal-frame-to-glass-wall seal), central deflection of the lid, pressure required to crack or collapse the lid or the base, and the equivalence of external pressure and centrifuge acceleration insofar as lid behavior and seal stresses are concerned.

Numerical examples have been presented to illustrate the use of the formulas, and experimental data have been referred to which tend to confirm some of the formulas and hypotheses related to loss of hermeticity under external pressure.

Chapter 2 - CONSTANT ACCELERATION

Constant acceleration in a centrifuge is one of the standard tests to which microcircuit packages may be subjected (e.g., see Method 2001.2 of Reference 1). Microelectronic devices in rocket-launched equipment may also experience periods of constant or nearly constant acceleration during the launch.

Depending on the orientation of the package in relation to the inertia loading (the centrifugal force, in the case of the centrifuge), this environment can produce stresses and deflections in the lid or base, tensions in the internal wires and their bonds, flexure and torsion of the internal wires, and tension or shear in the chip-to-substrate and substrate-to-package attachments. In this chapter, which is based for the most part on Reference 7, the magnitudes of these effects are assessed, especially with a view toward evaluating the effectiveness of the centrifuge as a stressing device for screening purposes.

In that part of the study related to the tensile stressing of internal wires and bonds, the extensibility of the wire is taken into account; this is a factor that is usually negligible but that can be important for wires with small initial loop height. The wire stressing capability of the pull test is also evaluated (again with wire extensibility taken into account), in order to provide a standard against which the effectiveness of the centrifuge can be measured.

I. WIRE AND WIRE BOND TENSIONS

In this section we assume the package so oriented in the centrifuge that the centrifugal force tends to pull the wire away from the base, creating a stress condition in the wire that is primarily tensile. In Section IV we will assume a different orientation, one in which the centrifugal force acts parallel to the base of the package and normal to the plane of the wire loop, so that the primary mode of stressing in the wire is flexure, with a very small amount of torsion.

A. Nomenclature and Physical Constants.- We consider a wire (Figure 1) that spans a horizontal distance S and, in its unstressed state, has a length of L_0 and a cross-sectional area of A . Its Young's modulus and unstressed specific weight will be denoted by E and γ , respectively, and the assumed values of these constants for two common wire materials are tabulated below (Table 1).

Table 1.- Properties of Gold and Aluminum

	Gold	Aluminum
E (psi)	12×10^6	10×10^6
γ (lb/in. ³)	.7	.1

A parameter that will be needed later is the "excess-length parameter" R , defined as follows:

$$R = \frac{L_0 - S}{S} \quad \text{or} \quad \frac{L_0}{S} = 1 + R \quad (1)$$

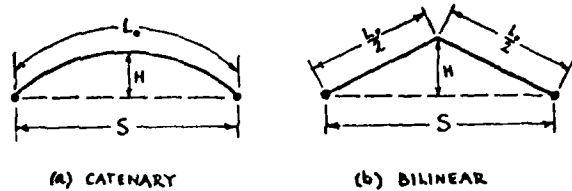


Figure 1.- Unstressed wire in a catenary or bilinear shape.

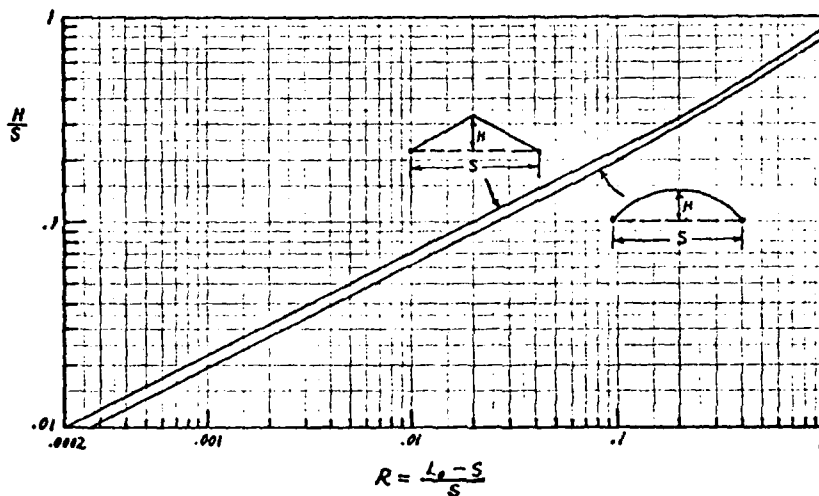


Figure 2.- Graphs relating excess-length parameter R and dimensionless loop-height parameter H/S.

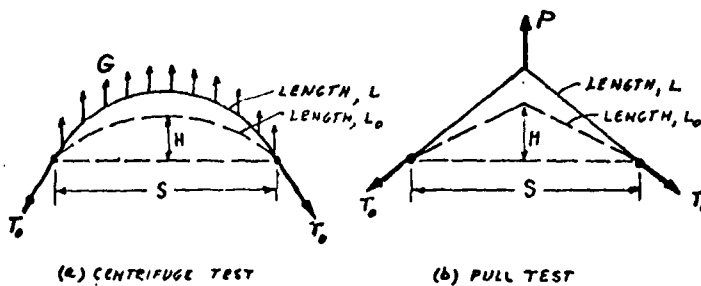


Figure 3.- Wire as stressed in a centrifuge or pull test. (Dashed lines represent unstressed wire.)

In principle, R can be determined by measuring L_0 and S and substituting their values in Eq. (1). However, L_0 may be rather difficult to measure. Much easier to estimate is the loop height H when the unstressed wire is in the curved (assumed to be catenary) shape of Figure 1(a) or is gently pulled into the bilinear shape of Figure 1(b) (the two values of H for a given wire will of course be different). Therefore, graphs are provided in Figure 2 from which R can be determined if the dimensionless loop-height parameter H/S is known for either of these two shapes. The curves in Figure 2 can be accurately approximated by the following equations if H/S is less than 0.2:

$$R = \frac{8}{3}(H/S)^2 \quad (\text{lower curve}) \quad (2)$$

$$R = 2(H/S)^2 \quad (\text{upper curve}) \quad (3)$$

It will be noted that R is usually of a much smaller order of magnitude than H/S .

Under its distributed inertia loading in a centrifuge or its concentrated loading in a pull test, the wire will develop a stressed length of L and will exert forces of magnitude T_0 on its bonds (Figure 3). The corresponding maximum nominal tension stress in the wire will be

$$\sigma = T_0/A \quad (4)$$

occurring at the ends.

The magnitude of the inertia loading in a centrifuge test will be characterized by the parameter G , defined as the number of g 's (g = acceleration of gravity) of centripetal acceleration that the wire is experiencing. The

intensity of the loading in a pull test will be described by the magnitude P of the pulling force shown in Figure 3(b). Both loads are assumed to be so oriented as to maintain the wire in a symmetrical shape.

B. Wire Stress in a Centrifuge Test.- The stress analysis of a wire in a centrifuge test, taking extensibility into account on the basis of Hooke's Law, and assuming negligible bending stiffness, is carried out in Reference 7. The results are summarized in Figure 4, where the dimensionless wire-stress parameter T_0/AE is plotted as a function of the dimensionless inertia-loading parameter $G\gamma S/E$ for different values of the excess-length parameter R . For any given test one would know the value of the abscissa. For that abscissa the ordinate value of T_0/AE would be read from the appropriate R curve. Multiplication of the T_0/AE value by the known value of AE or E would give the bond force T_0 or the maximum wire stress T_0/A .

To facilitate the use of Figure 4, two "bench-mark" values of the abscissa, corresponding to certain test conditions, are indicated by arrows. Since the abscissa is directly proportional to G and S , it is easy to compute its value in any test of a gold or aluminum wire by multiplying one of the bench-mark values by appropriate ratios.

A bench-mark ordinate is also marked on Figure 4 which indicates that $T_0/AE = .001$ corresponds to a maximum tensile stress of 10,000 psi in aluminum wire and 12,000 psi in gold wire. The gold and aluminum wire stresses associated with any other T_0/AE value, say $(T_0/AE)_1$, can be found by multiplying the above stresses by the ratio of $(T_0/AE)_1$ to .001.

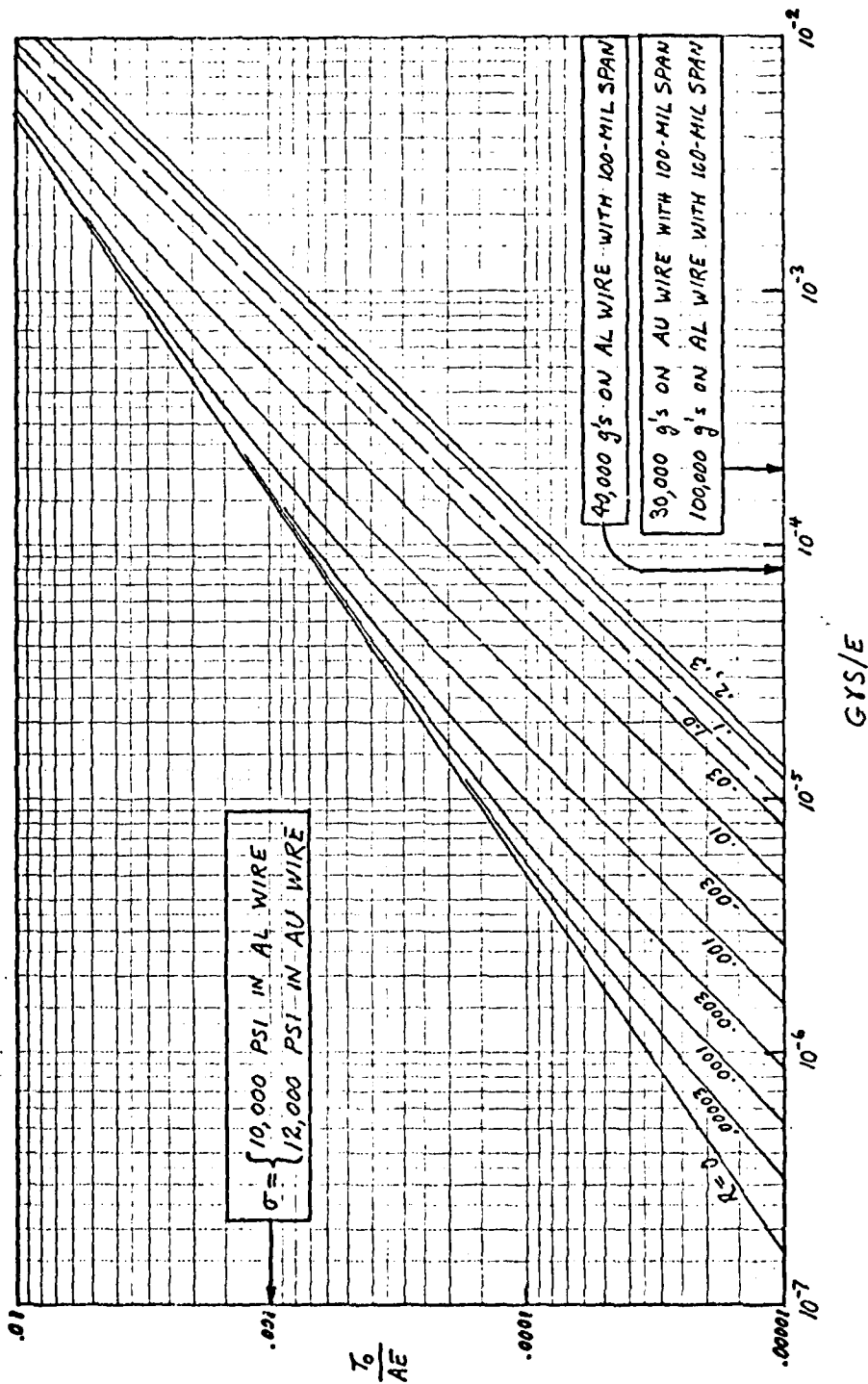


Figure 4.- Graphs for determining bond force T_0 or maximum wire stress T_0/A in a centrifuge test.

In order to judge whether or not a certain wire stress, $\sigma = T_0/A$, is significant, one could compare it with the ultimate tensile strength σ_u of the material. This varies greatly with the manufacturer and the temper of the wire. Typical values are given in Table 2 below for small diameter wires (1.5 mils and less). Manufacturers' guaranteed values may be lower than the ones in the table.

Table 2.- Typical Values of σ_u (psi) for Wire

	Gold	Aluminum
Annealed Temper	25,000	37,000
Hard Temper	60,000	60,000

Whether or not wire extensibility has a significant effect on the stresses can be judged from the slopes of the curves in Figure 4. A slope that is 45° or nearly so indicates that wire extensibility has a negligible effect. Where the curves have such a slope, T_0/AE is proportional to $G\gamma S/E$; then T_0 and T_0/A are actually independent of E . Where the slope is significantly different from 45° , wire extensibility has a significant effect; this happens for the smaller values of R when $G\gamma S/E$ is sufficiently high.

Figure 4 is based on the assumption that the wire material obeys Hooke's law. Therefore, strictly speaking, any data obtained from that figure are valid only if the maximum stress, $\sigma = T_0/A$, is below the proportional-limit stress σ_p associated with the point P of the stress-strain curve where stress stops being proportional to strain (see Figure 5). If the stress $\sigma = T_0/A$ falls above point P , say at Q , the curves of Figure 4 will still be approximately correct provided that E in the ordinate and abscissa

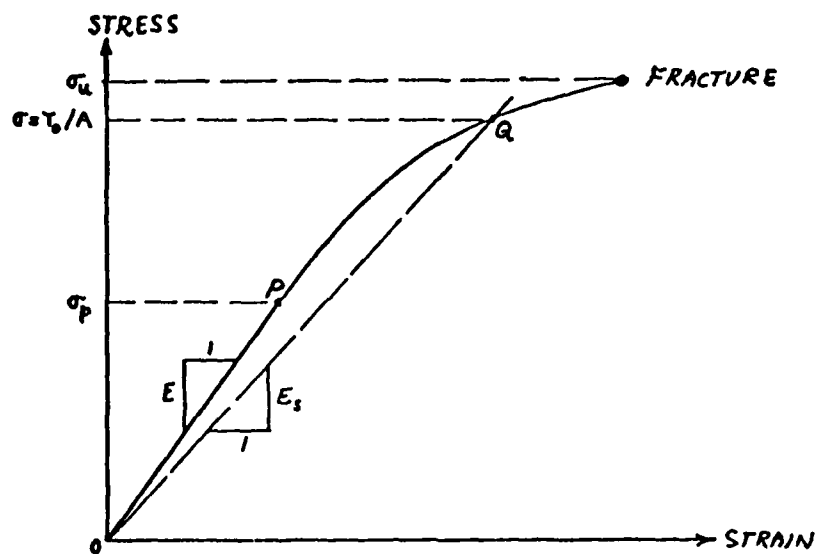


Figure 5.- Tensile stress-strain curve for a ductile material.

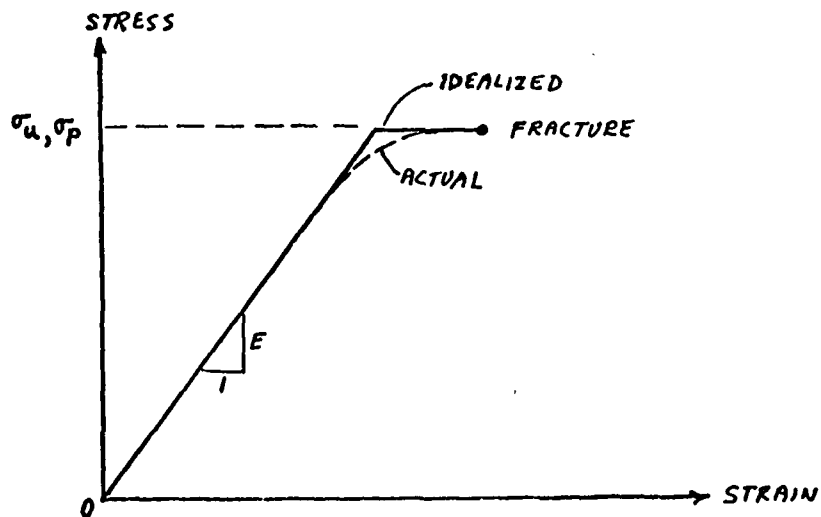


Figure 6.- Actual and idealized stress-strain curves for hard-temper wire.

labels is changed to E_s , where E_s is the secant modulus associated with the stress $\sigma = T_o/A$ (see Figure 5). The approximation becomes better as H/S becomes smaller, for then the stress is more nearly constant at the value σ along the entire length of the wire. Since E_s is itself a function of σ , it is clear that trial-and error calculation will be required to determine σ when $\sigma > \sigma_p$.

For hard-tempered wires it may be permissible to idealize the actual (curving) stress-strain curve to a bilinear form, as in Figure 6. Then Figure 4 would be valid without modification for all σ 's up to σ_u .

C. Wire Stress in a Pull Test.- The pull test of Figure 3(b) is analyzed in Reference 7 and the results are given in Figure 7 by graphs that are similar to those in Figure 4. The dimensionless loading parameter in this case is P/AE , and three "bench-mark" values of this parameter are indicated, corresponding to minimum pre-seal pull strengths specified for test condition D in Table 1 of Method 2011.2 of Reference 1.

As indicated in Figure 7, $R = .155$ represents a dividing line. For wires with less excess length (which is the usual case) the bond force T_o will be greater than the pull force P , while for wires with more excess length the opposite will be true.

As in the case of Figure 4, the more the slope of a curve deviates from 45° , the more significant is the effect of wire extensibility. Also as in Figure 4, the curves of Figure 7 can be used for $\sigma = T_o/A > \sigma_p$ provided that the Young's modulus E is replaced by the secant modulus E_s associated with the stress σ . In fact, this procedure is more accurate

in the present case, because the wire stress is constant along the entire length of the wire in the pull test, whereas it is only approximately so in the centrifuge test.

D. Comparison of Centrifuge and Pull Test.- A comparison of Figures 4 and 7 shows that the centrifuge is generally much less effective than the pull test in stressing wires and wire bonds. For example, let us consider the three bench-mark pull tests of Figure 7, which, as already noted, represent minimum required pre-seal pull strengths specified in MIL-STD-883B. Supposing R to be .03, which is a reasonable value, we find that all of those pull tests produce tensile stresses exceeding 10,000 psi in aluminum wires or 12,000 psi in gold wires ($T_0/AE = .001$). On the other hand, for the same R the three bench-mark centrifuge tests of Figure 4 produce T_0/AE values of .0001 and .00026, implying wire stresses that are at most 10% and 26% of those produced by the pull tests.

In order to achieve a stress of 10,000 psi in an aluminum wire with $R = .03$ at 40,000 g's, Figure 4 shows that the span would have to be one inch. To achieve 12,000 psi at 30,000 g's in a gold wire the span would have to be four-tenths of an inch. Since such large spans are unlikely to occur in practice in microelectronic devices, and since centrifuge accelerations exceeding 30,000 or 40,000 g's are difficult to achieve and may be destructive of other package components, it appears that the centrifuge will generally be incapable of producing wire stresses comparable to those produced in the MIL-STD-883B pull tests. A similar conclusion was reached by other investigators (see, for example, Reference 8).

A more thorough comparison of the centrifuge and pull tests can be made by comparing the $G\gamma S/E$ value from Figure 4 and the P/AE value from Figure 7 for many selected combinations of R and T_0/AE . Each such compari-

son will give us a pair of tests (one centrifuge, the other pull) that are equivalent in the sense that they will produce the same stress in a wire with the given value of R . Such comparisons show that the ratio r of the equivalent load parameters, that is,

$$\frac{P/AE}{G\gamma S/E} = \frac{P}{G\gamma SA} \equiv r, \quad (5)$$

depends on R but is virtually independent of T_o/AE . The results of the comparisons can therefore be put in the form of a single curve, Figure 8. Using Eq. (5) in the form

$$P = rG\gamma SA \quad \text{or} \quad G = P/r\gamma SA \quad (6)$$

and taking r from Figure 8, one can readily find the P of a pull test that will stress any wire and its bonds as severely as a given number (G) of g 's in a centrifuge test. Conversely, given the P of a pull test, one can find how many (G) g 's of centrifuge acceleration will be equivalent in severity to that pull test.

For wires without excessive loop height, R will usually be close to zero. Then r may be taken as 0.59 with little error, and the equivalence relation (6) will become

$$P = .59G\gamma SA \quad \text{or} \quad G = P/.59\gamma SA \quad (7)$$

To illustrate the use of this result, let us ask what centrifuge acceleration is equivalent to a 3-gram pull on a 1-mil diameter gold wire with a 100-mil span. From the given data we have

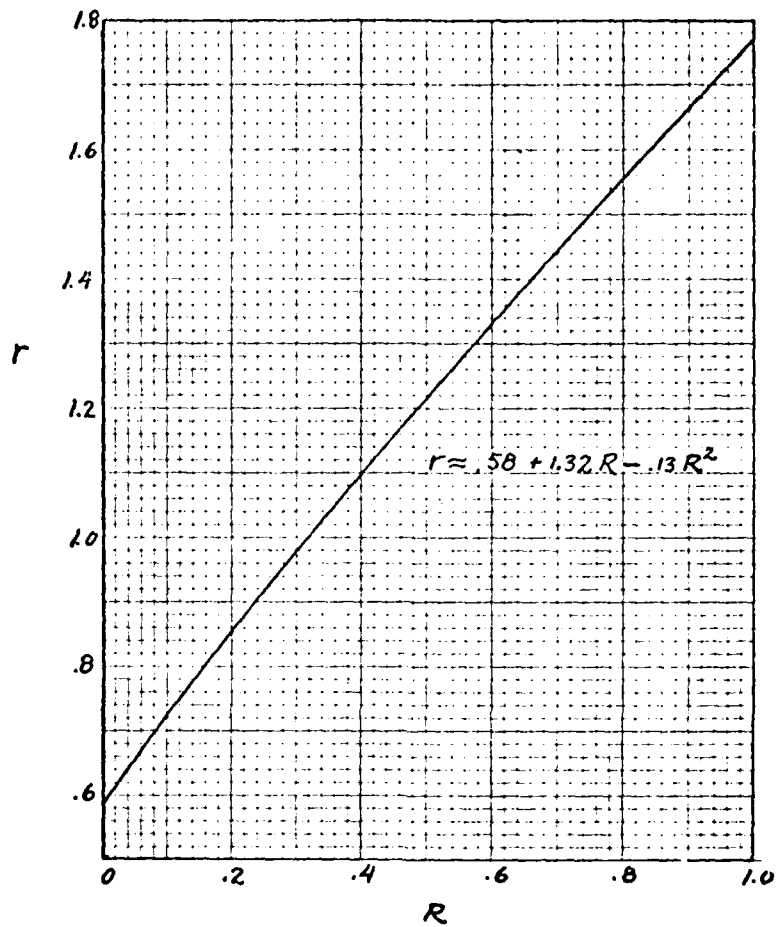


Figure 8.- Graph for determining equivalent values of G and P. (For Equivalence, $P = G\gamma SAr$ or $G = P/\gamma SAr$.)

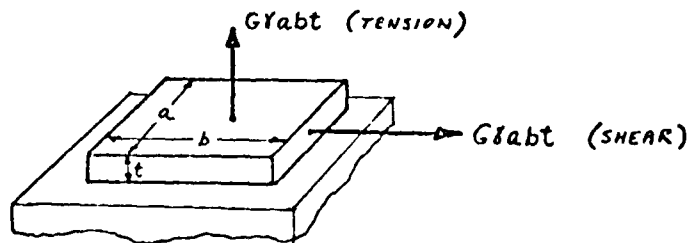


Figure 9.- Two types of centrifuge-induced inertia load on chip or substrate.

AD-A113 594

SYRACUSE UNIV NY
MICROCIRCUIT PACKAGE STRESS ANALYSIS.(U)

F/G 9/5

JAN 82 C LIBOVE, R W PERKINS, K KOKINI

F30602-80-C-0155

UNCLASSIFIED

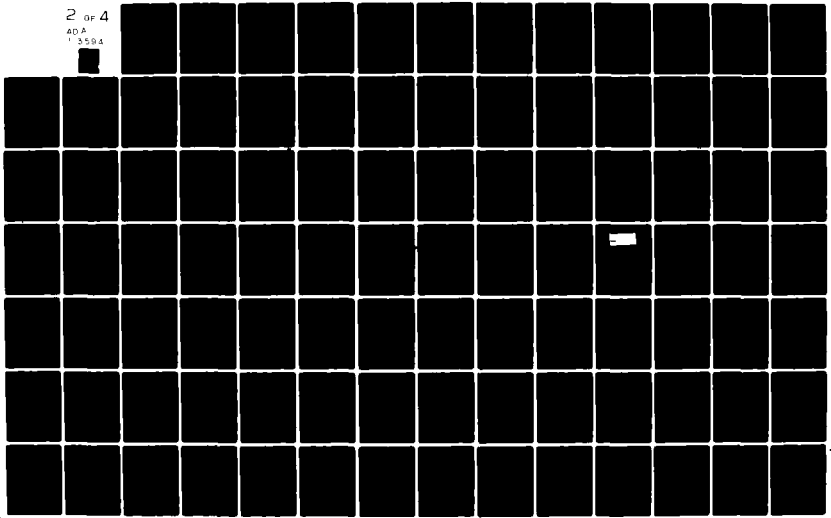
MAE-1237-F1

RADC-TR-81-382

NL

2 of 4

AD A
13584



$$P = 3(.002205) = .006615 \text{ lb}$$

$$\gamma = .7 \text{ lb/in.}^3$$

$$S = .100 \text{ in.}$$

$$A = \frac{\pi}{4} (.001)^2 = .785 \times 10^{-6} \text{ in.}^2$$

Substitution of this information into the second form of Eq. (7) gives

$$G = \frac{.006615}{.59(.7)(.1)(.785 \times 10^{-6})} = 204,000$$

Thus, 204,000 g's of centrifuge acceleration would be required to produce the same wire and bond stresses as the given pull test. This is an impractically high value.

II. CHIP AND SUBSTRATE ATTACHMENT STRESSES

A. Conventional Bonding.- The rectangular parallelepiped in Figure 9, of dimensions a , b and t and specific weight γ , represents a chip bonded to a substrate, or a substrate bonded to a package base. The two vectors represent two possible orientations of a centrifugal force that might tend to cause separation of the object from the thing to which it is attached. In either case the magnitude of the force is

$$G\gamma abt \quad (8)$$

where G is the number of g's of acceleration of the object. The corresponding nominal stress in the bond, obtained by dividing (8) by the gross bonding area, ab , is

$$S_{\text{nominal}} = G\gamma t \quad (9)$$

and this is either a tensile or a shear stress, depending on the orientation of the package in the centrifuge. If there is a "voids ratio" V in the bond, the net bond area will be $(1 - V)ab$, and the actual mean stress in the bond will be

$$S_{\text{actual}} = \frac{G\gamma t}{1-V} \quad (10)$$

On the basis of Eq. (10) we can investigate the likelihood of the centrifuge producing separation of a poorly bonded substrate. For this purpose let us set G at 50,000, which is Reference 8's estimate of the largest number of g's one can conveniently and safely use, and set γ at .140 lb/in.³ (3.89 grams/cc), which corresponds to one of the denser substrate ceramics. With this input, Eq. (10) gives the stress versus thickness relationship shown in Figure 10. Figure 10 can be used for other values of G and γ by simply multiplying the ordinate values by

$$\frac{G}{50,000} \cdot \frac{\gamma}{3.89} \quad (11)$$

where γ is the specific gravity (i.e., the density in grams/cc). Thus, for silicon chips ($\gamma = 2.4$) tested at 50,000 g's, one should multiply the ordinates of Figure 10 by 2.4/3.89, or .62.

From Figure 10 we can conclude that 50,000 g's of centrifuge acceleration are not likely to significantly stress a silicon chip attachment, even if the voids ratio is very large. For example, considering a chip thickness t of 6 mils and a voids ratio V of 90 percent, we obtain a bond stress of only

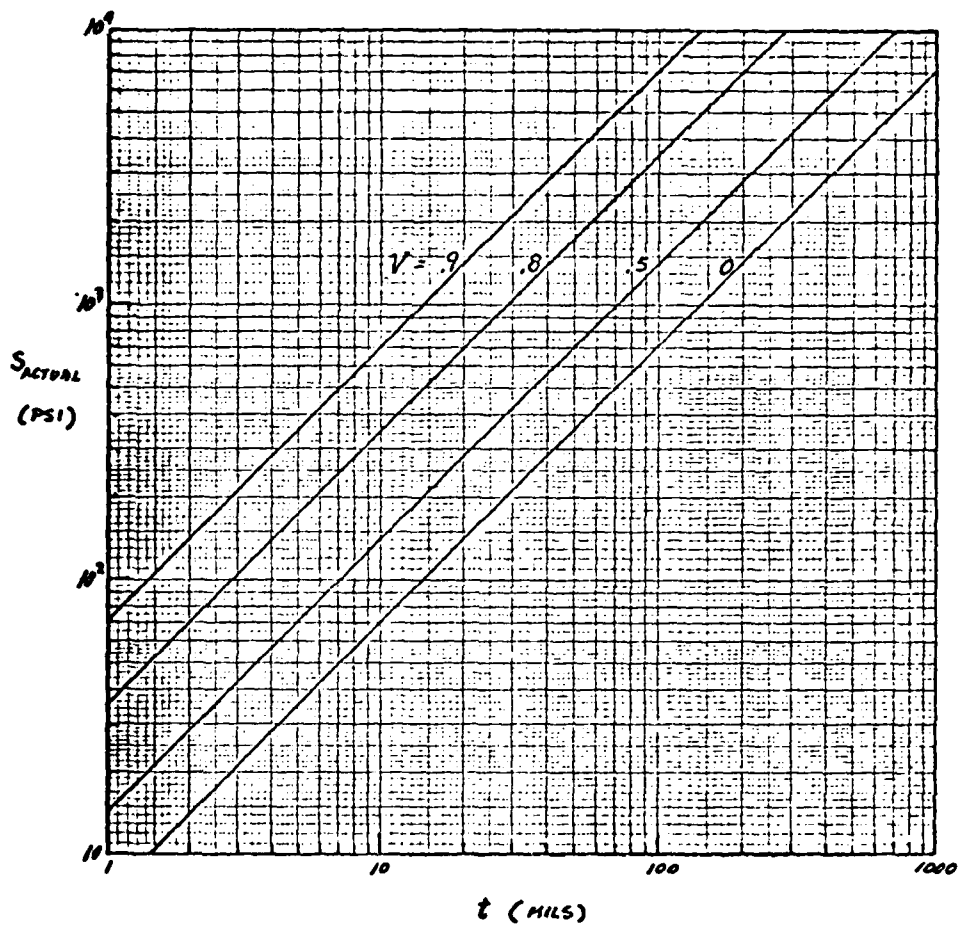


Figure 10.- Bond stress for 3.89 grams/cm³ substrate at 50,000 g's. (For silicon chip of 2.4 grams/cm³ density, multiply ordinates by .62. For G g's, multiply ordinates by g/50,000.)

$$S_{\text{actual}} = (420)(.62) = 260 \text{ psi}$$

Since bond strengths are measured in thousands of psi for most bonding materials, the developed stress of 260 psi is not likely to cause separation of this poorly bonded chip.

The situation is slightly better in the case of a ceramic substrate, because of its greater thickness. For example, a substrate of 50 mils thickness with a voids ratio of 0.9 will develop a bond stress of 3500 psi, and this might be sufficient to cause separation for some bonding materials. It should be remembered, however, that this result is predicated on the assumption of 50,000 g's of centrifuge acceleration. As discussed in Section III, such high accelerations may be unusable for the larger size packages because of their destructive flexural effect on the lid or base.

B. Face-Down Bonding.- If a chip is bonded face down to a few pedestals or bumps, there is effectively a high voids ratio and therefore some hope of creating significant bond stress, despite the small mass of the chip. When dealing with such chips, the pedestal area is somewhat uncertain, and it may therefore be more appropriate to study the force B per bump, rather than the bond stress, per se. Dividing the total inertia load (8) by the number of bumps, N, we obtain the following formula for B:

$$B = \frac{Gyabt}{N} \quad (12)$$

To study the implications of this formula, let us consider the following specific case, based on data in Reference 9:

$$\gamma = 2.4 \text{ grams/cc (silicon)}$$

$$a = b = 40 \text{ mils}$$

$$t = 6 \text{ mils}$$

$$N = 10 \text{ bumps}$$

Then the chip volume is

$$abt = (.040)(.040)(.006) \text{ in.}^3 = 96 \times 10^{-7} \text{ in.}^3 = 157 \times 10^{-6} \text{ cm}^3$$

and for a 40,000-g centrifuge acceleration, Eq. (12) will give

$$B = \frac{(40,000)(2.4)(157 \times 10^{-6})}{10} = 1.5 \text{ grams} \quad (13)$$

as the force per bump. Approximating the contact surfaces as circles and estimating their diameters to be between .0010 in. and .0018 in., we can compute from the above result the following possible range of stress in the bond:

$$S_{\text{actual}} = 4210 \text{ psi to } 1300 \text{ psi} \quad (14)$$

For such a chip, Method 2011.2 of MIL-STD-883B (Reference 1) specifies a required strength of 5 grams per bump. Thus, the 1.5-gram force obtained in Eq. (13) can be considered to be at the threshold of significance, but not severe enough to be equivalent to the MIL-STD-883B requirement. The stress values of Eq. (14) are also at the threshold of significance. One can scale up the results in Eqs. (13) and (14) by increasing G, but the remarks at the end of the previous section regarding the danger of high G's are equally pertinent here.

III. LIDS AND BASES OF RECTANGULAR FLATPACKS

As discussed in Chapter 1, an acceleration of G g's normal to the lid or base of a package is equivalent to a uniform lateral pressure p of the following magnitude:

As discussed in Reference 2, an acceleration of G g's normal to the lid or base of a package is equivalent to a uniform lateral pressure p of the following magnitude:

$$p = G\gamma t \quad (15)$$

where t is the thickness of the lid or base and γ is the specific weight of its material*.

The equivalent pressures given by Eq. (15) can indeed be significant, as the following example will show: Take $G = 15,000$, $\gamma = .140$ lb/in.³ (ceramic), and $t = .025$ in. Then the equivalent pressure is

$$p = (15,000)(.140)(.025) = 52.5 \text{ psi}$$

This is in the range of pressures specified for hermeticity testing in Method 1014.2 of Reference 1. Such "pressures" can be expected to produce the following significant mechanical effects, as discussed in Chapter 1:

- (a) Flexing of the lid, leading to bending moments in lid-to-wall seal which tend to aggravate defects in that seal. This effect is most pronounced in the middle of the longer sides.

*Equation (15) assumes the lid or base to be of a single material. In the case of a two-component base (e.g., a ceramic and Kovar combination), γt should be replaced by Γ , the weight per unit area of the base.

- (b) Collapse of a ductile lid and cracking of a ceramic lid or base. The likelihood of these effects increases as the package size goes up.

Another effect, not discussed in Chapter 1, is the following:

- (c) Flexing of the base, which induces interlaminar shear stress in the bond between the base and a substrate attached to it, or between a substrate and a chip attached to it. These shear stresses, which are analogous to the "VQ/I" shear stresses of beam theory, can be more significant than the ones induced directly by the inertia loading and which were discussed in Section II.

Thus, it appears that centrifuge acceleration can produce significant flexural effects on the lids and bases of flat-packs, thus simulating the flexure produced by lateral pressure, constant acceleration as in a cannon-launched device, squeezing of the package during normal handling, or flat-wise impact due to accidental dropping of the package onto the floor (see Chapter 3).

However, although the centrifuge is capable of the above important simulations, it is not necessarily to be recommended for that purpose. The same flexural actions can be produced with less difficulty by placing the package in a closed vessel which is then pressurized or evacuated. In this way the troublesome problem of properly supporting the package in the centrifuge is avoided. At the same time, if external pressure is used, one has accomplished the first step of a gross leak test for hermeticity. (The follow-up step

would consist of inserting the package into a warmed fluid bath and watching for bubbles.) One sacrifices only the capability of exerting more than 14.7 psi of outward effective pressure on a lid or base, capability which the centrifuge has in principle if the complicated support problem can be overcome.

IV. WIRE FLEXURE

In Section I the wire stressing effectiveness of the centrifuge was evaluated for the case in which the centrifugal force tends to pull the wire away from the base, i.e., to stretch the wire. In the present section we consider the package so oriented in the centrifuge that the centrifugal force acts parallel to the base of the package and perpendicular to the plane of the wire loop. With this orientation, flexure, rather than extension, is the primary stressing mode, with the maximum bending moments in the wire occurring at its ends.

The determination of the maximum flexural stress is straightforward if one assumes the wire to be linearly elastic and to have the shape of a circular arc, for then the theory in pp. 364 and 365 of Reference 20 is immediately applicable. For an H/S ratio of .076 it leads to the following formula for the maximum extreme-fiber cross-sectional bending stress σ (psi) in the wire:

$$\sigma = .7GS^2\gamma/d \quad (16)$$

where G is the number of g's of centrifuge acceleration, S is the wire span (in.), d the wire diameter (in.), and γ the specific weight of the

wire material (lb/in.^3). Although Equation (16) was obtained for an H/S ratio of .076, it may be used for all H/S ratios from 0 to 0.13 with an error of less than 5%.

Wires can tolerate a higher stress in flexure than in tension, inasmuch as the flexural stress is localized at the extreme fibers. Taking $\sigma = 20,000$ psi to be a flexural stress that sound wires should reasonably be able to withstand (this is about 1/3 the ultimate tensile strength of gold and aluminum wires in the hard temper), we can use Equation (16) to calculate combinations of G, S and d leading to that stress. The results of those calculations are given in Figure 11. From it we see, for example, that 10,000 g's suffice to produce 20,000 psi flexural stress in gold wires of .001-in. diameter with spans of .064 in.

On the other hand, 10,000 g's of acceleration applied to aluminum wires of the same diameter would produce flexural stress exceeding 20,000 psi only in wires of 0.17-in. span or longer.

Equation (16) shows the flexural stress to depend on the square of the span S, which implies that centrifuge accelerations required to adequately stress the shorter wires could easily overstress the longer wires. Therefore the choice of a G-level should be governed by the longest wires in the package. In other words, it may be necessary to accept an understressing of the shorter wires for the sake of not damaging the longer wires.

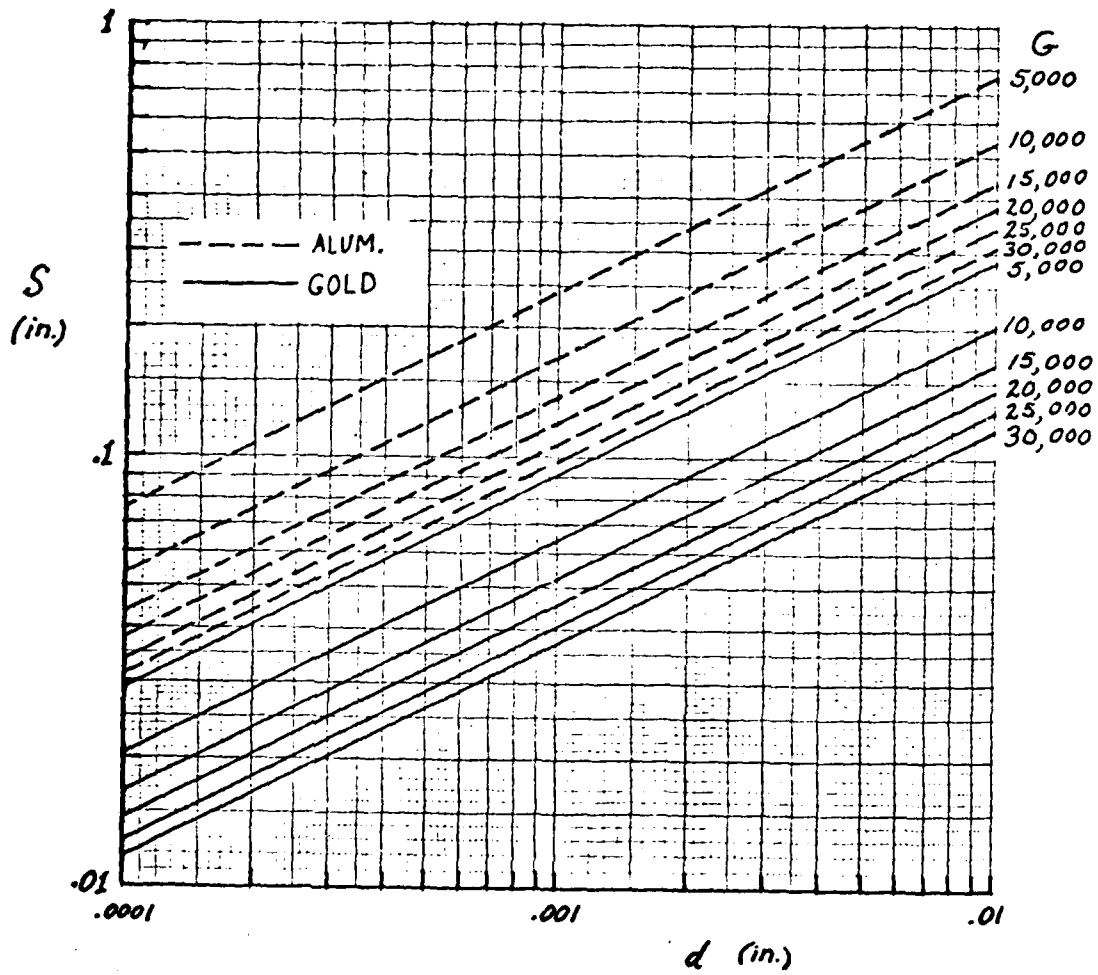


Figure 11.- Combinations of span S , diameter d , and centrifuge acceleration G leading to extreme-fiber flexural stress of 20,000 psi in gold and aluminum wires. (G = number of g's of centrifuge acceleration. Centrifugal force is perpendicular to the plane of the wire loop.)

V. REMARKS

In this chapter we have assessed the capabilities of the centrifuge as a stressing device for the following microelectronic components: wires and wire bonds, chip and substrate attachments, lids and bases of rectangular flat-packs. The conclusions to be drawn from this study are as follows:

(1) The centrifuge is of marginal utility for the tensile stressing of wires and wire bonds, because of the low mass of these components and possible strength limitations of the package. (2) For the same reasons, the centrifuge is of marginal (or less) utility for stressing normal chip-to-substrate attachments. (3) However, the centrifuge might be capable of producing significant bond stresses in chips which are bonded to a few pedestals or bumps, as in face-down bonding. (4) The centrifuge might also be capable of producing significant stresses in substrate-to-package bonds. (5) The centrifuge can produce significant flexural stresses in lids and bases of the larger flat-packs, but these effects can be more easily produced by hydrostatic pressure. (6) The centrifuge can produce significant flexural stressing of gold wires if the centrifugal force acts parallel to the base and perpendicular to the plane of the wire loop.

The following is a listing of the main quantitative results presented in this chapter.

- (a) Figures 4 and 7, which embody the results of the stress analyses of a wire in a centrifuge or pull test, taking the extensibility of the wire into account. (The wire extensibility effect, which has been ignored in prior analyses, is usually not important, but it can become important if the wire has very little or no initial slack.)

- (b) Figure 8, which enables one to determine pull tests and centrifuge tests that are equivalent insofar as their stressing of wires and wire bonds is concerned.
- (c) Equation (7), which epitomizes the above equivalence information into a simple formula that is valid for wires of normal loop height.
- (d) Figure 10, which enables one to estimate centrifuge-induced bond stresses in chip-to-substrate and substrate-to-package bonds as a function of the fraction V of voids in the bonding area.
- (e) Equation (12), which enables one to estimate the centrifuge-induced force per pedestal for chips which are bonded face down to a few pedestals or bumps.
- (f) Equation (15), which enables one to determine hydrostatic pressures and centrifuge accelerations that are equivalent insofar as their flexing of the lids and bases of flatpacks is concerned.
- (g) Equation (16), which gives the extreme-fiber flexural stress for the case in which the centrifugal force acts parallel to the base and perpendicular to the plane of the wire loop.

Chapter 3 - FLATWISE IMPACT

In this chapter we consider a horizontal flatpack falling vertically and impacting upon a horizontal rigid surface, so that its motion is arrested in an extremely short time, and we investigate some of the stresses resulting from this rapid deceleration.

In particular, in Section I we consider the package falling with an upside-down orientation, so that the arrest of the motion will produce tension in the internal wires and wire leads. In that section we provide formulas and graphs that can be used to estimate the maximum wire tension as a function of the impact velocity and the arresting time, thereby enabling one to judge if the tensions achievable are significant enough to make the flatwise upside-down drop test a practical screen for the internal wires in closed packages. The wires are assumed to obey Hooke's law.

In Section II, theory is provided for estimating the flexural stresses in the base of the package undergoing the flatwise upside-down drop test. With the aid of this theory one can tell whether or not the impact velocities high enough to produce significant stressing of the internal wires will at the same time be too severe (i.e., damaging) for the package base. In this section also Hooke's law is assumed to hold.

In Section III the flexural response of the package lid in a right-side-up drop test is discussed.

Finally, in Section IV the question of feasibility of the upside-down flatwise drop test as a mechanical screen for the internal wires in closed packages is discussed, and a type of apparatus for such a test is described which merits investigation.

Although the discussion and results presented in this chapter are consistently referenced to the drop test, they may apply to other situations as well. For example, bringing a falling package to rest with constant deceleration from a pre-impact velocity v_0 in a stopping time t_s is equivalent to accelerating the same package upward with constant acceleration from a state of rest to a velocity v_0 in a time t_s .

I. WIRE STRESSES

A. Upper Bound Estimate.- The wire and an upside-down falling package just prior to their impact on a rigid surface are shown in Figure 1. The wire, BC, is assumed to have its ends at the same level and an initial loop height H that is small compared to the span S . The initial shape of the wire is represented by the function $y_0(x)$ in Figure 2. The wire is assumed to have negligible bending stiffness.

An upper-bound estimate of the maximum tension produced in the wire by the impact can be obtained by assuming that at impact the motion of the ends of the wire (B and C) is instantaneously arrested and the wire achieves an extreme deflected shape $y_1(x)$ (see Fig. 2) that is completely devoid of kinetic energy (as in a standing wave vibration). Assuming conservation of energy, we may equate the strain energy of the configuration $y_1(x)$ to the initial kinetic energy of the wire just prior to impact and thus determine the amount of stretch of the wire in its extreme deflected shape. An analysis on this basis has been carried out in Reference 11. The result, for wires that obey Hooke's law, is

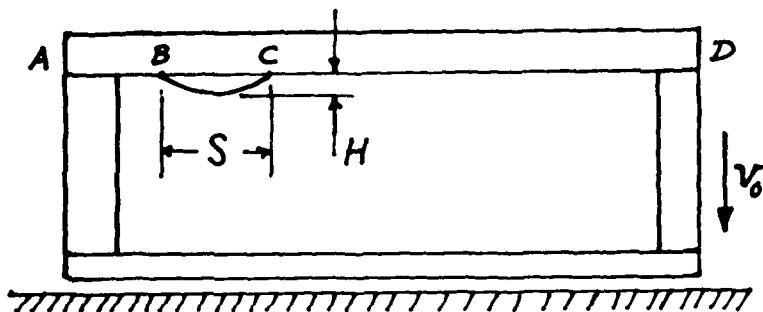


Figure 1.- Wire (BC) in a package undergoing upside-down flatwise impact.

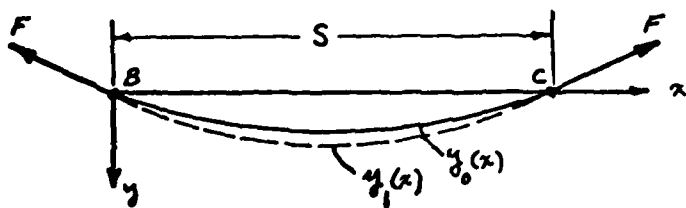


Figure 2.- Wire configurations (initial and deformed).

$$\epsilon_{\max} = v_o \sqrt{\frac{\rho}{E}} = \frac{v_o}{c} \quad (1)$$

$$\sigma_{\max} = E\epsilon_{\max} = v_o \sqrt{\rho E} = Ev_o/c \quad (2)$$

where ϵ_{\max} is the maximum strain produced in the wire, σ_{\max} is the corresponding maximum tensile stress, v_o is the velocity of fall just prior to the instantaneous arrest of the ends of the wire, ρ is the density of the wire material, E is the Young's modulus of the wire material and

$$c = \sqrt{E/\rho} \quad (3)$$

is the speed of sound in the wire. (These results, it will be noted, are independent of the spans.) The maximum bond force F_{\max} is obtained by multiplying σ_{\max} by the cross-sectional area A ; thus,

$$F_{\max} = \sigma_{\max} A = v_o \sqrt{\rho E} A \quad (4)$$

Equations (2) and (4) predict rather significant wire stresses and bond forces. For example, the following table gives the σ_{\max} and F_{\max} computed in Reference 11 for gold and aluminum wires of 1.2 mils diameter as a result of a 4-foot flatwise drop ($v_o = 16$ ft/sec):

	Gold	Aluminum
σ_{\max} (ksi)	28.3	9.77
F_{\max} (grams)	14.5	5.0

The stresses are a significant fraction of the ultimate tensile strengths of the wire materials, which are on the order of 60 ksi, and the bond forces are comparable to or greater than those that would be developed in the Method 2011.2 MIL-STD-883B pre-cap pull tests (see Figure 7 of Chapter 2).

B. More Accurate Analyses.- The assumptions of instantaneous arrest and subsequent standing wave motion, in the approach of Reference 11 just described, were considered to be possibly serious limitations on the validity of the results obtained; therefore more refined analyses were undertaken.

The first of these was presented in Reference 12. It retained the assumption of instantaneous arrest, but dropped the standing wave assumption, allowing instead for the travelling wave nature of the wire motion subsequent to the arrest of its ends; and it added an additional restriction to the effect that there was no initial slack, i.e., the initial loop height was zero. For this case, Reference 12 showed that the upper bound Equations (1), (2), and (4) are remarkably accurate -- only 5% too high*. However, Reference 12 still retained the assumption of instantaneous arrest and it had added a new assumption, that of zero initial slack; therefore, the acceptability of Equations (1), (2), and (4) was still in doubt, and additional work was undertaken.

This additional work consisted of a fairly straightforward extension of the analysis of Reference 12 to include both finite (non-zero) arresting time and finite (though small compared to S) loop height, with an initial parabolic wire shape. This analysis led to dimensionless graphs of wire strain versus time for given initial loop heights and arresting times. Typical graphs of this kind are shown in Figure 3. In this figure, e is a "reduced" strain parameter, T a dimensionless time, T_s a dimensionless

* It showed the strain rising to a peak value of $.95 v_0/c$ in a time of $t = .68 S/\sqrt{v_0 c}$, then diminishing rapidly, with the occurrence of the maximum strain coincident with the meeting of a pair of travelling deflection waves, one from each end of the wire.

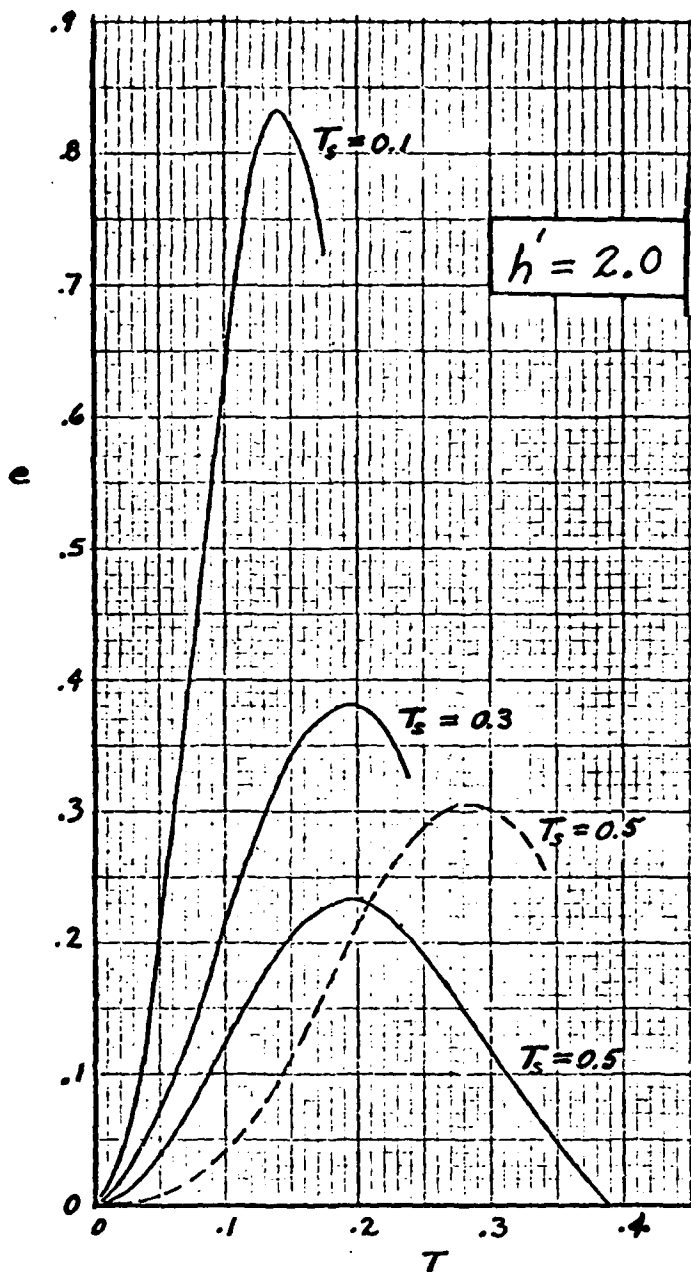


Figure 3.- Graphs of "reduced strain" e versus dimensionless time T for different dimensionless stopping times T_s and a dimensionless loop height of $h' = 2.0$. (Solid curves are for constant deceleration, dashed curve for sinusoidal deceleration.)

stopping time, and h' a dimensionless initial loop height. Their definitions are:

$$e = \frac{\epsilon c}{v_0} \quad (5)$$

$$T = \frac{t}{S} \sqrt{v_0 c} \quad (6)$$

$$T_s = \frac{t_s}{S} \sqrt{v_0 c} \quad (7)$$

$$h' = \frac{H}{S} \sqrt{\frac{c}{v_0}} \quad (8)$$

where ϵ is the actual strain (elongation divided by original length), t is actual time, t_s is actual stopping time (i.e., the time required for the velocity of the wire ends to drop from v_0 to 0), and H is the actual initial loop height. For simplicity, the deceleration during the arresting period was assumed to be constant, however the dashed curve shows the results of one set of calculations in which the deceleration was assumed to vary like a half-sine wave instead. It is seen that the latter assumption leads to somewhat higher strains.

By reading the peak values of e from many curves of the kind shown in Figure 3, it was possible to plot the curves of Figure 4, which gives the peak value, e_{\max} , as a function of T_s and h' , for the case of constant deceleration of the wire ends during the arresting period. In accordance with Equation (5) the actual maximum strain ϵ_{\max} can be recovered from the "reduced" maximum strain e_{\max} by means of the relationship

$$\epsilon_{\max} = e_{\max} \frac{v_0}{c} \quad (9)$$

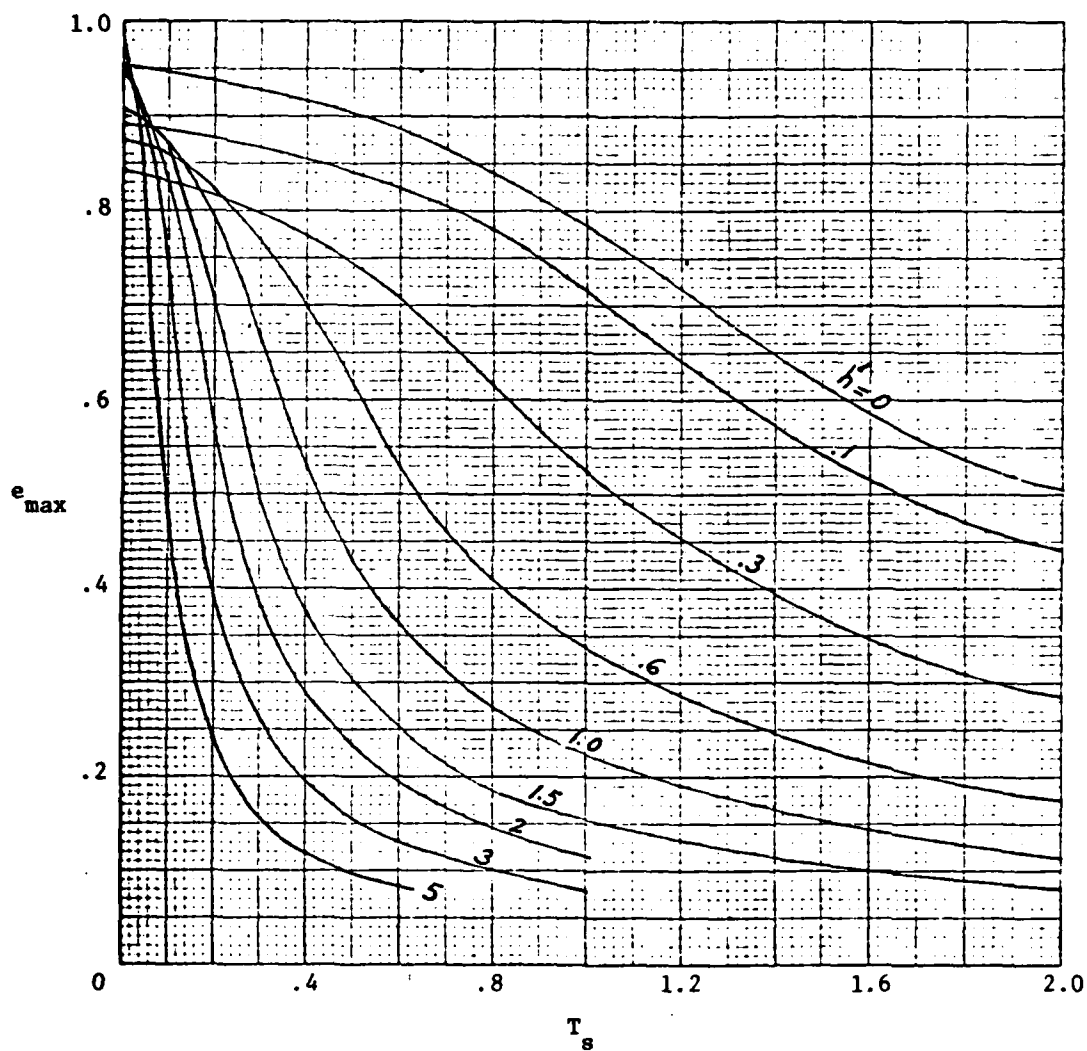


Figure 4.- Dimensionless graphs of maximum reduced strain as a function of stopping time and loop height.

As an aid in judging the degree of inaccuracy of the upper bound solution, Equation (1), as compared with Figure 4, it may be noted that Equation (1) is equivalent to

$$e_{\max} = 1 \quad (10)$$

The results in Figure 4 are interesting and revealing. All of the graphs start out at $T_s = 0$ with e_{\max} not much below 1.0; thus, if the arrest is instantaneous, finite loop height does not produce much reduction of e_{\max} from the upper bound value. Also, for small loop height ($h' \approx 0$) the graphs of e_{\max} drop down rather slowly as T_s increases; thus, finite stopping time does not produce much reduction of e_{\max} if the loop height is small. Therefore loop height alone and finite stopping time alone do not cause much reduction in the maximum strain below that predicted by the upper bound solution. However, the graphs show that finite loop height and finite stopping time together can indeed cause the e_{\max} to be very much less than the upper bound prediction. Also, in contrast to the upper bound solution, the more accurate analysis shows that the span S has a very important effect on e_{\max} . Equation (7) shows that a reduction in S will increase T_s and therefore (see Figure 4) reduce e_{\max} . Thus, it will be more difficult to stress short wires in a drop test than long wires. By the same token, any lengthening of t_s will also reduce the stressing capability of the drop test.

The maximum wire stress and bond force corresponding to any given wire geometry and stopping time can be obtained from Figure 4 through the following steps: Compute T_s and h' via Equations (7) and (8). Enter these in

Figure 4 to get e_{\max} . Then Equation (9) will give ϵ_{\max} and the relations

$$\sigma_{\max} = E\epsilon_{\max} \quad F_{\max} = A\sigma_{\max} \quad (11)$$

will give the maximum wire stress and bond force.

C. Numerical Examples.- In order to demonstrate the calculation procedures just outlined, we shall consider a 1-mil diameter wire made of gold ($E = 12 \times 10^6$ psi, $\gamma =$ specific weight = 0.7 lb/in.³, $\rho = .00181$ lb-sec²/in.⁴), with a span of $S = .100$ in. and an initial loop height of $H = .006$ in., falling with a pre-impact velocity of $v_0 = 8$ ft/sec (which corresponds to a 1-foot drop) and, by virtue of highly polished and highly parallel impacting surfaces, having its ends arrested in 9 micro-seconds (which corresponds to an average deceleration of 27,600 g's), and compute the resulting maximum tensile stress and bond force.

From the given data we have

$$c = \sqrt{\frac{E}{\rho}} = \sqrt{\frac{12 \times 10^6}{.00181}} = 81,424 \frac{\text{in.}}{\text{sec}} = 6785 \frac{\text{ft.}}{\text{sec}}$$

$$h' = \frac{H}{S} \sqrt{\frac{c}{v_0}} = \frac{.006}{.100} \sqrt{\frac{6785}{8}} = 1.75$$

$$T_s = \frac{t_s}{S} \sqrt{v_0 c} = \frac{9 \times 10^{-6}}{(.100)} \sqrt{8(6785)} = .25$$

Entering Figure 4 with $T_s = .25$ and interpolating between the curves for $h' = 1.5$ and 2.0 , we read $e_{\max} = .525$, whence

$$\epsilon_{\max} = e_{\max} \frac{v_0}{c} = (.525) \frac{8}{6785} = .000619$$

$$\sigma_{\max} = E\epsilon_{\max} = (12,000,000)(.000619) = 7428 \text{ psi}$$

$$F_{\max} = A\sigma_{\max} = \frac{\pi}{4} (.001)^2 (7428) = .00583 \text{ lb} = 2.65 \text{ grams}$$

We note that the wire stress of 7428 psi is a significant fraction of the ultimate tensile strength of gold wires (which is around 60,000 psi). In order to judge the significance of the 2.65-gram bond force, we may use Figures 2 and 7 of Chapter 2 to compute the pull P that would be required in a pull test to produce the same bond force. We first enter Figure 2 with $H/S = .006/.100 = .06$ and read $R = .01$ from the "catenary" curve. For this R and an ordinate of $T_0/AE = \epsilon_{\max} = .000619$, Figure 7 gives $P/AE = 1.8 \times 10^{-4}$. Thus, the required pull is $P = (1.8 \times 10^{-4}) \times [\frac{\pi}{4} (.001)^2] \times 12,000,000 = .00170 \text{ lb} = 0.77 \text{ grams}$. This is considerably less than the pre-seal pull strength of 3.0 grams and post-seal pull strength of 2.5 grams specified in the MIL-STD-883B Method 2011.2.

Thus, the postulated drop test is not as effective as the pull test. However, it has the advantage of being applicable to a closed package; furthermore it is more effective than the centrifuge. According to Equation (7) of Chapter 2 the number of g's of centrifuge acceleration equivalent to the postulated drop test is

$$G = \frac{P}{.59\gamma SA} = \frac{.00170}{(.59)(.7)(.100)[\frac{\pi}{4} (.001)^2]} = 52,400$$

It is not practical to attempt to subject a package to that many g's in a centrifuge. If arresting times t_s shorter than 9 microseconds can be achieved, the effectiveness of the drop test will, of course, be improved.

The effects of changing the material from gold to aluminum and the impact velocity from 8 to 16 ft/sec are seen in the tables below, where the results of the above calculation and three others are summarized. Because aluminum has a much lower density than gold, any test methods that depend on the inertia of the wire will be less effective for aluminum than for gold. This is well known in the case of the centrifuge; it is equally true for the drop test, as the tables show. However, as the second table shows, even for the aluminum the drop test retains its advantage in relation to the centrifuge.

Gold Wire

v_o (ft/sec)	σ_{max} (psi)	F_{max} (grams)	Equivalent P in a Pull Test (grams)	Equivalent g's in a Centrifuge
8	7,428	2.65	.77	52,300
16	14,150	5.0	1.5	101,000

Aluminum Wire

v_o (ft/sec)	σ_{max} (psi)	F_{max} (grams)	Equivalent P in a Pull Test (grams)	Equivalent g's in a Centrifuge
8	1112	.40	.11	50,800
16	2150	.76	.21	102,000

II. BASE STRESSES

We now focus attention upon the base AD of the package in Figure 1 and examine its flexural response to the suddenly imposed assumedly constant deceleration of the walls to which it is attached. For this purpose we shall regard the base as a clamped elastic rectangular plate undergoing small oscillations during and after the deceleration period and make use of the approximate analysis of those oscillations in Appendix C, as well as other approximate techniques.

A. Equivalent Lateral Pressure.- Assuming small deflections and Hooke's law, Appendix C describes the state of deformation of the plate (relative to its boundary supports) at any instant t by means of an "equivalent" uniform lateral pressure p , defined as that pressure which, if applied statically, would produce approximately the same state of deformation. Once this equivalent lateral pressure p is known for any instant t , the dynamic deflections and stresses at that instant can be taken from the static deflections and stresses produced by it. Inasmuch as many static solutions are available for uniformly loaded plates, the use of the equivalent lateral pressure concept greatly simplifies the dynamic stress analysis.

For constant deceleration of the package walls during the stopping period, Figure 1 of Appendix C shows typical graphs of the equivalent lateral pressure p as a function of time t for different stopping times t_s , using however dimensionless measures of p , t and t_s , instead of p , t and t_s directly. The dimensionless measures are Q , τ and τ_s , respectively, defined as follows:

$$Q \equiv \frac{p}{m \omega_n v_o} \quad (12)$$

$$\tau = \omega_n t \quad (13)$$

$$\tau_s = \omega_n t_s \quad (14)$$

where m is the mass per unit area of the plate, and ω_n is the natural circular frequency of its fundamental mode of vibration. Constant deceleration during the stopping period is assumed.

Of special interest are the maximum downward and maximum upward equivalent pressures. The values of Q corresponding to these maximums can be read from the positive and negative peaks of the curve for that τ_s in Figure 1. These maximums are summarized in Figure 2 of Appendix C. For any given τ_s , as determined from Equation (14), the ordinate of the solid curve of Figure 2, in conjunction with Equation (12), will give the maximum downward equivalent pressure for base AD of the package, and the ordinate to the dashed curve will similarly give the maximum upward equivalent pressure.

In order to use Figure 2 of Appendix C in the manner just described, one must know the fundamental natural circular frequency ω_n of the base, and it can be found with the aid of Figure 3 of Appendix C. In this figure, a and b are the length and width of the base, as measured inside the cavity, m is its mass per unit area, and D is its plate flexural stiffness. If the base is homogeneous with Young's modulus E , Poisson's ratio ν , thickness h , and density ρ , then m and D are given by

$$m = \rho h \quad D = Eh^3/12[1 - \nu^2] \quad (15)$$

and the conversion from equivalent pressure p to deflections and stresses can be done with the aid of the formulas and graphs in Chapter 1 or the tables in Reference 3, the most useful of which are reproduced in Appendix B of the present report. If the base is a two-component composite, like that shown in Figure 1 of Appendix B, D is computed by means of Equation (5) of Appendix B, and m from the formula $m = \rho_1 h_1 + \rho_2 h_2$, where ρ_1 and h_1 are the density and thickness of the upper component, ρ_2 and h_2 those of the lower component. (In such a composite base the upper component would typically be Kovar, the lower component a ceramic.) The conversion from equivalent pressure to deflections and stresses would be done on the basis of the procedures described in Section V of Chapter I.

B. Numerical Examples.- For the first of two numerical examples we shall assume that the base AD of the package in Figure 1 is a square ceramic clamped plate with the following properties:

$$a = b = .875 \text{ in.}$$

$$h = \text{thickness} = .040 \text{ in.}$$

$$\rho = 3.85 \text{ grams/cm}^3 = .0003603 \text{ lb/sec}^2/\text{in.}^4$$

$$E = 50 \times 10^6 \text{ psi}$$

$$\nu = 0.22$$

$$\sigma_b = \text{flexural strength} = 65,000 \text{ psi,}$$

compute the maximum tensile stress produced in it by the constant-deceleration arrest assumed for the gold wire in Section IC (namely an arrest in 9 microseconds from a pre-impact velocity of 8 ft/sec), and then judge whether or not the base is likely to be damaged in such a test.

From the given data, we have, for the one-component base under consideration,

$$m = \rho h = (.0003603)(.040) = 14.41 \times 10^{-6} \text{ lb-sec}^2/\text{in.}^3$$

$$D = \frac{Eh^3}{12(1-\nu^2)} = \frac{(50 \times 10^6)(.040)^3}{12[1 - (.22)^2]} = 280.2 \text{ lb-in.}$$

Entering Figure 3 of Appendix C with $a/b = 1$, we get

$$\omega_n = 36 \sqrt{\frac{D}{ma^4}} = 36 \sqrt{\frac{280.2}{(14.41 \times 10^{-6})(.875)^4}} = 207,343 \text{ sec}^{-1}$$

whence

$$\tau_s = \omega_n t_s = (207,343)(9 \times 10^{-6}) = 1.87$$

For this τ_s , Figure 2 of Appendix C gives

$$Q_{\max} = (-Q)_{\max} = .86$$

The corresponding equivalent pressures are

$$\begin{aligned} p &= \pm .86 m \omega_n^2 v_0 \\ &= \pm .86 (14.41 \times 10^{-6})(207,343)^2 (8 \times 12) \\ &= \pm 247 \text{ psi} \end{aligned}$$

where plus means downward and minus upward.

The simplest procedure for estimating the maximum tensile stress due to this pressure is with the aid of Table 1 of Appendix B. It shows the maximum bending moment in the clamped base under uniform pressure to occur at the middle of the sides and to have the magnitude

$$M_{\max} = .0513 \text{ pa}^2 = .0513(247)(.875)^2 = 9.70 \text{ in-lb/in.}$$

The stress due to this moment is zero at the middle surface and varies linearly through the thickness. Its maximum value therefore occurs at the extreme fibers and is

$$\sigma_{\max} = \frac{6 M_{\max}}{h^2} = \frac{6(9.70)}{(.040)^2} = 36,400 \text{ psi}$$

This is less than the ceramic's flexural strength of 65,000 psi, and the base is therefore not likely to be damaged by the postulated drop test.

For the second example we assume the same conditions as before, except that the base AB of Figure 1 is now a two-component base, like that of Figure 1 of Appendix B, with the upper component .015-in. thick Kovar and the lower component .025-in. thick ceramic of the same kind as before, making the total thickness the same as before. Again let us calculate the maximum tensile stress in the ceramic and judge whether or not it will fracture under the postulated drop test.

This two-component base has figured in a previous example (Example 7 of Section VIII of Chapter 1). Therefore, with no additional calculation we have

$$D = 179.929 \text{ lb-in.}$$

$$\nu = .261$$

for its plate bending stiffnesses and flexural Poisson's ratio. Taking the density of Kovar to be $0.30 \text{ lb/in.}^3 = .000777 \text{ lb-sec}^2/\text{in.}^4$, and the density of the ceramic to be $.0003603 \text{ lb-sec}^2/\text{in.}^4$ as before, we obtain

$$\begin{aligned}
 m &= (.000777)(.015) + (.0003603)(.025) \\
 &= 20.66 \times 10^{-6} \text{ lb-sec}^2/\text{in.}^3
 \end{aligned}$$

for the mass per unit area. The fundamental circular frequency is then

$$\begin{aligned}
 \omega_n &= 36 \sqrt{\frac{D}{ma^4}} = 36 \sqrt{\frac{179.929}{(20.66 \times 10^{-6})(.875)^4}} \\
 &= 138,762 \text{ sec}^{-1}
 \end{aligned}$$

Therefore

$$\tau_s = \omega_n t_s = (138,762)(9 \times 10^{-6}) = 1.25$$

for which Figure 2 of Appendix C gives

$$Q_{\max} = (-Q)_{\max} = .94$$

Again the maximum downward and maximum upward equivalent pressures have the same magnitude.

The pressures themselves are

$$\begin{aligned}
 p &= \pm .94 m \omega_n^2 v_0 \\
 &= \pm .94(20.66 \times 10^{-6})(138,762)(8 \times 12) \\
 &= \pm 259 \text{ psi}
 \end{aligned}$$

Visualizing the curvatures of the clamped base under each of these two "pressures," we take the following four stresses as candidates for the maximum tension in the ceramic: $\sigma_{x_{21}}$ and $\sigma_{x_{22}}$ at the center of the plate; $\sigma_{x_{21}}$ and $\sigma_{x_{22}}$ at the middle of the edge $x = 0$. (The notation is that of

Figures 1 and 4 of Appendix B.) Utilizing the procedure described in Chapter 1, Section V, we obtain the following values for these stresses due to the equivalent pressures of ± 259 psi

Location	Stress Symbol	Stress Value (psi)
Center of Base	$\sigma_{x_{21}}$	$\mp 12,100$
	$\sigma_{x_{22}}$	$\pm 24,400$
Middle of Edge $x = 0$	$\sigma_{x_{21}}$	$\pm 29,300$
	$\sigma_{x_{22}}$	$\mp 57,000$

Thus the maximum tensile stress in the ceramic is the extreme-fiber stress of $\sigma_{x_{22}} = 57,000$ psi developed at the edge of the base during the upward flexing phase of its motion. This is smaller than the flexural strength of 65,000 psi and would therefore appear to be safe. However, the judgment of "safe" must be changed to "probably safe" when we take into account the likelihood that there will be a small gap between the periphery of the ceramic substrate and the walls of the package, examine the calculated edge bending moment in the Kovar within that gap, and compare it with the fully plastic bending strength of the Kovar, which was found to be $m_e = 4.01$ in-lb/in. in the Chapter 1 example referred to earlier. That calculated edge bending moment is

$$M_{\text{edge}} = .0513 \text{ pa}^2 = .0513(259)(.875)^2 = 10.2 \text{ in-lb/in.}$$

which exceeds m_e by some $2 \frac{1}{2}$ times. Thus, we can expect some plastic

hinge development in the central region of each edge. This would reduce the edge stress $\sigma_{x_{22}}$ in the ceramic to the still safer value of

$$\frac{4.01}{10.2} \times 57,000 = 22,400 \text{ psi}$$

but it would increase the ceramic stress $\sigma_{x_{22}}$ in the center of the plate above its calculated value of 24,400 psi by some unknown amount. Conceivably, the increase could bring the total stress in the ceramic up to the breaking point of 65,000 psi.

C. Incorporation of Elastic Large Deflection Effects: A Simple Expedient.— Small deflection theory was used in the derivations connected with "equivalent lateral pressure" (Appendix C). Therefore if the method of Section A above leads to small-deflection-theory deflections that are large (i.e., of the same order as the base thickness), those deflections, the associated stresses, and the equivalent pressure are, strictly speaking, not correct. The simplest expedient for correcting the deflections and stresses is to accept the equivalent pressure as correct, but calculate the deflections and stresses from a large-deflection theory (e.g., Figures 12, 14 and 15 of Chapter 1 for a single component base), rather than a small-deflection theory. There is an admitted inconsistency in this procedure, but the results obtained thereby will be more accurate than those obtained by a strict adherence to small-deflection theory.

D. Incorporation of Elastic Large Deflection Effects: A More Rigorous Approach.— A somewhat more rigorous procedure for incorporating large-deflection effects into the dynamic analysis of base response is given in

Reference 13, but is restricted to a single-component base and instantaneous or near-instantaneous arrest of motion ($Q \approx 1$). For a clamped base, that procedure gives Figure 5 as the relationship between impact velocity v_0 and equivalent lateral pressure p . With p known, existing large-deflection solutions (e.g., Figures 12, 14 and 15 of Chapter 1) can be used to determine maximum tensile stress and central deflections. If we assume the boundary restraints of Figure 12(c) and 15(c) of Chapter 1, in particular, Figures 6 and 7 of the present section are obtained for the maximum tensile stress σ'_{\max} and central deflection δ as functions of the impact velocity v_0 .

III. LID RESPONSE

Obviously, most of the material in Section II is applicable to the lid of a flatpack in a right-side-up flatwise drop test. If the lid is of a ductile metal, however, an additional consideration may be important that was not covered in Section II, namely the effect of plasticity on the maximum central deflection. This consideration will be taken up in the present section, with attention restricted to the case of instantaneous or near-instantaneous arrest ($Q \approx 1$).

A. Plasticity Considerations.- For the lower v_0 's there may be no plastic yielding at all or the plastic regions may be quite localized, which means that the computed central deflection neglecting plasticity may still be reasonably accurate. (It has been suggested in Reference 5 that the computed central deflections neglecting plasticity are correct even if the computed elastic stresses exceed the tensile yield stress by as

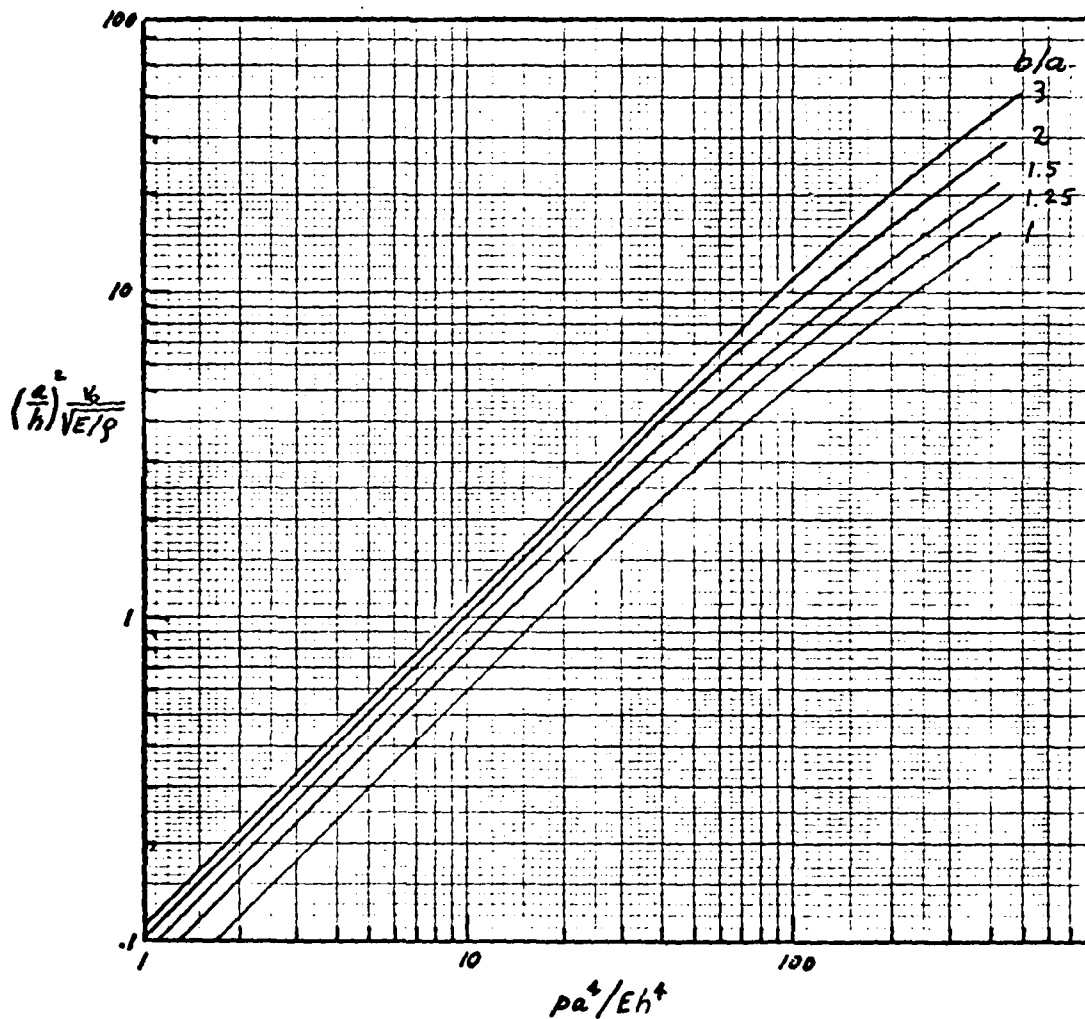


Figure 5.- Graphs for determining lateral pressure p approximately equivalent to a given impact velocity v_0 for a clamped rectangular base in an upside-down flatwise drop test. (Based on approximate elastic large-deflection theory and instantaneous arrest of boundary motion upon impact. Taken from Reference 13.)

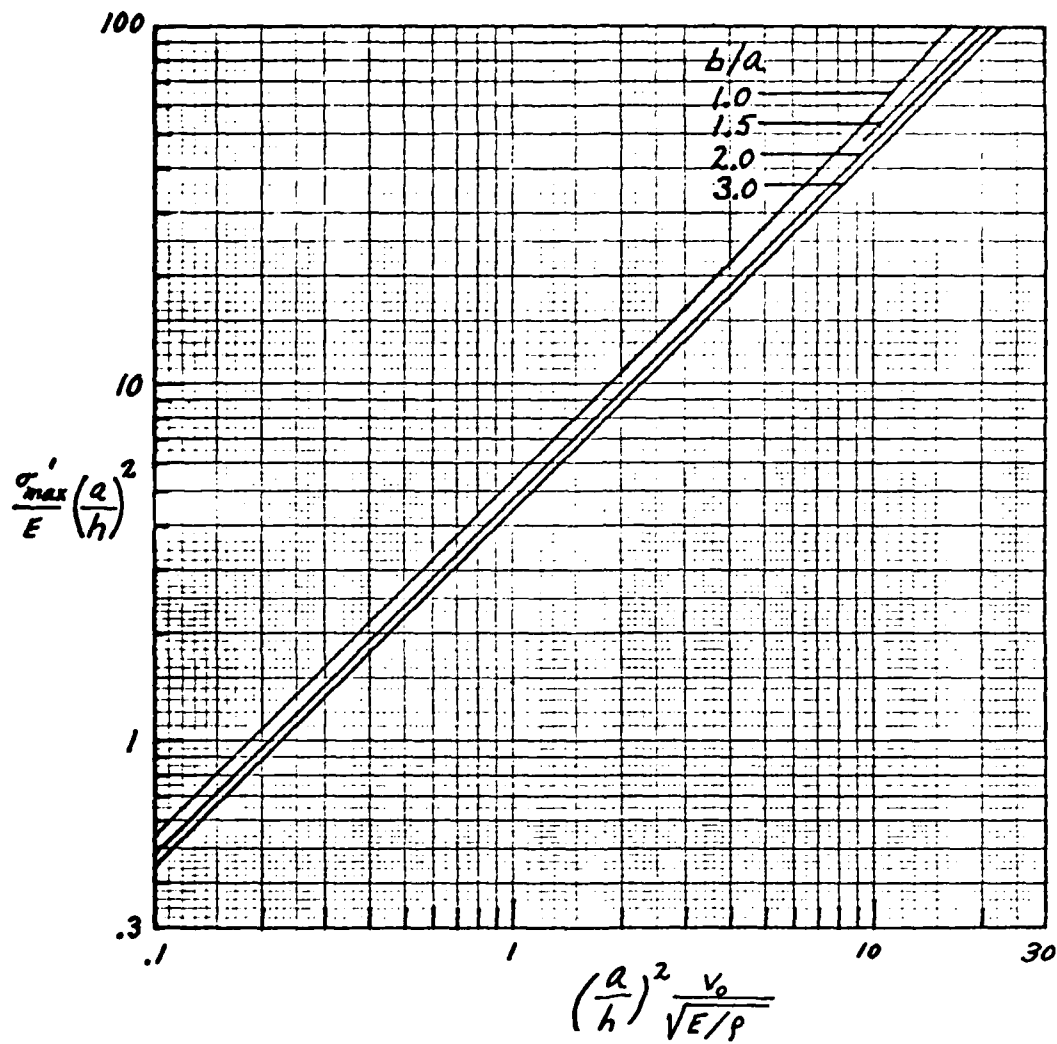


Figure 6.- Graphs for determining maximum tensile stress σ'_{\max} in a clamped rectangular base in a flatwise upside-down drop test due to instantaneous arrest of its boundary from a velocity v_0 . (Based on approximate elastic large-deflection theory. Taken from Reference 13.)

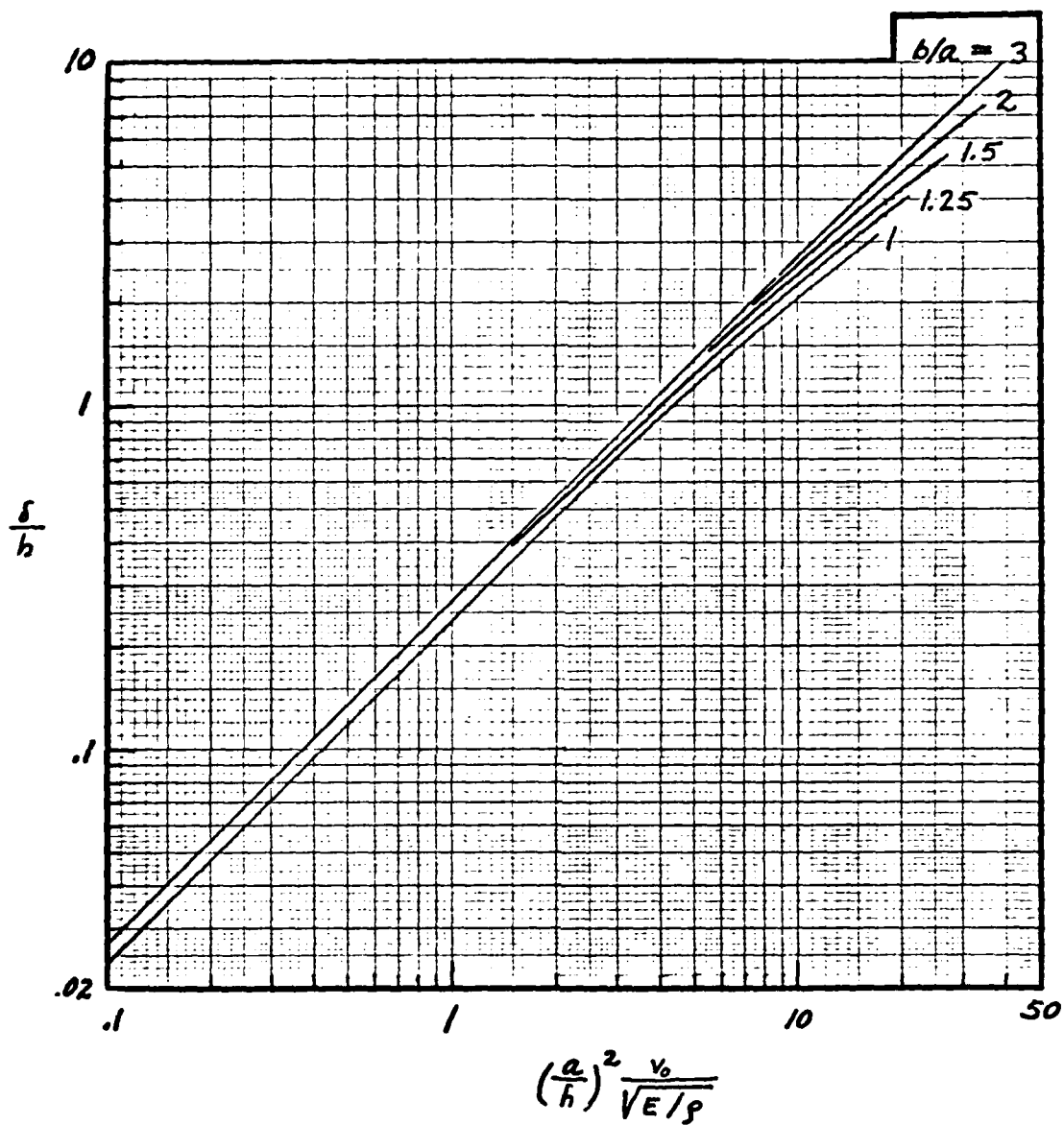


Figure 7.- Graphs for determining maximum central deflection δ produced in a clamped rectangular base in a flatwise upside-down drop test due to instantaneous arrest of its boundary from a velocity v_0 . (Based on approximate elastic large-deflection theory. Taken from Reference 13.)

much as 50%.) For more severe impacts the regions of plastic flow may become comparable in extent with those of elastic deformation, and then the elastic calculations could seriously under-estimate the central deflection. Unfortunately, the analysis of rectangular plates in which elastic and inelastic deformations are of comparable importance is very difficult, and we shall not attempt it here. Paradoxically, the case of very highly developed plasticity, as might occur with the larger v_0 's in instantaneous or near-instantaneous ($Q \approx 1$) arrests, can be handled more easily, using limit or yield-line analysis. Such an analysis was carried out in Reference 13, and the following result was obtained for the maximum central deflection δ of a constant-thickness clamped rectangular lid as a function of the pre-impact velocity v_0 for the case of instantaneous or near-instantaneous arrest:

$$\delta = \frac{3}{4Z} \frac{ba}{h} \frac{v_0^2 \rho}{\sigma_b} \quad (16)$$

where h , a and b are the thickness, width and length of the lid; ρ is the density of the lid material; σ_b is the modulus of rupture of the lid material; and

$$Z = \frac{2}{3} \left[\frac{a}{b} + 3 \frac{b}{a} + \sqrt{\left(\frac{a}{b}\right)^2 + 3} \right] \quad (17)$$

The modulus of rupture σ_b is related to the fully plastic bending strength m_p as follows:

$$m_p = \sigma_b h^2 / 6 \quad (18)$$

Therefore Equation (16) may be written as

$$\delta = \frac{h}{8Z} \frac{bav_o^2 \rho}{m_p} \quad (19)$$

If the lid has a thinned edge, as in Figure 2 of Chapter 1, with thickness h_e less than the thickness h of the rest of the lid, the fully plastic bending strength in the edge region will be

$$m_{pe} = \sigma_b h_e^2 / 6 \quad (20)$$

and instead of (19) the following deflection formula is obtained:

$$\delta = \frac{h}{4Z} \frac{bav_o^2 \rho}{m_{pe} + m_p} \quad (21)$$

Inasmuch as m_{pe} and m_p are proportional to the squares of h_{pe} and h_p , m_{pe} will usually be much smaller than m_p , allowing Equation (21) to be simplified to

$$\delta = \frac{h}{4Z} \frac{bav_o^2 \rho}{m_p} \quad (22)$$

B. Maximum Deflection of a Constant-Thickness Ductile Lid.- Given the v_o of a right-side-up flatwise drop test of a package with a constant-thickness ductile lid, we do not know at the outset if plasticity effects need to be considered in calculating the maximum central deflection δ in an instantaneous or near-instantaneous ($Q \approx 1$) arrest. Therefore the following procedure is recommended for arriving at this deflection:

- (a) Compute δ considering the lid as a clamped plate and ignoring plasticity -- i.e., by the methods of Section II.
- (b) Compute δ on the basis of yield-line analysis -- i.e., using Equation (16) or (19).

Both of these calculations will probably under-estimate δ , the first because it neglects plasticity, the second because it assumes the lid to be rigid everywhere except along the yield lines. Therefore take the larger of the two results as the better estimate of the maximum central deflection.

C. Maximum Deflection of a Ductile Lid with Thinned Edges.— The following steps are recommended in this case:

- (a) Compute the edge bending moment normal to the middle of the longer edges considering the lid to be a clamped plate and ignoring plasticity -- i.e., by the methods of Section II. If this bending moment is smaller than m_{pe} , you may assume that there are no plasticity effects; therefore do step (a) of the preceding section and go no further. If the bending moment is larger than m_e , plastic hinges will have formed over some portions of the edges, and the lid may actually be behaving more like a simply supported plate than a clamped plate. Therefore do the following steps.
- (b) Compute δ considering the lid to be a simply supported plate and ignoring plasticity -- i.e., by the methods of Section II, using tables and/or graphs that apply to simply supported plates, rather than to clamped plates. This will be a conservative (i.e., too large) estimate of the elastic central deflection.
- (c) Compute δ on the basis of yield-line analysis -- i.e., using Equation (21) or (22).
- (d) Take the larger of the above two δ 's as the best estimate of maximum central deflection.

D. Numerical Examples.- Let us determine the maximum inward central deflection of a constant-thickness Kovar lid due to a 16 ft/sec impact in a flatwise right-side-up drop test, assuming essentially instantaneous arrest of the package walls. The dimensions and properties of the lid are: $a = .92$ in., $b = 1.84$ in., $h = .010$ in., $E = 20 \times 10^6$ psi, $\nu = 0.3$, $\sigma_b = 107,000$ psi, $\rho = 0.3$ lb/in³ = .000777 lb-sec²/in.⁴.

From the given data,

$$\frac{b}{a} = 2 \quad \frac{a}{b} = 0.5$$

$$m = \rho h = (.000777)(.01) = 7.77 \times 10^{-6} \text{ lb-sec}^2/\text{in.}^3$$

$$D = \frac{Eh^3}{12(1-\nu^2)} = \frac{(20 \times 10^6)(.01)^3}{12[1 - (.3)^2]} = 1.8315 \text{ lb-in.}$$

Figure 3 of Appendix C then gives

$$\omega_n = 24.5 \sqrt{\frac{D}{ma^4}} = 24.5 \sqrt{\frac{1.8315}{(7.77 \times 10^{-6})(.92)^4}} = 14053 \text{ sec}^{-1}$$

For near-instantaneous arrest, Figure 2 of Appendix C gives $Q_{\max} = 1$.

Therefore Equation (12) gives the equivalent pressure as

$$p = m\omega_n v_o = (7.77 \times 10^{-6})(14053)(16 \times 12) = 20.965 \text{ psi}$$

The corresponding small-deflection-theory center deflection from Table 1 of Appendix B or Figure 14 of Chapter 1, is,

$$\delta = .00254 \frac{pa^4}{D} = .00254 \frac{(20.965)(.92)^4}{1.8315} = .0208 \text{ in.}$$

This is larger than the lid thickness of .010 in. Therefore a correction is needed. Adopting the suggestion of Section IIC, we shall accept the

calculated p and use Figure 15(c) of Chapter 1 to obtain the deflection correction factor n_5 for that p . To that end we compute

$$\frac{pa^4}{Eh^4} = \frac{(20.965)(.92)^4}{(20 \times 10^6)(.01)^4} = 75$$

Entering this and $b/a = 2$ into Figure 15(c) of Chapter 1, we find that $n_5 = .89$. The corrected central deflection is therefore

$$\delta = (.0208)(.89) = .018 \text{ in.}$$

This completes step (a) of the Section B procedure.

For Step (b), we use Equations (17) and (16) to compute a second δ estimate, based on yield-line theory, as follows:

$$z = \frac{2}{3} \left[0.5 + 3(2) + \sqrt{(0.5)^2 + 3} \right] = 5.535$$

$$\delta = \frac{3}{4(5.535)} \cdot \frac{(1.84)(.92)}{.01} \cdot \frac{(16 \times 12)^2 (.000777)}{107,000} = .006 \text{ in.}$$

The larger of the two δ estimates, namely .018 in., is taken as the better one.

IV. FEASIBILITY OF THE DROP TEST AS A SCREEN

On the basis of the studies in Sections I and II, some observations can be made about the feasibility of the flatwise upside-down drop test as a stressing device for the wires in closed flatpacks.

First, it is clear that, as far as the wires alone are concerned, any significant stressing will require rather short stopping times t_s -- stopping times on the order of several microseconds.

Secondly, in order for those short stopping times not to result in damage to the base of the package, the pre-impact velocity v_0 will have to be small -- say of the order of 8 ft/sec.

Thirdly, if these conditions can be met, there will be at least some (not all) wire configurations that can be stressed sufficiently to rupture poor quality wires or bonds. The stressing will be most effective for the longer wires (say $S \geq .1$ in) of denser material (e.g., gold) and least effective for the shorter ($S < .1$ in) and lighter (aluminum) wires.

The requirement of small v_0 can be met by having the package drop from a sufficiently small height. Meeting the small t_s requirement is more difficult; it will require that the surfaces that come in contact during the impact be highly polished and highly parallel, so that the closure of the gap between them can be accomplished in a very short time.

A suggested apparatus for the drop test is shown schematically in Figure 8. It would consist of two equal-diameter hardened solid cylinders A and B, of bearing steel (say AISI 52100), one above the other and with their axes vertical. The lower and slightly longer cylinder would be firmly grounded. The upper cylinder with surfaces ab and cd highly polished and parallel, would carry the test package firmly pressed to its upper surface ab, and, suitably guided, would fall and strike the lower cylinder. If the impacting surfaces cd and ef were flat and parallel to within close tolerances, surface cd would experience a near-instantaneous velocity change. Through wave action this velocity change would be replicated, with a time delay, at the upper surface ab, and there imparted to the package. (Note that if v_0 is the desired impact velocity, the falling speed v_1 of the

upper cylinder would have to be $2v_0$, as indicated in the sketch. The reason is that surface cd is brought to rest only with respect to a reference frame in which the two cylinders are approaching each other with equal speed; such a reference frame is one that is moving downward with a speed of $v_1/2$. Relative to this reference frame, the surface cd is brought to rest from a speed of $v_1/2$. Therefore $v_1/2$ must equal the desired v_0 .)

The crucial question is whether the surface asperities can be made small enough and the parallelism maintained well enough to produce gap closures in times as short as several microseconds. Experiments performed in another context suggest that this may indeed be possible. The experiments referred to are those conducted at the Sandia Laboratories and elsewhere for determining material properties at high strain rates. These experiments involved the impact of highly polished parallel surfaces, and the literature resulting from them (e.g., References 14 and 15) reports closures occurring in nanoseconds. Of course, the impacting velocities in these experiments were several orders of magnitude higher than the 8 ft/sec velocity proposed for the drop test, but then the required closure times in the drop test are correspondingly several orders of magnitude slower, being measured in microseconds, rather than nanoseconds.

Thus, it is likely that techniques are available for achieving the degree of surface flatness and parallelism needed in the drop test. It is conceivable that the air in the gap between the two cylinders might serve as a cushion to impede rapid closure, in which case that gap should be evacuated or the apparatus enclosed in a vacuum chamber. Also, some developmental effort would undoubtedly be needed in order to achieve firm

contact between the package base and surface ab of the cylinder holding the package; lapping of the package base and the use of a thin liquid film between package base and cylinder surface are two techniques that could be tried.

It does not appear that further analysis and reasoning can provide a definitive answer to the question of the feasibility of the proposed drop test apparatus. However, the concept does seem promising enough to make the development of a prototype device a worthwhile undertaking, if entrusted to one of the groups experienced in the study of material properties at high strain rates through the impact of highly polished parallel surfaces.

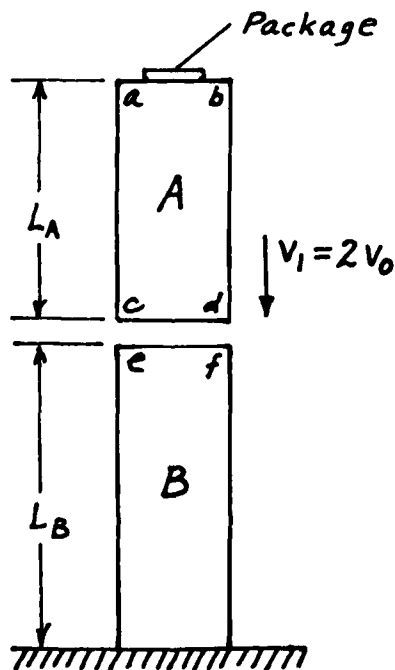


Figure 8.- Schematic diagram of drop test apparatus ($L_B > L_A$).

Chapter 4 - EDGEWISE IMPACT

In this chapter (which is based largely on Reference 13) we consider a flatpack in edgewise impact on a rigid surface (Figure 1) with a velocity v parallel to the longer dimension, and review some possibly damaging effects this impact could have on the lid or base. The lid and base types to be considered are shown in Figure 2.

I. SINGLE-COMPONENT LID OR BASE

A. Elastic.- The single-component lid or base impacting edgewise with velocity v on a rigid surface (Figure 3) can, in first approximation, be treated as a uniform rod. When the material is linearly elastic (obeys Hooke's law), the classical theory of impact for a rod (Reference 16) indicates that a compressive stress σ will start to propagate upward immediately upon contact, travel with the speed of sound c in the material, and eventually encompass the entire length of the lid or base (Figures 3(c) and (d)). A tensile stress of the same magnitude will then propagate downward, cancelling out the compressive stress as it goes (Figure 3(e)).

If E is the Young's modulus of the material and ρ its density, the magnitude of the compressive stress will be

$$\sigma = \frac{v}{c} E \quad (1)$$

where

$$c = \sqrt{E/\rho} \quad (2)$$

is the speed of sound in the material. Supposing that the velocity v is due to a free fall from a height h , we may write

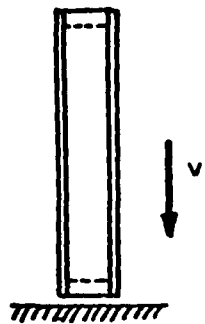


Figure 1.- Edgewise impact of a rectangular flat-pack on a rigid surface.

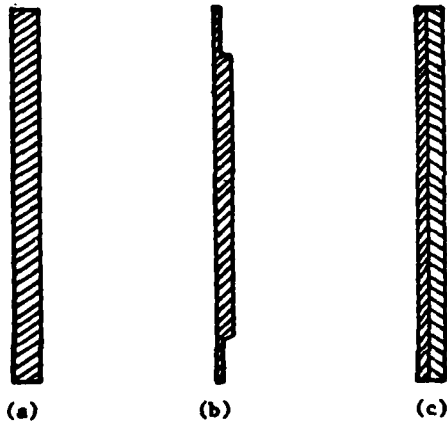


Figure 2.- Lid and base variations considered: (a) Constant-thickness lid or base. (b) Lid with thinned edges. (c) Two-component base.

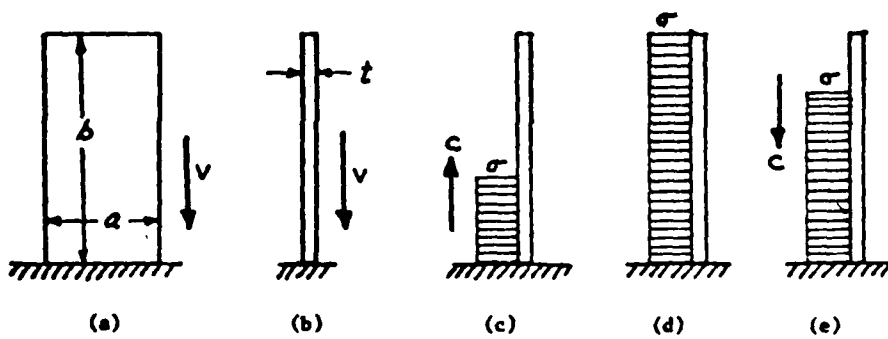


Figure 3.- Edgewise impact of lid or base on rigid surface. (a) Front view. (b) Side view. (c) Compressive stress wave travelling upward. (d) Wave front has reached top edge. (e) Unloading wave travelling downward. (v = impact velocity; c = speed of sound in the material.)

$$v = \sqrt{2gh} \quad (3)$$

where g = acceleration of gravity = $32.2 \text{ ft/sec}^2 = 386 \text{ in/sec}^2 = 9.8 \text{ m/s}^2$.

Using this to eliminate v in Eq. (1), and Eq. (2) to eliminate c , we arrive at the following alternate formula for σ :

$$\sigma = \sqrt{2gh\rho E} \quad (4)$$

The compressive strain ϵ corresponding to σ is σ/E . Thus,

$$\epsilon = v/c = v\sqrt{\rho/E} = \sqrt{2gh\rho/E} \quad (5)$$

In a free fall from a small height, v and h are rather small, but E is generally very large; therefore Eq. (1) or (4) can lead to significant stresses. For example, let us consider two specific materials, a Kovar lid and a ceramic base with the following properties:

	Kovar	Ceramic
E (lb/in ²)	20×10^6	47×10^6
E (lb/ft ²)	2880×10^6	6800×10^6
ρ (lb-sec ² /ft ⁴)	16.2	7.18
$c = \sqrt{E/\rho}$ (ft/sec)	13,300	30,700

An impact velocity of 16 ft/sec, which corresponds to a 4-foot drop, will lead to a compressive stress of

$$\sigma = \frac{v}{c} E = \frac{16}{13,300} (20 \times 10^6) = 24,000 \text{ psi} \quad (6)$$

in the Kovar and

$$\sigma = \frac{16}{30,700} (47 \times 10^6) = 24,500 \text{ psi} \quad (7)$$

in the ceramic.

The likelihood of these stresses causing damage can be judged by comparing σ with the compressive buckling stress σ_{cr} of the component under consideration and, in the case of ceramic, also with the compressive strength σ_c of the material. The elastic compressive buckling stress σ_{cr} of the lid or base shown in Figures 3(a) and (b), taking into account the edge fixity furnished by the package walls, is

$$\sigma_{cr} = kE(t/a)^2 \quad (8)$$

where k is the function of b/a given by the solid curve in Figure 4 (adapted from Reference 17). The compressive strength σ_c of a ceramic is generally an item of information supplied by the manufacturer.

For illustrative purposes, let us apply these damage criteria to the Kovar lid and ceramic base considered previously, assuming the following additional characteristics:

	Kovar	Ceramic
a (in.)	.92	.92
b (in.)	2.22	2.22
b/a	2.5	2.5
t (in.)	.010	.030
σ_c (psi)	-----	375,000

From Figure 4 (solid curve) we find that $k = 6.95$, whence Eq. (8) gives the following buckling stresses:

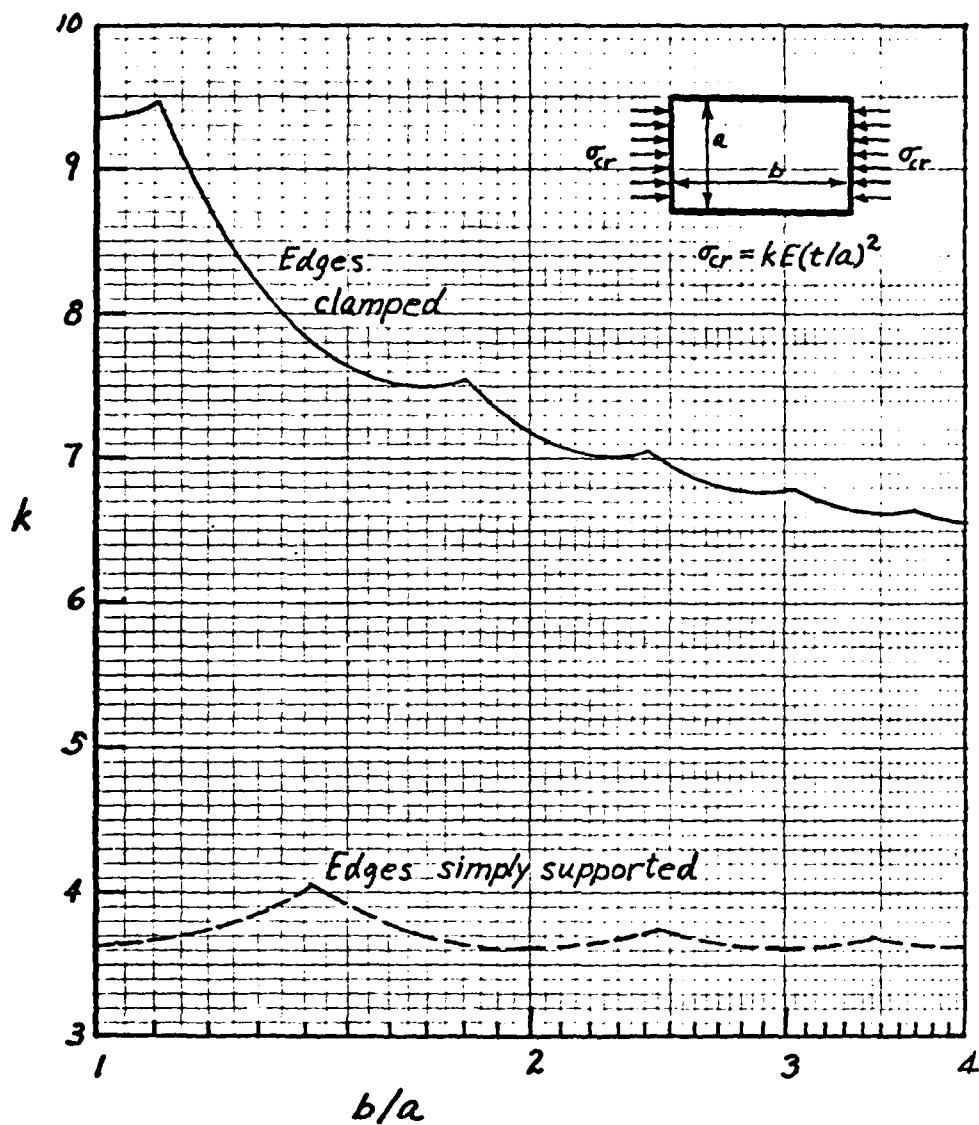


Figure 4.- Buckling stress coefficient for rectangular elastic plates in longitudinal compression (Poisson's ratio taken as 0.3).

$$\sigma_{cr} = 6.95 (20 \times 10^6) \left(\frac{.01}{.92}\right)^2 = 16,400 \text{ psi (Kovar)} \quad (9)$$

$$\sigma_{cr} = 6.95 (47 \times 10^6) \left(\frac{.03}{.92}\right)^2 = 348,000 \text{ psi (Ceramic)} \quad (10)$$

Comparing (6) and (9), we conclude that the Kovar lid is very likely to buckle under its impact-induced compressive stress of 24,000 psi. On the other hand, the corresponding stress of 24,500 psi in the ceramic base (see Eq. (7)) is well below both the buckling stress, Eq. (10), and the material compressive strength quoted in the table above.

The buckling of a Kovar lid may be tolerable if the out-of-flatness resulting from any permanent buckles is acceptable. In the case of a Kovar base to which a ceramic substrate is attached with only a few bonds, the impact-induced buckling could conceivably damage the bonds and cause separation of the substrate from the base, which suggests the possible usefulness of the edgewise drop test as a screen for such bonds.

The fact that a thin Kovar lid or base can indeed buckle under impact of the severity assumed in the illustrative example is evidenced by Figure 5, which shows the buckles observed in a Kovar base after it had been dropped (with random orientations) onto a linoleum-covered floor several times from a height of 3 or 4 feet.

B. Inelastic.— The formulas given above are based on the assumption that the material obeys Hooke's law, that is, that the ratio of the compressive stress σ to the corresponding strain ϵ is constant. In brittle materials like ceramics, the proportionality of stress to strain is thought to hold up fairly well up to the point of fracture. Therefore the assumption



Figure 5.- Kovar package bases (.92 in. \times 2.22 in. \times .010 in.)
 Left: Undropped base. Right: Base that had been
 dropped onto a linoleum-covered floor several times
 with random orientations from a height of 3 or 4
 feet; note permanent buckles produced by the impacts.

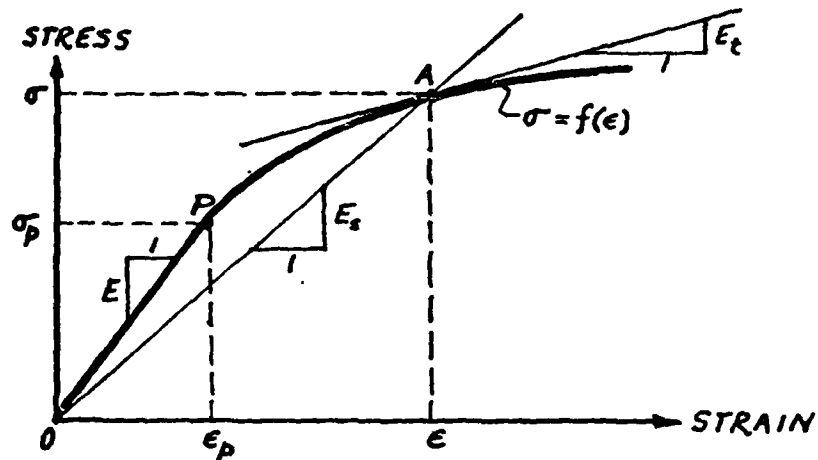


Figure 6.- Compressive stress-strain curve of a ductile
 material.

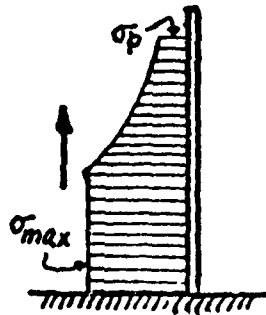


Figure 7.- Shape of advancing stress wave in inelastic impact.

of Hooke's law probably does not seriously limit the validity of the Section A formulas when we are dealing with a ceramic lid or base. However, for ductile materials such as Kovar, which possess a compressive stress-strain curve like that shown in Figure 6, the linear relationship between stress and strain breaks down at a point called the "proportional limit," symbolized by P in Figure 6. Consequently, Eqs. (1), (4) and (8) are invalid for a Kovar lid or base if the stresses they predict exceed the proportional limit stress σ_p . This is possible for Eqs. (1) and (4) if the height of fall is sufficiently great and for Eq. (8) if t/a is sufficiently large. In order to allow for those possibilities we shall now generalize the considerations of Section A to the so-called inelastic case.

We shall assume that the material property information needed for this generalization is available, namely the compressive stress-strain curve, whose equation we symbolize by $\sigma = f(\epsilon)$. From the stress-strain curve two other quantities can be obtained as functions of ϵ . They are the tangent modulus $E_t(\epsilon)$ and the secant modulus $E_s(\epsilon)$, defined by

$$E_t = df/d\epsilon \quad E_s = f(\epsilon)/\epsilon \quad (11)$$

and representing, respectively, the slope of a tangent and the slope of a secant at the point (σ, ϵ) (see Figure 6).

With E_t and E_s defined, we can now give the formulas related to inelastic edgewise impact, that is, impact in which v is sufficiently large to produce compressive stresses exceeding the proportional limit. When this is the case, the distribution of stress along the height of the package is no longer as shown in Figure 3. Instead the advancing stress wave has the shape shown in Figure 7, and different parts of the wave travel

with different velocities, all of them less than or equal to c . The maximum compressive stress σ_{\max} is of main concern to us here, along with the associated strain ϵ_{\max} . The latter is defined implicitly by the following equation from Reference 3:

$$v = \int_0^{\epsilon_{\max}} \sqrt{E_t(\epsilon)/\rho} \, d\epsilon \quad (12)$$

To use this equation we need a graph of the right side as a function of its upper limit ϵ_{\max} . Once ϵ_{\max} is known, the corresponding stress σ_{\max} can be obtained from the stress-strain curve; that is,

$$\sigma_{\max} = f(\epsilon_{\max}) \quad (13)$$

Equations (13) and (12) take the place of Eq. (1) or (4) whenever the latter two lead to $\sigma > \sigma_p$.

The usual modification of Eq. (8) to account for inelastic material behavior consists of introducing a "plasticity reduction factor" η on the right side to get

$$\sigma_{cr} = \eta k E (t/a)^2 \quad (14)$$

For η we adopt the following formula from Reference 18:

$$\eta = \left(\frac{1 - \nu^2}{1 - \nu_p^2} \right) \frac{E_s}{E} \left[\frac{1}{2} + \frac{1}{2} \left(\frac{1}{4} + \frac{3}{4} \frac{E_t}{E_s} \right)^{1/2} \right] \quad (15)$$

where ν = the elastic value of Poisson's ratio ≈ 0.3 and ν_p is the plastic value given by

$$v_p = 0.5 - \frac{E_s}{E} (0.5 - v) \quad (16)$$

The E_s and E_t values in Eqs. (15) and (16) must be the ones associated with the buckling stress σ_{cr} . Therefore η is itself a function of σ_{cr} , which implies that Eq. (14) must be solved by a trial-and-error or iterative technique. However, Eq. (14) can be rewritten as

$$\sigma_{cr}/\eta = kE(t/a)^2 \quad (17)$$

and the left side plotted as a function of σ_{cr} . From this graph the value of σ_{cr} at which σ_{cr}/η equals $kE(t/a)^2$ can be picked off, thus avoiding trial-and-error or iterative calculation.

C. Lid with Thinned Edges.- In Sections A and B it was tacitly assumed that the lid or base was a constant thickness. When the lid has thinned edges, as in Figure 2(b), and the thickness of the edges is much smaller than that of the rest of the lid, their moment resisting capacity is very small compared to that of the rest of the lid. For simplicity and conservatism we may neglect this capacity entirely; that is, we may assume that the edges of the lid are simply supported (hinged).

This assumption leads to the following change in the preceding material: The value of k in Equations (8), (14) and (17) should now be based on the dashed curve in Figure 4 (taken from Reference 19).

II. TWO-COMPONENT BASE

We now assume the base to be a well-bonded two-component plate as in Figure 2(c), with the Young's moduli of the individual components being E_1 and E_2 , the corresponding thickness t_1 and t_2 and the corresponding densities

ρ_1 and ρ_2 . For such a base many of the formulas of the preceding section are still valid provided that the symbols are re-defined.

A. Elastic.- If a strip of such a base is stretched to a strain of ϵ in the elastic range, the stresses in the individual components will be

$$\sigma_1 = E_1 \epsilon \quad \sigma_2 = E_2 \epsilon \quad (18)^*$$

and the mean stress σ on the cross section will be

$$\sigma = \left(\frac{E_1 t_1 + E_2 t_2}{t_1 + t_2} \right) \epsilon \quad (19)$$

Thus, such a strip behaves in extension or compression like a homogeneous material with an effective Young's modulus of

$$E = \frac{E_1 t_1 + E_2 t_2}{t_1 + t_2} \quad (20)$$

The mean density ρ of such a strip is given by a similar formula :

$$\rho = \frac{\rho_1 t_1 + \rho_2 t_2}{t_1 + t_2} \quad (21)$$

With E and ρ now defined as above, and with σ now interpreted as mean stress on the cross section, Equations (1) through (5) become valid for the two-component base. Corresponding to any σ , the stresses in the individual components are

$$\sigma_1 = \frac{E_1}{E} \sigma \quad \sigma_2 = \frac{E_2}{E} \sigma \quad (22)$$

in accordance with Equations (18), (19) and (20).

* Here we are neglecting small stresses that arise in the transverse direction if the two components have different Poisson's ratios.

The value of σ required to cause buckling can be found from the formula

$$\sigma_{cr} = \frac{10.9 kD}{a^2 (t_1 + t_2)} \quad (23)$$

where k is the function of b/a plotted in Figure 4, and D is the plate bending stiffness computed from Equation (5) of Appendix B.

B. Inelastic.— From the compressive stress-strain curves of the individual components, or by means of experiment, one can determine an effective compressive stress-strain curve for the two-component composite. Let us suppose the graph in Figure 6, with σ now defined as the mean stress on the cross section, to be that stress-strain curve. Then Equations (11), (12) and (13) become valid for the composite.

For determining the value of σ required to cause buckling, it is suggested that the following modification of Equation (23) be used:

$$\sigma_{cr} = \eta \frac{10.9 kD}{a^2 (t_1 + t_2)} \quad (24)$$

with η calculated from Equations (15) and (16).

Chapter 5 - SINUSOIDAL VIBRATION

It has been suggested that sinusoidal vibration could be used as a means of stressing the internal wires of microcircuit packages. In this chapter the practicality of this suggestion will be considered, with special reference to vibration parallel to the package base and perpendicular to the plane of the wire loop, so that the predominant mode of stressing is flexure with a small amount of torsion.

We first note that commercially available shakers have peak accelerations that are relatively low (in the 100's of g's) compared to the accelerations of 1000's of g's that were found to be needed in Chapter 2, Section IV, in order to produce significant wire flexure in a centrifuge. Therefore one can hope to achieve significant wire stressing with a commercially available shaker only if it can provide frequencies that are at or near the natural frequencies of the wire for normal mode vibration in a direction perpendicular to the plane of the wire -- i.e., only if a state of resonance or near-resonance can be developed. Therefore it is important to know what these natural frequencies are.

The fundamental natural frequency f of any wire for vibration normal to its plane can be estimated with the aid of Figure 1. The symbols in Figure 1 are defined as follows:

f = fundamental natural frequency (Hz)(cycles/sec)

S = span (in.)

d = diameter (in.)

H = loop height (in.)

$$c = \text{speed of sound in the wire material (in./sec.)} = \sqrt{E/\rho}$$

$$E = \text{Young's modulus (lb/in.}^2\text{)}$$

$$\rho = \text{density (lb-sec}^2\text{/in.}^4\text{)}$$

The units indicated in parentheses are typical; any other set of consistent units may be used. In computing the data for Figure 1 the wire shape was assumed, for simplicity, to be a circular arc and Poisson's ratio was taken to range from 0.3 to 0.4 (the values for aluminum and gold, respectively). The analysis leading to Figure 1 was based on the curved beam equations (6.1.7) and (6.1.8) of Reference 20, converted to dynamic form. The conversion consisted of changing all the ordinary derivatives to partial derivatives and replacing the distributed loading term p by the inertia loading $m\partial^2 v/\partial t^2$ (m = mass per unit length, v = deflection perpendicular to the plane of the wire, t = time). The resulting equations were solved in a more or less standard fashion for an excitation that consisted of a simple harmonic motion of the attachment points in a direction perpendicular to the plane of the wire. In this approach, a natural frequency is an excitation frequency that produces infinite response for any finite excitation amplitude, no matter how small.

In order to illustrate the use of Figure 1, let us determine the fundamental natural frequency f of a .001-in. diameter gold wire ($E = 12,000,000$ psi, $\rho = .00181$ lb-sec²/in.⁴) of .100-in. span and .010-in. loop height. For this wire

$$\frac{H}{S} = \frac{.010}{.100} = 0.1 \quad c = \sqrt{\frac{E}{\rho}} = \sqrt{\frac{12,000,000}{.00181}} = 81424 \text{ in./sec}$$

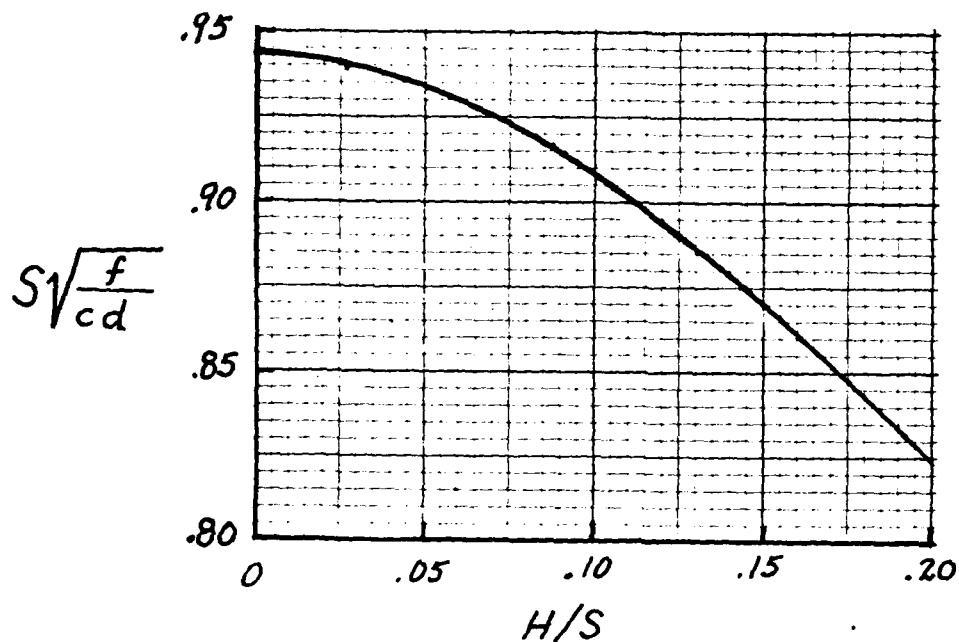
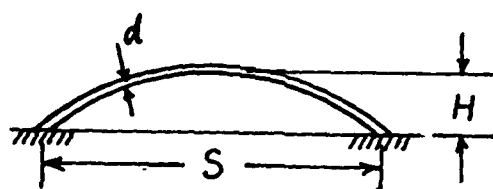


Figure 1.- Graph for determining fundamental natural frequency f (Hz) of a circular-arc wire with circular cross section, for vibration perpendicular to the plane of the wire.

For this H/S, Figure 1 gives $S\sqrt{f/cd} = .908$, whence

$$f = (.908)^2 \frac{cd}{S^2} = (.908)^2 \frac{(81424)(.001)}{(.100)^2} = 6700 \text{ Hz}$$

This is a frequency that commercially available shakers are capable of developing.

In order to gain further insight into the natural frequencies of microcircuit wires, we may consider H/S = .11 to be a representative height to span ratio, giving $S\sqrt{f/cd} = .9$, and use this relationship to plot graphs of S and d combinations leading to selected frequencies f. Those graphs are shown in Figure 2 for aluminum wires and Figure 3 for gold wires.

Focussing attention on 1-mil diameter wires (.001 in.) as typical, and considering that 50,000 Hz is about the upper limit of frequencies achievable with commercially available shakers, we see from Figure 2 that resonance can be induced in aluminum wires if their spans are greater than 55 mils, and in gold wires if their spans are greater than 36 mils.

Thus, it would appear that significant flexural stressing can be induced in a large fraction of microcircuit wires through sinusoidal vibration on a shaker capable of a frequency sweep up to 50,000 Hz. Despite this capability, sinusoidal vibration is not necessarily to be recommended as a mechanical screen for microcircuit wires. One reason is that the internal damping of these wires might not be large, with the result that resonance could destroy good wires as well as bad ones, unless the frequency sweep were fast enough to avoid excess dwell in the vicinity of any one natural frequency. How fast the sweep should be is something that would have to be determined by trial and error. A second reason is that

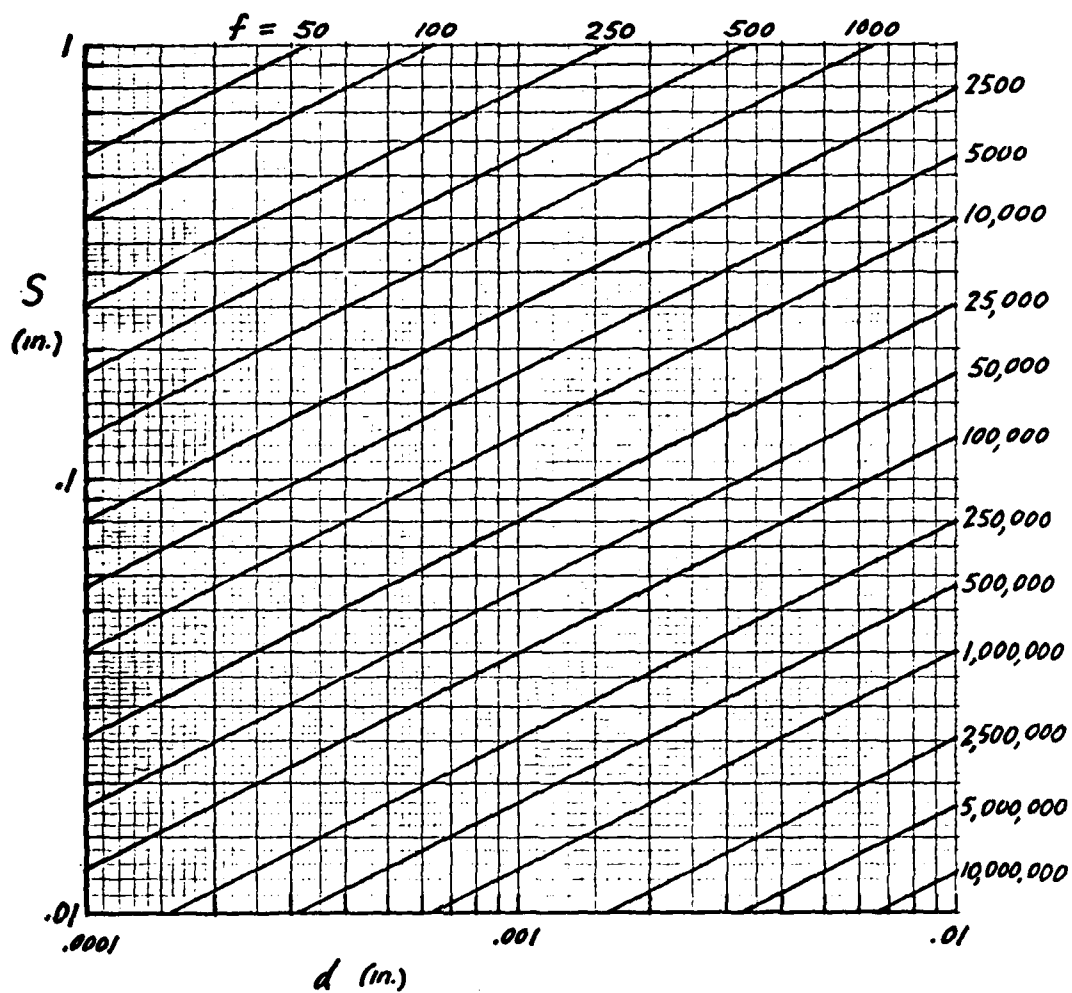


Figure 2.- Relationship between span S , diameter d , and fundamental natural frequency f (Hz) for aluminum wires vibrating normal to their plane ($H/S = .11$).

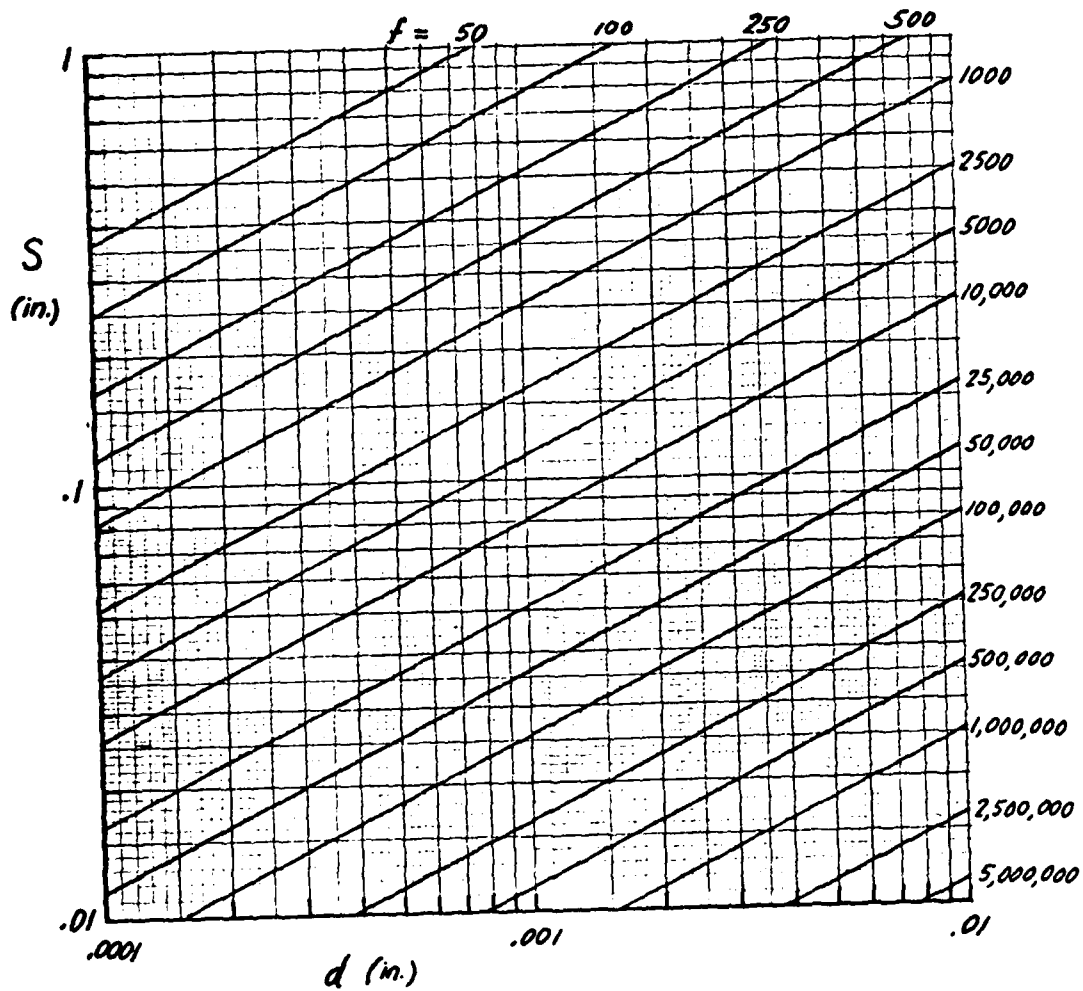


Figure 3.- Same as Figure 2, but for gold wires.

shakers capable of developing frequencies up to 50,000 Hz can accommodate only very small masses; thus only one package could be tested at a time. And a third reason is that similar wire flexing can be produced more easily and in a more controlled fashion by means of the centrifuge, as was shown in Chapter 2.

Chapter 6 - THERMAL SHOCK: FLEXURAL STRESS
IN FLATPACK LID SEALS

The screening of microelectronic flatpacks by means of thermal shock, via Method 1011.2 of MIL-STD-883B, involves the sudden insertion of the package into hot and cold fluid baths alternately for fifteen or more cycles. The package is allowed to remain in each bath at least 5 minutes. Increasing severity levels of screening are achieved by increasing the temperature of the hot bath and/or reducing the temperature of the cold bath.

In the first moments after the package is transferred into a bath a very marked variation of temperature is developed through the thickness of the lid. This non-uniformity of temperature would cause a curvature to develop in the lid if it were detached from the rest of the package. However, because the lid is not detached from the rest of the package, but is instead bonded to rather short (therefore stiff) side walls, this curvature tends to be suppressed, the mechanism of suppression being bending moments transmitted from the side walls to the edges of the lid. These bending moments produce flexural stresses in the wall-to-lid seal; that is, stresses that vary from tension to compression across the width of the wall. These stresses can exceed the allowable working stresses for the seal material, thereby producing some damage and a possible loss of hermeticity.

Consequently, it is important for both the designer and the purchaser of the flatpack to have some means - preferably simple formulas - of estimating the flexural stresses induced in the seal during thermal-shock screening. Having such formulas and knowing the level of severity of the screening that his package will have to

undergo, the designer of the package can so design it as to keep the flexural stresses at or below their allowable values for the seal material he plans to use. Having the same formulas and knowing what the minimum acceptable strength of satisfactory seal should be, the purchaser of an already designed package can select a screening level severe enough to damage seals whose strengths are below this acceptable minimum, but not so severe as to damage seals whose strengths are greater than it.*

This chapter, which is based on Reference 21, presents formulas of the kind just referred to. The formulas are developed with particular reference to thin packages with constant-thickness lids; their planform may be rectangular, as in Figure 1, or of any other shape. They are based on a simplified one-dimensional heat-flow analysis and on the assumption of linear elasticity (Hooke's Law) for the lid material. Two kinds of seal geometry are considered. In the "wide seal" (Figure 2(a)) the seal width w_s is essentially equal to the thickness w of the wall. In the "narrow seal" (Figure 2(b)), the seal is much narrower than the wall ($w_s \ll w$) and is located along the outside rim of the wall-lid interface.

I. SYMBOLS

The symbols related to package and seal geometry are shown in Figures 1 and 2. The symbols to be used for the fluid and lid physical constants are as follows;

* It should be noted, however that the latter objective (the screening out of low quality seals) can be achieved in other ways as well; for example, through the use of external pressure (see Chapter 1).

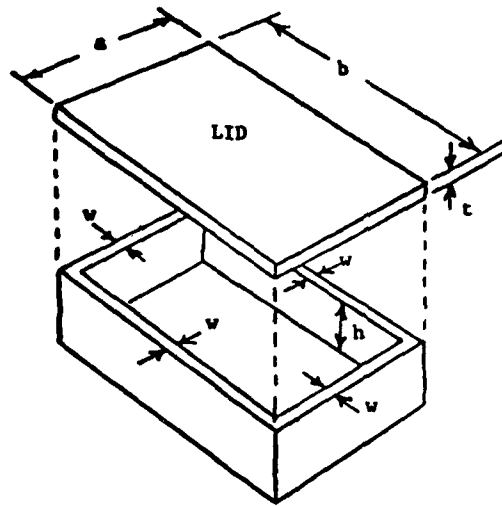


Figure 1. - Flatpack configuration.

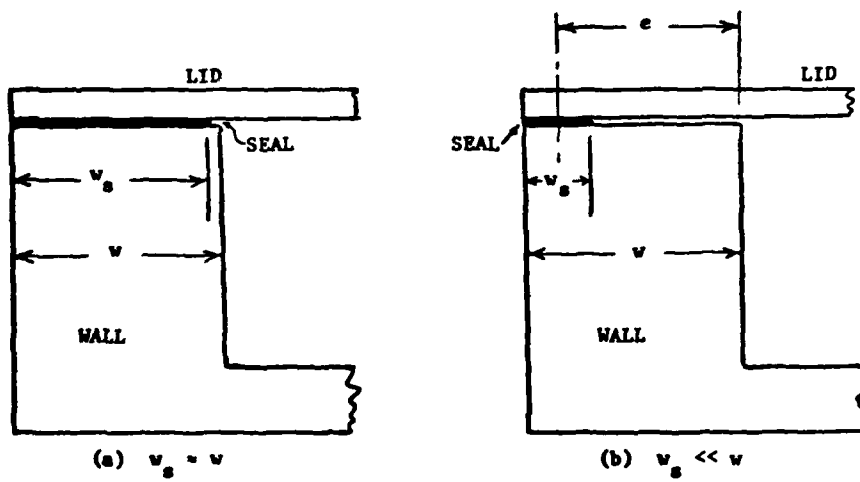


Figure 2. - Seal geometries.

T_f = temperature	}	of a fluid
k_f = thermal conductivity		
c_f = specific heat		
ρ_f = density		
T_2 = temperature	}	of the high- temperature fluid
k_2 = thermal conductivity		
c_2 = specific heat		
ρ_2 = density		
T_1 = temperature	}	of the low- temperature fluid
k_1 = thermal conductivity		
c_1 = specific heat		
ρ_1 = density		
E = Young's modulus	}	of the lid material
ν = Poisson's ratio		
α = thermal expansion coefficient		
k = thermal conductivity		
c = specific heat		
ρ = density		

Also,

T_r = room temperature
 T_c = uniform lid (cover) temperature just prior
to the immersion of the package in a bath

It should be noted that T_c will equal T_r for the first immersion and T_2 or T_1 (alternately) for the subsequent immersions.* Similarly,

* We are assuming here that the package remains in each bath long enough for its temperature to become uniform and stabilized at the bath temperature.

T_f will equal T_2 or T_1 , depending on whether the package is going into the high-temperature or low-temperature bath, respectively.

Corresponding statements apply to k_f , c_f and ρ_f .

Any consistent units may be employed for the above defined quantities. Here we give some commonly used ones for the sake of illustration and in order to show the dimensions of the quantities:

Temperature (T_f, T_2, T_1, T_r, T_c)	:	$^{\circ}\text{F}$
Thermal conductivity (k_f, k_2, k_1, k)	:	$\text{Btu-ft}/(\text{ft}^2\text{-}^{\circ}\text{F-sec})$
Specific heat (c_f, c_2, c_1, c)	:	Btu/lb
Density ($\rho_f, \rho_2, \rho_1, \rho$)	:	lb/ft^3
Young's modulus (E)	:	psi
Poisson's ratio (ν)	:	[dimensionless]
Coefficient of expansion (α)	:	$(^{\circ}\text{F})^{-1}$

Two dimensionless groupings of the physical quantities arise naturally in the course of the analysis; they will be represented by the symbols R and S , defined as follows:

$$R \equiv \sqrt{\frac{\rho_f c_f k}{\rho c k_f}}$$

$$S \equiv \sqrt{\frac{\rho_f c_f k_f}{\rho c k}}$$

Also,

$$S_2 \equiv \sqrt{\frac{\rho_2 c_2 k_2}{\rho c k}}$$

$$S_1 \equiv \sqrt{\frac{\rho_1 c_1 k_1}{\rho c k}}$$

Other symbols will be introduced as they are needed.

II. THERMAL ANALYSIS

The maximum seal stresses occur in the very first moments after immersion of the package into a bath. We shall assume that in this short time (a) convection has not had a chance to develop and (b) any significant temperature perturbation in the fluid is confined to a thin layer adjacent to the surface of the lid. These assumptions permit the following additional ones to be made: (c) The transfer of heat between lid and fluid occurs only by conduction. (d) The direction of this conduction is perpendicular to the lid. (e) At any instant the temperature variation (in fluid and lid) along a line perpendicular to the lid is the same at all points of the lid surface. We have thus reduced the temperature analysis to a one-dimensional heat-conduction problem.

To expedite the solution of this heat-conduction problem in a manner that will lead to simple formulas, we shall make the following further idealizations: (f) At any instant the temperature perturbations have penetrated only a finite distance into the fluid and lid. (g) Within each of these penetration regions the temperature varies linearly with respect to distance from the lid-fluid interface. Similar simplifications were first employed by Levy (Réference 22) in another context.

On the basis of the above, we shall now analyze the transient temperature conditions that follow the (assumedly instantaneous) insertion of a package into a fluid bath. We take the fluid and lid temperatures to be uniform at T_f and T_c , respectively, just prior to the insertion. These uniform temperatures are indicated by the

dashed lines in Figure 3(a). The solid lines in Figure 3(a) show the temperature distribution at some time after insertion, when the temperature perturbations have penetrated a distance d_f into the fluid and d_c into the lid, with d_c still less than the thickness t of the lid. The lid and fluid are assumed to have a common interface temperature T_i . In accordance with assumption (g) above, we show a linear variation of temperature from T_i to T_c in the temperature-perturbed region of the lid and a linear variation from T_i to T_f in the temperature-perturbed region of the fluid. Figure 3(b) similarly shows the temperature distribution at a later time, when the temperature perturbation has already penetrated through the entire thickness of the lid. The temperature of the inner face of the lid is no longer constant at T_c ; its value, which now varies with time, is denoted by T_c' .

The penetration distance d_f is a time-like parameter since it changes monotonically with time. It is appropriate, therefore, to first determine d_c , T_i and T_c' as functions of d_f , then relate d_f explicitly to the time τ (measured from the instant of insertion). In the analysis, the two regimes represented by parts (a) and (b) of Figure 3 must be considered separately.

A. Case (a): $d_c < t$. - We start with Figure 3(a) and consider a heat balance for the tube of material, of unit cross-sectional area, shown at the left of the figure. First, the heat loss from the fluid, represented by triangle ABC, must equal the heat gain of the lid, represented by triangle ADE; thus

$$\frac{1}{2} d_f (T_f - T_i) \rho_f c_f = \frac{1}{2} d_c (T_i - T_c) \rho_c \quad (1)$$

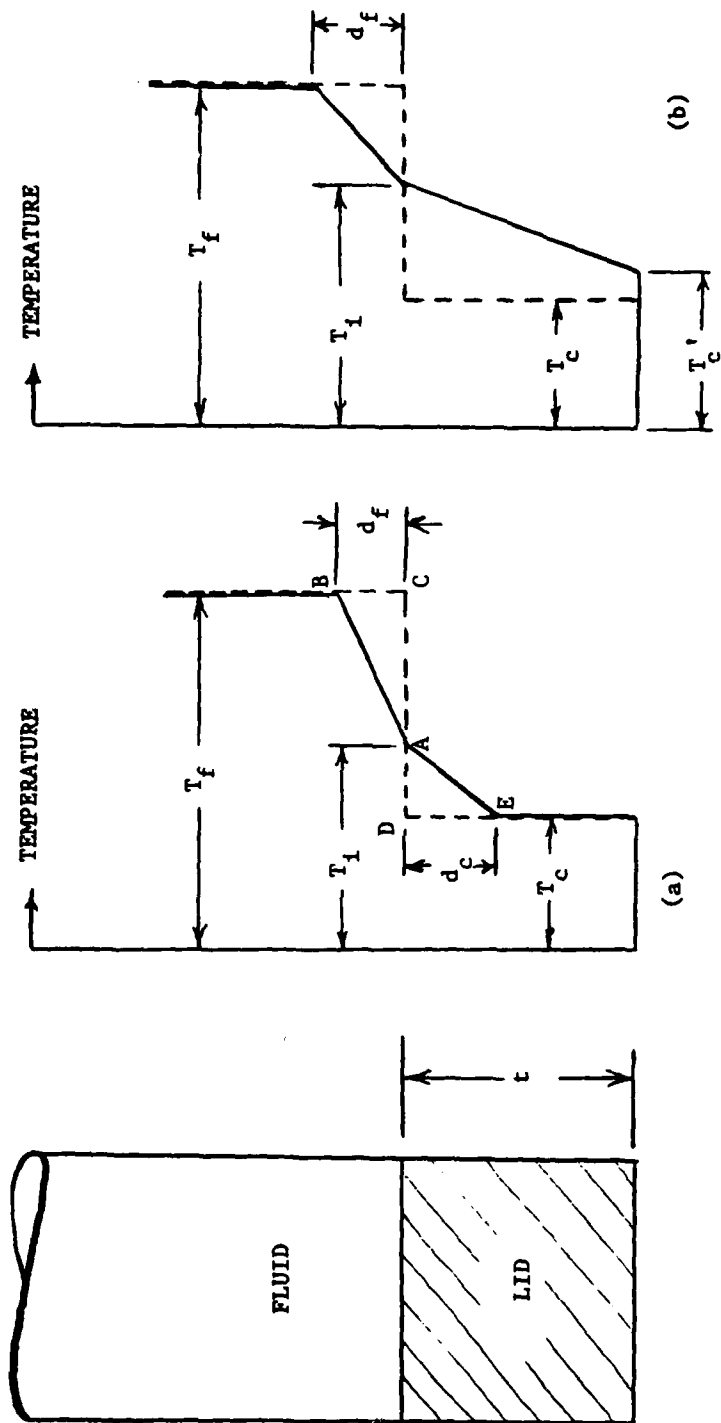


Figure 3. - Temperature distributions in fluid and lid.

(a) Temperature perturbation has not yet penetrated through the lid ($d_c < t$).

(b) Temperature perturbation has penetrated through the lid ($d_f \geq t/R$).

Secondly, the temperature gradients in the two materials must represent the same rate of heat flow across the interface; that is,

$$k_f \frac{T_f - T_i}{d_f} = k \frac{T_i - T_c}{d_c} \quad (2)$$

Division of one equation by the other gives the following formula for the penetration distance d_c :

$$d_c = R d_f \quad (3)$$

$$R \equiv \sqrt{\frac{\rho_f c_f k}{\rho c k_f}} \quad (4)$$

Equation (2), with d_c eliminated via equation (3), now gives

$$T_i = \frac{T_f S + T_c}{S + 1} \quad (5)$$

where

$$S \equiv \sqrt{\frac{\rho_f c_f k_f}{\rho c k}} \quad (6)$$

We have thus determined d_c and T_i as functions of d_f . The absence of d_f from Equation (5) indicates that the interface temperature T_i remains constant as long as d_c is less than t . Equation (5) can be re-worked to give the temperature differences $T_i - T_c$ and $T_f - T_i$ as fractions of the temperature difference $T_f - T_c$. The result is

$$\frac{T_i - T_c}{T_f - T_c} = \frac{S}{S + 1}; \quad \frac{T_f - T_i}{T_f - T_c} = \frac{1}{S + 1} \quad (7a, b)$$

It is interesting that the interface temperature T_i obtained above on the basis of rather extreme simplifying assumptions agrees with the exact result cited in Reference 23 for the interface temperature instantaneously developed in the case of two semi-infinite solids at different uniform temperatures placed together in perfect contact.

B. Case (b): Temperature Perturbation Extends Through Entire Thickness of Lid* - The above analysis is valid as long as the d_c given by Equation (3) is less than the lid thickness t ; that is, as long as $d_f < t/R$. Here we consider the case $d_f \geq t/R$, which is depicted in Figure 3(b). For this case the equations corresponding to (1) and (2) are,

$$\frac{1}{2} d_f (T_f - T_i) \rho_f c_f = \frac{1}{2} t [(T_i - T_c) + (T_c' - T_c)] \rho c \quad (8)$$

$$k_f \frac{T_f - T_i}{d_f} = k \frac{T_i - T_c'}{t} \quad (9)$$

Solving simultaneously for T_i and T_c' , we obtain

$$T_i = \frac{T_f \left(\frac{k_f t}{k d_f} + \frac{\rho_f c_f d_f}{\rho c t} \right) + 2T_c}{\frac{k_f t}{k d_f} + \frac{\rho_f c_f d_f}{\rho c t} + 2} \quad (10)$$

$$T_c' = \frac{T_f \left(-\frac{k_f t}{k d_f} + \frac{\rho_f c_f d_f}{\rho c t} \right) + 2T_c \left(1 + \frac{k_f t}{k d_f} \right)}{\frac{k_f t}{k d_f} + \frac{\rho_f c_f d_f}{\rho c t} + 2} \quad (11)$$

* It will be shown subsequently that the maximum stress in the seal occurs in the regime described by Figure 3(a). Consequently, the reader who is interested only in knowing what this stress is, and is not concerned with the entire time-temperature history, can skip directly to the section entitled STRESS ANALYSIS.

These results lead to the following temperature ratio formulas:

$$\frac{T_i - T_c}{T_f - T_c} = \frac{\frac{k_f t}{k d_f} + \frac{\rho_f c_f d_f}{\rho c t}}{\frac{k_f t}{k d_f} + \frac{\rho_f c_f d_f}{\rho c t} + 2} \quad (12a)$$

$$\frac{T_f - T_i}{T_f - T_c} = \frac{2}{\frac{k_f t}{k d_f} + \frac{\rho_f c_f d_f}{\rho c t} + 2} \quad (12b)$$

$$\frac{T_c' - T_c}{T_f - T_c} = \frac{-\frac{k_f t}{k d_f} + \frac{\rho_f c_f d_f}{\rho c t}}{\frac{k_f t}{k d_f} + \frac{\rho_f c_f d_f}{\rho c t} + 2} \quad (13)$$

$$\frac{T_i - T_c'}{T_f - T_c} = \frac{2 \frac{k_f t}{k d_f}}{\frac{k_f t}{k d_f} + \frac{\rho_f c_f d_f}{\rho c t} + 2} \quad (14)$$

Equations (10) to (14) define various temperature quantities as functions of the time-like parameter d_f for the range $d_f \geq t/R$.

C. Time-Temperature Relation for Case (a). - We shall now study the dependence of d_f on the time τ , starting with Case (a). The left side of Equation (1) is the heat Q lost by the fluid tube per unit cross-sectional area, and the left side of Equation (2) is the time rate of increase of this heat loss. We may thus write

$$Q = \frac{1}{2} d_f (T_f - T_i) \rho_f c_f \quad (15)$$

$$\dot{Q} = k_f \frac{T_f - T_i}{d_f} \quad (16)$$

where the dot over a symbol denotes differentiation with respect to time τ . Another expression for \dot{Q} can be obtained by differentiating Equation (15), taking into account that T_i is constant for Case (a):

$$\dot{Q} = \frac{1}{2} \dot{d}_f (T_f - T_i) \rho_f c_f \quad (17)$$

Equating the two expressions for \dot{Q} , we obtain the following differential equation defining d_f as a function of time:

$$\frac{k_f}{d_f} = \frac{1}{2} \dot{d}_f \rho_f c_f \quad (18)$$

The solution of this equation, for the initial condition $d_f = 0$ when $\tau = 0$, is

$$d_f = \sqrt{\frac{4k_f \tau}{\rho_f c_f}} \quad (19)$$

Equation (19) gives the penetration distance d_f as a function of the time τ . Using the relationship to eliminate d_f in Equations (3), we obtain the following relationship between d_c and τ :

$$d_c = \sqrt{\frac{4k \tau}{\rho c}} \quad \text{or} \quad \tau = \frac{\rho c d_c^2}{4k} \quad (20)$$

Two times are of special interest: The time τ_1 at which $d_c = .75t$ (as will be seen later, this is the time at which the seal flexural stresses reach their maximum value) and the time τ_2 at which $d_c = t$. From Equation (20) these times are found to be

$$\tau_1 = \frac{9}{64} \frac{\rho c t^2}{k} \quad (21)$$

$$\tau_2 = \frac{1}{4} \frac{\rho c t^2}{k} \quad (22)$$

D. Time-Temperature Relations for Case (b). - In this case the heat Q lost by the fluid tube and the time-derivative of this heat are given by the left sides of Equations (8) and (9). Thus

$$Q = \frac{1}{2} d_f (T_f - T_i) \rho_f c_f \quad (23)$$

$$\dot{Q} = k_f \frac{T_f - T_i}{d_f} \quad (24)$$

An alternate expression for \dot{Q} is obtained by differentiating Equation (23), taking into account the fact that T_i is now time-dependent because of its dependence on d_f (see Eq. (10)). The result of the differentiation is

$$\dot{Q} = 2 \rho_f c_f (T_f - T_c) \dot{d}_f \frac{\left(\frac{k_f}{k} + \frac{d_f}{t} \right) \frac{d_f}{t}}{\left[\frac{k_f}{k} + \frac{\rho_f c_f}{\rho c} \left(\frac{d_f}{t} \right)^2 + 2 \frac{d_f}{t} \right]^2} \quad (25)$$

Equating the two expressions for \dot{Q} , and eliminating $T_f - T_i$ by means of Equation (12b), we obtain the following differential equation for d_f as a function of τ :

$$\frac{\dot{d}_f}{t} \left(\frac{k_f}{k} + \frac{d_f}{t} \right) \frac{d_f}{t} = \frac{k_f}{\rho_f c_f t^2} \left[\frac{k_f}{k} + \frac{\rho_f c_f}{\rho c} \left(\frac{d_f}{t} \right)^2 + 2 \frac{d_f}{t} \right] \quad (26)$$

Separating the variables, integrating, and imposing the initial condition $d_f = t/R$ when $\tau = \tau_2$, we obtain

$$\frac{k_f(\tau - \tau_2)}{\rho_f c_f t^2} = \int_{1/R}^{d_f/t} \frac{\left(\frac{k_f}{k} + x\right) x dx}{\frac{k_f}{k} + 2x + \frac{\rho_f}{\rho} \frac{c_f}{c} x^2} \quad (27)$$

as the relationship between d_f/t and τ valid for times greater than τ_2 (or d_f/t greater than $1/R$). Introducing $y = Rx$ as a new dummy variable, we convert Equation (27) to

$$\frac{k(\tau - \tau_2)}{\rho c t^2} = I\left(\frac{Rd_f}{t}; S\right) \quad (28)$$

where

$$I\left(\frac{Rd_f}{t}; S\right) \equiv \int_1^{Rd_f/t} \frac{(S+y)y dy}{S+2y+Sy^2} \quad (29)$$

Making use of Equation (22), we can put Equation (28) into the more convenient form

$$\tau = \frac{\rho c t^2}{k} [.25 + I(Rd_f/t; S)] \quad (30)$$

Equation (30) gives the time τ required for the temperature perturbation in the fluid to penetrate a distance d_f when d_f is any value greater than t/R . The right side of Equation (29) is readily integrated, giving the following explicit expressions for the function $I(Rd_f/t; S)$:

$$I\left(\frac{Rd_f}{t}; S\right) = \begin{cases} (p^2 - 1)/4 & \text{when } S = 0; & (31a) \\ \frac{p-1}{S} - \frac{2-S^2}{2S^2} \ln\left(\frac{p^2S + 2p + S}{2S + 2}\right) \\ + \frac{\sqrt{1-S^2}}{S^2} \ln\left(\frac{S+1+\sqrt{1-S^2}}{S+1-\sqrt{1-S^2}} \cdot \frac{pS+1-\sqrt{1-S^2}}{pS+1+\sqrt{1-S^2}}\right) & \text{when } 0 < S \leq 1; & (31b) \\ \frac{p-1}{S} - \frac{2-S^2}{2S^2} \ln\left(\frac{p^2S + 2p + S}{2S + 2}\right) \\ - \frac{2\sqrt{S^2-1}}{S^2} \text{Arctan}\left(\frac{p-1}{p+1} \sqrt{\frac{S-1}{S+1}}\right) & \text{when } S \geq 1 & (31c) \end{cases}$$

In these expressions p is a short-hand symbol for Rd_f/t .

To facilitate the use of Equation (30), Figure 4 gives the bracketed term of that equation as a function of Rd_f/t for selected values of S . Equation (30), in conjunction with Equations (31) or Figure 4, enables one to convert the right sides of equations (10) through (14) into functions of time. Thus, one can determine, for example, how long it takes for the temperature difference $T_1 - T_c$ to reach some specified fraction, say 95%, of its ultimate value, $T_f - T_c$; or what T_1 will be after a specified period of time, say five minutes.

III. STRESS ANALYSIS

We turn now to the stress analysis, which consists of two parts: First, the determination of the maximum transient bending moment developed in the lid and seal after insertion of the package in the fluid bath. Second, the translation of this bending moment into flexural stresses in the seal.

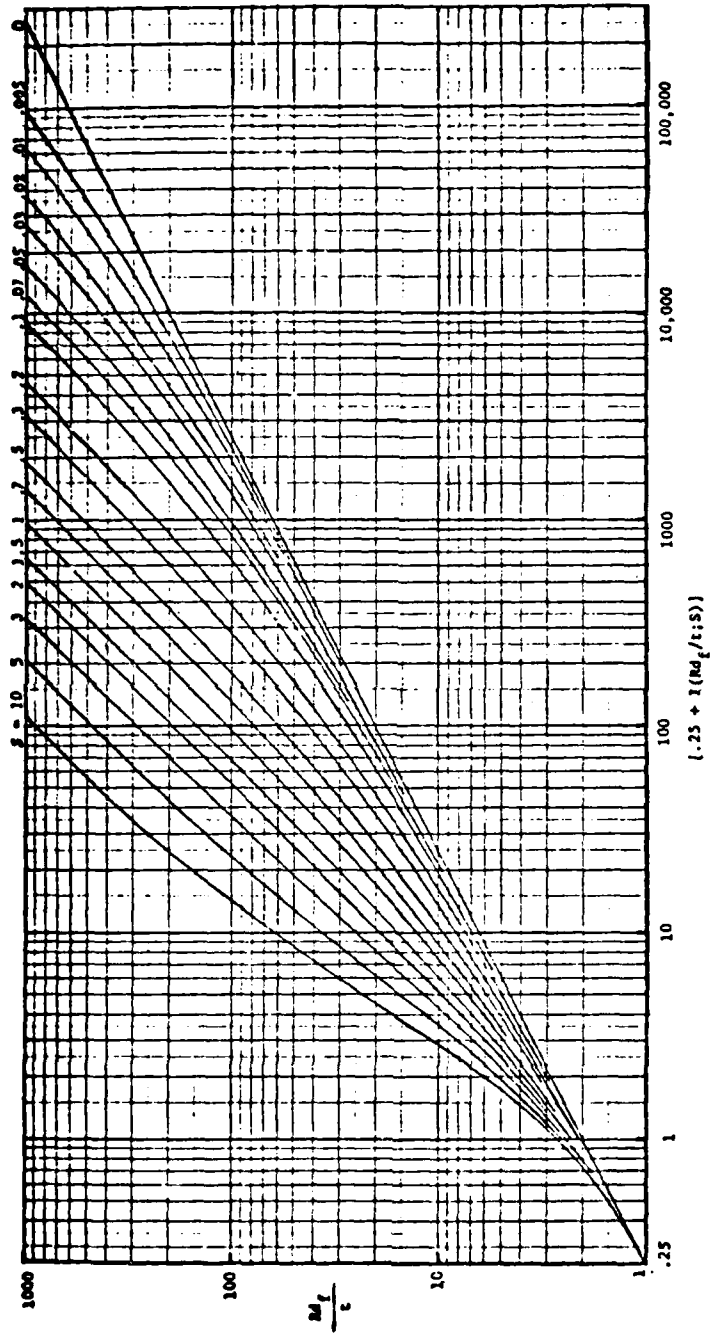


Figure 4. - Graph of bracketed term in equation (30).

A. Maximum Bending Moment.- We regard the lid as a thin elastic plate and make the usual assumption of plate theory: That material lines normal to the middle surface remain straight and remain normal to the middle surface.

By our earlier assumptions, the temperature variation through the thickness of the lid is the same in all parts of the lid, and the edges of the lid are clamped against rotation by the walls of the package. Under those circumstances, an argument similar to that on pp. 49-50 of Reference 3 will show that the lid remains flat; that is, a uniform bending moment is transmitted from the walls to the lid, through the seal, of sufficient magnitude to suppress the spherical curvature that would be produced by the thickness-wise temperature variation. We shall now compute this bending moment for the case $d_c < t$ (Fig. 3(a)).

We first assume that, beside the curvature, all middle-surface strains are also suppressed. Then the stress distribution through the thickness will be as shown in Figure 5(a), where

$$\sigma_1 = \frac{E\alpha(T_f - T_c)}{1 - \nu} \quad (32)$$

and is positive for compression. We now assume that the constraint against middle-surface expansion is completely removed.* This

* The walls of the package may actually provide some constraint against the middle-surface expansion. The main effect of this, when the lid is thin, is to put some horizontal compression into the lid (which implies horizontal shear in the seal) without substantially altering the bending moment from that given by Equation (34).

corresponds to superimposing a uniform tensile stress σ_2 , as shown in Figure 5(b), with σ_2 of sufficient magnitude to cancel out the resultant thrust due to σ_1 . That is,

$$\sigma_2 = \sigma_1 \frac{d_c}{2t} \quad (33)$$

The final stress distribution is then as shown in Figure 5(c).

Since there is no resultant thrust, this stress distribution represents a pure couple. The bending moment M per unit width can, therefore, be computed by taking moments of the Figure 5(a) and (b) stress distributions about any convenient point. Choosing that point in the middle surface, we eliminate the moment due to σ_2 and obtain

$$M = \frac{1}{2} \sigma_1 d_c \left(\frac{t}{2} - \frac{d_c}{3} \right)$$

or, with σ_1 replaced by its expression from equation (32),

$$M = \frac{1}{2} \frac{E\alpha(T_f - T_c)}{1 - \nu} d_c \left(\frac{t}{2} - \frac{d_c}{3} \right) \quad (34)$$

where, it will be recalled, $T_f - T_c$ is independent of d_c .

Differentiating Equation (34) with respect to d_c and setting the derivative equal to zero, we find that M is a maximum when

$d_c = .75t$. (The same result was obtained in Reference 22 in the case of a beam.) With d_c replaced by $.75t$, equation (34) gives the following expression for the maximum bending moment per unit width in the regime $0 \leq \tau \leq \tau_2$:

$$M_{\max} = \frac{3}{32} \frac{E\alpha(T_1 - T_c) t^2}{1 - \nu} \quad (35)$$

This maximum bending moment occurs at the time τ_1 defined by Equation (21).

There is no need to investigate bending moments for the Figure 3(b) regime (i.e., for $\tau > \tau_2$). In this regime, the temperature gradient through the thickness is always linear and always less than it is at $\tau = \tau_2$. The bending moment will, therefore, be less than at $\tau = \tau_2$; and, since τ_2 belongs to both regimes, its bending moment is in turn less than that for $\tau = \tau_1$.

Using Equation (7a) to eliminate $T_1 - T_c$ in Equation (35), we arrive at the following final form of the M_{\max} expression:

$$M_{\max} = \frac{3}{32} \frac{S}{S+1} \frac{E\alpha(T_f - T_c) t^2}{1 - \nu} \quad (36)$$

The sign obtained for M_{\max} must be interpreted as follows:

A positive M_{\max} implies compression in the upper fibers of the lid and the outer portions of the lid-wall interface. A negative M_{\max} implies tension in those locations.

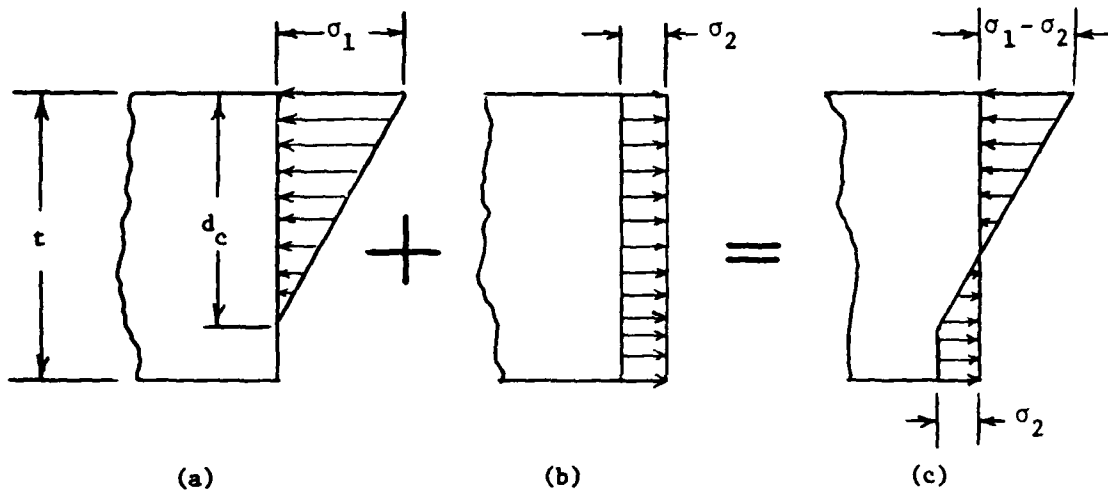


Figure 5. - Superposition of stress distributions on lid cross sections for the case $d_c < t$.

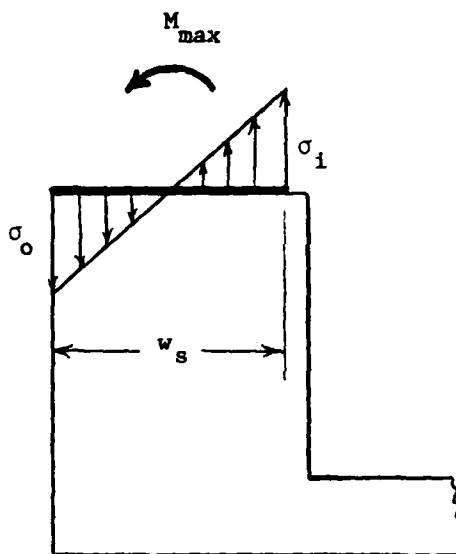


Figure 6. - Flexural stresses in a wide seal.

B. Flexural Stresses in the Seal.- We shall now estimate the flexural stresses produced in the seal by the bending moment of Equation (36). We shall consider separately the two cases shown in Figure 2 ($w_s = w$ and $w_s \ll w$), the "wide seal" and "narrow seal" cases, respectively. The following symbols and sign convention will be used for the seal stresses.

σ_o = stress at outer edge of seal, positive for tension

σ_i = stress at inner edge of seal, positive for tension

(1) Wide Seal.- Figure 6 shows the wide seal and the assumedly linear stress distribution (as in Chapter 1) produced across its width by the bending moment M_{\max} . The static equivalence of the stress distribution and M_{\max} requires that

$$\begin{aligned}\sigma_o &= -6 M_{\max} / w_s^2 \\ \sigma_i &= +6 M_{\max} / w_s^2\end{aligned}\quad (37)$$

or, using Equation (36),

$$\left. \begin{array}{l} \sigma_o \\ \sigma_i \end{array} \right\} = \frac{-9}{+16} \cdot \frac{s}{s+1} \cdot \frac{E\alpha(T_f - T_c)}{1-\nu} \left(\frac{t}{w_s}\right)^2 \quad (38)$$

(2) Narrow Seal. - For the narrow seal, we distinguish between two situations, depending on whether the temperature variation through the thickness tends to produce an outward or an inward bulging of the lid. In the former case, M_{\max} is positive and is transmitted from lid to wall entirely through the seal, as shown in Figure 7(a). In the latter case, M_{\max} is negative, and we can then expect it to be transmitted from lid to wall by means of a concentrated compressive line load along the inner edge of the wall plus a nearly uniform tensile stress in the seal material (see Fig. 7(b)).

Considerations of static equivalence lead to the following seal stresses for these two cases:

M_{\max} POSITIVE [i.e., $\alpha(T_f - T_c) > 0$]

$$\frac{\sigma_o}{\sigma_i} = \frac{-9}{+16} \cdot \frac{S}{S+1} \cdot \frac{E\alpha(T_f - T_c)}{1-\nu} \left(\frac{t}{w_s}\right)^2 \quad (39)$$

M_{\max} NEGATIVE [i.e., $\alpha(T_f - T_c) < 0$]

$$\sigma_o = \sigma_i = \frac{-M_{\max}}{ew_s} = -\frac{3}{32} \cdot \frac{S}{S+1} \cdot \frac{E\alpha(T_f - T_c)}{1-\nu} \frac{t^2}{ew_s} \quad (40)$$

where e is the dimension shown in Figure 7(b).

(3) Implications of Equations (38) - (40). - Equations (38) to (40) show the parameters which have a significant effect on the stresses in the seal. They show, in particular, that the seal stress magnitudes can be reduced by increasing w_s and e or by decreasing S , E , $|\alpha(T_f - T_c)|$, or t . Decreasing S means decreasing the density - specific heat - thermal conductivity product for the fluid or increasing it for the lid.

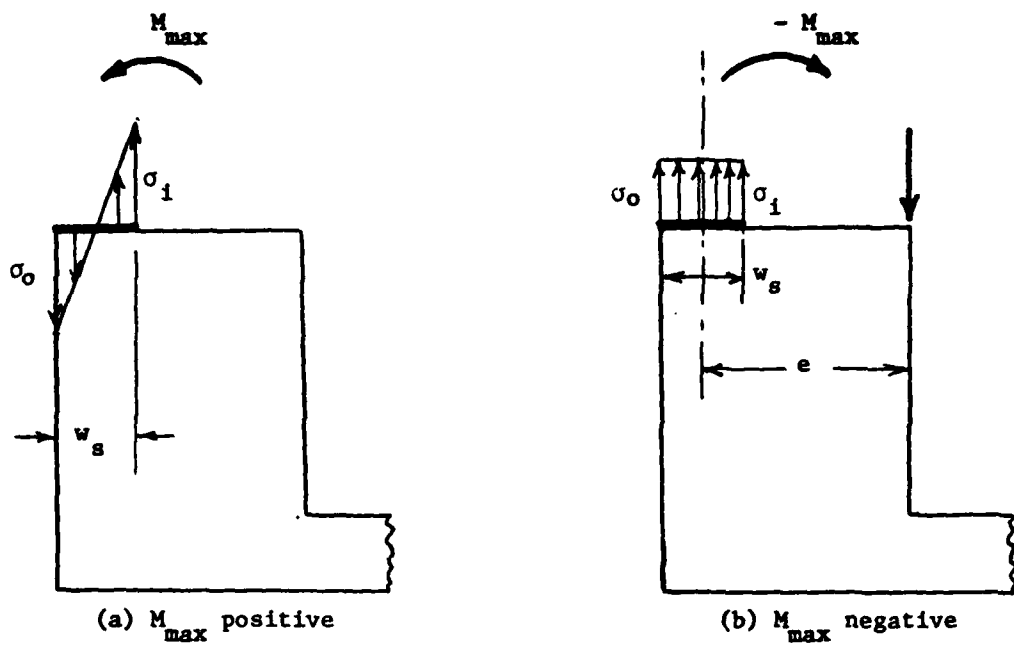


Figure 7. - Flexural stresses in a narrow seal.

IV. NUMERICAL EXAMPLE

A. Problem.- A package whose temperature has been stabilized at -65°C is immersed in a fluid bath of 150°C temperature. The lid properties are:

$$t = .015 \text{ in}$$

$$E = 20,000,000 \text{ psi}$$

$$\nu = 0.3$$

$$\alpha = 5.3 \times 10^{-6}/^{\circ}\text{C}$$

$$k = 10 \text{ Btu-ft}/(\text{hr-ft}^2\text{-}^{\circ}\text{F}) = .00023 \text{ Btu-in}/(\text{sec-in}^2\text{-}^{\circ}\text{F})$$

$$c = .12 \text{ Btu}/(\text{lb-}^{\circ}\text{F})$$

$$\rho = .302 \text{ lb/in}^3$$

The fluid properties are:

$$k_f = .09 \text{ Btu-ft}/(\text{hr-ft}^2\text{-}^{\circ}\text{F})$$

$$c_f = .52 \text{ Btu}/(\text{lb-}^{\circ}\text{F})$$

$$\rho_f = .035 \text{ lb/in}^3$$

The seal is narrow, as in Figures 2(b) and 7, with

$$w_s = .010 \text{ in}, \quad w = .040 \text{ in}, \quad \text{and} \quad e = .035 \text{ in}$$

Determine: (a) The initial interface temperature, (b) the maximum stresses developed in the seal, (c) the time at which these stresses occur, and (d) the interface temperature and inside face temperature five minutes after immersion.

B. Solution.- We first compute R and S, using Equations (4) and (6):

$$R = \sqrt{\frac{.035}{.302} \frac{.52}{.12} \frac{10}{.09}} = 7.47 \quad S = \sqrt{\frac{.035}{.302} \frac{.52}{.12} \frac{.09}{10}} = .0671$$

Equation (5) then gives the following solution to part (a) of the problem:

$$T_1 = \frac{150 (.0671) + (-65)}{1.0671} = -51^\circ\text{C}$$

Since this is a narrow seal and $\alpha(T_f - T_c)$ is positive, Equation (39) must be used to solve part (b). It gives

$$\left. \begin{array}{l} \sigma_o \\ \sigma_i \end{array} \right\} = \begin{array}{l} - \frac{9}{16} \frac{.0671}{1.0671} \frac{(20 \times 10^6)(5.3 \times 10^{-6})[150 - (-65)]}{1 - 0.3} \left(\frac{.015}{.010} \right)^2 \\ + 2590 \text{ psi} \end{array}$$

Thus, the outer edge of the seal experiences a maximum transient compressive stress of 2590 psi, while the inner edge experiences a tensile stress of the same magnitude.

For part (c) we turn to Equation (21). It gives the following time at which the stress maximums occur:

$$\tau_1 = \frac{9}{64} \frac{\left(.302 \frac{\text{lb}}{\text{in}^3} \right) \left(.12 \frac{\text{Btu}}{\text{lb} \cdot ^\circ\text{F}} \right) (.015 \text{ in})^2}{.00023 \frac{\text{Btu-in}}{\text{sec-in}^2 \cdot ^\circ\text{F}}} = .005 \text{ sec}$$

Equations (22) and (21) give $\tau_2 = (16/9)\tau_1 = .89 \text{ sec}$. Thus, at $\tau = 5 \text{ min} = 300 \text{ sec}$ we are well into the Figure 3(b) regime. This means

that to solve part (d) of the problem, we must use Equation (30).

Solving this equation for the bracketed term, we obtain

$$[.25 + I(Rd_f/t; S)] = \frac{\tau k}{\rho c t^2} = \frac{(300)(.00023)}{(.302)(.12)(.015)^2} = 8450$$

Entering this as the abscissa in Figure 4 and interpolating to find the ordinate associated with $S = .0671$ (or, alternatively, using Eq. (31b) and solving for Rd_f/t by trial and error), we obtain $Rd_f/t = 688$, whence

$$\frac{d_f}{t} = \frac{688}{7.47} = 92.1$$

and

$$d_f = 92.1 t = 1.38 \text{ in}^*$$

Equation (10) may now be used to compute T_i . As a preliminary useful step, however, we first compute the following quantities:

$$\frac{k_f}{k} \frac{t}{d_f} = \frac{.09}{10} \frac{1}{92.1} = .0000976$$

$$\frac{\rho_f}{\rho} \frac{c_f}{c} \frac{d_f}{t} = \frac{.035}{.302} \frac{.52}{.12} (92.1) = 46.5$$

Then Equation (10) gives the interface temperature as

* This rather large penetration distance could be of the same order as, or greater than, the length or width of the package. In that case the assumption of one-dimensional heat flow would no longer be valid, and the remaining calculations would have to be viewed with caution.

$$T_i = \frac{T_f (.0000976 + 46.5) + 2T_c}{.0000976 + 46.5 + 2} = .959 T_f + .041 T_c$$

$$= .959 (150) + .041 (-65) = 141^\circ\text{C}$$

Similarly, Equation (11) gives the following inside-face temperature:

$$T_c' = \frac{T_f (-0.0000976 + 46.5) + 2T_c (1.0000976)}{.0000976 + 46.5 + 2} = 141^\circ\text{C}$$

Thus, at the end of five minutes the lid temperature is essentially uniform ($T_i = T_c'$) but at a temperature that is still 9°C below the fluid bath temperature. However, as suggested by the last footnote, the validity of this result may be questionable.

V. FLEXURAL STRESSES PRODUCED IN SCREENING

We shall now apply equations (38) to (40) specifically to the thermal-shock screening procedure. The first three steps of this procedure are as follows:

Step 1 (preconditioning): The package at room temperature is immersed in the high temperature bath for a minimum of 5 minutes.

Step 2: The package is transferred from the high-temperature to the low-temperature bath and left there for a minimum of 5 minutes.

Step 3: The package is transferred from the low-temperature to the high-temperature bath and left there for a minimum of 5 minutes.

The remaining steps are a repetition of Steps 2 and 3 for at least fourteen times.

In using the stress formulas to determine the effects of Step 1, we would set T_c equal to T_r (room temperature) and T_f equal to T_2 . We shall assume that the five-minute dwell time is sufficient to make the package temperature the same as the bath temperature. Therefore, in studying the

effects of Step 2, we would assume T_c equal to T_2 and set T_f equal to T_1 . Similarly, for Step 3, we would take T_c equal to T_1 and set T_f equal to T_2 . In general, T_r will lie between T_1 and T_2 . It is clear, therefore, that Step 1 will produce less severe stresses than Step 3. Consequently, we need only study the stresses developed in Steps 2 and 3.

The application of Equations (38) to (40) to these two steps of the screening process is straightforward. The resulting maximum stress formulas are summarized in Tables 1 and 2. In these Tables, S_2 and S_1 are defined by equation (6) with the fluid constants those of the high-temperature and low-temperature fluid, respectively. I.e.,

$$S_2 \equiv \sqrt{\frac{\rho_2}{\rho} \frac{c_2}{c} \frac{k_2}{k}} \quad , \quad S_1 \equiv \sqrt{\frac{\rho_1}{\rho} \frac{c_1}{c} \frac{k_1}{k}} \quad (41)$$

Note that $\frac{E\alpha(T_2 - T_1)}{1 - \nu}$ appears as a factor in all the stress formulas.

The significant information in these Tables can be summarized as follows: In the case of a wide seal (Table 1) the magnitude of the maximum tension and compression stress are both given by

$$\sigma_{\max} = \frac{9}{16} \frac{E\alpha(T_2 - T_1)}{1 - \nu} \left(\frac{t}{w_s} \right)^2 \cdot N \quad (42)$$

	σ_o	σ_i
Step 2: Transfer from T_2 to T_1	$\frac{9}{16} \frac{S_1}{S_1+1} \frac{E\alpha(T_2-T_1)}{1-\nu} \left(\frac{t}{w_s}\right)^2$	$-\frac{9}{16} \frac{S_1}{S_1+1} \frac{E\alpha(T_2-T_1)}{1-\nu} \left(\frac{t}{w_s}\right)^2$
Step 3: Transfer from T_1 to T_2	$-\frac{9}{16} \frac{S_2}{S_2+1} \frac{E\alpha(T_2-T_1)}{1-\nu} \left(\frac{t}{w_s}\right)^2$	$\frac{9}{16} \frac{S_2}{S_2+1} \frac{E\alpha(T_2-T_1)}{1-\nu} \left(\frac{t}{w_s}\right)^2$

Table 1. Wide-Seal Flexural Stresses

	σ_o	σ_i
Step 2: Transfer from T_2 to T_1	$\frac{3}{32} \frac{S_1}{S_1+1} \frac{E\alpha(T_2-T_1)}{1-\nu} \frac{t^2}{ew_s}$	$\frac{3}{32} \frac{S_1}{S_1+1} \frac{E\alpha(T_2-T_1)}{1-\nu} \frac{t^2}{ew_s}$
Step 3: Transfer from T_1 to T_2	$-\frac{9}{16} \frac{S_2}{S_2+1} \frac{E\alpha(T_2-T_1)}{1-\nu} \left(\frac{t}{w_s}\right)^2$	$\frac{9}{16} \frac{S_2}{S_2+1} \frac{E\alpha(T_2-T_1)}{1-\nu} \left(\frac{t}{w_s}\right)^2$

Table 2. Narrow-Seal Flexural Stresses

where

$$N \equiv \text{the larger of } \frac{S_1}{S_1 + 1} \text{ and } \frac{S_2}{S_2 + 1} \quad (43)$$

In the case of a narrow seal (Table 2), the maximum tension is given by

$$\sigma_{\text{max tension}} = \frac{E\alpha(T_2 - T_1)}{1 - \nu} \cdot N' \quad (44)$$

where

$$N' \equiv \text{the larger of } \frac{3}{32} \frac{S_1}{S_1 + 1} \frac{t^2}{ew_s} \\ \text{and } \frac{9}{16} \frac{S_2}{S_2 + 1} \left(\frac{t}{w_s} \right)^2 \quad (45)$$

The magnitude (absolute value) of the maximum compressive stress is

$$\sigma_{\text{max compression}} = \frac{9}{16} \frac{S_2}{S_2 + 1} \frac{E\alpha(T_2 - T_1)}{1 - \nu} \left(\frac{t}{w_s} \right)^2 \quad (46)$$

It is very likely that any damage to the seal arises from the tension stress, rather than the compressive stress (which in any case never exceeds the maximum tension stress). Therefore, Equations (42) and (44) are the results of greatest interest.

VI. APPLICATION TO PACKAGE OR SCREEN DESIGN

The usefulness of these results to the package designer can be stated as follows: Knowing the screening bath parameters (T_2 , T_1 , S_2 , S_1), the designer can design the package so that the σ_{\max} given by Equation (42) or (44) (whichever applies) is less than some conservatively assumed allowable tensile stress for the seal material. On the other hand, the purchaser of an already designed package can use the same formulas to select screening parameters that will produce a σ_{\max} equal to some selected minimum acceptable tensile-strength value for the seal material, thereby rupturing those seals whose strength is below that value. It should be noted, however, that other screening techniques (e.g., external pressure, as discussed in Chapter 1) may be more effective for the latter purpose.

VII. INCLUSION OF BOILING

In Section II (THERMAL ANALYSIS) it was tacitly assumed that no boiling of the low-temperature liquid occurs when the package is transferred into it from the high-temperature fluid. Thus, the thermal analysis presented there is valid if the computed interface temperature T_i turns out to be lower than the boiling temperature T_b of the low-temperature liquid. If T_i turns out to be higher than T_b , a generalized thermal analysis is needed which takes into account the heat of vaporization of the low-temperature liquid.

Here we present the starting point of such an analysis with the aid of Figure 8, which is Figure 3(a) generalized to include a vapor phase of depth d_v adjacent to the cover. Also, Figure 8 has been drawn consistent with the fact that boiling can occur only for the case $T_c > T_f$. The following new symbols will be needed. They are:

T_b = known boiling temperature of low-temperature liquid

d_v = thickness of vapor layer produced by boiling of the low-temperature liquid.

c_{fv} = heat of vaporization of low-temperature liquid

k_v = thermal conductivity

c_v = specific heat

ρ_v = density

} of the vapor at atmospheric pressure

Implied by Figure 8 is the assumption that in the vapor layer the temperature varies linearly from the value T_i at the interface with the cover to the boiling temperature T_b at the interface with the liquid. In the liquid, the temperature varies linearly from T_b to the unperturbed liquid temperature T_f in a penetration distance d_f measured from the vapor-liquid interface.

In place of Equation (1), we now have the following energy balance equation, which states that the cover heat loss represented by triangle AGH is equal to the sum of (a) the heat that was required to heat the liquid that is now vapor to its boiling point, (b) the heat of vaporization of that mass of liquid, (c) the heat gain of the vapor represented by triangle ABF, due to its mean temperature rise above the boiling point, and (d) the heat gain of the unboiled liquid, represented by triangle BCD:

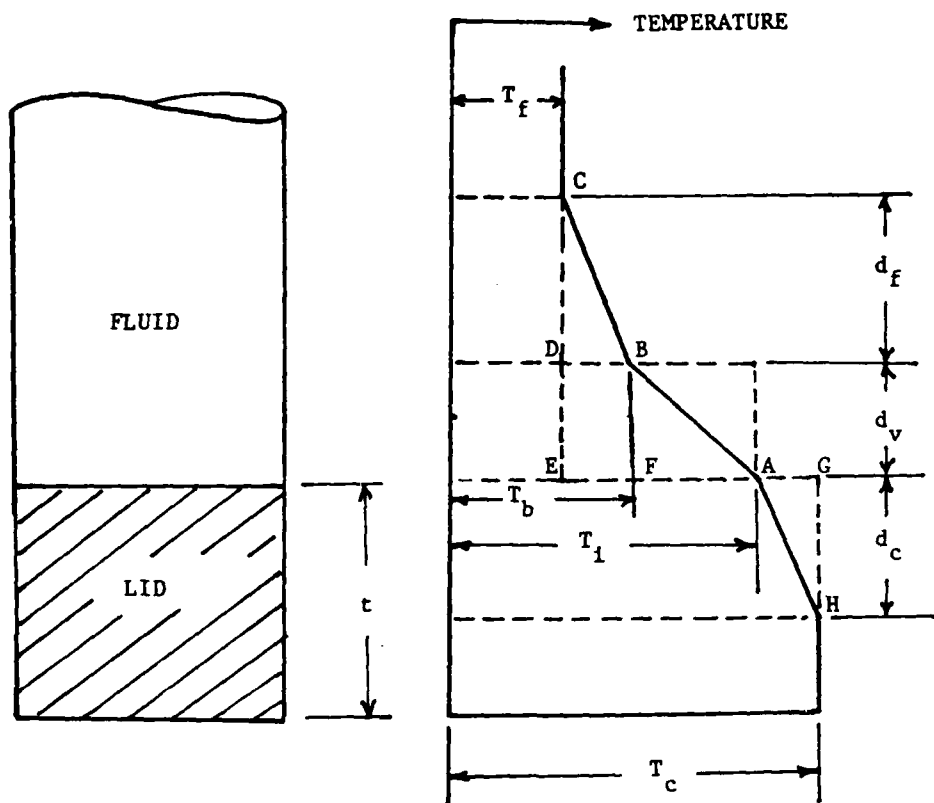


Figure 8.- Temperature distribution in low-temperature fluid and lid for the case in which boiling occurs and the temperature perturbation has not yet penetrated through the lid ($d_c < t$).

AD-A113 594

SYRACUSE UNIV NY
MICROCIRCUIT PACKAGE STRESS ANALYSIS. (U)
JAN 82 C LIBOVE, R W PERKINS, K KOKINI

F/6 9/5

UNCLASSIFIED

MAE-1237-F1

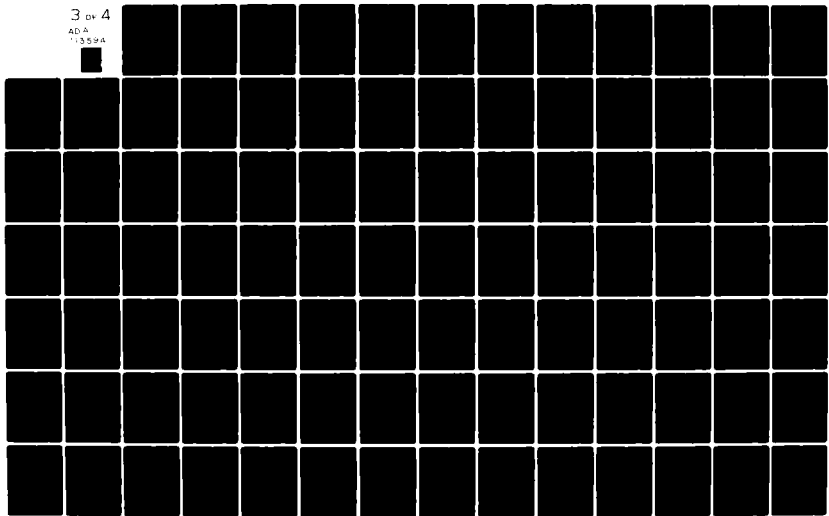
RADC-TR-81-382

F30602-80-C-0155

NL

3 of 4

ADA
1359A



$$\begin{aligned}
\frac{1}{2} d_c \rho (T_c - T_i) c &= d_v \rho_v (T_b - T_f) c_f \\
&+ d_v \rho_v c_{fv} \\
&+ \frac{1}{2} d_v \rho_v (T_i - T_b) c_v \\
&+ \frac{1}{2} d_f \rho_f (T_b - T_f) c_f
\end{aligned} \tag{47}$$

There are now two interfaces: cover-vapor and vapor-liquid; therefore there are now two equations corresponding to Equation (2). They are

$$k \frac{T_c - T_i}{d_c} = k_v \frac{T_i - T_b}{d_v} \tag{48}$$

$$k_v \frac{T_i - T_b}{d_v} = k_f \frac{T_b - T_f}{d_f} \tag{49}$$

Equations (47), (48) and (49) can be regarded as three equations defining T_i , d_v and d_f as functions of the time-like parameter d_c . They are valid only for the phase $d_c < t$ of the heat transfer process and only if their solution gives $T_i > T_b$.

To solve Equations (47), (48) and (49) most expeditiously, we first solve (48) and (49) for d_v and d_f in terms of d_c , then substitute the results into (47), cancel the common factor d_c , and thereby obtain a quadratic equation for T_i in which T_i is the only unknown. The outcome of these steps is:

$$d_v = d_c \frac{k_v}{k} \frac{T_i - T_b}{T_c - T_i} = d_c \frac{k_v}{k} \left(\frac{T_{cb}}{T_{ci}} - 1 \right) \tag{50}$$

$$d_f = d_c \frac{k_f}{k} \frac{T_b - T_f}{T_c - T_i} = d_c \frac{k_f}{k} \frac{T_{bf}}{T_{ci}} \tag{51}$$

$$\frac{1}{2} T_{ci}^2 (1-K_v) + T_{ci} (T_{bf}K_{vf} + k_{vfv} + T_{cb}K_v) - (T_{bf}T_{cb}K_{vf} + T_{cb}K_{vfv} + \frac{1}{2} T_{cb}^2 K_v + \frac{1}{2} T_{bf}^2 K_f) = 0 \quad (52)$$

in which the following notation has been employed:

$$T_{ci} = T_c - T_i \quad T_{cb} = T_c - T_b \quad T_{bf} = T_b - T_f \quad (53, 54, 55)$$

$$K_v = k_v \rho_v c_v / k \rho c$$

$$K_{vf} = k_v \rho_v c_f / k \rho c$$

(56)

$$K_{vfv} = k_v \rho_v c_{fv} / k \rho c$$

$$K_f = k_f \rho_f c_f / k \rho c$$

In using these results, the quadratic equation (52) is first solved for T_{ci} , after which (53) gives T_i and (50) and (51) give d_v and d_f for any d_c .

VIII. REMARKS

Simple formulas have been developed for the maximum flexural stresses produced in the lid-to-wall seal of a microelectronic flatpack under conditions of thermal-shock screening. In the derivation of these formulas, attention has been restricted to the case of a constant-thickness lid. If the lid is of a ductile material with a thinned edge, the thinness of the edge and the plasticity of the material will very likely provide an effective barrier against the transmission of damaging bending moments across the lid-to-wall seal, as discussed in Chapter 1.

The formulas are based on a number of other simplifying assumptions, one of them being the assumption of temperature-independence for the thermal and elastic properties of the materials involved. It is known, however, that the properties of the package lid and the screening fluids are to some extent temperature-dependent, and that in the screening process marked temperature variations (both spatial and temporal) may occur. Consequently, the user of the formulas must exercise some judgment in estimating appropriate average values for the material constants appearing in them, based on the anticipated ranges of temperature variation over the time period of interest. Since the computed temperature variations themselves depend on the assumed values of the material thermal constants, an iterative calculation may be required in extreme cases.

Chapter 7 - THERMAL SHOCK: BIAXIAL SURFACE TENSION IN DIP SEALS

If a solid object at a uniform high temperature T_c is plunged into a liquid bath of lower temperature T_f , then, according to Equation (7a) of Chapter 6, the surface of the solid will immediately experience a temperature drop of

$$\Delta T = T_c - T_1 = \frac{S}{S+1} (T_c - T_f) \quad (1)$$

where

$$S = \sqrt{\rho_f c_f k_f / \rho c k} \quad (2)$$

with ρ_f , c_f , k_f the properties of liquid and ρ , c , k the local properties of the surface material of the solid.* Thus, at the instant of immersion, there develops an infinitely thin surface layer of cooled material in the solid. Despite its cooling, there can be no thermal contraction of this surface layer, because the bulk of the solid, with a volume that is infinite in comparison with that of the surface layer, is still at its original temperature T_c . The suppressed contraction will give rise to biaxial surface tensions. If these are sufficiently large, and the surface material brittle, fracture of the surface material can occur.

* In using Equation 7(a) of Chapter 6, we are assuming that the liquid is not brought to its boiling temperature T_b ; that is, that the interface temperature $T_1 = T_c - \Delta T$ implied by Equation (1) does not exceed T_b . If Equation (1) yields a T_1 that does exceed T_b , Equation (52) of Chapter 6 may be used to compute a more correct T_1 . Alternatively, if one wishes to be conservative, one may simply assume $T_1 = T_b$. The corresponding surface temperature drop $\Delta T = T_c - T_b$ will be too large, causing Equation (4) to predict a surface tension σ that is also too large.

I. EVALUATION OF SURFACE TENSION

Inasmuch as the stress in the third direction (normal to the surface) is zero, the magnitude σ of the biaxial surface tension at any location can be obtained from the biaxial stress-strain relations for plane stress, namely

$$\sigma_x = \frac{E}{1-\nu^2} (\epsilon_x + \nu\epsilon_y) \quad \sigma_y = \frac{E}{1-\nu^2} (\epsilon_y + \nu\epsilon_x) \quad (3)$$

where E and ν are the local Young's modulus and Poisson's ratio. The surface tension σ will be the common value of σ_x and σ_y required to produce the strains $\epsilon_x = \epsilon_y = \alpha\Delta T$, where α is the local coefficient of thermal expansion of the surface material. Thus,

$$\sigma = \frac{E}{1-\nu^2} (1+\nu)\alpha\Delta T = \frac{E\alpha\Delta T}{1-\nu} \quad (4)$$

Equation (4) will give the tensile stresses produced at any location in the exposed surface. If applied to the seal area of a glass-sealed dual-in-line package (DIP) or other kind of package, in particular, it can reveal whether or not damaging surface tensile stresses are likely to be produced in the glass seal during the high-to-low temperature step of the MIL-STD-883B thermal shock test or during any similar experience*. In making this judgment it should be kept in mind that the surface tension can be exacerbated by stress concentrations due to lead frames and lead wires.

* We are assuming here that the components of the package are "thermally matched", so that the seal stresses under the high initial uniform temperature are negligible. If that is not the case, and there are some stresses under the initial temperature, then Equation (4) gives the changes in stress produced by immersion of the package into the low-temperature fluid.

II. APPLICATIONS

In order to demonstrate the above-mentioned use of Equation (4), let us assume that a glass-sealed ceramic dual-in-line package (CERDIP) has been brought to a uniform temperature of 260C in a lead-tinning operation, then, for purposes of slag removal, rapidly quenched in water at room temperature (20C), and let us compute the resulting surface tension in the exposed glass of the seal, assuming the surface to have been stress-free at the 260C uniform temperature.

The properties of the water are taken as

$$\rho_f = 1 \text{ g/cm}^3$$

$$c_f = 1 \text{ cal/g}^\circ\text{C}$$

$$k_f = 4.1 \text{ Btu-in./hr-ft}^2\text{-}^\circ\text{F}$$

and those of the sealing glass are estimated to be

$$\rho = 6.85 \text{ g/cm}^3$$

$$c = .02 \text{ cal/g}^\circ\text{C}$$

$$k = 6.3 \text{ Btu-in/hr-ft}^2\text{-}^\circ\text{F}$$

$$E = 9.5 \times 10^6 \text{ lb/in.}^2$$

$$\nu = 0.22$$

$$\alpha = 64 \times 10^{-7}/^\circ\text{C}$$

Then

$$S = \sqrt{\frac{1}{6.85} \frac{1}{.02} \frac{4.1}{6.3}} = 2.18$$

whence

$$\Delta T = \frac{2.18}{2.18 + 1} (260 - 20) = 165 \text{ C}$$

$$T_i = T_c - \Delta T = 260 - 165 = 95 \text{ C}$$

$$\sigma = \frac{(9.5 \times 10^6)(64 \times 10^{-7})(165)}{1 - 0.22} = 12,900 \text{ psi}$$

Thus a rather large surface tension of 12,900 psi is predicted. The strength properties of this glass are unknown, but if they are comparable to those cited in Section VIII of Chapter 1, we should expect fracture of the seal to occur in around 96% of the packages subjected to the assumed quench.

In an experimental simulation of the event assumed in this example, two CERDIPS were heated to 260 C in molten solder, then dipped in 20 C water. Subsequent measurement of their lid torque strength (torque required to remove the lid, applied coplanar with the lid) gave values of 20 in.-lb and 0 in.-lb, as compared with lid torque strengths of 50 in.-lb obtained for two virgin packages, thus confirming the damage predicted above. Two packages that were quenched in crank-case oil (properties unknown), instead of in water, had subsequent lid torque strengths of 60 in.-lb and 50 in.-lb; that is, their seals suffered no damage.

It should be mentioned that during the water quench a very short duration sizzling was heard, indicating that the actual interface temperature was at or slightly above the boiling temperature of 100 C. Thus, the above-computed interface temperature of 95 C is slightly low, therefore slightly conservative. Taking 100 C as the more nearly correct interface tempera-

ture, we would get a ΔT of $260 - 100 = 160$ C instead of 165 C, leading to a surface tension some 3% lower than the 12,900 psi computed above.

As a second example, let us consider the same CERDIP as in the previous calculation and compute the seal surface tension it experiences during the level C thermal shock test of MIL-STD-883B. This involves heating the package in a 150 C liquid bath and then immersing it in -65 C liquid bath. (The temperature difference of the two baths is 215 C, which is only 10% less than the 240 C temperature difference in the previous example.) The low-temperature fluid will be assumed to be FC77 as suggested in MIL-STD-883B. Its pertinent properties as taken from Appendix A, are

$$\rho_f = 1.84 \text{ g/cm}^3$$

$$c_f = .237 \text{ cal/g}^\circ\text{C}$$

$$k_f = .65 \text{ Milliwatts/cm-}^\circ\text{C}$$

$$= .451 \text{ Btu-in/hr-ft}^2\text{-}^\circ\text{F}$$

(These values are for a temperature of 0° C, which is about the middle of the anticipated temperature rise of the FC77 in immediate contact with the package. A somewhat lower temperature would have been appropriate, inasmuch as the rest of the temperature-perturbed fluid experiences smaller temperature rises; however k_f data are not given for temperatures below 0° C.)

The calculations for this example are as follows:

$$S = \sqrt{\frac{1.84}{6.85} \frac{.237}{.02} \frac{.451}{6.3}} = .477$$

$$\Delta T = \frac{.477}{.477 + 1} [150 - (-65)] = 69.4 \text{ C}$$

$$T_1 = T_c - \Delta T = 150 - 69.4 = 80.6$$

$$\sigma = \frac{(9.5 \times 10^6)(64 \times 10^{-7})(69.4)}{1 - 0.22} = 5400 \text{ psi}$$

We note that even though the bath temperature difference in this example is almost the same as that in the previous example, the 5400 psi seal surface tension produced is less than half as severe as the stress of 12,900 psi obtained in the previous example. The large difference is due, of course, to the use of FC77, rather than water, as the low-temperature fluid. Again assuming the glass to have strength properties comparable to those cited in Section VIII of Chapter 1, we would expect seal damage in about 6.7% of the packages subjected to this screen, as compared with 96% damage for the previous treatment.

This and the previous example, taken together, show that the severity of a thermal shock test should not be measured solely by the temperature difference of the two baths involved in the test. The properties of the fluids, especially those of the low temperature fluid, play a very important role, as well.

Chapter 8 - THERMAL SHOCK: ANNULAR GLASS SEALS*

Where a Kovar lead of circular cross section emerges from a Kovar package it is commonly sealed by an annular glass bead. Figure 1 shows a typical package containing such seals around lead wires emerging through the base; in other packages the lead wires might emerge through the side walls.

In the design of such packages the glass selected is usually one whose thermal contraction from the set point down to room temperature matches the thermal contraction of the Kovar over the same temperature range, so that at room temperature the seal is free of thermal stress. However, the glass and Kovar, though matched over that temperature range, would generally not be matched for another temperature range. Therefore, if the package is brought from room temperature to another uniform temperature thermal stresses will develop in the glass seals and the metal surrounding them. Thermal stresses will also develop as a result of any non-uniformity in temperature within the glass seal or between the glass and the metals, whether or not the seals are matched. Severe (though transient) non-uniformities of temperature can arise during the MIL-STD-883B thermal shock tests immediately after the package is transferred into another bath after its 5-minute dwell in one bath, the reason for the nonuniformities being the different thermal conductivities, specific heats and densities of the glass and metal. The associated thermal stresses in the seal could conceivably result in a loss of hermeticity. For example, a sufficiently large radial tensile stress at a glass-metal interface could cause a gap to develop at that interface if the stress exceeded the tensile strength of the interface material, leading to the ingestion of the thermal shock

*This chapter supersedes the analytic portions (Appendixes A through C) of Ref. 26.

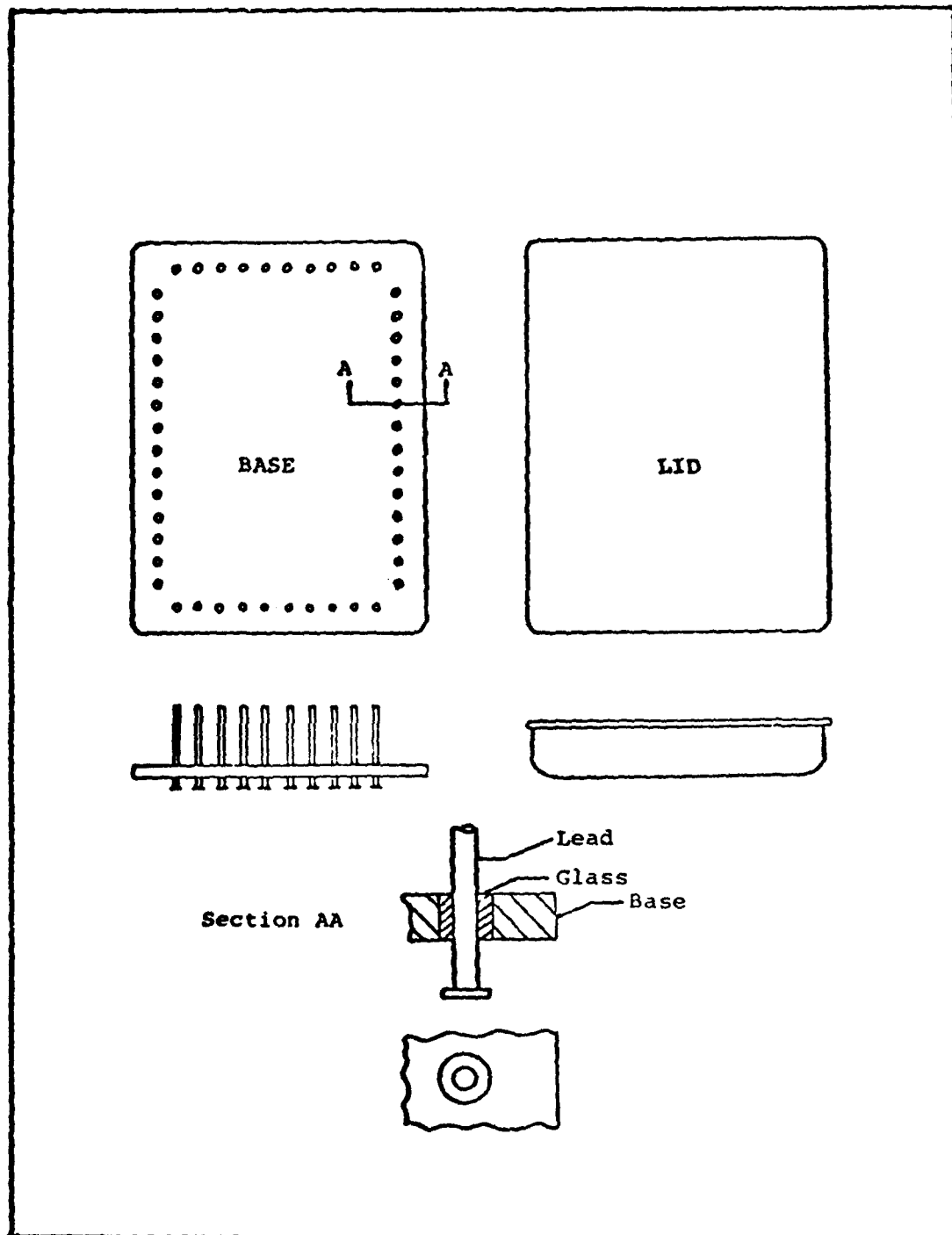


Figure 1.- Package with annular glass lead-through seals.

test fluid into the package. To make matters worse, inasmuch as the temperature gradients are transient, the existence of the gap might also be transient and therefore undetectable once the temperature has become uniform again. Sufficiently large circumferential tension in the glass could also cause radial cracks to develop.

The capability of the thermal shock test to produce loss of hermeticity and ingestion of contaminants was first pointed out by R.W. Thomas (Reference 24). Thomas conducted an experimental study of packages subjected to thermal shock and found that leakage appeared to be directly correlated with the thermal shock. He suggested that thermal stresses in the vicinity of the lead-through seals may be large enough to permit leakage during the thermal shock which might go undetected during subsequent gross leak testing of the package. Other literature (Reference 25) also indicates that stresses during thermal shock testing can lead to fracture of the glass seal.

In view of these findings it appears desirable to have a procedure for predicting or estimating the magnitudes of the thermal stresses that might develop in the annular glass lead-through seals of microcircuit packages when subjected to thermal shock testing. The predicted stress conditions can be used by the screeener of the package to select a thermal shock test level consistent with the level of stress desired in the test package. A thermal shock stress analysis capability would also help the package designer arrive at a seal that would remain hermetic during any anticipated thermal shock testing of the package.

The purpose of this chapter is to develop a stress analysis procedure of the kind just referred to, based on some simplifying assumptions and idealized modelling. The point of view is essentially that of Reference 26, except for two differences: The finite difference method, rather than the finite element method, is used for the temperature analysis, because it appears to be more accurate; and in the stress analysis, plane stress is assumed, rather than generalized plane strain, because it is simpler and there is no strong reason to believe it is less valid.

The stress analysis procedure to be described below consists of two parts: the temperature analysis, and the stress analysis proper, both of which are embodied in a single APL computer program that prints out changes of temperature and stress in the glass as functions of radial position and time during any phase of the thermal shock test. In an illustrative application of the computer program, the history of radial stress at the glass-lead interface in a specific package during a specific thermal shock test is tracked.

I. MODELLING

Apart from the annular glass seals, the package is assumed to be an all-metal package consisting of N identical leads and a base, lid and side-walls of the same material as the leads. (For simplicity, the base, lid and side-walls collectively will be referred to henceforth as the "base".) Ceramic and other components inside the package will be ignored, although, if desired, they can be accounted for by adding an equivalent (in the sense of total heat capacity) amount of metal to the base.

As noted above, whenever the term "base" is used it should be understood to mean the actual base, lid and side-walls taken together as a single entity. The total volume of this base will be denoted by V_b and that part of its surface area in contact with the thermal shock test fluid by A_b . Additional notation will be introduced as needed.

A. Modelling for Temperature Analysis.- Different models will be used for the temperature analysis and for the stress analysis proper. The model for temperature analysis is shown in Figure 2. It consists of a single lead of volume V_l , radius a , surface area A_o in contact with the thermal shock test fluid, surface area A_2 in contact with the glass seal, an annular glass seal of inner radius a and outer radius b , and, surrounding the glass, a proportionate share V_b/N of the total base volume. The surface area of that proportionate share of base that is in contact with the test fluid is A_b/N .

Inasmuch as the metal has a much higher thermal conductivity than the glass, heat conduction in the lead and in the base will be assumed to be instantaneous; that is, the temperature is assumed to be uniform throughout the lead and uniform throughout the base. These two uniform temperatures are allowed to be different and, of course, to vary with time.

Inasmuch as the surface area of glass exposed to the fluid will usually be much smaller than the surface area of the glass in contact with the metal (i.e., lead-glass interface area plus the glass-base interface area), any direct transfer of heat between the fluid and the glass will be neglected. All of the heat transfer to or from the glass will be assumed to occur through the two interface areas that it shares with the metal. Continuity of temperature between metal and glass is assumed at these interfaces.

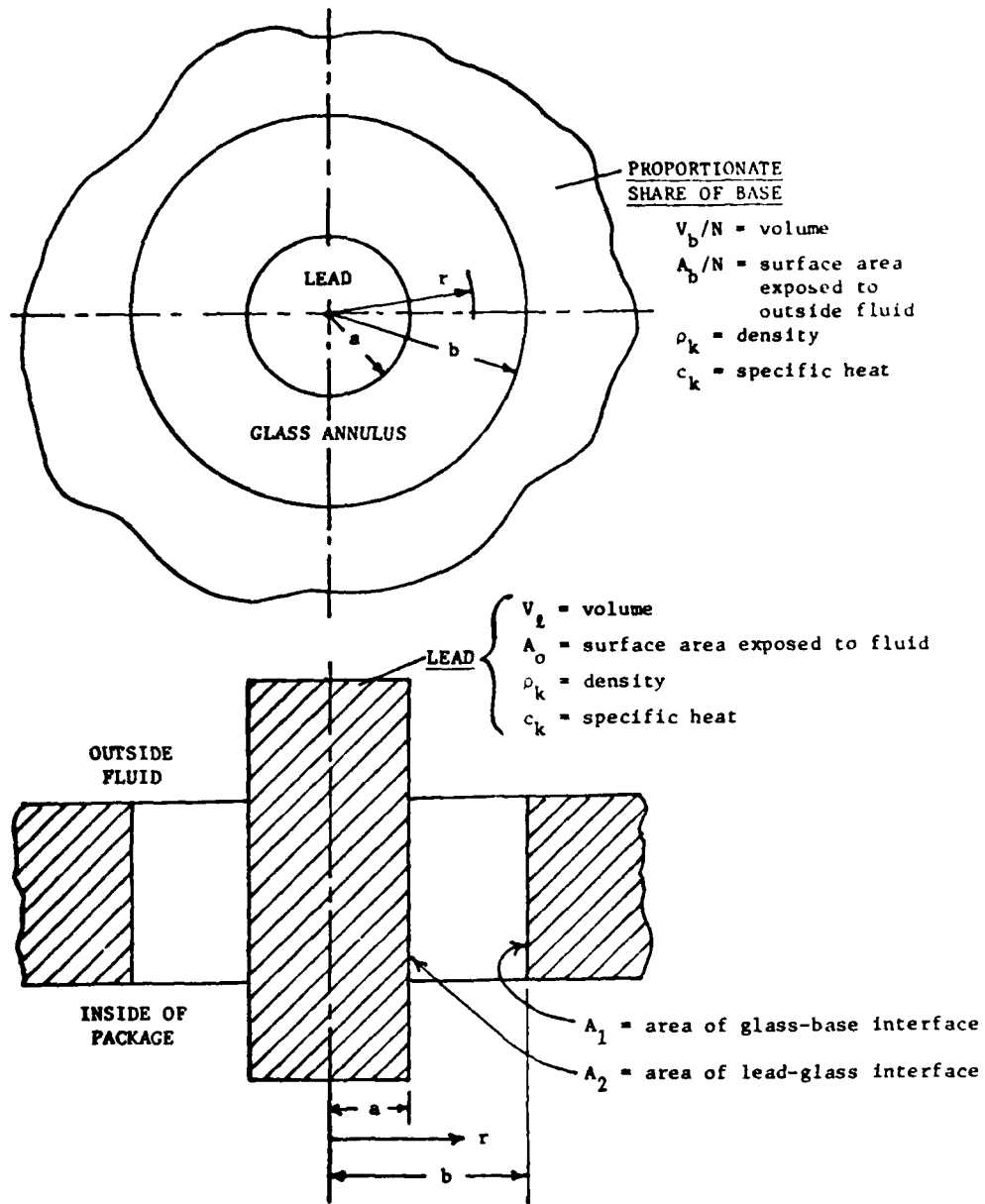


Figure 2.- Modelling for temperature analysis.

Those surfaces of the lead, base and glass that are inside the package are assumed to be adiabatic; that is, there is no transfer of heat across those surfaces.

In view of the above assumptions, the temperature T in the glass will be a function only of the radial coordinate r and time τ ; that is $T = T(r, \tau)$. The temperature will not vary in the axial (i.e., parallel to the lead) direction.

The flow of heat between the fluid and the metal surfaces in contact with it is assumed to be governed by a heat transfer coefficient \bar{h} that is the same for the fluid-lead interface as for the fluid-base interface. This heat transfer coefficient is best determined experimentally by the method described in Reference 26. In that reference the value of $\bar{h} = 210 \text{ Btu/ft}^2\text{-hr-}^\circ\text{F} = 4.051 \times 10^{-4} \text{ Btu/in.}^2\text{-sec-}^\circ\text{F}$ is cited for the case in which the fluid is water and the package is Kovar.

The density, specific heat and thermal conductivity of the glass are denoted by ρ_g , c_g and k_g , respectively, and assumed to be constant. Inasmuch as these properties are to some extent temperature dependent, average values based on anticipated temperature ranges should be used for them. Similarly, the density and specific heat of the metal will be denoted by ρ_k and c_k (subscript k standing for Kovar, although the analysis is not restricted to that metal), respectively, and also assumed to be constant. The thermal conductivity of the metal will play no role in the analysis, in view of the assumption of uniform temperature throughout the base and throughout the lead.

Certain combinations of the parameters defined above will arise naturally in the course of the temperature analysis. We introduce them now along with the short-hand symbols A, B, C, D and a_g that will be used to represent them:

$$\begin{aligned}
 A &\equiv \frac{\bar{h}A_o a}{A_2 k_g} & B &\equiv \frac{\rho_k c_k V_l}{\rho_g c_g A_2 a} \\
 C &\equiv \frac{\bar{h}A_b a}{a_1 N k_g} & D &\equiv \frac{\rho_k c_k V_b}{\rho_g c_g A_1 N a}
 \end{aligned}
 \tag{1}$$

$$a_g = \text{thermal diffusivity of the glass} = k_g / \rho_g c_g \tag{2}$$

B. Modelling for Stress Analysis.- The modelling of the lead-glass-base unit for purposes of stress analysis is shown in Figure 3. It will be seen from the model that for stress analysis purposes only that portion of the lead clinched by the glass is assumed to be effective; also that the metal surrounding the glass is assumed to be representable by a metal annulus of radius c with stress-free outer boundary. Some judgment will have to be exercised in selecting an appropriate value for c . For the case in which the lead comes through the side-wall of the package, it is suggested that c be taken equal to half the height of the wall. When the lead protrudes through the bottom of the package, as in Figure 1, it is suggested that c be taken as the distance from the center of the lead to the nearest edge of the package. (For c sufficiently large the stresses in the glass will become relatively insensitive to its value.)

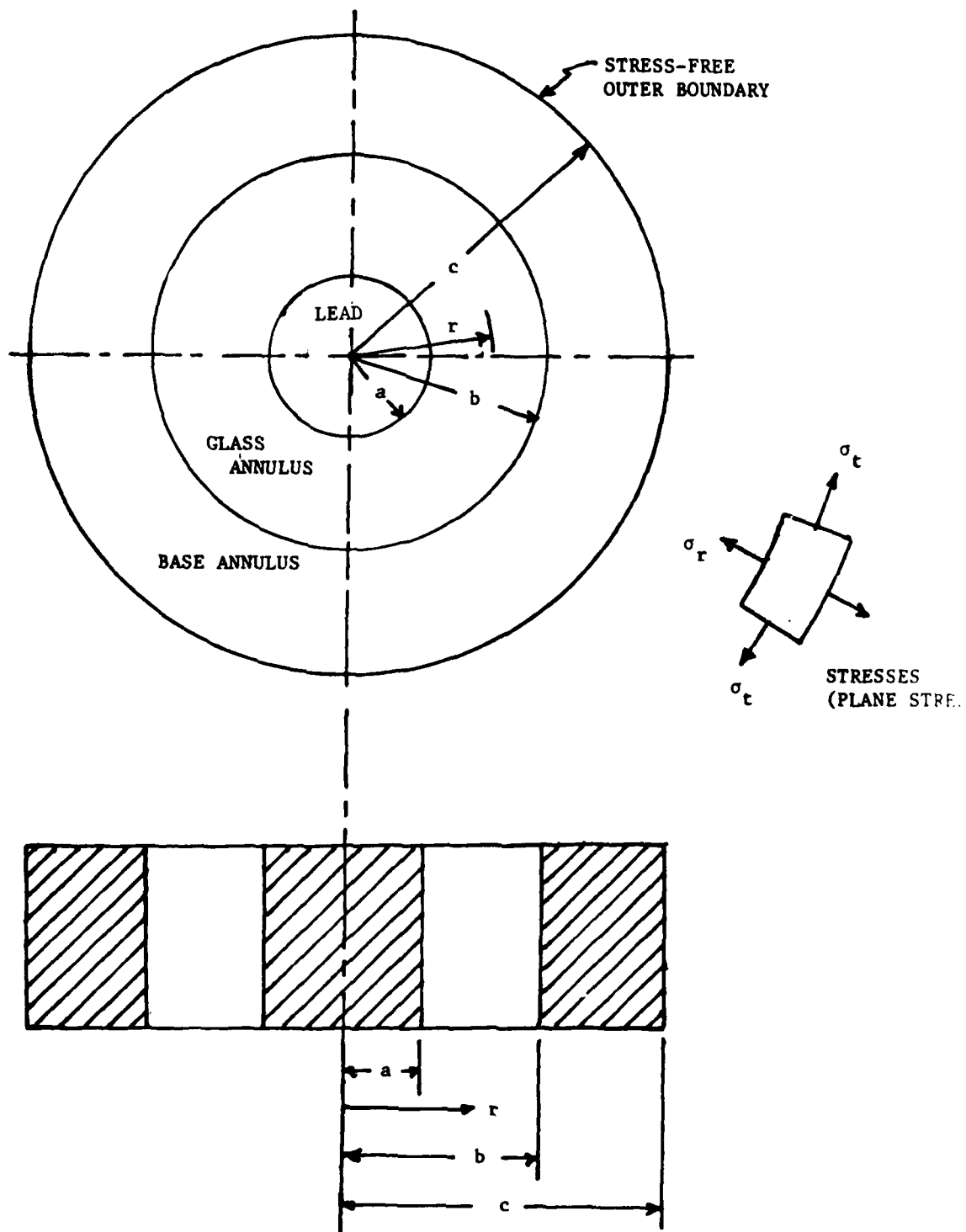


Figure 3.- Modelling for the stress analysis.

A state of plane stress will be assumed in the glass, in which the glass normal stresses (σ_r in the radial direction and σ_t in the transverse direction, both positive for tension) are functions of the radial coordinate r and independent of the axial (parallel to the lead) coordinate. These stresses will also vary with time by virtue of the fact that the temperatures and temperature distributions vary with time.

The Young's modulus, Poisson's ratio and thermal expansion coefficient of the glass will be denoted by E_g , ν_g and α_g , respectively; those of the metal by E_k , ν_k and α_k . Inasmuch as they may be temperature dependent (especially the α 's), average values based on anticipated temperature ranges should be used for these constants.

II. TEMPERATURE ANALYSIS

A. Basic Equations.- The initial uniform temperature of the package prior to its immersion in the fluid will be denoted to T_0 , that of the fluid by T_∞ . The fluid bath is assumed to be sufficiently large so that its temperature is not affected by the immersion of the package; therefore T_∞ is also the uniform temperature that the package approaches asymptotically if left in the fluid for a long enough time.

The temperature $T(r, \tau)$ in the glass is governed by the following equations:

$$\frac{\partial T}{\partial \tau} = a_g \left(\frac{\partial^2 T}{\partial r^2} + \frac{1}{r} \frac{\partial T}{\partial r} \right) \quad (a < r < b) \quad (3)$$

$$\rho_k c_k \frac{V_l}{A_2} \left(\frac{\partial T}{\partial \tau} \right)_{r=a} = \frac{\bar{h}A_o}{A_2} [T_\infty - (T)_{r=a}] + k_g \left(\frac{\partial T}{\partial r} \right)_{r=a} \quad (4)$$

$$\rho_k c_k \frac{V_b}{A_1 N} \left(\frac{\partial T}{\partial \tau} \right)_{r=b} = \frac{\bar{h}A_b}{A_1 N} [T_\infty - (T)_{r=b}] - k_g \left(\frac{\partial T}{\partial r} \right)_{r=b} \quad (5)$$

The first of these is the familiar field equation for non-steady state heat conduction. The second equation is a statement that the rate of heat storage in the lead is equal to the rate of heat flow into the lead through the fluid-lead interface plus the rate of heat flow into the lead through the glass-lead interface. And the third equation is an analogous statement for the base.

Rearranging terms, and introducing a dimensionless radial coordinate x , a dimensionless time y , and a dimensionless temperature t , defined as follows:

$$x \equiv r/a \quad (6)$$

$$y \equiv \tau a_g^2 / a^2 = \tau k_g / \rho_g c_g a^2 \quad (7)$$

$$t \equiv \frac{T_\infty - T(r, \tau)}{T_\infty - T_o} \equiv t(x, y) \quad (8)$$

we can convert Equations (3), (4) and (5) to the following dimensionless form:

$$\frac{\partial t}{\partial y} = \frac{\partial^2 t}{\partial x^2} + \frac{1}{x} \frac{\partial t}{\partial x} \quad (1 < x < b/a) \quad (9)$$

$$\left(\frac{\partial t}{\partial x}\right)_{x=1} = At(1,y) + B\left(\frac{\partial t}{\partial y}\right)_{x=1} \quad (10)$$

$$-\left(\frac{\partial t}{\partial x}\right)_{x=b/a} = Ct(b/a,y) + D\left(\frac{\partial t}{\partial y}\right)_{x=b/a} \quad (11)$$

in which the notation of Equations (1) has also been employed. These equations are to be solved subject to the initial condition

$$t(x,0) = 1 \quad (12)$$

B. Finite-Difference Formulation.- We will express Equations (9)-(11) in finite-difference form, using the grid shown in Figure 4. In this grid, the labels $i = 1, 2, \dots, M-1, M$ identify equally spaced stations in the radial or x -direction, with stations $i = 2$ and $M-1$ being at the lead-glass and glass-base interfaces ($x = 1$, $x = b/a$), stations $i = 3, 4, \dots, M-2$ lying entirely within the glass, and stations $i = 1$ and $i = M$ being "phantom" stations lying outside the glass. The labels $n = 1, 2, 3, \dots$ identify equally spaced stations along the time or y -axis, with $n = 1$ corresponding to $y = 0$. The ordered number pair (i, n) will identify the grid point at station i in the x -direction and station n in the y -direction, and $t_{i,n}$ will stand for the value of t at this grid point. Δx and Δy will denote the grid-line spacing in the x and y directions, respectively.

Our objective in this section is to determine all the $t_{i,n}$ for the i, n combinations defined by $i = 2, 3, \dots, M-1$ and $n = 2, 3, 4, \dots$. To that end we shall employ the following finite-difference approximations for the derivatives of t at the grid point (i, n) :

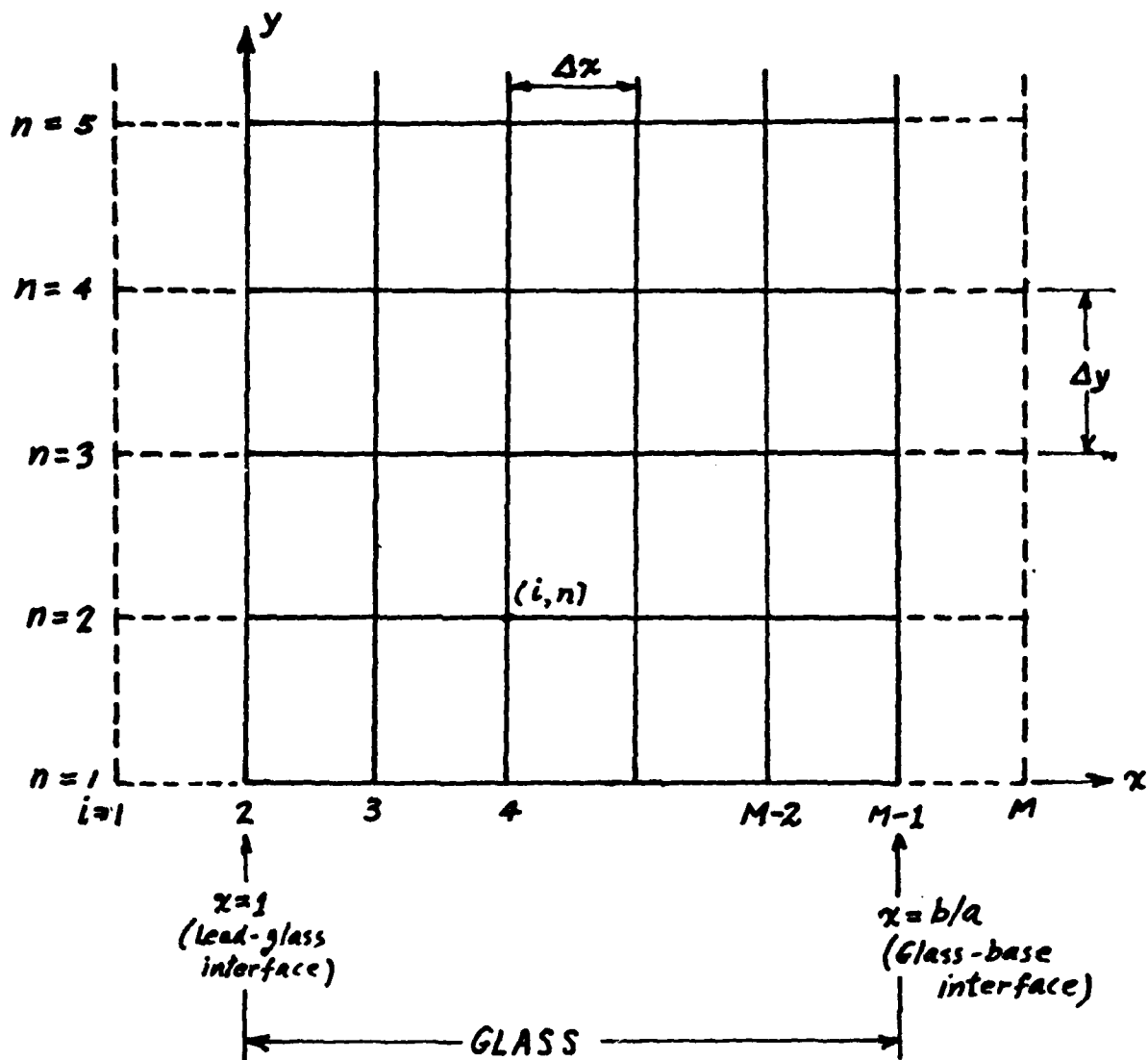


Figure 4.- Finite-difference grid for temperature analysis.

$$\frac{\partial t}{\partial y} = \frac{t_{i,n} - t_{i,n-1}}{\Delta y} \quad (13)$$

$$\frac{\partial t}{\partial x} = \frac{t_{i+1,n} - t_{i-1,n}}{2\Delta x} \quad (14)$$

$$\frac{\partial^2 t}{\partial x^2} = \frac{t_{i+1,n} - 2t_{i,n} + t_{i-1,n}}{(\Delta x)^2} \quad (15)$$

Writing Equations (10), (9) and (11) at the grid points where each applies, substituting the above expressions for the derivatives, and making minor rearrangements of terms, we obtain the following finite difference forms of Equations (10), (9) and (11), respectively:

$$t_{1,n}^F + t_{2,n}^G - t_{3,n}^F = t_{2,n-1} \quad (10')$$

$$-t_{i-1,n}^{H_i} + t_{i,n}^J - t_{i+1,n}^{K_i} = t_{i,n-1} \Delta x \quad (9')$$

$$-t_{M-2,n}^Q + t_{M-1,n}^P + t_{M,n}^Q = t_{M-1,n-1} \quad (11')$$

where

$$F = \frac{\Delta y}{2B\Delta x} \quad G = 1 + \frac{A\Delta y}{B} \quad (16)$$

$$H_i = \frac{\Delta y}{\Delta x} - \frac{\Delta y}{2x_i} \quad J = \frac{2\Delta y}{\Delta x} + \Delta x \quad K_i = \frac{\Delta y}{\Delta x} + \frac{\Delta y}{2x_i} \quad (17)$$

$$Q = \frac{\Delta y}{2D\Delta x} \quad P = 1 + \frac{C\Delta y}{D} \quad (18)$$

in which x_i denotes the value of x at radial station i . Equations (10') and (11') are to be written for $n = 2, 3, 4, \dots$; Equation (9') for $i = 2, 3, \dots, M-1$ and $n = 2, 3, 4, \dots$. These equations must be supplemented by the initial conditions

$$t_{i,1} = 0 \quad (i = 2, 3, \dots, M-1) \quad (19)$$

coming from Equations (12).

C. Solution of the Finite-Difference Equations.- For any fixed n , Equations (10'), (9') and (11') constitute a tri-diagonal system that can be solved expeditiously by the method of Reference 27, which leads to a solution in the form of a recursion formula. The method of Reference 27, as applied to the present system, is as follows: Postulate

$$t_{i,n} = \alpha_{i,n} + \beta_{i,n} t_{i+1,n} \quad (20)$$

where $\alpha_{i,n}$ and $\beta_{i,n}$ are as yet undetermined functions of i and n ; and, with i replaced by $i-1$, substitute this into the first term of Equation (9') to get

$$-(\alpha_{i-1,n} + \beta_{i-1,n} t_{i,n}) H_i + t_{i,n} J - t_{i+1,n} K_i = t_{i,n-1} \Delta x$$

or, solving for $t_{i,n}$,

$$t_{i,n} = \left(\frac{t_{i,n-1} \Delta x + \alpha_{i-1,n} H_i}{J - \beta_{i-1,n} H_i} \right) + \left(\frac{K_i}{J - \beta_{i-1,n} H_i} \right) t_{i+1,n} \quad (21)$$

Comparing Equations (21) and (20), we get the following recursion formulas for $\alpha_{i,n}$ and $\beta_{i,n}$:

$$\alpha_{i,n} = \frac{t_{i,n-1} \Delta x + \alpha_{i-1,n} H_i}{J - \beta_{i-1,n} H_i} \quad (22)$$

$$\beta_{i,n} = \frac{K_i}{J - \beta_{i-1,n} H_i} \quad (23)$$

Provided that the $t_{i,n-1}$ are known, these equations can be used to compute $\alpha_{i,n}$ and $\beta_{i,n}$ once $\alpha_{i-1,n}$ and $\beta_{i-1,n}$ have been determined. Thus, if $\alpha_{1,n}$ and $\beta_{1,n}$ are known, all the succeeding $\alpha_{i,n}$ and $\beta_{i,n}$ can be obtained by successive application of (22) and (23). The determination of $\alpha_{1,n}$ and $\beta_{1,n}$ proceeds as follows: From (9') and the $i=2$ equation of (10'), we have

$$t_{1,n}F + t_{2,n}G - t_{3,n}F = t_{2,n-1} \quad (24)$$

$$-t_{1,n}H_2 + t_{2,n}J - t_{3,n}K_2 = t_{2,n-1}\Delta x \quad (25)$$

Now solve (25) for $t_{3,n}$, use the result to eliminate $t_{3,n}$ in (24) and solve the resulting equation for $t_{1,n}$ to get

$$t_{1,n} = \left[\frac{t_{2,n-1}(K_2 - F\Delta x)}{F(K_2 + H_2)} \right] + \left[\frac{FJ - GK_2}{F(K_2 + H_2)} \right] t_{2,n} \quad (26)$$

and comparing this with Equation (20), we infer that

$$\alpha_{1,n} = \frac{t_{2,n-1}(K_2 - F\Delta x)}{F(K_2 + H_2)} \quad (27)$$

$$\beta_{1,n} = \frac{FJ - GK_2}{F(K_2 + H_2)} \quad (28)$$

Thus, we have the starting equations needed for the recursive application of Equations (22) and (23), provided that the $t_{i,n-1}$ are known. When $n=2$, the $t_{i,n-1}$ are indeed known, for then

$$t_{i,n-1} = t_{i,1} = 0 \quad (29)$$

by virtue of Equation (15). Therefore, at least for $n=2$ we can determine the following α 's and β 's:

$$\alpha_{2,n}; \alpha_{3,n}; \dots; \alpha_{M-1,n}$$

$$\beta_{2,n}; \beta_{3,n}; \dots; \beta_{M-1,n}$$

and for that same n , by successive application of Equation (20) we can determine successively $t_{M-1,n}$, $t_{M-2,n}$, ..., $t_{2,n}$, and $t_{1,n}$, if $t_{M,n}$ is known. A formula for $t_{M,n}$ will now be derived: Write Equation (20) for $i = M-1$ and $i = M-2$ to get

$$t_{M-1,n} = \alpha_{M-1,n} + \beta_{M-1,n} t_{M,n} \quad (30)$$

$$t_{M-2,n} = \alpha_{M-2,n} + \beta_{M-2,n} t_{M-1,n} \quad (31)$$

Use Equation (30) to eliminate $t_{M-1,n}$ in (31) to convert the latter equation to the form

$$t_{M-2,n} = \gamma + \delta \cdot t_{M,n} \quad (32)$$

where

$$\gamma = \alpha_{M-2,n} + \beta_{M-2,n} \alpha_{M-1,n} \quad (33)$$

$$\delta = \beta_{M-2,n} \beta_{M-1,n}$$

Substitute (30) and (32) into Equation (11'), which has not as yet been used, and solve the resulting equation for $t_{M,n}$ to get

$$t_{M,n} = \frac{t_{M-1,n-1} + Q\gamma - P\alpha_{M-1,n}}{Q + P\beta_{M-1,n} - Q\delta} \quad (34)$$

The procedure for computing the $t_{i,n}$ can now be summarized as follows:

Step 1: Taking cognizance of Equations (19), set $n = 2$ and use Equations (27) and (28) to compute $\alpha_{1,n}$ and $\beta_{1,n}$, then (22) and (23) to compute successively $\alpha_{2,n}$ and $\beta_{2,n}$; $\alpha_{3,n}$ and $\beta_{3,n}$; ...; $\alpha_{M-1,n}$ and $\beta_{M-1,n}$. Equations (33) will then give γ and δ , and Equation (34) $t_{M,n}$, after which Equation (20) with i successively equated to $M-1, M-2, \dots, 2, 1$ will give $t_{M-1,n}; t_{M-2,n}; \dots; t_{2,n}; t_{1,n}$ -- all for $n = 2$. At this point all the $t_{i,n}$ along the $n = 2$ gridline are known, including the $t_{i,n}$ at the phantom grid points (1,2) and (M,2). **Step 2:** Set $n = 3$ and repeat all of the foregoing calculations with the following difference: Whenever a value of $t_{i,n-1}$ is needed, take it from the results of Step 1, rather than from Equations (19). **Step 3:** Set $n = 4, 5, \dots$ successively, and for each n repeat the calculations in Step 1, using the results obtained for the preceding n whenever a value of $t_{i,n-1}$ is needed.

Fairly straightforward numerical experimentation can be used to determine the optimum grid-line spacings Δx and Δy -- optimum in the sense that they are sufficiently small to give accurate results, but not so small as to require excessive calculations.

III. STRESS ANALYSIS

In this section we analyze the plane stress model of Figure 3 for the σ_r and σ_t stresses produced at any time τ in the lead, the glass, and the base annulus by any given temperature distribution $T(r,\tau)$ in the glass, the spatially constant temperature $T(a,\tau)$ in the lead, and the spatially constant

temperature $T(b, \tau)$ in the base, assuming the system to have been stress-free at the uniform temperature T_0 . If the system was not stress-free at the uniform temperature T_0 , then the computed σ_r and σ_t will represent the changes of stress occurring as a result of the change in temperature from the uniform value T_0 to the distributions described above.

It will be convenient to introduce the following short-hand notation:

$$\theta(r, \tau) = T(r, \tau) - T_0 \quad (35)$$

Also, $u(r, \tau)$ will denote the radial displacements, $\epsilon_r(r, \tau)$ and $\epsilon_t(r, \tau)$ the radial and transverse strains. The corresponding normal stresses $\sigma_r(r, \tau)$ and $\sigma_t(r, \tau)$ have already been introduced and illustrated in Figure 3. E , ν and α , without subscripts, will be the general symbols for Young's modulus, Poisson's ratio and thermal expansion coefficient for any of the three components of the model shown in Figure 3. When dealing specifically with the glass we shall add the subscript g to these symbols, and when dealing with the lead or base the subscript k . The spatially constant values of θ in the lead and in the base will be denoted by θ_a and θ_b , respectively; that is,

$$\begin{aligned} \theta_a &= \theta(a, \tau) = T(a, \tau) - T_0 \\ \theta_b &= \theta(b, \tau) = T(b, \tau) - T_0 \end{aligned} \quad (36)$$

A. Basic Equations.- For each component of the Figure 3 model we have the following set of basic equations governing the distribution of σ_r , σ_t , ϵ_r , ϵ_t and u at any time τ :

$$\frac{\partial \sigma_r}{\partial r} + \frac{\sigma_r - \sigma_t}{r} = 0 \quad (37)$$

$$\epsilon_r - \alpha \theta = \frac{1}{E} (\sigma_r - \nu \sigma_t) \quad (38)$$

$$\epsilon_t - \alpha \theta = \frac{1}{E} (\sigma_t - \nu \sigma_r)$$

$$\epsilon_r = \frac{\partial u}{\partial r} \quad (39)$$

$$\epsilon_t = \frac{u}{r}$$

Equation (37) is the equation of equilibrium for the element shown on the right side of Figure 3, Equations (38) are the stress-strain-temperature relations for an isotropic material in plane stress, and (39) are the strain-displacement relations. These equations can be combined to yield a differential equation for $u(r, \tau)$ alone. It is

$$\frac{\partial^2 u}{\partial r^2} + \frac{1}{r} \frac{\partial u}{\partial r} - \frac{u}{r^2} = (1 + \nu) \alpha \frac{\partial \theta}{\partial r} \quad (40)$$

For the lead, in which θ is spatially constant at the value θ_a , $\partial \theta / \partial r = 0$, and u must be regular as $r \rightarrow 0$, Equation (40) then has the solution

$$u = (1 + \nu_k) \alpha_k \theta_a \frac{r}{2} + B_1 r \quad (41)$$

where B_1 is an as-yet-undetermined integration constant. These displacements substituted into (39) will give the strains, and those strains substituted into the inverted form of Equations (38) will give the stresses.

The result for σ_r in particular is

$$\sigma_r = \frac{E_k}{1 - \nu_k} \left[B_1 - \frac{1}{2} \alpha_k \theta_a (1 - \nu_k) \right] \quad (42)$$

The displacement and radial stress in the lead at the lead-glass interface ($r = a$) are therefore

$$u(a, r) = (1 + \nu_k) \alpha_k \theta \frac{a}{2} + B_1 a \quad (43)$$

$$\sigma_r(a, r) = \frac{E_k}{1 - \nu_k} \left[B_1 - \frac{1}{2} \alpha_k \theta a (1 - \nu_k) \right] \quad (44)$$

For the base annulus, in which θ is spatially constant at the value θ_b , $\partial\theta/\partial r$ is again zero, and Equation (40) has the solution

$$u = (1 + \nu_k) \alpha_k \theta_b \frac{r}{2} + D_1 r + \frac{D_2}{r} \quad (45)$$

where D_1 and D_2 are integration constants. This leads to

$$\sigma_r = \frac{E_k}{1 - \nu_k} \left[-\frac{1 - \nu_k^2}{2} \alpha_k \theta_b + (1 + \nu_k) D_1 - (1 - \nu_k) \frac{D_2}{r^2} \right] \quad (46)$$

The boundary condition $\sigma_r = 0$ at $r = c$ gives

$$D_2 = \frac{c^2}{1 - \nu_k} \left[(1 + \nu_k) D_1 - \frac{1 - \nu_k^2}{2} \alpha_k \theta_b \right] \quad (47)$$

With Equation (47) used to eliminate D_2 in (45) and (46), those equations yield the following displacement and radial stress at the glass-base interface ($r = b$):

$$u(b, r) = \frac{1 + \nu_k}{2} \alpha_k \theta_b \frac{b^2 - c^2}{b} + D_1 b \left[1 + \frac{c^2 (1 + \nu_k)}{b^2 (1 - \nu_k)} \right] \quad (48)$$

$$\sigma_r(b, r) = E_k \left(1 - \frac{c^2}{b^2} \right) \left(\frac{D_1}{1 - \nu_k} - \frac{\alpha_k \theta_b}{2} \right) \quad (49)$$

Finally, in the glass, Equation (40) has the solution

$$u = \frac{(1+\nu_g)\alpha_g}{r} \int_a^r \theta r' dr' + C_1 r + \frac{C_2}{r} \quad (50)$$

where C_1 and C_2 are integration constants, r' is a dummy variable representing r , and $\theta = \theta(r', \tau)$. These displacements lead to the following stresses:

$$\sigma_r = E_g \left[-\frac{\alpha_g}{r^2} \int_a^r \theta r' dr' + \frac{C_1}{1-\nu_g} - \frac{C_2}{(1+\nu_g)r^2} \right] \quad (51)$$

$$\sigma_t = E_g \left[-\alpha_g \theta(r, \tau) + \frac{\alpha_g}{r^2} \int_a^r \theta r' dr' + \frac{C_1}{1-\nu_g} + \frac{C_2}{(1+\nu_g)r^2} \right] \quad (52)$$

where, in any integrand, $\theta = \theta(r', \tau)$. At the interfaces $r = a$ and $r = b$ in particular, Equations (50) and (51) give the following displacements and radial stresses:

$$u(a, \tau) = C_1 a + \frac{C_2}{a} \quad (53)$$

$$u(b, \tau) = \frac{(1+\nu_g)\alpha_g}{b} \int_a^b \theta r' dr' + C_1 b + \frac{C_2}{b} \quad (54)$$

$$\sigma_r(a, \tau) = E_g \left[\frac{C_1}{1-\nu_g} - \frac{C_2}{(1+\nu_g)a^2} \right] \quad (55)$$

$$\sigma_r(b, \tau) = E_g \left[-\frac{\alpha_g}{b^2} \int_a^b \theta r' dr' + \frac{C_1}{1-\nu_g} - \frac{C_2}{(1+\nu_g)b^2} \right] \quad (56)$$

Thus, the stresses and displacements in all three components of the model in Figure 3 have been determined to within four constants: B_1 , C_1 , C_2 and D_1 . These constants can be evaluated in a straightforward way from four continuity conditions: Continuity of radial displacement u and of radial stress σ_r at each of the two interfaces, $r=a$ and $r=b$. These four continuity conditions will lead to four simultaneous equations that can be solved for B_1 , C_1 , C_2 and D_1 . The four equations are omitted here for the sake of brevity; they will be presented later in a dimensionless form.

B. Glass Stress Equations in Dimensionless Form.— We note that

$$\theta \equiv (T_\infty - T_0) \cdot (1 - t) \quad (57)$$

where t is the dimensionless temperature parameter defined earlier (Equation (8)). Substituting this expression for θ into Equations (51) and (52) and dividing through by appropriate constants, we can convert these equations to the form

$$S_r = -\frac{\alpha_g}{\alpha_k} \frac{W(x,y)}{x^2} + \frac{\bar{C}_1}{1-\nu_g} - \frac{\bar{C}_2}{(1+\nu_g)x^2} \quad (58)$$

$$S_t = \frac{\alpha_g}{\alpha_k} \left[t - 1 + \frac{W(x,y)}{x^2} \right] + \frac{\bar{C}_1}{1-\nu_g} - \frac{\bar{C}_2}{(1-\nu_g)x^2} \quad (59)$$

where

$$S_r \equiv \frac{\sigma_r}{(T_\infty - T_0) E_g \alpha_k} \quad S_t \equiv \frac{\sigma_t}{(T_\infty - T_0) E_g \alpha_k} \quad (60)$$

are dimensionless measures of σ_r and σ_t ;

$$\bar{C}_1 \equiv \frac{C_1}{(T_\infty - T_0) \alpha_k} \quad \bar{C}_2 \equiv \frac{C_2}{(T_\infty - T_0) \alpha_k a^2} \quad (61)$$

are dimensionless measures of C_1 and C_2 ; x and y are the dimensionless radial and time coordinates defined by Equations (6) and (7); and

$$W(x,y) \equiv \int_1^x [1 - t(x',y)] x' dx' \quad (62)$$

with x' a dummy variable representing x , and t henceforth regarded as a function of x and y ; i.e., $t = t(x,y)$.

The four simultaneous equations referred to earlier, which are to be solved for the four integration constants, can also be put into dimensionless form, with the following result:

$$\begin{aligned} \frac{\bar{C}_1}{1-\nu_g} - \frac{\bar{C}_2}{(1+\nu_g)(b/a)^2} + \frac{\bar{D}_1}{1-\nu_k} \frac{E_k}{E_g} [(c/b)^2 - 1] \\ = \frac{1}{2} \frac{E_k}{E_g} [(c/b)^2 - 1](1-t_b) + \frac{\alpha_g W(b/a,y)}{\alpha_k (b/a)^2} \end{aligned} \quad (63)$$

$$\frac{\bar{C}_1}{1-\nu_g} - \frac{\bar{C}_2}{1+\nu_g} - \frac{\bar{B}_1}{1-\nu_k} \frac{E_k}{E_g} = - \frac{E_k}{E_g} \frac{1-t_a}{2} \quad (64)$$

$$\begin{aligned} \bar{C}_1 + \frac{\bar{C}_2}{(b/a)^2} - \bar{D}_1 \left(1 + \frac{c^2}{b^2} \frac{1+\nu_k}{1-\nu_k} \right) \\ = \frac{1}{2} (1+\nu_k) (t_b - 1) \left(\frac{c^2}{b^2} - 1 \right) - \frac{\alpha_g (1+\nu_g) W(b/a, y)}{\alpha_k (b/a)^2} \end{aligned} \quad (65)$$

$$\bar{C}_1 + \bar{C}_2 - \bar{B}_1 = \frac{1}{2} (1+\nu_k) (1-t_a) \quad (66)$$

where

$$t_a \equiv [t(x, y)]_{x=1} = t(1, y) \quad (67)$$

$$t_b \equiv [t(x, y)]_{x=b/a} = t(b/a, y)$$

$$\bar{B}_1 \equiv \frac{B_1}{(T_\infty - T_0) \alpha_k} \quad (68)$$

$$\bar{D}_1 \equiv \frac{D_1}{(T_\infty - T_0) \alpha_k}$$

Equations (63), (64), (65) and (66) express the following continuity conditions, respectively: (a) radial stress continuity at $r=b$; (b) radial stress continuity at $r=a$; (c) radial displacement continuity at $r=b$; and (d) radial displacement continuity at $r=a$. The simultaneous solution of (63) through (66) will give the values of \bar{C}_1 and \bar{C}_2 needed in Equations (58) and (59).

C. The Limiting Case $c \rightarrow \infty$.— The limiting case in which the outer radius c of the base annulus becomes very large in comparison with the inner radius b can be handled as follows: Solve Equation (65) for \bar{D}_1 and

(66) for \bar{B}_1 and use the results to eliminate \bar{D}_1 and \bar{B}_1 in (63) and (64). Equations (63) and (64) will then constitute two equations in two unknowns \bar{C}_1 and \bar{C}_2 . If b/c is then allowed to approach zero in those two equations, they reduce to

$$\begin{aligned} \bar{C}_1 \left(\frac{1}{1-\nu_g} + \frac{E_k}{E_g} \frac{1}{1+\nu_k} \right) - \bar{C}_2 \left(\frac{1}{1+\nu_g} - \frac{E_k}{E_g} \frac{1}{1+\nu_k} \right) \frac{a^2}{b^2} \\ = \frac{\alpha_g}{\alpha_k} \left(1 - \frac{E_k}{E_g} \frac{1+\nu_g}{1+\nu_k} \right) \frac{a^2}{b^2} W(b/a, y) \\ - \frac{E_k}{E_g} \frac{1}{1+\nu_k} (1-t_b) \end{aligned} \quad (69)$$

$$\bar{C}_1 \left(\frac{1}{1-\nu_g} + \frac{E_k}{E_g} \frac{1}{1-\nu_k} \right) - \bar{C}_2 \left(\frac{1}{1+\nu_g} + \frac{E_k}{E_g} \frac{1}{1-\nu_k} \right) = \frac{E_k}{E_g} \frac{t_a-1}{1-\nu_k} \quad (70)$$

and these two equations are to be solved simultaneously for the values of \bar{C}_1 and \bar{C}_2 needed in Equations (58) and (59).

D. Numerical Evaluation of Stresses in the Glass.- By setting x equal to x_2, x_3, \dots, x_{M-1} in Equations (58) and (59), one can for any given y obtain the values of S_r and S_t at all of the radial stations $i = 2, 3, \dots, M-1$ ($x = 1, 1 + \Delta x, 1 + 2\Delta x, \dots, b/a$) in the glass, including the two interface stations ($i = 2$ and $i = M-1$). The integrals $W(x_i, y)$ called for in Equations (58) and (59) are, in accordance with (62), defined by

$$W(x_i, y) = \int_1^{x_i} f(x, y) dx \quad (71)$$

where $f(x,y) \equiv 1 - t(x,y)$. They can be evaluated numerically with the help of the following integration formula for the integral of $f(x,y)$ over one grid division:

$$W_i \equiv \int_{x_{i-1}}^{x_i} f(x,y) dx \approx \frac{\Delta x}{24} (-f_{i-2} + 13f_{i-1} + 13f_i - f_{i+1}) \quad (72)$$

where $i \geq 3$ and

$$f_{i-2} \equiv f(x_{i-2}, y), \quad f_{i-1} \equiv f(x_{i-1}, y), \quad \text{etc.} \quad (73)$$

The numerical integration formula (72) is obtained by passing a cubic equation through the ordinates f_{i-2} , f_{i-1} , f_i and f_{i+1} . The $W(x_i, y)$ can be expressed in terms of the W_i as follows:

$$\begin{aligned} W(x_2, y) &= 0 \\ W(x_3, y) &= W_3 \\ W(x_4, y) &= W_3 + W_4 \\ &\vdots \\ &\vdots \\ W(x_i, y) &= \sum_{j=3}^i W_j \end{aligned} \quad (74)$$

Alternatively,

$$\begin{aligned} W(x_2, y) &= 0 \\ W(x_1, y) &= W(x_{i-1}, y) + W_i \quad (i > 2) \end{aligned} \quad (75)$$

For the special case in which the temperature throughout the package is uniform at T_∞ , the temperature parameter t (also t_a and t_b) is identically zero. Then $f(x,y)$ becomes 1 and Equation (71) reduces to

$$W(x_i, y) = x_i - 1 \quad (76)$$

At the lead-glass interface ($x_1 = x_2 = 1$) in particular, we then have

$$W(x_1, y) = W(x_2, y) = W(1, y) = 0 \quad (77)$$

and at the glass-base interface ($x_1 = x_{M-1} = b/a$),

$$W(x_1, y) = W(x_{M-1}, y) = W(b/a, y) = (b/a) - 1 \quad (78)$$

IV. COMPUTER PROGRAM

An APL computer program, ANN, that calculates the dimensionless temperatures and the stresses in the glass at successive dimensionless times after insertion of the package into the thermal shock test fluid, is given in this section, in the pages that come after the text. The program computes dimensionless temperature and stresses at the grid stations $i = 2, 3, \dots, M-1$ of Figure 4 for the dimensionless times corresponding to the grid stations $n = 2, 3, 4, \dots$ ($y = \Delta y, 2\Delta y, 3\Delta y, \dots$). The program is based on the analyses in Sections II and III.

As explained in the first thirteen lines of the program, before calling on ANN one must assign numerical values to certain APL variables. These variables are listed below along with their meanings.

APL Variable	Meaning
ΔY	Δy
YMAX	Value of y at which calculations should stop
NSEGS	Number of radial segments in glass annulus; equals M-2 (see Figure 4)
A	A (see Equations (1))
B	B (see Equations (1))
C	C (see Equations (1))
D	D (see Equations (1))
NUG	ν_g
NUM	ν_k
ALGM	α_g / α_k
EGM	E_g / E_k
BA	b/a
CASE	Assign to CASE the value 1 if c/a is finite, 2 if c/a is infinite
CA	c/a (not used if CASE = 2)
PRINT	Assign to PRINT the value 1 if only interface results are to be printed, and the value 2 if results for all the glass stations are to be printed

The output will repeat some of the numerical input data, identified by words rather than symbols, then give the computed temperatures and stresses at successive times. If PRINT has been pre-assigned the value 1, the output data will be for the interface locations only (lead-glass, then

glass-base); if 2 the output will be for all stations in the glass, starting with the lead-glass interface. The APL symbols appearing in the output are listed below along with their meanings.

APL Output Symbol	Meaning
X	x at $l = 2, 3, \dots, M-1$
TIME	$y (= \tau k_g / \rho_g c_g a^2)$
TEMP	$1 - t (= [T(x,y) - T_o] / [T_\infty - T_o])$
TRANSVERSE STRESS	$S_t (= \frac{\sigma_t}{(T_\infty - T_o) E_g \alpha_k})$
RADIAL STRESS	$S_r (= \frac{\sigma_r}{(T_\infty - T_o) E_g \alpha_k})$
MAX	Largest number in a preceding line of output
MIN	Smallest number in a preceding line of output

When YMAX has been reached, a terminal message will ask DO YOU WANT TO GO FURTHER? and give instructions for terminating or for increasing YMAX and continuing the calculations further into time.

Following the program are the inputs and outputs of sample calculations for a test fluid and package with the following properties:

$$\bar{h} = 4.051 \times 10^{-4} \text{ Btu/in}^2\text{-sec-}^\circ\text{F} \quad (\text{water-to-Kovar heat transfer coefficient})$$

$$a = 0.009 \text{ in.}$$

$$b = 0.02175 \text{ in.}$$

$$\begin{aligned}
c &= 0.08 \text{ in.} \\
A_o &= 0.0115925 \text{ in.}^2 \\
A_b &= 4.2874 \text{ in.}^2 \\
V_l &= 0.000075068 \text{ in.}^3 \\
V_b &= 0.154346 \text{ in.}^3 \\
A_2 &= 0.002262 \text{ in.}^2 \\
A_1 &= 0.005466 \text{ in.}^2 \\
N &= 48 \text{ (number of leads)} \\
k_g &= 1.366 \times 10^{-5} \text{ Btu/sec-in-}^\circ\text{F} \\
\rho_g &= 0.082 \text{ lb/in.}^3 \\
c_g &= 0.23 \text{ Btu/lb-}^\circ\text{F} \\
\rho_k &= 0.302 \text{ lb/in.}^3 \\
c_k &= 0.105 \text{ Btu/lb-}^\circ\text{F} \\
v_g &= 0.22 \\
\alpha_g &= 2.56 \times 10^{-6}/^\circ\text{F} \\
E_g &= 8.2 \times 10^6 \text{ lb/in.}^2 \\
v_k &= 0.3 \\
\alpha_k &= 3.25 \times 10^{-6}/^\circ\text{F} = 5.85 \times 10^{-6}/^\circ\text{C} \\
E_k &= 20 \times 10^6 \text{ lb/in.}^2
\end{aligned}$$

leading to

$$\begin{aligned}
A &= 1.36785 && \text{(APL variable: A)} \\
B &= 6.19975 && \text{(APL variable: B)} \\
C &= 4.36151 && \text{(APL variable: C)} \\
D &= 109.89971 && \text{(APL variable: D)}
\end{aligned}$$

v_g	= 0.22	(APL variable: NUG)
v_k	= 0.3	(APL variable: NUM)
α_g/α_k	= 0.78769	(APL variable: ALGM)
E_g/E_k	= 0.41	(APL variable: EGM)
b/a	= 2.4167	(APL variable: BA)
c/a	= 8.88889	(APL variable: CA)
c/b	= 3.6781	

Inasmuch as c/a is finite, the APL variable CASE was assigned the value 1 by typing CASE+1. NSEGS was taken as 5 and ΔY as 0.2 (trial calculations showed that they led to a sufficiently fine grid).

In order to demonstrate both types of output capability, PRINT was assigned the value 1, leading to output at the interface locations only, then in a second calculation the value 2, leading to output at all the glass stations. In the first calculation YMAX was set equal to 6, then increased to 10; in the second YMAX was taken as 0.4.

The first calculation shows that S_r at the lead-glass interface reaches an extremum value of -0.2459 (see underlined number in the line of output for TIME = 6.4). This result will be used in the illustrative application of the next section.

APL PROGRAM

```

9 81111
[1] A THIS APL PROGRAM COMPUTES TEMPERATURES AND STRESSES AS FUNCTIONS OF TIME IN ANHULUS OF GLASS LEAD-THROUGH SEALS
[2] A OF MICROCIRCUIT PACKAGES UNDERGOING THERMAL SHOCK. X IS DIMENSIONLESS RADIAL COORDINATE, Y OR TIME IS
[3] A DIMENSIONLESS TIME COORDINATE. BEFORE CALLING ON PROGRAM, ASSIGN VALUES TO: AT; YMAX; NSEGS (NUMBER OF
[4] A RADIAL SEGMENTS IN GLASS ANHULUS); A,B,C,D (DIMENSIONLESS COEFFICIENTS IN BOUNDARY CONDITION EQUATIONS);
[5] A HUG AND HUM (POISSON RATIOS OF GLASS AND METAL, RESPECTIVELY); ALGM (RATIO OF THERMAL EXPANSION COEFFICIENTS,
[6] A GLASS/METAL); EGM (RATIO OF YOUNG'S MODULI, GLASS/METAL); RA (OUTER GLASS RADIUS DIVIDED BY LEAD-WIRE RADIUS)
[7] A AND CASE (-2 IF SURROUNDING METAL RADIUS IS INFINITE, OTHERWISE 1). ALSO, IF CASE IS 1, ASSIGN A VALUE TO
[8] A CA (OUTER RADIUS OF SURROUNDING METAL DIVIDED BY LEAD-WIRE RADIUS). INITIAL (T=0) TEMPERATURES AND STRESSES IN
[9] A ARE ZERO. MAIN OUTPUT WILL CONSIST OF DIMENSIONLESS TEMPERATURES, TRANSVERSE STRESSES, AND RADIAL STRESSES IN
[10] A GLASS AS FUNCTIONS OF RADIAL POSITION AND TIME. PRESPECIF) PRINT AS 1 IF OUTPUT IS NEEDED ONLY AT INNER AND
[11] A OUTER RADII, OR AS 2 IF OUTPUT IS NEEDED AT ALL RADIAL STATIONS. IN EITHER EVENT, THE OUTPUT SEQUENCE WILL
[12] A BE FROM INNER TO OUTER RADIUS. SUMMARY OF VARIABLES TO WHICH VALUES MUST BE PRE-ASSIGNED:
[13] A AT, YMAX, NSEGS, A, B, C, D, HUG, HUM, ALGM, EGM, RA, CASE, CA (IF CASE IS 1) PRINT
[14] . . . . . INPUT.
[15] . . . . .
[16] . . . . .
[17] 'RATIO OF OUTER GLASS RADIUS TO LEAD-WIRE RADIUS IS 'JBA
[18] -LJICASE=I
[19] 'RATIO OF OUTER METAL RADIUS TO LEAD-WIRE RADIUS IS INFINITE'
[20] +L2
[21] L1:'RATIO OF OUTER METAL RADIUS TO LEAD-WIRE RADIUS IS 'JCA
[22] L2:'RATIO OF THERMAL EXPANSION COEFFS (GLASS/METAL) IS 'JALOM
[23] L3:'RATIO OF YOUNG'S MODULI (GLASS/METAL) IS 'JEGM
[24] 'POISSON RATIOS ARE 'JHUG', FOR GLASS AND 'JHUM', FOR METAL'
[25] 'BOUNDARY CONDITION COEFFS A,B,C,D ARE 'JAB,C,D
[26] 'TIME INCREMENT AT IS 'JAY'. GLASS ANHULUS IS DIVIDED INTO 'JNSEGS' RADIAL SEGMENTS.
[27] EMO+EGM
[28] AX*(HA-1)-NSEGS
[29] Y1*(-1 13 13 -1)HX+24
[30] H+NSEGS+3
[31] X*(A+Y1M)+-2AX
[32] 'RADIAL STATIONS IN GLASS ARE AT X = 'J1+JHX
[33] . . . . .
[34] . . . . . RESULTS (AT FIRST AND LAST STATIONS IF ONLY TWO NOS. ARE GIVEN, AT ALL STATIONS OTHERWISE).
[35] . . . . . TEMPERATURE CALCULATION STARTS HERE
[36] F=AT-2EYAX
[37] G+IAXA+YB
[38] H+(AY-AX)-AY+2HX
[39] J+A+2HAY-AH
[40] K+(AT-AX)+AY-2HX
[41] L+A-2EDAX
[42] P+JCAAY-D
[43] DEN1+FI+H[2]-K[2]
[44] AALPB+YRIDOP+SR+SY+M2I
[45] FFI+(-G-FIX+H[2])+DEN1
[46] 0+1
[47] L1:RA[1]+(TPR1OR[2]X1-FIAX+H[2])+DEN1
[48] I+2
[49] I+2
[50] L4:DEN2+J-PP[I-1]H[I]
[51] AA[I]+((TPR1OR[I]IAX)+AA[I-1]H[I])+DEN2
[52] PP[I]+H[I]+DEN2
[53] -LSH1IEM-1
[54] I+I+1

```



```

[55] +L4
[56] L5:OAMMA+AA[M-2]+BB[M-2]XAA[M-1]
[57] DELTAA[B[M-2]BB[M-1]
[58] Y[M]+(TPROR[M-1]+(LXGAMMA)-PRAA[M-1])*(LXI-DELTA)+PBB[M-1]
[59] X[M-1]
[60] L6:T[I]+AA[I]+BB[I]X[I+1]
[61] +L7X[I+1]
[62] X[I-1]
[63] +L6
[64] L7:DKB+X[I-1]
[65] AREA+MFO
[66] I+3
[67] L8:OFA[I]+AREA[I-1]+V10K0[(I-2),(I-1),I,I+1]
[68] +L9X[I+M-1]
[69] I+1+1
[70] +L8
[71] A !PRESS CALCULATION STARTS HERE
[72] L9:+L10X1CASE#2
[73] CR+CA+KA
[74] V2*(-1-NUG)+(-(BA2)X1+NUG)+0,(EMG-1-NUM)X1+CB2
[75] V3*(-1-NUG)+(-1+NUG)+(EMG+NUM-1)+0
[76] V4*(+1+(-BA2)+0)+(-1+CB2)X(1+NUM)+(1-NUM)
[77] V5+ 1 1 -1 0
[78] RT+4/0.5XEMGAT[2]-1
[79] RT11+(0.5XEMG(-1+CB2)X1-TCM-1)+ALGMXAREA[M-1]+BA2
[80] RT13+(0.5X(1+NUM)X(TCM-1)+(-1+CB2)-ALGMX(1+NUM)XAREA[M-1]+BA2
[81] RT4)+0.5X(1+NUM)X1-T[2]
[82] MAP 4 4 PV2+V3+V4+V5
[83] +L11
[84] L10:V2+((-1-NUG)+EMG+1+NUM),(EMG+1+NUM)+(-1+NUG)+BA2
[85] V3+((-1-NUG)+EMG-1-NUM)+(-1+NUG)+EMG+1-NUM
[86] V4+2/EMG(T[2]-1)+1-NUM
[87] RT11+((ALGMXAREA[M-1]+BA2)X1-EMG(1+NUM)+1+NUM)+EMG(T[CM-1]-1)+1+NUM
[88] MAP 2 2 PV2+V3
[89] L11:CON+(RTBMA)[I 2]+(1-NUG),1+NUG
[90] I+2
[91] ST+CON[1]+(CON[2]+X2)+ALGMX(T-1)+AREA+X2
[92] SA+CON[1]+(CON[2]+ALGMXAREA)+X2
[93] +(PRINT#),PRINT#2)/L2+L3
[94] L12:TIME = 'IGRAY',TEMP = '(1-T)[2,M-1]', TRANSVERSE STRESS = 'JBT[2,M-1]', RADIAL STRESS = 'JBR[2,M-1]
[95] . . .
[96] +L14
[97] L13:TIME = 'IGRAY
[98] TEMP = '14-14-T
[99] TRANSVERSE STRESS = '14-14ST
[100] MAX = '1/14-14ST', MIN = '1/14-14ST
[101] RADIAL STRESS = '14-14R
[102] MAX = '1/14-14SR', MIN = '1/14-14SR
[103] . . .
[104] L14:+L16X1(GRAY)YMAX
[105] L15:OLG+1
[106] TPRID+T
[107] +L3
[108] L16:GO YOU WANT TO GO FURTHER? IF NO, TYPE THE NUMBER ZERO; IF YES, TYPE THE NEW VALUE OF YMAX, THEN PRESS RETURN.
[109] SIGNAL+0
[110] +0X1SIGNAL=0
[111] YMAX+ SIGNAL
[112] +L15

```

SAMPLE CALCULATIONS

AY+2
 YMAX+6
 NSEGS+5

 A+1.36785
 B+6.19975
 C+4.36151
 D+109.89971
 NUG+22
 NUM+3
 ALGHT+.78769
 EGM+.41
 BA+2.4167
 CASE+1
 CA+8.88889
 PRINT+1

ANN

INPUT

RATIO OF OUTER GLASS RADIUS TO LEAD-WIRE RADIUS IS 2.417
 RATIO OF OUTER METAL RADIUS TO LEAD-WIRE RADIUS IS 8.889
 RATIO OF THERMAL EXPANSION COEFFS (GLASS/METAL) IS 0.7877
 RATIO OF YOUNGS MODULI (GLASS/METAL) IS 0.41
 POISSON RATIOS ARE 0.22 FOR GLASS AND 0.3 FOR METAL
 BOUNDARY CONDITION COEFFS A,P,C,D ARE 1.368 6.2 4.362 109.9
 TIME INCREMENT ΔY IS 0.2 . GLASS ANNULUS IS DIVIDED INTO 5 RADIAL SEGMENTS
 RADIAL STATIONS IN GLASS ARE AT X = 1 1.283 1.567 1.85 2.133 2.417

RESULTS (AT FIRST AND LAST STATIONS IF ONLY TWO NOS. ARE GIVEN, AT ALL STATIONS OTHERWISE)

TIME = 0.2 TEMP = 0.03877 0.007855 TRANSVERSE STRESS = $\bar{0.003351}$ 0.003805 RADIAL STRESS = $\bar{0.02285}$ $\bar{0.005647}$
 TIME = 0.4 TEMP = 0.07447 0.01565 TRANSVERSE STRESS = $\bar{0.006582}$ 0.008039 RADIAL STRESS = $\bar{0.04417}$ $\bar{0.01246}$
 TIME = 0.6 TEMP = 0.1076 0.0234 TRANSVERSE STRESS = $\bar{0.009557}$ 0.01234 RADIAL STRESS = $\bar{0.06392}$ $\bar{0.01948}$
 TIME = 0.8 TEMP = 0.1386 0.03111 TRANSVERSE STRESS = $\bar{0.01223}$ 0.01655 RADIAL STRESS = $\bar{0.08214}$ $\bar{0.02628}$
 TIME = 1 TEMP = 0.1675 0.03878 TRANSVERSE STRESS = $\bar{0.01458}$ 0.02059 RADIAL STRESS = $\bar{0.0989}$ $\bar{0.03266}$

TIME = 1.2 TEMP = 0.1947 0.0464 TRANSVERSE STRESS = -0.01662 0.02444 RADIAL STRESS = -0.1143 -0.03856
 TIME = 1.4 TEMP = 0.2202 0.05398 TRANSVERSE STRESS = -0.01836 0.0281 RADIAL STRESS = -0.1284 -0.04396
 TIME = 1.6 TEMP = 0.2441 0.06152 TRANSVERSE STRESS = -0.01982 0.03155 RADIAL STRESS = -0.1413 -0.04886
 TIME = 1.8 TEMP = 0.2666 0.06901 TRANSVERSE STRESS = -0.02102 0.03482 RADIAL STRESS = -0.1531 -0.05329
 TIME = 2 TEMP = 0.2878 0.07646 TRANSVERSE STRESS = -0.02198 0.03791 RADIAL STRESS = -0.1639 -0.05727
 TIME = 2.2 TEMP = 0.3078 0.08386 TRANSVERSE STRESS = -0.02271 0.04083 RADIAL STRESS = -0.1737 -0.06084
 TIME = 2.4 TEMP = 0.3266 0.09121 TRANSVERSE STRESS = -0.02323 0.0436 RADIAL STRESS = -0.1826 -0.06402
 TIME = 2.6 TEMP = 0.3443 0.09852 TRANSVERSE STRESS = -0.02356 0.04622 RADIAL STRESS = -0.1906 -0.06685
 TIME = 2.8 TEMP = 0.361 0.1058 TRANSVERSE STRESS = -0.02372 0.0487 RADIAL STRESS = -0.198 -0.06934
 TIME = 3 TEMP = 0.3768 0.113 TRANSVERSE STRESS = -0.02371 0.05106 RADIAL STRESS = -0.2045 -0.07152
 TIME = 3.2 TEMP = 0.3917 0.1202 TRANSVERSE STRESS = -0.02355 0.05329 RADIAL STRESS = -0.2105 -0.07341
 TIME = 3.4 TEMP = 0.4058 0.1273 TRANSVERSE STRESS = -0.02325 0.05542 RADIAL STRESS = -0.2158 -0.07504
 TIME = 3.6 TEMP = 0.4192 0.1343 TRANSVERSE STRESS = -0.02282 0.05744 RADIAL STRESS = -0.2205 -0.07642
 TIME = 3.8 TEMP = 0.4318 0.1413 TRANSVERSE STRESS = -0.02227 0.05937 RADIAL STRESS = -0.2248 -0.07758
 TIME = 4 TEMP = 0.4438 0.1483 TRANSVERSE STRESS = -0.02161 0.06121 RADIAL STRESS = -0.2285 -0.07852
 TIME = 4.2 TEMP = 0.4552 0.1552 TRANSVERSE STRESS = -0.02086 0.06296 RADIAL STRESS = -0.2318 -0.07928
 TIME = 4.4 TEMP = 0.466 0.1621 TRANSVERSE STRESS = -0.02001 0.06463 RADIAL STRESS = -0.2346 -0.07985
 TIME = 4.6 TEMP = 0.4763 0.1689 TRANSVERSE STRESS = -0.01908 0.06623 RADIAL STRESS = -0.2371 -0.08025
 TIME = 4.8 TEMP = 0.4861 0.1757 TRANSVERSE STRESS = -0.01807 0.06776 RADIAL STRESS = -0.2392 -0.0805
 TIME = 5 TEMP = -0.4954 0.1824 TRANSVERSE STRESS = -0.01699 0.06923 RADIAL STRESS = -0.241 -0.08061
 TIME = 5.2 TEMP = 0.5043 0.1891 TRANSVERSE STRESS = -0.01584 0.07064 RADIAL STRESS = -0.2424 -0.08059
 TIME = 5.4 TEMP = 0.5128 0.1957 TRANSVERSE STRESS = -0.01464 0.07199 RADIAL STRESS = -0.2436 -0.08045
 TIME = 5.6 TEMP = 0.5209 0.2022 TRANSVERSE STRESS = -0.01339 0.07329 RADIAL STRESS = -0.2445 -0.0802

TIME = 5.8 TEMP = 0.5286 0.2087 TRANSVERSE STRESS = -0.01208 0.07454 RADIAL STRESS = -0.2452 -0.07984
 TIME = 6 TEMP = 0.5361 0.2152 TRANSVERSE STRESS = -0.01073 0.07574 RADIAL STRESS = -0.2456 -0.07939
 DO YOU WANT TO GO FURTHER? IF NO, TYPE THE NUMBER ZERO; IF YES, TYPE THE NEW VALUE OF YMAX, THEN PRESS RETURN.
 0:
 10
 TIME = 6.2 TEMP = 0.5432 0.2216 TRANSVERSE STRESS = -0.009345 0.0769 RADIAL STRESS = -0.2459 -0.07886
 TIME = 6.4 TEMP = 0.55 0.228 TRANSVERSE STRESS = -0.007922 0.07802 RADIAL STRESS = -0.2459 -0.07824
 TIME = 6.6 TEMP = 0.5565 0.2343 TRANSVERSE STRESS = -0.006465 0.0791 RADIAL STRESS = -0.2458 -0.07755
 TIME = 6.8 TEMP = 0.5628 0.2406 TRANSVERSE STRESS = -0.00498 0.08014 RADIAL STRESS = -0.2455 -0.0768
 TIME = 7 TEMP = 0.5689 0.2468 TRANSVERSE STRESS = -0.00347 0.08115 RADIAL STRESS = -0.2451 -0.07598
 TIME = 7.2 TEMP = 0.5747 0.253 TRANSVERSE STRESS = -0.001936 0.08213 RADIAL STRESS = -0.2445 -0.07511
 TIME = 7.4 TEMP = 0.5804 0.2591 TRANSVERSE STRESS = -0.000382 0.08308 RADIAL STRESS = -0.2438 -0.07419
 TIME = 7.6 TEMP = 0.5858 0.2652 TRANSVERSE STRESS = 0.00119 0.08401 RADIAL STRESS = -0.243 -0.07322
 TIME = 7.8 TEMP = 0.591 0.2712 TRANSVERSE STRESS = 0.002777 0.0849 RADIAL STRESS = -0.242 -0.0722
 TIME = 8 TEMP = 0.5961 0.2772 TRANSVERSE STRESS = 0.004378 0.08577 RADIAL STRESS = -0.241 -0.07115
 TIME = 8.2 TEMP = 0.601 0.2831 TRANSVERSE STRESS = 0.00599 0.08662 RADIAL STRESS = -0.2399 -0.07007
 TIME = 8.4 TEMP = 0.6058 0.289 TRANSVERSE STRESS = 0.007611 0.08745 RADIAL STRESS = -0.2387 -0.06895
 TIME = 8.6 TEMP = 0.6104 0.2948 TRANSVERSE STRESS = 0.009241 0.08825 RADIAL STRESS = -0.2374 -0.0678
 TIME = 8.8 TEMP = 0.6149 0.3006 TRANSVERSE STRESS = 0.01088 0.08904 RADIAL STRESS = -0.236 -0.06663
 TIME = 9 TEMP = 0.6193 0.3063 TRANSVERSE STRESS = 0.01252 0.0898 RADIAL STRESS = -0.2346 -0.06544
 TIME = 9.2 TEMP = 0.6235 0.312 TRANSVERSE STRESS = 0.01416 0.09055 RADIAL STRESS = -0.2332 -0.06422
 TIME = 9.4 TEMP = 0.6276 0.3177 TRANSVERSE STRESS = 0.01581 0.09129 RADIAL STRESS = -0.2316 -0.06299

TIME = 9.6 TEMP = 0.6317 0.3233 TRANSVERSE STRESS = 0.01746 0.092 RADIAL STRESS = -0.2301 -0.06174
 TIME = 9.8 TEMP = 0.6356 0.3289 TRANSVERSE STRESS = 0.0191 0.09271 RADIAL STRESS = -0.2285 -0.06047
 TIME = 10 TEMP = 0.6394 0.3344 TRANSVERSE STRESS = 0.02075 0.09339 RADIAL STRESS = -0.2268 -0.0592

DO YOU WANT TO GO FURTHER? IF NO, TYPE THE NUMBER ZERO; IF YES, TYPE THE NEW VALUE OF YMAX, THEN PRESS RETURN.
 0:

PRINT+2
 YMAX+.4
 ANN

INPUT

RATIO OF OUTER GLASS RADIUS TO LEAD-WIRE RADIUS IS 2.417
 RATIO OF OUTER METAL RADIUS TO LEAD-WIRE RADIUS IS 8.889
 RATIO OF THERMAL EXPANSION COEFFS (GLASS/METAL) IS 0.7877
 RATIO OF YOUNG'S MODULI (GLASS/METAL) IS 0.41
 POISSON RATIOS ARE 0.22 FOR GLASS AND 0.3 FOR METAL
 BOUNDARY CONDITION COEFFS A,P,C,D ARE 1.368 6.2 4.362 109.9
 TIME INCREMENT Δt IS 0.2. GLASS ANNULUS IS DIVIDED INTO 5 RADIAL SEGMENTS
 RADIAL STATIONS IN GLASS ARE AT X = 1 1.283 1.567 1.85 2.133 2.417

RESULTS (AT FIRST AND LAST STATIONS IF ONLY TWO NOS. ARE GIVEN, AT ALL STATIONS OTHERWISE)

TIME = 0.2
 TEMP = 0.03877 0.01911 0.01027 0.006677 0.006084 0.007855
 TRANSVERSE STRESS = -0.003351 0.006527 0.008913 0.008452 0.006659 0.003805
 MAX = 0.008913 MIN = -0.003351
 RADIAL STRESS = -0.02285 -0.01724 -0.01266 -0.009367 -0.007107 -0.005647
 MAX = -0.005647 MIN = -0.02285

TIME = 0.4
 TEMP = 0.07447 0.04281 0.02601 0.01779 0.01488 0.01565
 TRANSVERSE STRESS = -0.006582 0.008181 0.01323 0.01365 0.01162 0.008039
 MAX = 0.01365 MIN = -0.006582
 RADIAL STRESS = -0.04417 -0.03399 -0.02581 -0.01976 -0.01544 -0.01246
 MAX = -0.01246 MIN = -0.04417

DO YOU WANT TO GO FURTHER? IF NO, TYPE THE NUMBER ZERO; IF YES, TYPE THE NEW VALUE OF YMAX, THEN PRESS RETURN.
 0:

V. ILLUSTRATIVE APPLICATION

Let us assume that the package considered in the preceding section is subjected to level A of the MIL-STD-883B thermal shock test (Method 1011.2) and determine the maximum radial tensile stress developed at the lead-glass interface in the course of this test. (This is the stress that is most likely to create a gap between the lead and the glass if the bond between the two materials is poor.) The test fluids will be taken to be water at 100C and 0C, and the seal will be assumed to be stress-free at room temperature (20C).

We first take note of the extremum value of $S_r = -0.2459$ cited in the previous section for this package. The corresponding extremum value of the stress is

$$\begin{aligned}\sigma_r &= -0.2459 (T_\infty - T_0) E_g \alpha_k \\ &= -0.2459 (T_\infty - T_0) (8.2 \times 10^6) (5.85 \times 10^{-6}) \text{ psi/}^\circ\text{C} \\ &= -11.80 (T_\infty - T_0) \text{ psi/}^\circ\text{C}\end{aligned}$$

In the preconditioning step of the thermal shock test, the package at room temperature ($T_0 = 20\text{C}$) is immersed in the high-temperature fluid ($T_\infty = 100\text{C}$) and kept there long enough for the temperature to become virtually uniform at T_∞ . Therefore $T_\infty - T_0 = 80\text{C}$, and at some time during the package's dwell in the high-temperature fluid, an extremum lead-glass interface radial stress of

$$\sigma_r = -11.80 (80) = -944 \text{ psi} \quad (79)$$

is achieved. In subsequent steps, the package is transferred back and forth from the high- to the low-temperature baths after having been temperature-stabilized in each one. Therefore, in these subsequent steps $T_{\infty} - T_0$ will be -100C for the transfer from high to low, and +100C for the transfer from low to high. The corresponding changes of interface radial stress will be

$$\sigma_r = -11.80 (-100) = +1180 \text{ psi} \quad (80)$$

and

$$\sigma_r = -11.80 (100) = -1180 \text{ psi} \quad (81)$$

respectively.

The above are transient extremums of stress or change of stress that occur during the temperature stabilizations. We shall also need to know the change of stress that has taken place by the end of each step, that is, after the package temperature has become uniform at T_{∞} , the temperature of the bath in which it resides. In order to determine that quantity, we take note of the last paragraph of section IV, from which we find that

$$W(b/a, y) = (b/a) - 1 = 2.4167 - 1 = 1.4167$$

$$t_a = t_b = 0$$

With this information and other numerical data from Section IV substituted into them, Equations (63) to (66) become

$$1.2821 \bar{C}_1 - .14034 \bar{C}_2 + 43.653 \bar{D}_1 = 15.470$$

$$1.2821 \bar{C}_1 - .81967 \bar{C}_2 - 3.4843 \bar{B}_1 = -1.2195$$

$$\bar{C}_1 + .17122 \bar{C}_2 - 26.124 \bar{D}_1 = -8.3766$$

$$\bar{C}_1 + \bar{C}_2 - \bar{B}_1 = .65$$

Their solution is

$$\bar{C}_1 = 0.47065 \quad \bar{C}_2 = 0.56874 \quad \bar{B}_1 = 0.38939 \quad \bar{D}_1 = 0.34239$$

Substituting the \bar{C}_1 and \bar{C}_2 values into Equation (58), along with the values of the required material constants, and noting that $x = 1$ at the lead-glass interface, and that $W(1,y) = 0$ when the temperature is uniform (see Equation (73)), we get

$$S_r = 0 + \frac{0.47065}{.78} - \frac{0.56874}{(1.22)(1)^2} = .13722$$

as the stabilized value of S_r at the lead glass interface when the package is brought from an initial uniform temperature of T_o to a final uniform temperature of T_∞ . The corresponding stress change is

$$\begin{aligned} \sigma_r &= .13722 (T_\infty - T_o) E_g \alpha_k \\ &= .13722 (T_\infty - T_o) (8.2 \times 10^6) (5.85 \times 10^{-6}) \text{ psi/}^\circ\text{C} \\ &= 6.5824 (T_\infty - T_o) \text{ psi/}^\circ\text{C} \end{aligned}$$

In going from room temperature ($T_o = 20\text{C}$) to the high temperature bath ($T_\infty = 100\text{C}$), this gives

$$\sigma_r = 6.5824 (80) = + 527 \text{ psi} \quad (82)$$

In going from the high temperature bath ($T_o = 100\text{C}$) to the low temperature bath ($T_\infty = 0\text{C}$), it gives

$$\sigma_r = 6.5824 (-100) = - 658 \text{ psi} \quad (83)$$

And in going from the low temperature bath ($T_o = 0C$) to the high temperature bath ($T_{\infty} = 100C$), it gives

$$\sigma_r = 6.5824 (100) = + 658 \text{ psi} \quad (84)$$

In Equations (80) through (84) we have all the information needed in order to track the interface radial stress during the postulated thermal shock test. The details of the tracking are presented in Table 1 in which the units of σ_r and of $\Delta\sigma_r$ (change of stress) are psi, RT stands for room temperature (20C), HT for high temperature (100C), and LT for low temperature (0C). In reading Table 1, one should go entirely across one row before proceeding to the next row.

The results shown in Table 1 are very interesting and informative. Column 6 gives the steady state σ_r at the end of each step, i.e., after the temperature of the package has become uniform at the temperature of the bath that it is in. Those stresses are seen to be not very severe, alternating between 527 psi tension at the end of each high temperature dwell to 131 psi compression at the end of each low temperature dwell. However, the transient stresses occurring during the dwells, listed in Column 4, are seen to be much more severe, ranging from a maximum tension of 1707 psi to a maximum compression of 1311 psi. The transient tensile stress of 1707 psi is a rather significant stress for glass, and we note that it is developed in the thermal shock test of the very lowest level of severity (level A). This example tends to support the findings of Reference 24 and suggests that the thermal shock test should be used with caution. Too high a severity level could produce excessive transient

Table 1.- Tracking σ_r at Lead-Glass Interface

(1)	(2)	(3)	(4)	(5)	(6)
Step	σ_r at start of step	$\Delta\sigma_r$ extremum during step	σ_r at instant of $\Delta\sigma_r$ extremum (Col. 2 + Col. 3)	$\Delta\sigma_r$ at end of step	σ_r at end of step (Col. 2 + Col. 5)
RT to HT (preconditioning)	0 (seal assumed stress-free at RT)	-944 (Eq. 79)	-944	+527 (Eq. 82)	+527
HT to LT	+527	+1180 (Eq. 80)	+1707	-658 (Eq. 83)	-131
LT to HT	-131	-1180 (Eq. 81)	-1311	+658 (Eq. 84)	+527
HT to LT	+527	+1180	+1707	-658	-131
LT to HT	-131	-1180	-1311	+658	+527

Etc. (from the 4th row on, each row duplicates an earlier row)

tensions at the lead-glass interface, possibly creating gaps there during the test, even for well bonded seals. Furthermore, inasmuch as the excessive tensions are transient, those gaps might not be evident at the end of the test. Another interesting conclusion to be drawn from Table 1 is that the transient stress occurring during any step of the thermal shock test (Column 4) and the steady-state or final stress developed in that step (Column 6) can be of opposite sign.

APPENDIX A: MATERIAL PROPERTIES

In this appendix are compiled material property data that could be useful in connection with the formulas of the present report or that might be of general interest to stress analysts, designers, and screeners of microcircuit packages. The information has been gleaned from a variety of sources, including manufacturers' literature, certain standard handbooks, treatises, and monographs. Direct telephone contact with knowledgeable individuals was another valuable source of information.

The following list indicates the categories of materials covered, each in a section of its own: ADHESIVES, CERAMICS, FLUIDS, GLASSES, NICKEL-IRON ALLOYS, SOLDERS, and WIRES.

Unless other conditions are specified, it is to be understood that the data presented pertain to room temperature and standard atmospheric pressure conditions.

It should also be understood that, in the case of manufacturers' data, a more or less standard disclaimer usually applies, to the effect that although the data are believed to be reliable, the accuracy of the data is not guaranteed.

Because of the large amount of numerical data presented, it was not considered feasible to present it consistently in dual form (i.e., customary units and dual units). In order to assist the reader in making the conversion from one form to another, we list a few useful conversion equations:

Temperature

$$1^{\circ}\text{K} = 1^{\circ}\text{C} = 1.8^{\circ}\text{F} \quad 1^{\circ}\text{F} = \frac{5}{9}^{\circ}\text{C} = \frac{5}{9}^{\circ}\text{K}$$

Stress or Pressure

$$1 \text{ psi} = 6894.757 \text{ Pa} = 6894.757 \text{ N/m}^2 = .006894757 \text{ MN/m}^2$$

$$1 \text{ ksi} = 1000 \text{ psi}$$

$$1 \text{ GPa} = 145,038 \text{ psi} \quad 1 \text{ MPa} = 145.038 \text{ psi} \quad 1 \text{ Pa} = .000145038 \text{ psi}$$

Specific Heat

$$1 \text{ cal/g}^\circ\text{C} = 1 \text{ Btu/lb}^\circ\text{F} = 4184 \text{ J/kg}^\circ\text{K}$$

Thermal Conductivity

$$1 \text{ cal/cm}\cdot\text{s}\cdot^\circ\text{C} = 4.186 \text{ W/cm}\cdot^\circ\text{C} = 241.9 \text{ Btu/ft}\cdot\text{hr}\cdot^\circ\text{F} = 2903 \text{ Btu}\cdot\text{in/ft}^2\cdot\text{hr}\cdot^\circ\text{F}$$

Density

$$1 \text{ g/cm}^3 = 62.428 \text{ lb/ft}^3 = .03613 \text{ lb/in}^3$$

$$1 \text{ lb/ft}^3 = .01602 \text{ g/cm}^3$$

1. Adhesives

Here we present a compilation of material property data for a few adhesives of possible applicability to microelectronics. Much of the data presented is taken from company data sheets reproduced in "Investigation of the Application of Adhesives in Hybrid Integrated Circuits" (Report W2-683-TN04, U.S. Naval Undersea Center, June, 1972; abridgement available from Government-Industry Data Exchange Program, Corona, CA 91720 as GIDEP Report E151-1156); this report also contains some valuable qualitative information on adhesives. The rest of the data has come from additional company data sheets and brochures. The data presented do not reflect the considerable degree of scatter that may be present in measured shear strengths if pains are not taken to achieve uniformity of bond line thickness and filleting in the preparation of the test specimens. Some information on this type of scatter can be found in the report, "Organic Adhesives for Hybrid Microcircuits," by F.L. Perkins and J.J. Licari, Autonetics Div. of Rockwell International Corporation (3370 Miraloma Avenue, Anaheim, CA 92803), July 31, 1975, prepared under Contract NAS8-26384 for the George C. Marshall Space Flight Center, Alabama 35812.

"Ablefilm" and "Ablebond" Adhesives.- The following two tables give data on the "Ablefilm" and "Ablebond" adhesives manufactured by the Ablestick Laboratories (833 W. 182 St, Gardena, CA 90248). The "Ablefilm" adhesives are epoxy adhesives in film form. Those designated ECF518 and ECF535 contain fillers that make them electrically conductive.

Designation	Ablefilm 501	Ablefilm 507	Ablefilm 517	Ablefilm 517A	Ablefilm ECF518	Ablefilm ECF535	Ablefilm 550
Flatwire Tensile Strength, psi	6000	5600	5000	5000	5000		
Lap Shear Strength, psi	3700 3700 1800 1100 350	3600 3500 2200 820	2500 3000 800 500 400	2500 800	2400 2200 800 450 400	At R.T.: 2500 Au to Au, 3500 Al to Al	25C 6000 100C 2800 125C 1000 150C 300 on gold-plated steel
Lap Shear Strength, psi, after immersion in fluids for 7 or 14 days	7 days 3300 3550 3700 3500	14 days 3000					
Lap Shear Strength, psi, after 400 hrs @ 400F			500				
Lap Shear Strength, psi, after 15 days @ 165F and 100% RH					2200		
Lap Shear Strength, psi, after 20 days @ 185F and 100% RH							2300
Thermal Conductivity, Btu/ft-hr-°F					4.1		

Designation	Ablebond 71-1	Ablebond 606-1	Ablebond 761-6		Ablebond 798-1
Description	Polyimide paste, electrically conductive	Epoxy paste, electrically conductive	Epoxy paste, electrically conductive		Epoxy paste
Lap Shear Strength, psi	1000 to Au	1900 to Au 1500 to Al 1200 to Ag 1500 to Brass 800 to Cu 1200 to Solder	25C 150C 200C	1250 1500 700	>6400 to Au >6000 to Al
Lap Shear Strength, psi after 11 days @ 185F, 100% RH			to gold-plated stainless steel		>5700
Thermal Conductivity, Btu/ft·hr·°F	1.2				1.3 @ 250F

"Epo-Tek" Adhesives.- The table below gives some data on the "Epo-Tek" adhesives manufactured by Epoxy Technology, Inc., (65 Grove St., Watertown, MA 02172).

Epo-Tek Nos.	Description	Thermal Conductivity, Btu.in/ft ² ·hr·°F	Lap Shear Strength, psi	
			value, psi	adherends
H11 H20	Electrically Conductive		1000	
H21 through H24			1000	Aluminum
H40 H41 H43			2000 - 5000	Gold-plated beryllium copper
H54 H55	Electrically Insulating		3100 2000	Aluminum Aluminum
H61 H72 H74	Thermally Conductive	7.55 6.0 7.6	2500 2500	Aluminum Aluminum
H80	Electrically Conductive		2000	

Transene Company Adhesives.- The Transene Company (Route 1, Rowley, MA 01969) gives the following data for its epoxy adhesives. Those with the Epoxy-10 through Epoxy-17 designations are electrically insulative, the rest are electrically conductive.

Designation	Thermal Conductivity, Btu·in/ft ² ·hr·°F	Thermal Expansion Coefficient, 10 ⁻⁶ /°C	Shear Strength, psi	
Epoxy-10 Epoxy-11 Epoxy-12	15	40	25-100C	2000 min
			150C	1300 min
Epoxy-13 Epoxy-14 Epoxy-15	4 12 4	30 23 30	@ 25C 2000 1500 2000	@ 125C (1000 hrs) 1500 1000 1500
Epoxy-16	4	35	2000	
Epoxy-17	10	23	2000	
Ohmex - Ag	100	50	1000	
Silver-Epoxy, Types I & II	100	50	1500	
Silver-Bond Types 40,50,60	100		1500	
Microcircuit Silver, Types K & L	21(K) 20(L)	50	Cured 1/2 hr @ 135C	1500(K) >1500(L)
			Aged 200 hr @ 175C	>1000
Microcircuit Silver, Type N	20	50	Initial @ 175C	3500
			After 200 hr @ 175C	2750
Microcircuit Silver, Type O	22	50	Initial @ 175C	1500
			After 200 hr @ 175C	1000
Gold-Epoxy GE-10,20,30,40			1000	
Nickel-Bond, Types 40,50,60	6.1		1000	

Hysol Adhesives.- In its brochure the Hysol Division of the Dexter Corporation (15051 E. Don Julian Road, Industry, CA 91749) gives the following data for its epoxy adhesives:

Designation	Shear Strength, psi				Thermal Conductivity, 10^{-4} cal/cm·s·°C	Thermal Expansion Coefficient, $10^{-6}/^{\circ}\text{C}$
	77F		-40F	180F		
	Cured 2 hrs @ 140F	Cured 7 days @ 77F				
1C	2300	1750	1750	1600	10.4	30.3
907	3200	3000	1250	400	6.8	45
6c	2100	2000	1600	1850	10.7	24.4
615	3100	2950	2700	150	9.0	50.6
309	1630	1865	1020	960	5.0	53.9
608	2500	2000	1100	150	4.8	89.6
0151	2600	1850	2000	500	4.7	102.8
3x	2600	2200	2000	150	8.2	88.6
9340	2300	2000	2100	1850	7.3	29.4
9410	3600	3500	2500	450	5.2	50.4

Technical Wire Products, Inc.- This company, located at 120 Dermody St, Cranford, NJ 07016, gives the following strength properties of two of its conductive epoxy adhesives in its Data Sheet CS-724, dated 1975:

Designation	Minimum Shear Strength, psi	
	Cured at R.T.	Cured at 210F
72-00008	1000	900
72-08116	1400	1350

2. Ceramics

Ceramics are used for a variety of purposes in microcircuit packaging -- for example, as lids, bases and substrates in flatpacks. Here we summarize the thermal and mechanical properties of a number of ceramics, using data provided in several suppliers' literature.

One of the main suppliers of ceramics for microelectronic applications is the 3M Company (Chattanooga, Tenn. 37405), which produces a line of ceramics under the trade name "AlSiMag." The following two tables give the properties of a selection of those ceramics.

Material		Alumina (Al ₂ O ₃)									
			86Z	94Z	94Z	94Z	96Z	99.5Z	99.5Z	99.5Z	99 9*
"AlSiMag" Number		860	606	620	771	777	614	753	772	638	805
Specific Gravity		3.8	3.68	3.86	3.62	3.7	3.70	3.85	3.89	3.85	3.96
Color		white	russet	brown	white	black	white	white	white	white	off-white
Thermal Expansion Coeff.	10 ⁻⁶ /°F	70-400F 70-1300F 70-1650F			3.3 4.0 4.1	4.1 4.6 4.8	3.6 4.2 4.4	3.7 4.2 4.3	3.7 4.2 4.3	3.6 4.1 4.1	3.7 4.2 4.3
	10 ⁻⁶ /°C	25-300C 25-700C 25-900C	6.5 7.3 7.7	7.4 7.7 8.0	6.0 7.2 7.4	7.4 8.2 8.7	6.4 7.5 7.9	6.7 7.6 7.8	6.6 7.4 7.7	6.5 7.3 7.7	6.7 7.5 7.7
Tensile Strength, ksi					20	24	25	28			
Compressive Strength, ksi		400	350	300	315	240	375	380		370	495
Flexural Strength, ksi		74	45	37	44	30	46	48	70	65	100
Modulus of Elasticity, 10 ⁶ psi					43		47	55	55	50	58
Shear Modulus, 10 ⁶ psi					17		19	22	22	21	
Poisson's Ratio					.22		.22	.22	.22	.22	
Thermal Conductivity	$\frac{\text{Btu-in}}{\text{ft}^2 \cdot \text{hr} \cdot ^\circ\text{F}}$	25C 300C 500C 800C			192 99 70 46	192 99 70 46	244 119 75 58	255 128 78 52	255 130 81 61		
	$\frac{\text{W}}{\text{m} \cdot ^\circ\text{K}}$	25C 300C 500C 800C			27.7 14.2 10.1 6.6	27.7 14.2 10.1 6.6	35.1 17.1 10.8 8.3	36.7 18.4 11.3 7.5	36.7 18.7 11.6 8.8		

Material			Beryllia (BaO)		Titania (TiO ₂)	Fosterite (2MgO·SiO ₂)		Alkaline Earths (porcelains) (J ₂ P ₃ S ₅)	
"AlSiMag" Number			794	828	192, 193	243	842	531	825
Specific Gravity			2.92	2.85	4.0	2.8	2.9	2.6	2.8
Color			white	white	tan, gray	buff	off-white	white	white
Thermal Expansion Coeff.	10 ⁻⁶ /°F	70-400F	4.2		4.4	5.6	5.2		
		70-1300F	4.7		5.0	6.2	5.7		
		70-1650F	4.8			6.5	5.7		
Thermal Expansion Coeff.	10 ⁻⁶ /°C	25-300C	7.5	6.7	8.3	10.0	9.4	4.4	1.4
		25-700C	8.4	8.5	9.0	11.2	10.2	5.5	3.3
		25-900C	8.7	8.7		11.7	10.3		4.5
Tensile Strength, ksi			23	23	7.5	10	11		
Compressive Strength, ksi			260	>200	100	85	90	200	230
Flexural Strength, ksi			33	>32	20	20	20	15	25
Modulus of Elasticity, 10 ⁶ psi			47	47		21			
Shear Modulus, 10 ⁶ psi			19	19		9			
Poisson's Ratio			.23	.23		.23			
Thermal Conductivity	Btu-in ft ² ·hr·°F	25C	1741	>1600		55	55		
		300C	841			35	35		
Thermal Conductivity	W m ² ·K	500C	522			29	29		
		800C							
Thermal Conductivity	W m ² ·K	25C	250			7.9	7.9		
		300C	121			5.0	5.0		
		500C	75			4.2	4.2		
		800C							

The following is a selection of data from the brochure of the Center-flex Ceramics Corporation (188 Eighth Ave., Hawthorne, NJ 07507).

Material	Alumina, Al ₂ O ₃				Beryllia 99.5%	Fosterite 2MgO-SiO ₂	Titanium TiO ₂	Stentite
	85%	94+%	98+%	99.5%				
Designation	85D	SC-95AH	SC-98D	SC-99.5	SC-99.5B	SC-F	SC-TT	Sillite 5
Color	white	white or red	white or red	white	white	tan	tan	white
Specific Gravity	3.46	3.70	3.86	3.87	---	2.85	4.0	2.7
Flexural Strength, ksi	25C 38 500C 29.8 1375C 1.5	46 30 6.5	59 34 9.1	65	25 min, 35 typ	20 12	21 11	21
Tensile Strength, ksi	25C 20.2 500C 18.8 1375C 0.2	26 19 1.9	34 21.5 2.1	---	20	8	8	10
Compressive Strength, ksi	25C 396 500C 317 1375C ---	365 290	430.9 410.6 30.1	370	225 min, 250 typ	89	100	90
Modulus of Elasticity, 10 ⁶ psi	25C 36.7 300C 35.5 500C 34.9 1000C 25.5 1225C ---	48.0 46.0 45.1 42.7	51.6 51.0 49.4 44.9 41.9	50	50	---	---	---
Shear Modulus, 10 ⁶ psi	25C 14.6 300C 14.2 500C 14.0 1000C 11.0 1225C ---	15.3 15.1 14.6 12.8	20.6 20.1 19.7 18.3 16.4	21.0	20	---	---	---
Poisson's Ratio	25C .26 300C .25 500C .25 1000C .22 1225C ---	.237 .238 .240	.247 .250 .258 .268 .280	.22	.26	---	---	---
Thermal Expansion Coefficient, 10 ⁻⁶ /°C	25 - 200C 6.8 25 - 500C --- 25 - 750C 7.7 25 - 900C 7.8 25 - 950C --- 25 - 1100C 8.1 25 - 1375C 8.4	7.0	6.9	6.9	3.2	12.0	8.5	6.9
Thermal Conductivity, cal/cm.s.°C	25C .059 100C .051 1359C ---	.036 .032	.071 .066 .005	---	.65	.020 .015	.025 .020	---

Kyocera International, Inc. (8611 Balboa Ave., San Diego, CA 92123)

is another supplier of ceramics for microcircuit applications. The following is a selection of data from its brochure.

Material	Alumina (Al ₂ O ₃)									Fosterite (2MgO·SiO ₂)		Stoatite (MgO·SiO ₂)		Lithia (Li ₂ O·Al ₂ O ₃ ·SiO ₂)		Titania (TiO ₂)		Cermat
	99Z	91Z	92Z	96Z	99Z	99.5Z	99.8Z	99.5Z	99Z	F-1120	F-1123	S-210	S-211	L-560	T-744	T-792	TC-20	
Designation	A-440	A-445	A-473	A-476	A-479	A-479 24	A-480	A-490	A-499	F-1120	F-1123	S-210	S-211	L-560	T-744	T-792	TC-20	
Color	dark violet	dark brown	white	white	white	white	ivory	white	white	light yellow	ivory	white	dark brown	white	black	grayish yellow	silvery white	
Specific Gravity	3.6	3.9	3.6	3.8	3.8	3.8	3.9	3.8	3.9	2.8	2.8	2.7	3.1	2.2	3.7	4.4	6.1	
Flexural Strength, ksi	40	30	46	40	44	47	46	40	57	24	20	24	23	12	24	18	157	
Compressive Strength, ksi										126		126						
Modulus of Elasticity, 10 ⁶ psi			39		50	53	54		56	21	21						6.3	
Thermal Expansion Coefficient, 10 ⁻⁶ /°C	40-400C	6.5	7.0	6.5	6.7	6.8	6.8	6.8	6.8	9.8	8.8	7.2	8.1	8	7.7	9.3	7.7	
	40-800C	7.3	7.7	7.5	7.6	7.7	7.7	7.8	7.7			8.1	9.5	8.4			8.04	
Thermal Conductivity, cal/cm·s·°C	0.04	0.04	0.04	0.05	0.06	0.06	0.07	0.06	0.06	0.009	0.008	0.006	0.009					
Specific Heat, cal/g·°C	0.20	0.19	0.19	0.19	0.19	0.19	0.19	0.19	0.19									

Data are given below on some of the ceramics of the Coors Porcelain Co. (600 Ninth Street, Golden, Colorado 80401). Where minimum values are given, they are "a minimum mean for a sample of 10 specimens."

Material	Alumina (Al ₂ O ₃)							Beryllia (BeO)		
	94Z	96Z	96Z	99.5Z	99.5Z	99.9Z	99.9Z	96Z	99.5Z	
Designation	AD-94	AD-96	ADS-96F	AD-995	ADS-995	AD-999	VISTAL	BD-96	BD-995	
Specific Gravity	3.62	3.72	3.75	3.89	3.86	3.96	3.99	2.80	2.85	
Color	white	white	white	ivory	ivory	ivory	trans-lucent white	blue	white	
Compressive Strength, ksi	25C	305	300	---	380	---	550	370	225	310
	1000C	50	---	---	---	---	280	70	---	40
Flexural Strength, ksi	25C typ	51	52	60	55	68	80	41	25	40
	25C min	46	47	---	---	---	75	---	20	35
	1000C typ	20	25	---	---	---	60	25	9	---
	1000C min	17	20	---	---	---	55	---	---	---
Tensile Strength, ksi	25C	28	28	---	38	---	45	30	---	20
	1000C	15	14	---	---	---	32	15	---	5
Modulus of Elasticity, 10 ⁶ psi		41	44	---	54	---	56	57	44	51
Shear Modulus, 10 ⁶ psi		17	18	---	22	---	23	23.5	17	20
Bulk Modulus, 10 ⁶ psi		24	25	---	33	---	33	34	31	35
Transverse Sonic Velocity, 10 ³ m/s		8.9	9.1	---	9.8	---	9.9	9.9	10.7	11.1
Poisson's Ratio		.21	.21	---	.22	---	.22	.22	.30	.26
Thermal Expansion Coefficient, 10 ⁻⁶ /°C	-200 - 25C	3.4	3.4	---	3.4	---	3.4	3.4	2.4	2.4
	25 - 200C	6.3	6.0	6.2	7.1	---	5.9	6.5	6.3	6.4
	25 - 500C	7.1	7.4	7.0	7.6	6.7	7.4	7.4	7.5	7.7
	25 - 800C	7.6	8.0	7.7	8.0	7.3	7.8	7.8	8.4	8.5
	25 - 1000C	7.9	8.2	8.1	8.3	7.7	8.0	8.0	8.9	8.9
	25 - 1200C	8.1	8.4	---	---	---	8.3	8.3	9.2	9.4
Thermal Conductivity, W/m-°K	20C	18.0	24.7	26.3	35.6	32.6	38.9	39.7	159.0	260.3
	100C	14.2	18.8	20.1	25.9	28.9	27.6	28.4	133.9	200.8
	400C	7.9	10.0	17.1	12.1	12.6	13.4	13.4	66.9	83.7
	800C	5.0	5.4	---	6.3	---	6.3	6.3	25.1	29.3
Specific Heat at 100C, J/kg-°K		880	880	880	880	880	880	880	1255	1297

Augat, Inc. Ceramic Materials Division (12 Coffin Ave., New Bedford, MA, 02746) gives the following properties for three of its alumina ceramics:

Al ₂ O ₃ Content (min)	95.0%	97.6%	99.5%
Compressive Strength, ksi	>300	>250	>300
Flexural Strength, ksi	64	46	62
Specific Gravity	3.70	3.76	3.89
Thermal Conductivity, cal/cm·s·°C	.055	.064	.070

The Alberox Corp. (Industrial Park, New Bedford, Ma 02745) gives the following data for its 95% alumina ceramic (designation A-950):

Color	white
Specific Gravity	3.69
Tensile Strength, ksi	31
Compressive Strength, ksi	385
Flexural Strength, ksi	53
Modulus of Elasticity, 10 ⁶ psi	41
Thermal Expansion Coefficient, 10 ⁻⁶ /°C	9.2
Thermal Conductivity, Btu-in/ft ² -hr-°F	145
Specific Heat, cal/g·°C	0.19

Ceramaseal, Inc. gives the following thermo-mechanical data for its alumina ceramics:

Material		85% min. Alumina	92.5% min. Alumina	96% min. Alumina	99% min. Alumina
Tensile Strength, ksi		17.5	18.5	25	34
Compressive Strength, ksi		240	280	400	300
Flexural Strength, ksi		42	46.2	60	58
Thermal Conductivity, cal/cm-s. ^{°C}		0.031	0.02	0.043	0.036
Thermal Expansion Coefficient, 10 ⁻⁶ /°C	25 - 200C	5.68	6.18	6.5	6.7
	400 - 600C	7.83	8.5	8.9	8.9

The following table gives properties of three of the alumina ceramics obtainable from Duramic Products, Inc. (426 Commercial Ave., Palisades Park, NJ):

Material		96% Alumina	99% Alumina	99.7% Alumina
Designation		HT-960	HT-990	HT-997
Color		white	white	ivory
Specific Gravity		3.76	3.85	3.94
Tensile Strength, ksi		25	30	30
Compressive Strength, ksi		340	375	380
Flexural Strength, ksi		46	50	50
Modulus of Elasticity, 10 ⁶ psi		45	50	55
Thermal Expansion Coefficient	10 ⁻⁶ /°F	3.5	4.1	3.5
	10 ⁻⁶ /°C	6.4	7.4	6.4
Thermal Conductivity	Btu-in/ft ² -hr-°F	220	205	225
	W/m-°K	31	29	32
Specific Heat	Btu/lb-°F, cal/g-°C	0.19	0.20	0.20
	J/kg-°K	795	837	837

A particular 99.5% alumina ceramic utilized by the Sandia Laboratories is reported by them to have the following properties ("Ceramic Substrates for Hybrid Microcircuit Applications," by R.E. Kuntson, Report SLA-73-0886, Sandia Laboratories, Albuquerque, NM 87115, Sept. 1973):

Color	white	
Specific Gravity	3.90	
Compressive Strength, ksi	> 400	
Flexural Strength, ksi	68	
Thermal Conductivity, cal/cm-s. ^o C	20C	.075
	100C	.065
	400C	.028
Thermal Expansion Coefficient, 10 ⁻⁶ /°C	25 - 200C	6.0
	25 - 500C	7.3
	25 - 800C	7.9

The Corning Glass Company of Corning, NY produces a white, non-porous machinable glass-ceramic with the trade name MACOR and the company code number 9658. The following data is abstracted from the Corning company's brochure on this material.

Specific Gravity at 4C	2.52	
Thermal Expansion Coefficient, 10 ⁻⁶ /°C	RT to 400C	9.4
	RT to 600C	11.0
	RT to 800C	12.3
Thermal Conductivity	25C	0.004 cal/cm-s. ^o C
	77F	11.68 Btu-in/hr-ft ² -°F
Flexural Strength, ksi	15	
Compressive Strength, ksi	50	
Modulus of Elasticity, 10 ⁶ psi	9.3	
Shear Modulus, 10 ⁶ psi	3.7	
Poisson's Ratio	.26	

At least two companies manufacture alumina substrates in tape form for thick film and/or thin film microelectronic circuits. They are Materials Research Corporation (Orangeburg, NY 10962) and Coors Porcelain Company (600 Ninth Street, Golden, Colorado 80401). Some of the properties of these substrates are listed below. The three Materials Research Corp. ceramics have the general company designation Thin Film "Superstrate" 996.

Source	Materials Research Corp.			Coors Porcelain Co.	
	Hi-REL996A Std 996 S	Hybrid 996B	Commercial 996C	Thick film ADS-96R	Thin film ADS-995
Alumina Content, %	99.6	99.6	99.6	96	99.6
Specific Gravity	3.86-3.90	3.87	> 3.81	3.74	3.89
Thermal Conductivity, cal/cm-s. °C	20C			0.063	0.078
	25C	0.090	0.090	0.090	
	100C			0.048	0.069
	300C	0.050	0.050	0.050	
	400C			0.029	0.030
Thermal Expansion Coefficient, 10 ⁻⁶ /°C	500C	0.038	0.038	0.038	
	25-200C			6.3	5.9
	25-300C	6.3	6.3	6.3	
	25-500C			7.1	6.7
	25-600C	7.1	7.1	7.1	
Flexural Strength, ksi	25-800C	7.3	7.3	7.3	7.3
	25-1000C			8.0	7.7
Compressive Strength, ksi	90	90	90		
	400	400	400		

Porcelain enameled steel has been proposed as an alternative to pure ceramic substrates. According to one supplier of such substrates (The Erie Ceramic Arts Co., 3120 W. 22 Street, Erie, PA 16505), 20 gauge steel (.034-.038 in.) is normally used, and the enamel can be applied to only one or to both sides of the steel in a thickness that is normally 5 or 6 mils (per side) but that can be varied if requested from 3 to 15 mils. The following properties are cited for the two components:

	Porcelain Enamel	Steel
Thermal Conductivity, W/cm.°C	.01	.45
Thermal Expansion Coefficient, $10^{-6}/^{\circ}\text{C}$	12.5-13.5	15

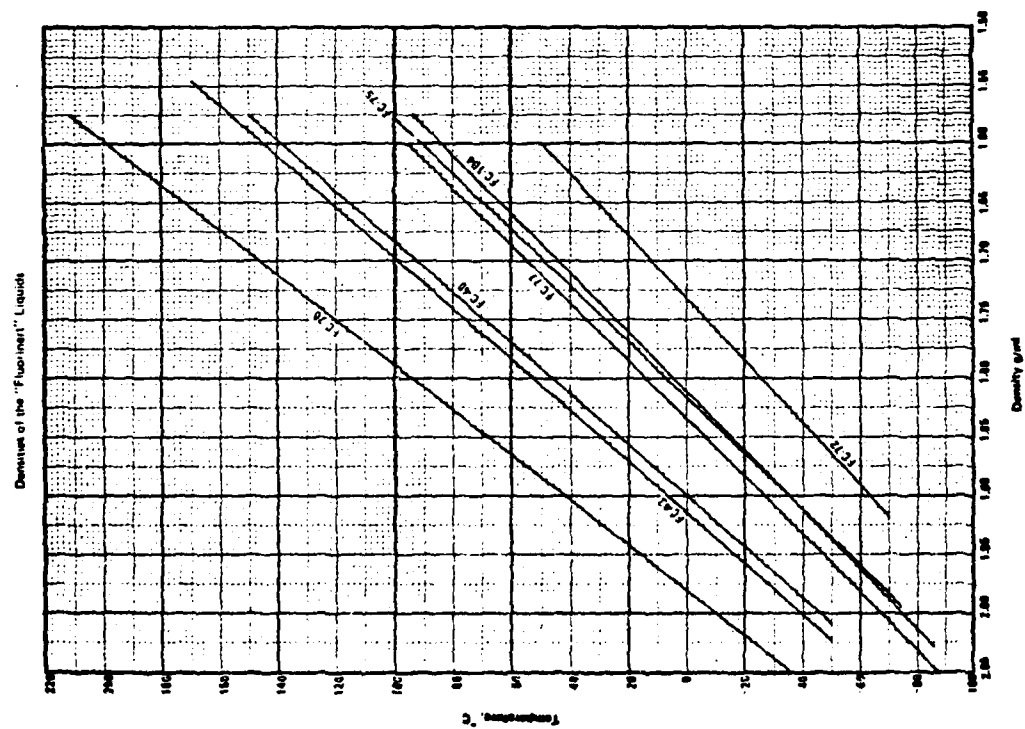
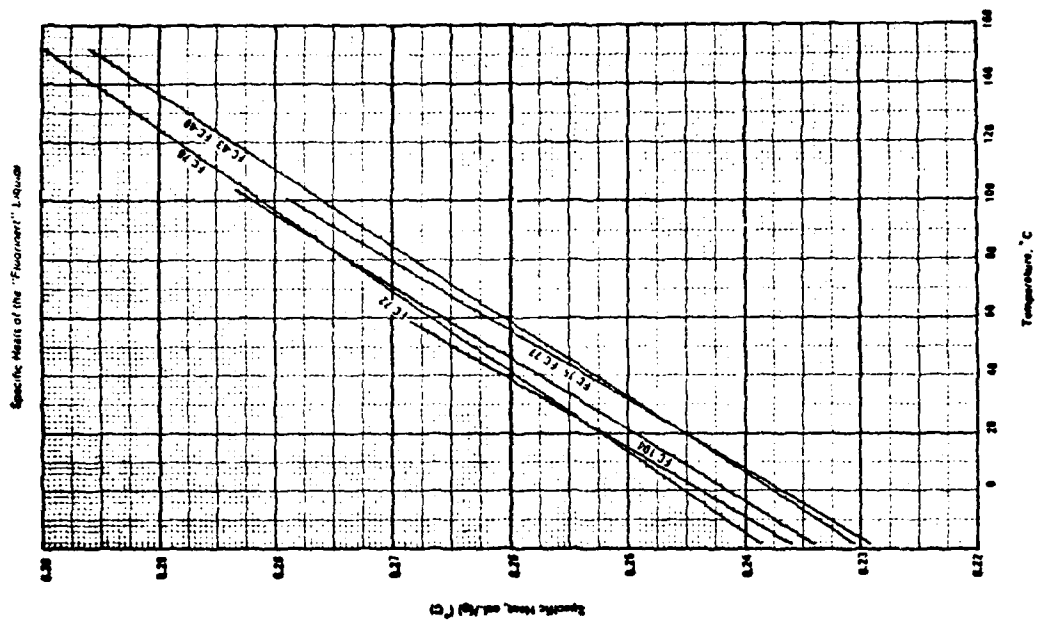
The enamel is fired at 800 to 870 C. The larger expansion coefficient of the steel puts the porcelain in a state of compression at room temperature.

3. Fluids

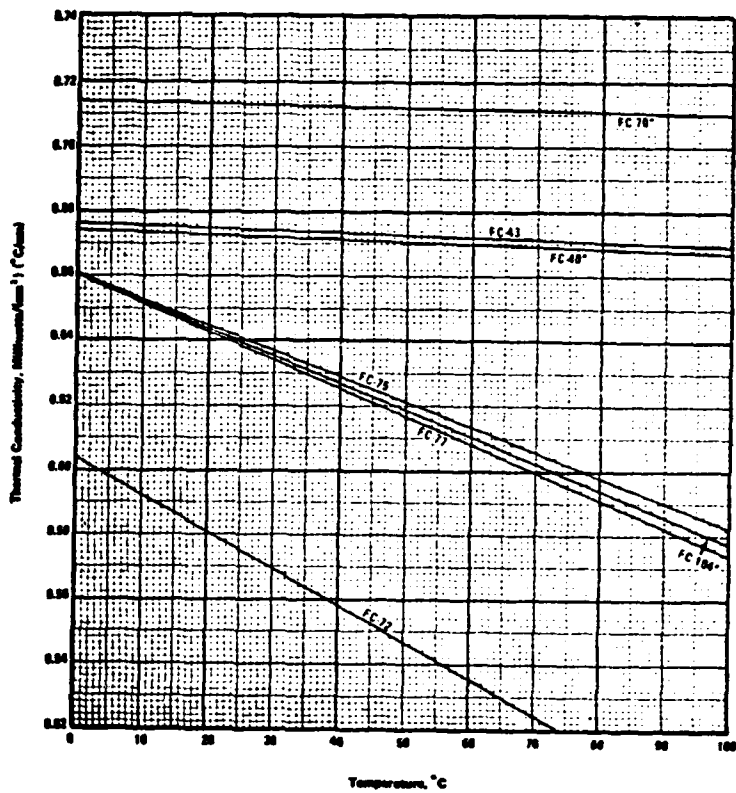
Here are assembled some thermal and mechanical properties of several fluids (including air) that are of possible use as the low or high temperature fluids for thermal shock and thermal cycling tests (e.g., those of Methods 1011.2 and 1010.2 of "Test Methods and Procedures for Microelectronics," MIL-STD-883B, Dept. of Defense, 31 Aug. 1977).

3M "Fluorinert" Fluids.- The following table and graphs give properties of seven of the "Fluorinert" liquids manufactured by the 3M Company of St. Paul, Minnesota. Three of these substances (FC-40, FC-70, FC-77) are among the thermal shock test fluids suggested in Method 1011.2 of the MIL-STD-883B document referred to above.

Designation		FC-72	FC-84	FC-77	FC-104	FC-75	FC-40	FC-43	FC-70
Boiling Point	°F	133	176	207	214	216	311	345	419
	°C	56	80	97	101	102	155	174	215
Pour Point	°F	-13	-139	-166	-85	-126	-70	-58	-13
	°C	-90	-95	-110	-65	-88	-57	-50	-25
Heat of Vaporization at B.P., Btu/lb		38	35	36	40	38	31	30	29
Specific Heat of the Vapor, Btu/lb·°F	214F					0.230			
	230F					0.234			
	250F					0.236			
	300F					0.242			
	350F					0.246			
	400F					0.250			
	450F					0.252			
500F					0.26				
Thermal Conductivity of the Vapor, Btu/ft·hr·°F	216F					0.0080			
	250F					0.0112			
	300F					0.0251			
	350F							0.0135	
	380F							0.0130	



Thermal Conductivities of the "Fluorinert" Liquids



* Estimated

UCON 100.- "UCON 100" is a suggested high temperature fluid for levels D and F of the MIL-STD-883B thermal shock test. This product, which is sold by the Blue M Electric Co. (Blue Island, Illinois), originates as "UCON Heat Transfer Fluid 500" of the Union Carbide Corporation (270 Park Avenue, New York, NY 10017), where it also is designated as "UCON Fluid 50-HB-280X." Its following properties are taken from graphs in the 1981 "UCON Heat Transfer Fluid 500" brochure of the Union Carbide Corporation. The thermal conductivity values given below differ somewhat from those cited in the Blue M Electric catalog for UCON 100; however, being the more recent, they are also probably the more reliable. The pour point of this fluid is given as -37C (-35F) and the boiling point as >260C (500F).

Temperature °F	Temperature °C	Thermal Conductivity, Btu/ft·hr·°F	Specific Heat, Btu/lb·°F	Density, lb/ft ³
0	-18	0.100	0.436	65.7
100	38	0.095	0.480	63.5
200	93	0.090	0.517	61.0
300	149	0.085	0.543	58.7
400	204	0.080	0.560	56.1
500	260	0.075	0.570	53.6

Nitrogen.- Liquid nitrogen is the suggested low-temperature fluid for levels E and F of the thermal shock test in MIL-STD-883B. Nitrogen has a melting point of -209.86C and a boiling point of -195.8C. Its heat of vaporization at the boiling point is 2.80 kilojoules per gram atom (= 47.6 cal/g = 85.6 Btu/lb). Some of its other properties at 1 atmosphere absolute pressure are given in the following table.

State	Temperature		Thermal Conductivity Btu/ft.-hr.-°F	Specific Heat Btu/lb.-°F	Density lb./ft. ³
	°F	°C			
Liquid	-345.7	-209.86	.0945	.48	54.5
	-342	-208	.0924	.48	54.0
	-333	-203	.0869	.48	52.5
	-324	-198	.0815	.48	51.1
	-320	-195.8	.0793	.48	50.4
Gas	-320	-195.8		.266	
	-315	-193	.0044		.277
	-297	-183	.0050		.243
	-294	-181	.0051	.256	.237
	-279	-173	.0055		.218
	-261	-163	.0061		.197
	-243	-153	.0065		.180
	-225	-143	.0069		.165
	-207	-133	.0075		.153
	-189	-123	.0080		.143
	-171	-113	.0085		.134
	-153	-103	.0091		.126
	-135	-93	.0096		.119
	-117	-83	.0101		.113
	-99	-73	.0106		.107
	-63	-53	.0116		.0970
	-27	-33	.0124		.0889
	8.6	-13	.0132		.0820
	32	0	.0138	.249	.0781
	44.6	7	.0141		.0762
	80.6	27	.0150		.0711
	117	47	.0158		
	122	50	.0159		.0660
	171	77	.0169		
	212	100	.0178		.0571
	261	127	.0189		
	302	150	.0197		.0504
351	177	.0207			
392	200	.0215	.250	.0450	
441	227	.0225			
531	277	.0241			
572	300	.0249		.0372	
621	327	.0258			
711	377	.0273			
752	400		.253	.0317	

Water.- Water is the MIL-STD-883B suggested fluid for level A of the thermal shock test. Some of its properties at atmospheric pressure are tabulated below.

State	Temperature		Thermal Conductivity Btu/ft·hr·°F	Specific Heat Btu/lb·°F	Density lb/ft ³
	°F	°C			
Liquid	32	0	.33	1.00	62.5
	50	10	.333	1.00	62.5
	100	37.8	.363	1.00	62.0
	200	93.3	.382	1.00	61.2
	212	100	.345	1.00	59.9
Steam	212	100	.0145	.489	.0372
	240	116	.0148	.482	.0356
	280	138	.0159	.475	.0336
	320	160	.0170	.471	.0322
	360	182	.0182	.470	.0316
	400	204	.0193	.471	.0289
	500	260	.0226	.474	.0258
	600	316	.0260	.482	.0233
	700	371	.0297	.489	.0213

Its heat of vaporization at the boiling point, 212F, is 970 Btu/lb (540 cal/gm).

Air.- The corresponding data for dry air are given in the following table. Air is the fluid generally used in temperature cycling.

Temperature		Thermal Conductivity	Specific Heat, c_p	Density
$^{\circ}\text{F}$	$^{\circ}\text{C}$	Btu/ft·hr· $^{\circ}\text{F}$	Btu/lb· $^{\circ}\text{F}$	lb/ft ³
-300	-184	.0050	.252	.236
-250	-157	.0064	.244	.181
-200	-129	.0078	.243	.145
-150	-101	.0092	.242	.123
-100	-73.3	.0106	.241	.107
-40	-40	.0121	.24	.092
-20	-28.9	.0126	.24	.089
0	-17.8	.0131	.239	.0863
32	0	.0140	.239	.0806
60	15.6	.0146	.240	.0763
100	37.8	.0155	.241	.0709
150	65.6	.0166	.241	.0650
200	93.3	.0176	.242	.0601
250	121	.0186	.243	.0558
300	149	.0195	.244	.0520
350	177	.0205	.245	.0488
400	204	.022	.246	.0460
450	232	.023	.247	.0436
500	260	.024	.248	.0413
550	288	.025	.249	.0391
600	316	.026	.251	.0373
700	371	.027	.253	.0341
800	427	.028	.256	.0314
900	482	.030	.258	.0291
1000	530	.032	.263	.0271
1500	816	.040	.277	.0202
2000	1093	.047	.287	.0161
2500	1371	.046	.291	.0133
3000	1649	.054	.296	.0114

4. Glasses

Corning Glass Data. - Mechanical and thermal properties of a number of glasses manufactured by the Corning Glass Works of Corning, NY are presented in the tables that follow. The terms working point, softening point, anneal point and strain point, that appear among the column headings, refer to temperatures at which the glass has certain viscosities. The following definitions of these terms are adapted from the report, "Thick Film Glasses," by R.W. Vest, Purdue University, West Lafayette, Indiana 47907, Nov. 15, 1978 (final technical report to the Naval Research Laboratory under contract N00173-77-C-0142):

Working Point - The temperature at which the viscosity is 10^3 Pa·s (10^4 poises).

This temperature is the upper end of the working range, which extends from a viscosity of $10^{6.6}$ to 10^3 Pa·s ($10^{7.6}$ to 10^4 poises).

Softening Point - The temperature at which a fiber elongation rate of

1 mm/min is measured by ASTM Method C-338. For a glass with a specific gravity near 2.5, the softening point corresponds to a viscosity of $10^{6.6}$ Pa·s ($10^{7.6}$ poises).

Anneal Point - The temperature at which a fiber elongation rate of

0.0136 cm/min is measured by ASTM Method C-336. Internal strains will be relieved in about 15 minutes at this temperature, and the viscosity is approximately 10^{12} Pa·s (10^{13} poises).

Strain Point - The temperature at which a fiber elongation rate of

0.00443 cm/min is measured by ASTM Method C-336. Internal strains will be relieved in about 4 hours at this temperature, and the viscosity is approximately $10^{13.5}$ Pa·s (10^{13} poises).

The "set point," which appears in a column heading related to thermal expansion, is defined as the strain point plus 5°C.

The graphs that follow the tables give more detailed thermal expansion and viscosity data for some of the glasses. For two of the glasses (codes 7056 and 7059) the graphs include thermal conductivity as a function of temperature, and for one of these (7056) also specific heat as a function of temperature.

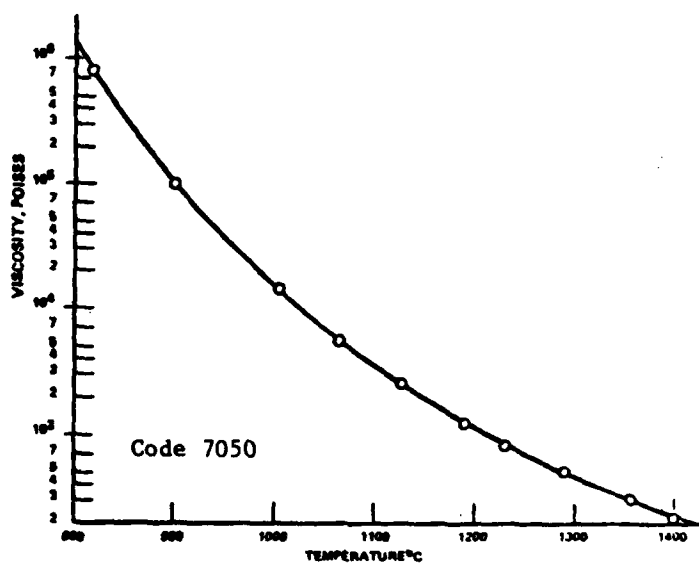
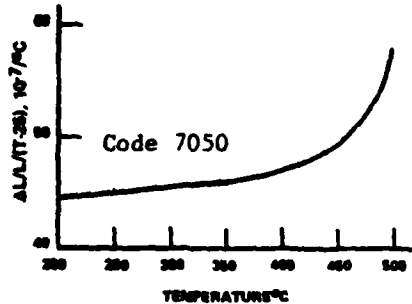
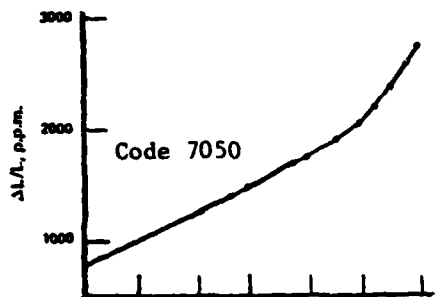
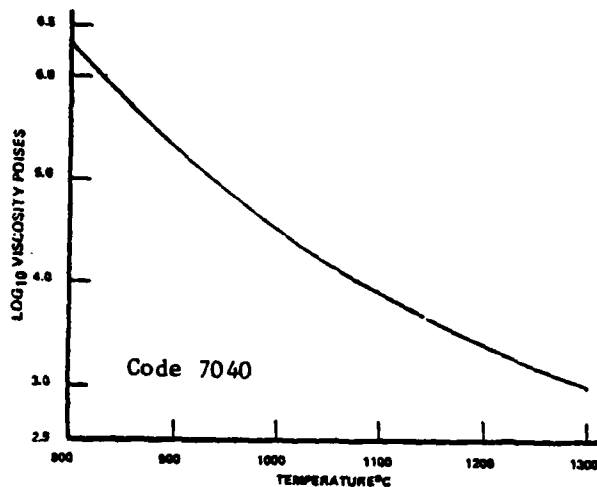
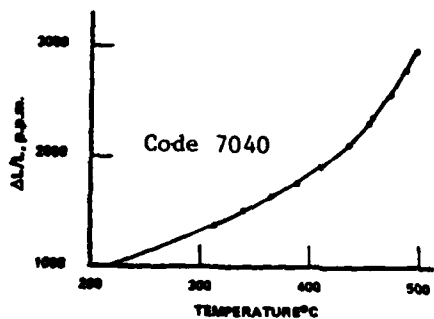
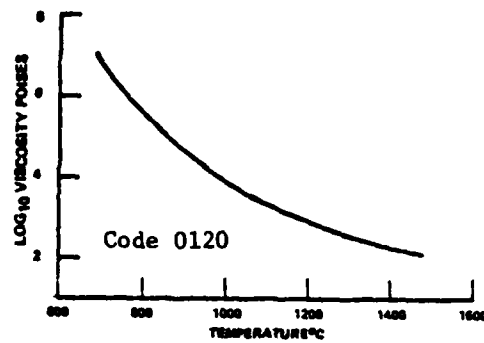
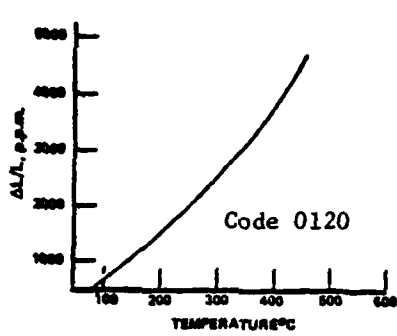
Corning Glass Code	Seal Temp., °C	Viscosity Data, °C				Density, g/cm ³	Th. Exp. Coeff., 10 ⁻⁷ /°C	
		Working Point	Softening Point	Anneal Point	Strain Point		0 to 300 C	25 C to Set Point
7191BP	415		350	312		5.2	68	
0081	1000		696	514	473	2.47	93.5	
0120	980	985	630	435	395	3.05	89.5	99
1415			776	654	620	3.64	79	97
1416			463	386	364	5.26	81	91
1417			427	356	336	5.60	89	96
7040	1050	1080	702	490	449	2.24	47.5	54
7050	1050	1027	703	501	461	2.24	46.0	51.1
7052	1050	1128	712	480	436	2.27	46.0	53.1
7056	1050	1058	718	512	472	2.29	51.5	54.5
7059		1160	844	639	593	2.76	46.0	50.1
7062	975	984	680	488	450	2.31	49.0	57
7063		917	635	488	455	3.13	45.5	54.5
7070	1075	1068		496	456	2.13	32.0	39
7280	1250		873	624	576	2.62	65.0	
7555	450		415	350	330	5.7	90	88
7556	450		330			4.68	67	67 (to 300 C)
7570	470	560	440	363	342	5.42	84	91.9
7572	450		370			-6.3	95	95
7574	750		644	552	527	-6.3	34	45 (to 750 C)
7575	450		370			-6.3	89	89 (to 450 C)
7578	530		445			5.82	65.4	70 (to 460 C)
7581	430		375			6.45	97	97
7583	480		370			-6	83	83 (to 480 C)
7585	415	430	365	309		5.1	68	68
7589	400		335			-6	80	78 (to 400 C)
7590	440		374			6.45	97	97
7592	425		373			6.45	97	97
7593	650		470			5.6	42 ^(a)	42 (to 440 C) ^(a)
7594	580		460			-5.6	47.6	39.4 (to 420 C)
7595	415		362					97
7732	450		315			5.80	91.6	-82 (to 420 C)
7740		1252	821	560	510	2.23	32.5	37

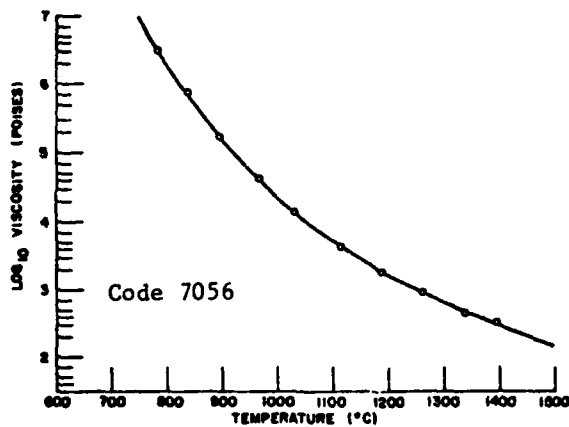
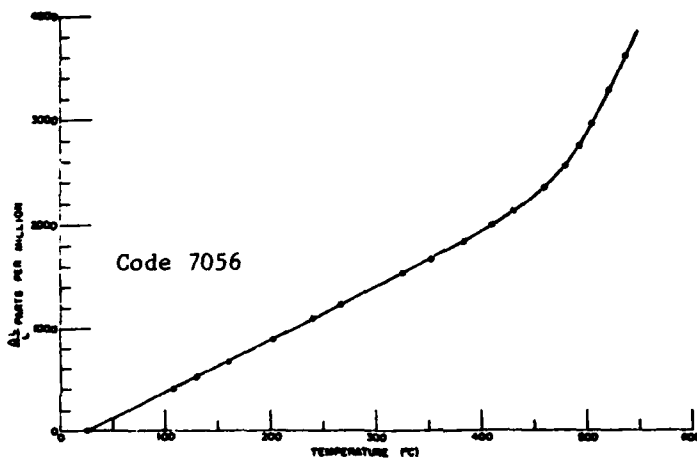
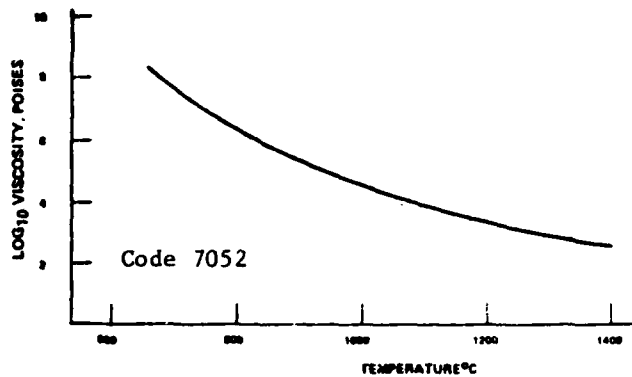
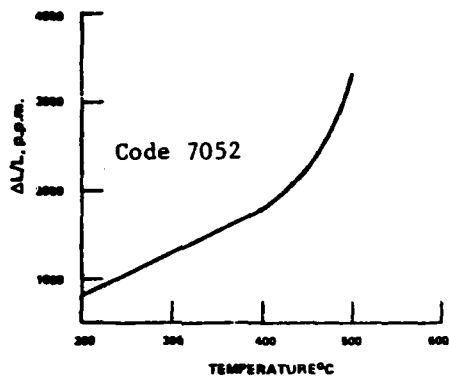
Corning Glass Code	Seal Temp., °C	Viscosity Data, °C				Density, g/cm ³	Th. Exp. Coeff., 10 ⁻⁷ /°C	
		Working Point	Softening Point	Anneal Point	Strain Point		0 to 300 C	25 C to Set Point
8161			600	435	400	3.99	90.0	95
8445			714	623	592	4.03	84	100
8463			377	316	300	6.22	104.0	105
8830			708	501	460	2.24	49.5	
8870	800	823	578	427	389	4.33	91.0	96.2
9010	1000		646	446	408	2.66	89.0	
9013	1000		659	462	423	2.64	89.0	
9108			742	538	496	2.35	53	
9119			754	512	465	2.35	53	
9155	1000		729	557	515	2.67	88.5	
9182	510		450	369	347	4.80 ^(b)	79.0	83
9362	975	975	627	435	395	3.1	91.5	101.5
9363		975	627	435	395	3.08	89.5	99.3
9365		995	630	434	394	2.55	91.5	102.8

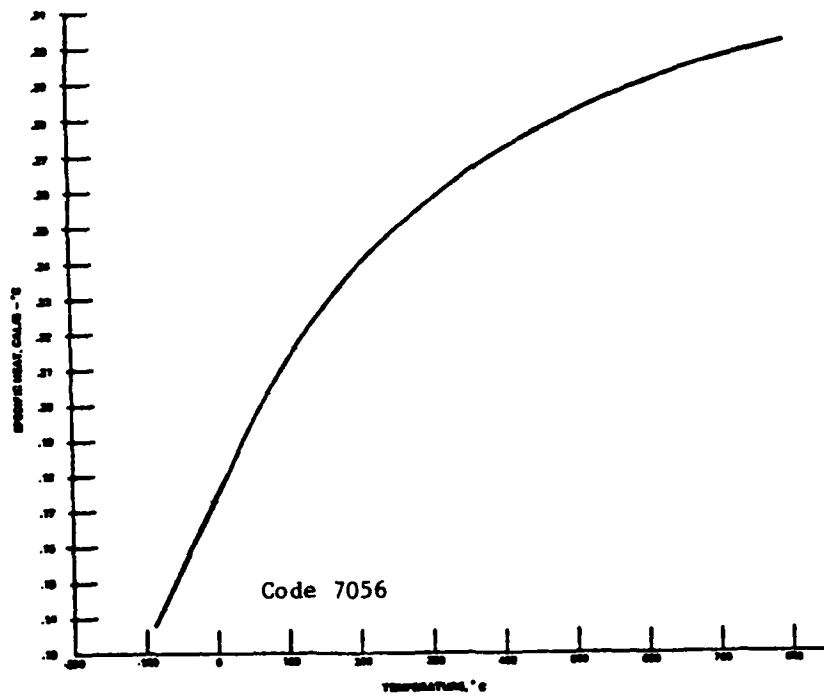
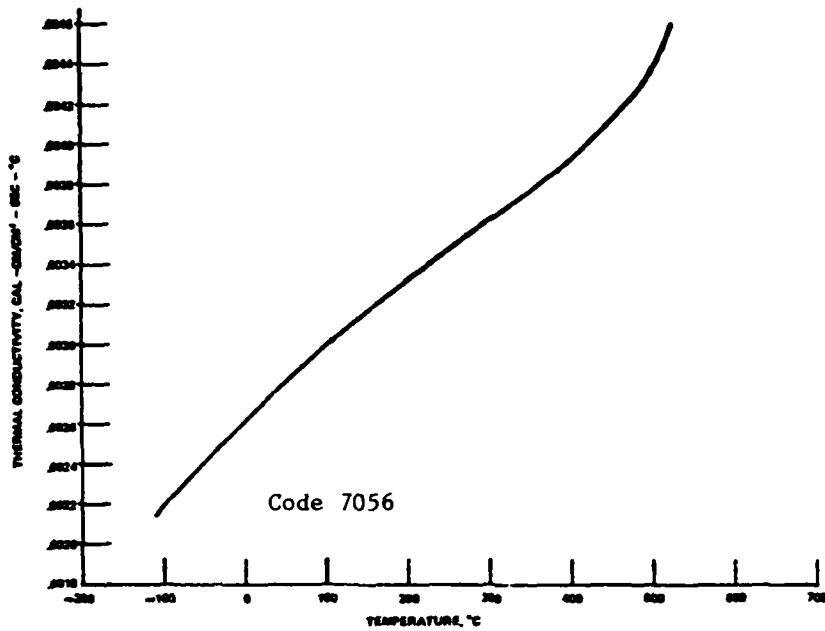
(a) Data are for glass fired at 640 C. If fired at 540 C, the 0-300 C expansion coefficient is $54 \times 10^{-7}/^{\circ}\text{C}$.

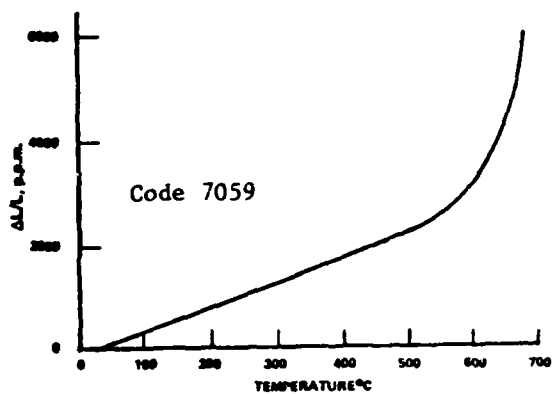
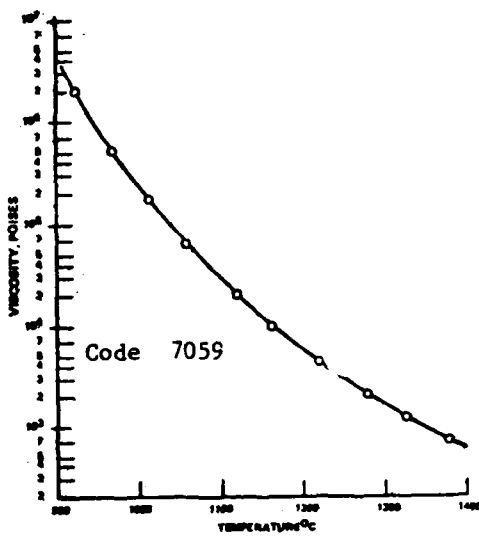
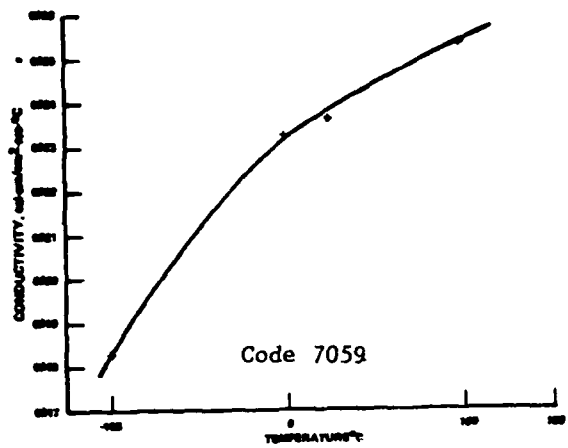
(b) Preform density

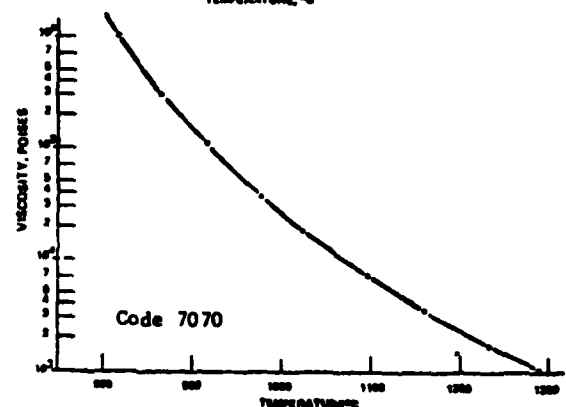
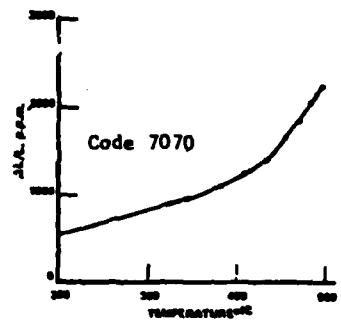
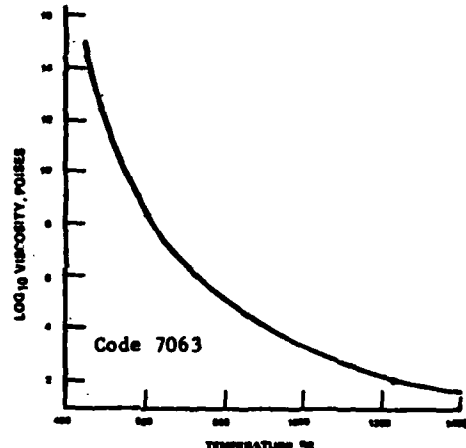
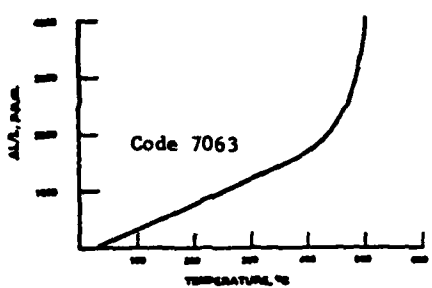
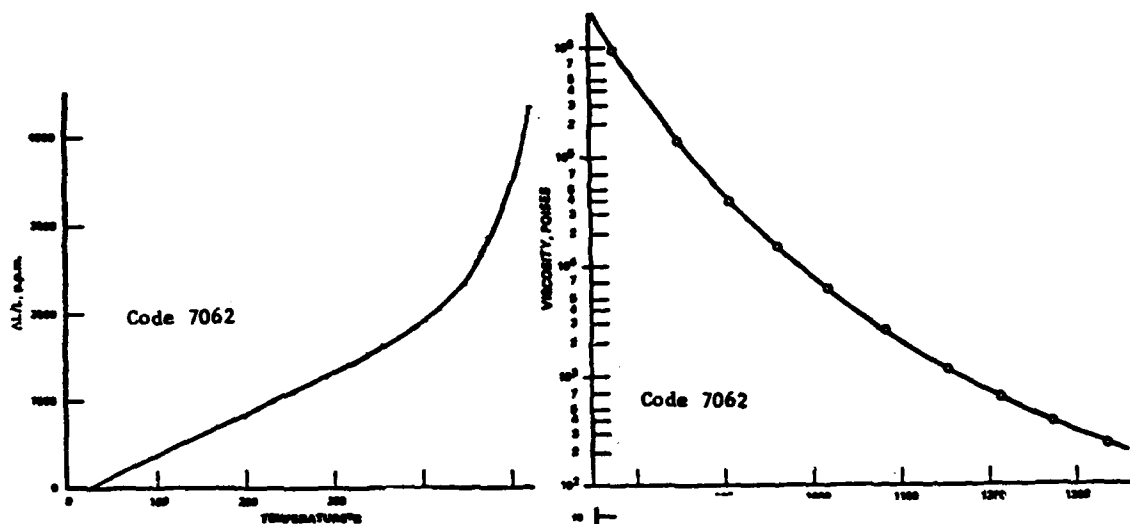
Corning Glass Code	Specific Heat, cal/g·°C	Thermal Conduc- tivity, cal/cm·s·°C	Elastic Moduli, 10 ⁶ psi		Poisson's Ratio ν	Modulus of Rupture, ksi
			Tensile E	Shear G		
T191BF		.0023				
0120	.14	.0018	8.6	3.5	.22	
7040			8.6		.23	
7050			8.7		.22	
7052			8.2	3.4	.22	
7056		SEE GRAPHS	9.2	3.8	.21	
7059		SEE GRAPL	9.8	3.8	.28	
7070			7.4		.22	
7570			8.0		.28	
7572			6.7	2.62	.27	-6 (-1.5 at 400 C)
7574			9			10 (12 at 500 C)
7575			7.44	3	.25	6

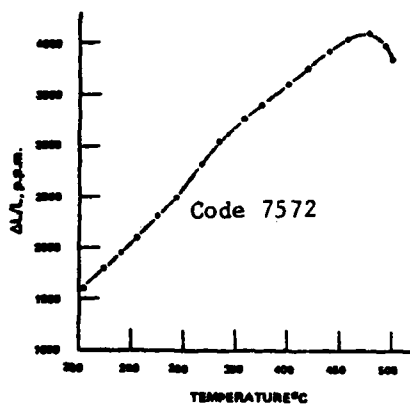
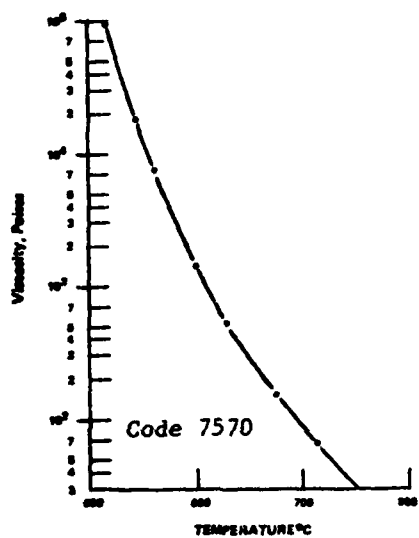
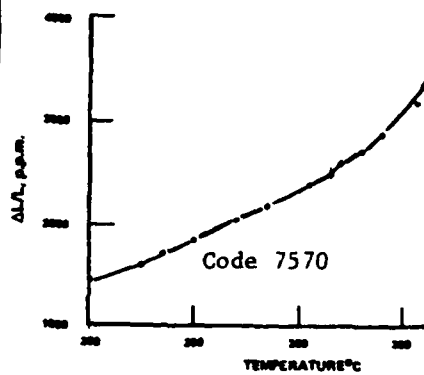
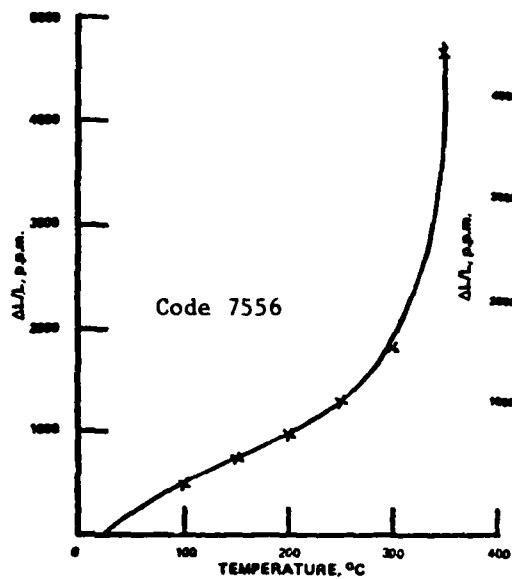


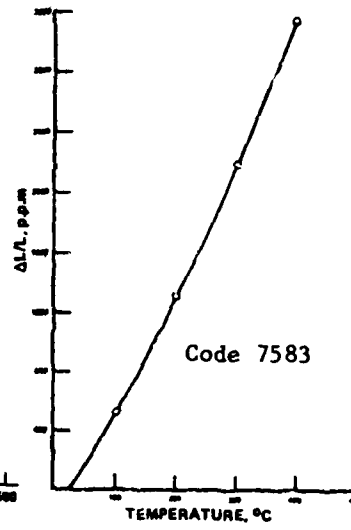
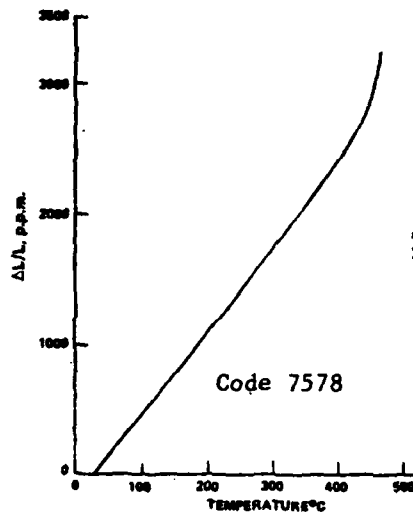
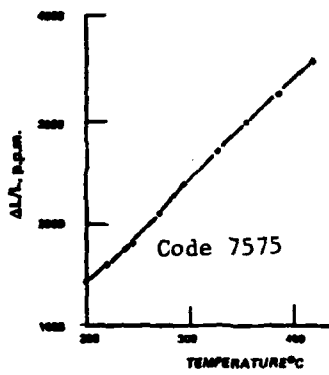
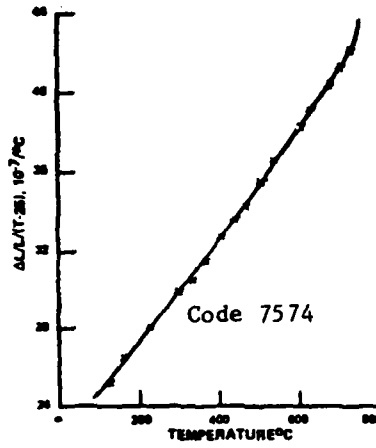
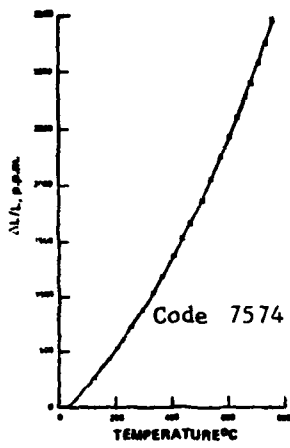


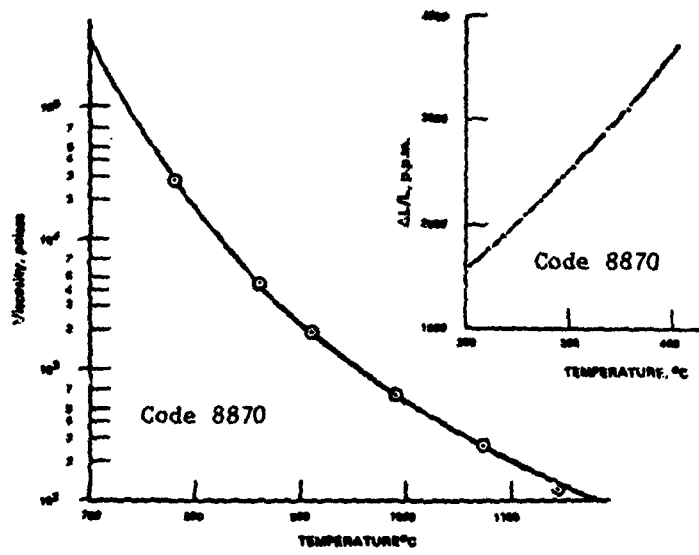
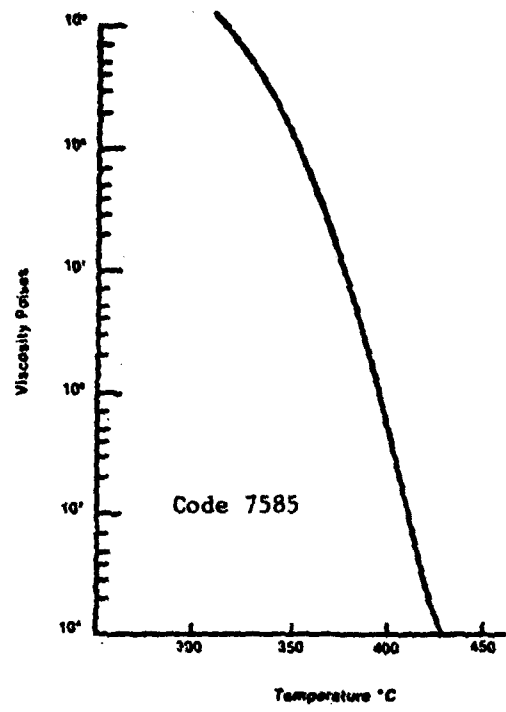


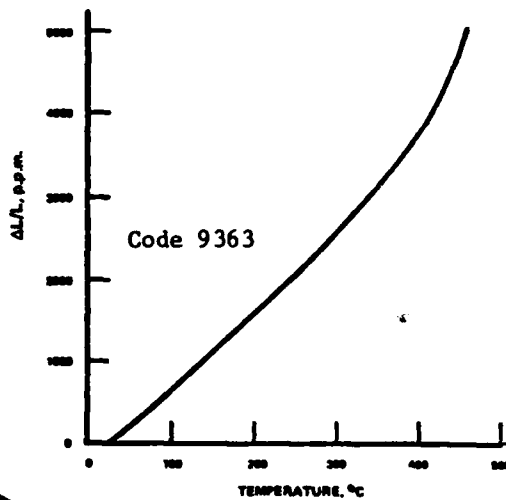
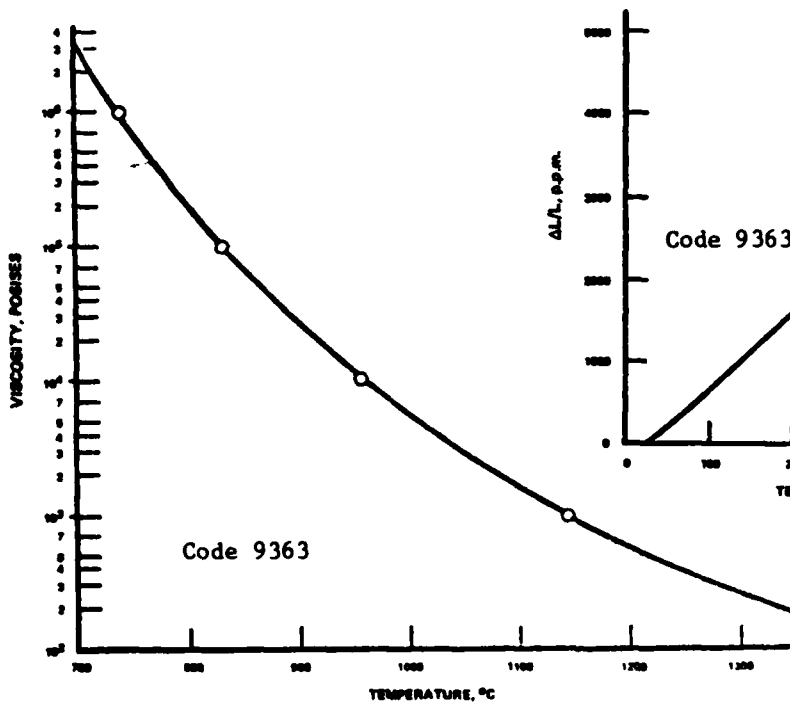
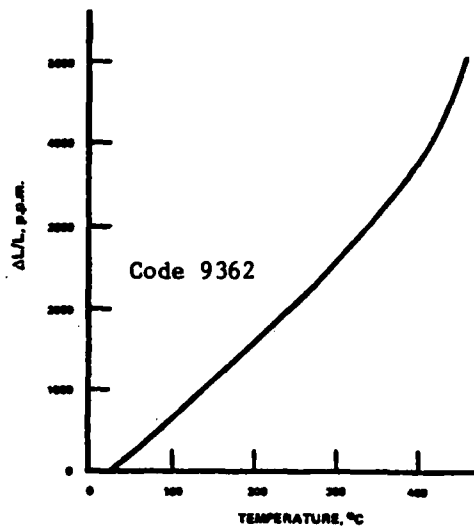
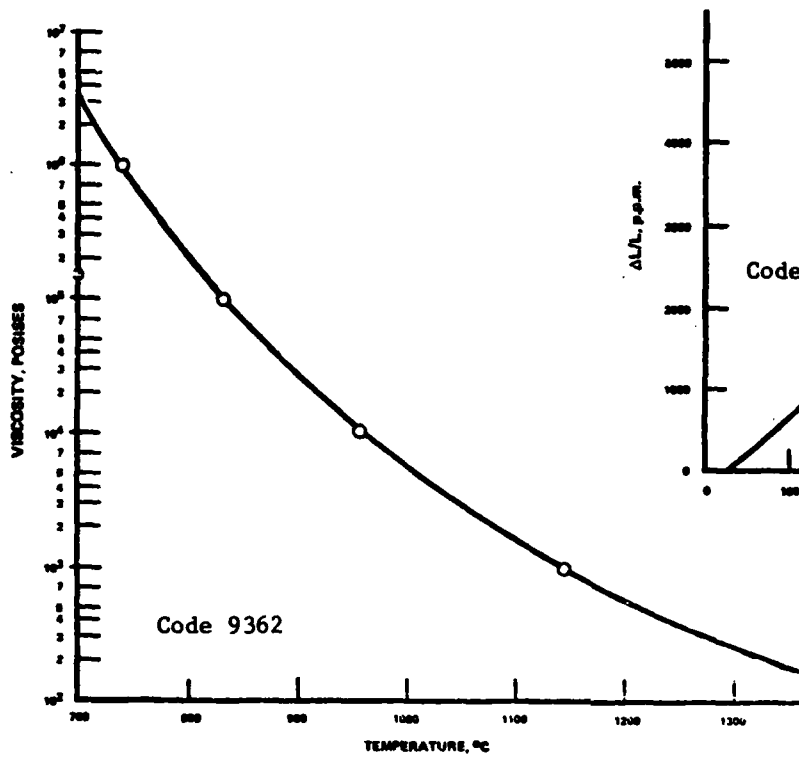


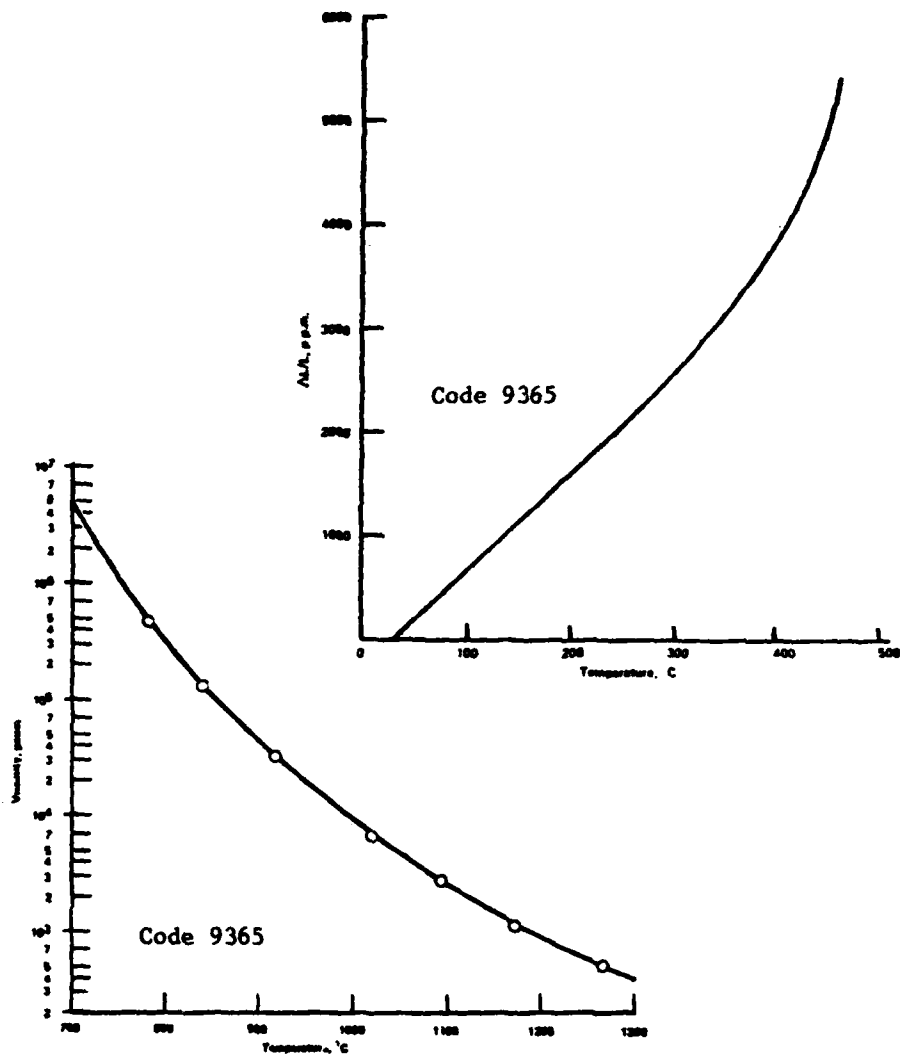












Technology Glass Data.- The Technology Glass Company (390 Potrero Ave., Sunnyvale, CA 94086) supplies glasses that are intended for microcircuit package sealing. Some of the properties of these glasses are tabulated below. Except for the thermal conductivities, which were obtained through telephone contact with the company, all of the data are taken from the Technology Glass Company's brochure CD180-0.

Technology Glass Code	Equivalent Codes	Sealing Temp., °C	Softening Point, °C	Density, g/cm ³	Thermal Exp. Coeff. (30-250 C), 10 ⁻⁷ /°C	Thermal Conductivity, cal/cm·s·°C
CV-111		485	380	5.92	68.8	
7583		485	370	6.0	84.0	
LS-0110	KC-1 NCG-556	460	400	4.77	53.0	.0019 ₇
LS-0113	KC-1M NCG-560 DC-5	450	400	6.85	64.0	.0021 ₇
LS-0802	NCG-558	410	360	6.78	77.0	
LS-0803	KC-400 NCG-564 DC-10	400	350	7.19	67.5	
TG370		400	320	6.25	78.0	
XS-1175		420	345	4.70	74.0	
XS-1175M		420	345	4.70	74.0	
7585		415	365	5.1	67.5	
T191BF	KC-402	415	350	5.2	68	
LS-0120	NCG-566	415	385	6.92	67.5	
LS-1001	NCG-569	410	370	5.74	65.5	

High Expansion Coefficient Glasses.— The Westinghouse Electric Corp., under contract to the Lewis Research Center of the National Aeronautics and Space Administration, has developed a series of high expansion coefficient glasses which are described in the following report: "Development and Evaluation of Controlled Viscosity Coatings for Superalloys," NASA-CR-72520 (NTIS designation: N70-14570). The characteristics of three of these glasses, as given in NASA Tech Brief 70-10429 (Dec. 1970), are listed below. The sag point is defined as "the temperature at which the glass begins to soften or flow."

Glass Sample No.		53	54	6
Composition (wt %)	SiO ₂	39.6	37.3	64.8
	Na ₂ O	11.6	11.8	9.6
	Al ₂ O ₃	18.4	22.4	9.4
	K ₂ O	----	----	13.1
	MgO	----	----	3.1
	CaO	18.4	14.0	----
	TiO ₂	6.9	4.7	----
	BaO	----	4.7	----
	NaF	5.1	5.1	----
Sag Point, °C		593	602	530
Thermal Expansion Coeff., 10 ⁻⁷ /°C		111	94	131

Additional Strength Data*.- In the above tabulations modulus of rupture data were given for three of the Corning glasses. Here we give some additional information, qualitative as well as quantitative, on the mechanical strength of glass.

At room temperature glass is a brittle material. That is to say, it can be assumed to remain perfectly elastic up to the point of fracture, and fracture occurs when the maximum tensile stress reaches a critical value. The Corning company's booklet on "Properties of Glasses and Glass-Ceramics" states that theoretical calculations place the intrinsic strength of glass as high as 5×10^6 psi and tests on very small diameter glass fibers (5×10^{-5} in.) have shown tensile strengths on the order of 10^6 psi, but "the useful strength of glass is but a small fraction of these figures because of stress concentrations introduced by surface imperfections." The booklet goes on to say that 1/4 in. diameter rods with pristine surfaces may show tensile strengths of 250,000 psi, but normal handling in service may introduce surface imperfections that reduce this strength to around 10,000 psi. For an adequate design safety factor, the booklet suggests a 1000 psi working stress for annealed (stress-free) glass under sustained load for 1000 hours or more, regardless of the chemical composition of the glass.

From the above discussion it is clear that there is a size effect on the strength of glass, related to surface flaws. G.O. Jones ("Glass," John Wiley & Sons, Inc., 1956, p. 94) describes this effect in the following terms: "The average strength is a function of specimen size, smaller specimens being, on the average, stronger than large specimens. Reduction by a factor of 10 in linear dimensions causes an increase of about 10 percent in the

* See also Section IX of Chapter 1.

average strength. A corollary to this is that higher values are always observed in bending than in tensile tests -- because the maximum stresses are here applied to only a small part of each specimen."

The problem of strength prediction for glass is further complicated by the phenomenon of "static fatigue" -- that is, the dependence of static strength on the duration of the applied stress. This dependence is illustrated by the following data for glass broken in flexure tests at room temperature (abstracted from graphs in E.B. Shand's "Glass Engineering Handbook," 2nd edition, McGraw-Hill Book Co., Inc., NY, 1958, p. 51):

Duration of stress, seconds	Breaking Stress, ksi		
	Annealed Glass Tested in Air	Annealed Glass Tested in Vacuum	Tempered Glass Tested in Air
0.1	20	25	
1	16	24.5	33
10	13.5	24	31
100	11	23.5	29.5
1000	9.3	23	28
10,000	8.1	23	27.5
100,000	7.5	23	27
1,000,000	7	23	26.5
10,000,000	6.9	23	

Shand states that "for loads of indefinite duration, the breaking stresses are of the order of 40 to 45 percent of the 5-sec breaking stress." The data in the above table suggests that atmosphere and humidity effects may also play a role in the static fatigue of glass. There seems to be little or no information available on the conventional fatigue of glass.

The strength variability of nominally identical specimens is somewhat greater for glass -- especially annealed glass -- than for metals. In order

to illustrate this variability we give below the probability of breakage as a function of stress for three types of float glass, as cited in the booklet entitled "PPG Glass Thickness Recommendations to Meet Architects' Specified 1-Minute Wind Load" (April 23, 1979, PPG Industries, Inc., Pittsburgh, PA 15222).

Probability of Breakage	Stress, psi		
	Annealed Glass (coefficient of variation = 22%)	Heat-Strengthened Glass (coefficient of variation = 15%)	Tempered Glass (coefficient of variation = 10%)
50%	6,000	11,000	23,000
5%	3,800	8,300	19,000
0.8%	2,800	7,000	17,200
0.4%	2,500	6,600	16,600
0.2%	2,200	6,200	16,600
0.1%	1,900	5,900	15,500

"Flat Glass Technology," by Rune Persson (1969, London, Butterworth's, p. 31) implies the following relationship between pressure and probability of breakage for a window glass, in which p stands for the median strength, i.e., the pressure giving a 50% probability of failure:

Probability of Breakage	50%	9.2%	2.3%	0.8%	0.4%	0.14%	0.07%	0.02%
Pressure	p	$.67p$	$.50p$	$.40p$	$.33p$	$.25p$	$.20p$	$.10p$

Finally, as in the case of metals, temperature has an effect on the elastic constants as well as the strength of glass. For selected glasses these effects are described by Shand on pp. 38 and 53 of the earlier cited reference. It is interesting to note that the effects of temperature are not always monotonic, and that for some glasses an increase in temperature causes an increase, rather than a decrease, in the elastic moduli. Here we cite only the following data on the modulus of rupture of soda-lime plate glass, as given by Shand:

Conditions	Exposure to Temperature, hrs	Modulus of Rupture, ksi		
		24 C	205 C	285 C
Annealed	1	14.8	11.4	12.5
Annealed	500	14.8	13.7	12.9
Tempered	1	32.0	29.5	28.7
Tempered	500	32.0	29.0	24.0

Effect of Dissolved Alumina.- A substantial amount of data on the viscous and electrical properties of glass, particularly as affected by the dissolution of alumina in the glass, can be found in the following two reports by R.W. Vest of Purdue University's Turner Laboratory for Electroceramics, in West Lafayette, Indiana:

"Thick Film Glasses," 15 Nov. 1978, report prepared for the Naval Research Laboratory under Contract No. N00173-77-C-0142.

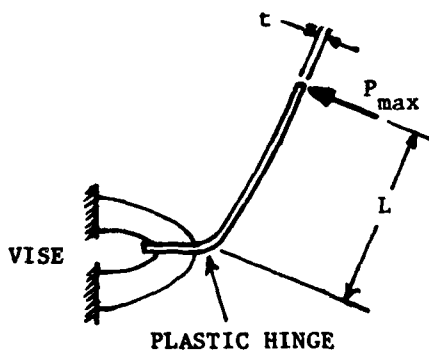
"The Effect of Substrate Composition on Thick Film Circuit Reliability," 28 Feb. 1980, report prepared for the Naval Air Systems Command under Contract No. N00019-79-C-0240.

5. Nickel-Iron Alloys

The nickel-iron-cobalt alloy with the ASTM designation F-15, but possessing various trade names, of which the best known is Kovar, is frequently used as the lead-frame, lead-wire, or case material in microelectronic packages. Representative properties of this material and of two other nickel-iron alloys that are sometimes used are given in the table that follows. The data presented in that table are a composite from several sources, including the 1976 "Handbook for Clad Metals" of Technical Materials, Inc. (5 Wellington Road, Lincoln, Rhode Island 02865), the "Nicoseal" data sheet of the Carpenter Technology Corporation (101 W. Bern St., P.O. Box 662, Reading, PA 19603), Technical Data Sheet No. 29 of the Teledyne Rodney Metals Company (1357 East Rodney French Blvd., New Bedford, MA 02742), and the "Uniseal 29-17" and "Uniseal 42" data sheets of the Cyclops Corp. (850 Washington Rd., Pittsburgh, PA 15228). For some of the data average values have been used to resolve discrepancies among different sources.

Designation	ASTM F-15	ASTM F-30 ("Alloy 42")	"Rodneal 36"
Typical Composition (Weight %)	29 Ni, 17 Co, .60 Mn, .10 Si, .02 C, Balance Fe	41.5 Ni, .80 Mn, .15 Si, .03 C, Balance Fe	36 Ni, .35 Mn, .12 Si, .04 C (max), Balance Fe
Density, lb/in ³	.302	.293	.291
Modulus of Elasticity, 10 ⁶ psi	20	21	21
Thermal Conductivity, Btu-in/ft ² -hr.-°F	120	74.5	72.6
	20C		
	900C		
Thermal Expansion Coefficient, 10 ⁻⁶ /°F	77-212F 3.25 77-392F 2.41-2.94 77-572F 2.45-2.87 77-662F 2.72 77-752F 2.52-2.82 77-842F 2.79-2.98 77-932F 3.17-3.45 77-1112F 4.36 77-1292F 5.12 77-1472F 5.75 77-1652F 6.30	2.57 2.64 2.71 2.79 3.14 3.83 4.32 5.50 6.11 6.65 7.10	1.11 1.60
Tensile Strength, ksi:	75-85 40-73 83-94 70-88 92-100 85-94 98-105 93-100 104 min 99 min 106 min 102 min 106 min 102 min 106 min 102 min	70-82 35-72 80-92 70-88 90-98 86-95 95-102 91-100 98-105 95-102 104 min 102 min 104 min 102 min 104 min 102 min	65.5 38 33
0.2% Offset Yield Strength, ksi:	18-32 10-19 7-12 5-8 3-5 2-4 2-3.5 1-3	19-32 10-20 6-12 4-8 3-6 2-4 2-3 1-3	
% Elongation in 2 inches	Ex. Hard Spring Ex. Spring		

There appears to be no published information on the modulus of rupture or flexural strength of the nickel-iron alloys. By means of simple cantilever bending tests on narrow strips cut from commercially available package lids, the writer has obtained 107 ksi as a typical value of the modulus of rupture of "Kovar" lids*. In these tests one end of the strip was clamped in a vise, and load was applied to the other (free) end through a hand-held force gage, with the direction of the load constantly changed so that it remained perpendicular to the strip as the strip deflected (see sketch below). The modulus of rupture σ_b was easily computed from the measured values of the maximum load P_{\max} and the distance L between the load and the kink or plastic hinge which forms at the clamped end, through the formula $\sigma_b = 6 P_{\max} L / bt^2$, where b is the width of the strip and t is its thickness. Such tests are recommended whenever estimates are needed of the modulus of rupture of a lid or base material.



*With a coefficient of variation of 8%

6. Solders

Gold-Based Solders.- Semi-Alloys, Inc. (888 So. Columbus Ave., Mt. Vernon, NY 10550) produces a large variety of solder and brazing alloys, including four gold-based eutectics of possible use for microcircuit package assembly. From their Technical Bulletin AU-80 and direct telephone contact with individuals in the company, the following data have been obtained on those four alloys:

Alloy Designation		A905	A911	A912	A914
Composition, Weight %		80 Au 20 Sn	88 Au 12 Ge	75 Au 25 Sb	96.9 Au 3.1 Si
Melting Point	°C	280	356	360	370
	°F	536	673	680	698
Thermal Conductivity, cal/cm·s·°C		0.60	0.63	0.54	0.68
Thermal Expansion Coefficient, 10 ⁻⁶ /°C		16.0	12.6	12.9	13.7
Density, g/cm ³		14.53			
Young's Modulus, 10 ⁶ psi	R.T.	8.5	12.1		
	100C	8.8			
Tensile Strength, ksi		44	50		

Indium Solders.- The Indium Corporation of America (Utica, NY 13503) specializes in the production of solders containing indium. The following table gives data on several of those solders (those included in their "micro-electronics kit") as well as on two of their tin-lead solders (#106, #171), all of it abstracted from the Indium Corporation booklet entitled "Indalloy Speciality Solders."

Alloy Designation	290	2	4	204	205	7	206	10	150	164	106	171
Composition, Weight %	97 In 3 Ag	80 In 15 Pb 5 Ag	100 In	70 In 30 Pb	60 In 40 Pb	50 In 50 Pb	40 In 60 Pb	25 In 75 Pb	19 In 81 Pb	5 In 92.5 Pb 2.5 Ag	63 Sn 37 Pb	5 Sn 95 Pb
Liquidus °C	143	149	157	174	185	209	225	264	280	300	183	314
°F	290	300	313	345	365	408	437	508	536	572	361	597
Solidus °C	143	142	157	160	174	180	195	250	270		183	311
°F	290	290	313	320	345	356	383	482	518		361	592
Density, lb/in ³	.2664	.2834	.2640	.2956	.3077	.3198	.3355	.3599	.3707	.3978	.3032	.3980
Electrical Conductivity, % of Cu	23.0	13.0	24.0	8.8	7.0	6.0	5.2	4.6	4.5	5.5	11.5	8.8
Thermal Conductivity at 85C, Watts/cm°C	0.73	0.43	0.78	0.38	0.29	0.22	0.19	0.18	0.17	0.25		.23
Thermal Expansion Coefficient, 10 ⁻⁶ /°C	22	10	29	28	27	27	26	26	27	25	25	29.8
Tensile Strength, psi	800	2550	575	3450	4150	4670	5000	5450	5550	4560	7700	3400
Shear Strength, psi		2150	890			2680		3520		2830		

Tin-Lead and Tin-Lead-Antimony Solders.- In the previous table data were given on two tin-lead solders of the Indium Corporation. In the following table are summarized the properties of the tin-lead and tin-lead-antimony solders of Alpha Metals, Inc. (600 Route 440, Jersey City, NJ 07304). The information was obtained through the company's literature (Catalog S/M-62) and direct telephone contact.

Alloy Designation	63/37	60/40	50/50	82	83	64	54	44
Composition (Weight %)	63 Sn 37 Pb	60 Sn 40 Pb	50 Sn 50 Pb	55 Sn 42.5 Pb 2.5 Sb	52 Sn 45 Pb 3.0 Sb	54 Sn 44 Pb 2 Sb	45 Sn 53 Pb 2 Sb	35 Sn 63.5 Pb 1.5 Sb
Form	Bar Wire	Bar Wire	Bar Wire	Bar	Bar	Wire	Wire	Wire
Melting Temp. Range, °F	361	361- 374	361- 421	368- 378	368- 382	368- 385	368- 419	368- 464
Tensile Strength, psi	7000	6900	5500	7800	8000	7700	6600	6000
Shear Strength, psi	5000	5100	4700	6400	6600	6400	5500	5000
% Elongation	25-35	25-40	40-70	36-40	36-40			
Thermal Conductivity, cal/cm-s.°C	R.T.	.118						
	140 C	.111						
Specific Heat, cal/g.°C	25-183 C		.051					
	216-300 C		.046					

A more extensive survey of tin-lead and tin-lead-antimony solders is contained in the following table. The data have been compiled from several sources, including: The Alpha Metals Co.; "Solders and Soldering," by H.H. Manko (McGraw-Hill, 1964); "Soft-Soldering Handbook," by C.H. Thwaites (International Tin Research Institute, Frazer Road, Perivale, Greenford, Middlesex, England; U.S. Office: 1353 Perry St., Columbus, Ohio 43201); the 1976 "Handbook for Clad Metals" (Technical Materials, Inc., 5 Wellington Rd., Lincoln, RI 02865); the 1981 "Handbook of Printed Circuit Design, Manufacture, Components and Assembly," by Giovanni Leonida (Electrochemical Publications, Ltd., Ayr, Scotland); and the "Development of Highly Reliable Soldered Joints for Printed Circuit Boards" (report on Contract No. NAS8-21233, Westinghouse Defense and Space Center, Aerospace Division, Baltimore, MD, Aug. 1968; NTIS No. N69-25697.)

Composition, Weight %		Specific Gravity	Strength, psi		Elongation %	Thermal Expansion Coefficient		Thermal Conductivity	Specific Heat
Sa	Sb		Tensile	Shear		Temp. Range °C	10 ⁻⁶ /°C		
100	7.29	1400			0-100	23.3*	.156	
100	.0007		1880	2560	55				
97	2.975	7.25	4080	4080	40				
94.8	5.17	7.43	5300	5360	38				
94.4	5.59		5620	5720	42				
93.7	6.2		5800	6020	32				
90	7.55	6400			15-110	22.1	.148	
85	7.71						.139	
80	7.85	7200					.13	
75	8.01							
70	8.17	7800			15-100	21.6		
66.1	8.34	6860	5540	31				
65		7600						
63.9	.985	8.42	7780	5720	20				
63	8.52	7300	5000	25-35	15-100	24.7 ⁸⁰ 24.7 ⁸⁰	.121	
60		6900	5100	25-40			.118**	
59.9	3.4		9000	6140	17.5				
59.35	3.55		8840	6140	17.5				
58.85	3.85		9100	6160	12.5				
56.1	8.70	5900	5580	38.7				
55		6500						
55	2.5		7800	6400	36-40				
54	2		7700	6400					
52.82	1.62		6720	5840	31.2				
52	3		8000	6600	36-40				
50.67	2.75		7360	5980	30				
50.15	3.00	8.7	7500	6120	29				
50	8.89	5700	4700	40-70	15-110	23.4	.111	***

(For footnotes and conclusion of table, see next page.)

Composition, Weight %		Specific Gravity	Strength, psi		Elongation %	Thermal Expansion Coefficient		Thermal Conductivity	Specific Heat.
Sn	Sb		Pb	Tensile		Shear	Temp. Range °C		
49.65	3.13	47.22	7520	6020	27.5				
45	55	5600	5500					
45	2	53	6600	5500	45				
44.8	55.2	5300	4660	36.2				
42.4	1.22	56.38	6830	5100	33.8				
40.4	2.24	57.36	6780	5100	33.8				
40	2.45	57.55	7100	5280	33.8	15-110	24.1	.096	.040
40	60	5400						
39.72	2.61	57.65	7020	5300	32.5				
35	1.5	63.5	6000	5000					
35	65	5200						
33.7	66.3	5740	4260	25				
31.8	.94	67.26	6120	4500	20				
30.2	1.65	68.15	6460	4520	21				
30.1	1.75	68.15	6580	4380	21				
30	70	5000				25.1	.094	
29.8	1.92	68.28	6600	4440	18.8				
25	75	4800						
20	80	4800			15-110	26.5	.089	
15	85	4600						
10	90	4400						
5	95	4000			15-110	28.7	.085	
....	100	1500			17-100	29.2	.083	

* 15.5 - 30.5, depending on crystal axis direction.
 ** .118 at room temperature; .111 at 140 C
 *** .051 from 25 - 183 C; .046 from 216 - 300 C
 ** - 130 C to + 25 C: 21.2
 + 25 C to + 125 C: 23.2
 + 125 C to + 150 C: 15.5
 - 130 C to + 150 C: 21.4

Thermal expansion data in a recent report by B.D. Dunn ("The Resistance of Space-Quality Solder Joints to Thermal Fatigue," European Space Research & Technology Centre, Noordwijk, The Netherlands, EAS STM-207, Sept. 1978) raises questions as to the validity of the thermal expansion coefficients presented in the previous table. Dunn reports the following thermal expansion coefficients for 63/37 tin/lead solder:

Temperature Range, °C	-100 to 0	0 to 50	0 to 100	-100 to 100
Thermal Expansion Coeff., $10^{-6}/^{\circ}\text{C}$	17.5	16.1	14.7	15.9

These are somewhat lower than the values given for this solder in the previous table (including the footnote). In a private communication to the author, Dunn explains that the difference is probably due to (a) the purity of his solder and (b) the fact that previously reported measurements were all made on cast bars which were relatively slow-cooled and hence possessed a large eutectic grain structure, whereas his measurements were performed on samples cut from fast-cooled castings with a smaller grain structure. It is believed that the latter specimens (and therefore Dunn's values) are more representative of a solidified high purity solder joint.

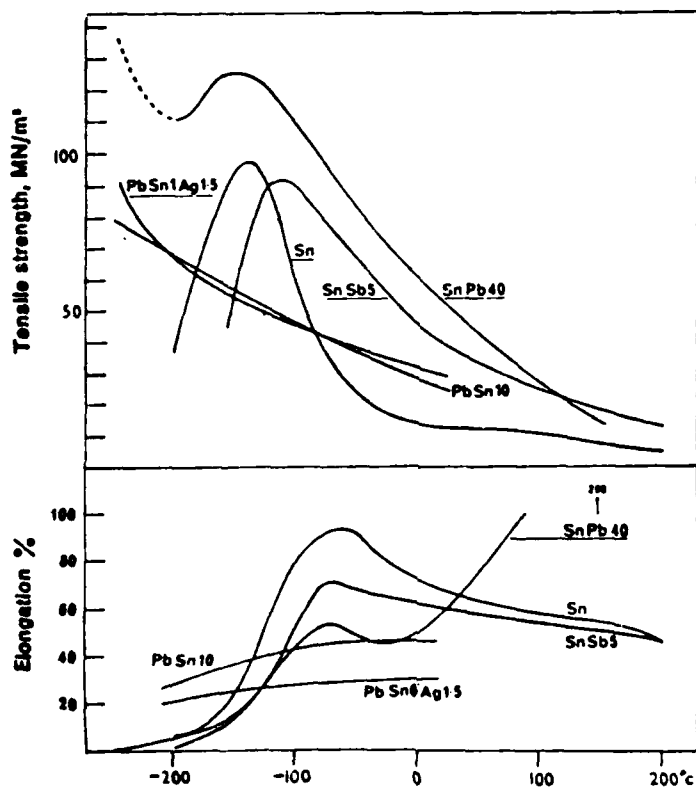
Effects of Temperature and Rate of Testing.- As is to be expected, the mechanical properties of solders are temperature dependent, and inasmuch as solders tend to creep, one can expect the mechanical properties to be sensitive also to the rate of testing, i.e., to the rate at which the load or deformation is imposed.

For the tensile and shear strengths of 63/37 tin/lead solder, in particular, the temperature dependence is shown in the following table. In

this tabulation the tensile data are from the "Handbook of Printed Circuit Design, Manufacture, Components & Assembly," by G. Leonida (Electrochemical Publications Ltd., Ayr, Scotland, 1981), and the shear data are adapted from the report, "Development of Highly Reliable Soldered Joints for Printed Circuit Boards" (Westinghouse Defense and Space Center, Aerospace Div., Baltimore, MD, Aug. 1968; NTIS No. N69-25697).

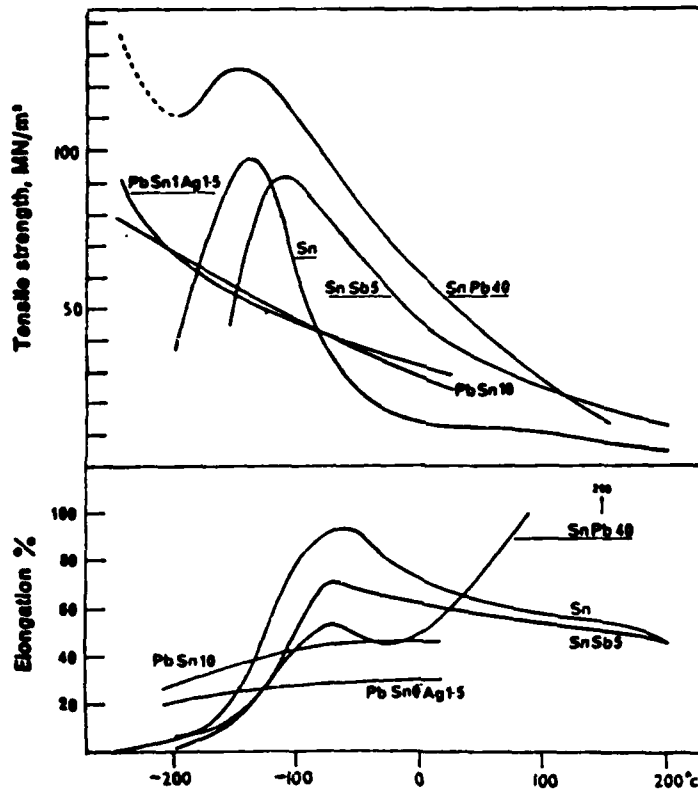
Temperature, °C	Tensile Strength		Shear Strength	
	MN/m ²	psi	MN/m ²	psi
-130			89	12,900
-60			58	8,300
0	55	8,000		
20	54	7,800		
25			29	4,300
40	49	7,100		
60	44	6,400		
80	39	5,700	18	2,600
100	30	4,400		
120	21	3,000	12	1,700
140	15	2,100		
150			8.6	1,300
160	9	1,400		
180	.5	70		

The following graphs from the "Soft-Soldering Handbook," by C.J. Thwaites, referred to earlier, show the effect of temperature on the tensile strength and elongation of several other solders.



Variation in tensile properties of bulk solder alloys with temperature of testing: note the loss in ductility of tin-rich alloys below about minus 100°C.

The following graphs from the "Soft-Soldering Handbook," by C.J. Thwaites, referred to earlier, show the effect of temperature on the tensile strength and elongation of several other solders.



Variation in tensile properties of bulk solder alloys with temperature of testing: note the loss in ductility of tin-rich alloys below about minus 100°C.

this tabulation the tensile data are from the "Handbook of Printed Circuit Design, Manufacture, Components & Assembly," by G. Leonida (Electrochemical Publications Ltd., Ayr, Scotland, 1981), and the shear data are adapted from the report, "Development of Highly Reliable Soldered Joints for Printed Circuit Boards" (Westinghouse Defense and Space Center, Aerospace Div., Baltimore, MD, Aug. 1968; NTIS No. N69-25697).

Temperature, °C	Tensile Strength		Shear Strength	
	MN/m ²	psi	MN/m ²	psi
-130			89	12,900
-60			58	8,300
0	55	8,000		
20	54	7,800		
25			29	4,300
40	49	7,100		
60	44	6,400		
80	39	5,700	18	2,600
100	30	4,400		
120	21	3,000	12	1,700
140	15	2,100		
150			8.6	1,300
160	9	1,400		
180	.5	70		

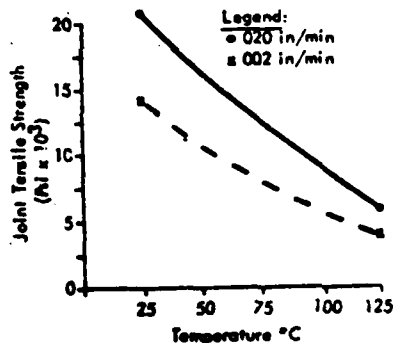
B.D. Dunn, in the report cited earlier, gives additional data on the temperature dependence of the tensile properties of 63/37 tin/lead solder, which is reproduced in the table below. Dunn's tests were conducted at the relatively low strain rate of $1.3 \times 10^{-4} \text{ s}^{-1}$. This strain rate was used in order to more nearly represent the strain rates associated with thermal fatigue, and the associated creep effects cause the strengths to be somewhat lower than those obtained in standard tests at higher strain rates.

Temperature °C	Young's Modulus, 10^6 psi	Proportional Limit, psi	Tensile Strength, MN/m ² psi		Permanent Elongation after Fracture, %
-70	6.96	8240	86.0	12,500	30
-20	6.11	7020	63.9	9,270	20
+20	4.58	5110	46.8	6,790	26
+60	3.83	3260	33.5	4,860	38

Young's modulus values for four solders at three temperatures were measured by R.W. Rhode and J.C. Swearingen ("Deformation Modeling Applied to Stress Relaxation of Four Solder Alloys," J. of Engineering Materials and Technology, ASME, April 1980, pp. 207-214). Their results, which are based on measurement of stress and strain decrements upon unloading from 0.2% total applied strain, are given in the following table.

Material	Young's modulus, 10^6 psi		
	-51C	25C	71C
63 Sn - 37 Pb	5.25	4.18	3.76
62.5 Sn - 37 Pb - 0.5 Ag	5.34	4.35	4.05
37.5 Sn - 37.5 Pb - 25 In	5.00	4.50	3.80
50 Pb - 50 In	3.76	2.89	2.34

The strength of a relatively thin butted tensile joint of 63/37 tin/lead solder as a function of temperature and for two different extension rates is shown in the figure below, which is taken from the paper "Fatigue Properties of Solder Joints," by Roger N. Wild, Welding Research Supplement to the Welding Journal, Nov. 1972, pp. 521-s to 526-s. It will be noted that the room temperature (25C) tensile strength of the joint is considerably higher than the previously cited tensile strengths for the bulk solder. This undoubtedly reflects the rather significant constraint against lateral contraction for the thin solder in a tensile butt joint as compared with the relatively free lateral contraction for the bulk solder in a standard tensile test. In this figure the strain rate effect, which is related to creep, is again evident.



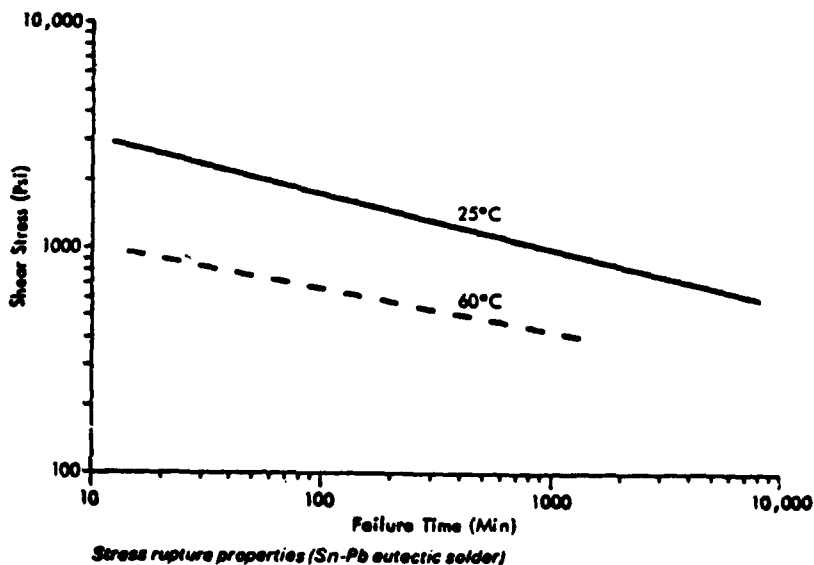
Note the Reduction in Joint Tensile Strength with Higher Temperatures and Lower Strain Rates

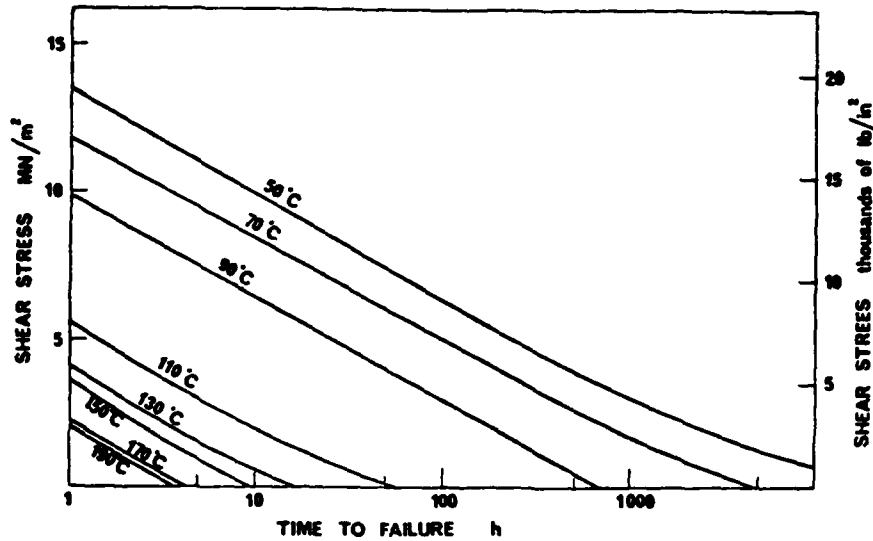
Additional data on the temperature and strain effects are provided by the following table, which gives shear strength values for six different soldered joints at 20C and 100C obtained at the very low strain rate of .05 mm/min. The table is taken from the "Soft Soldering Handbook," by C.J. Thwaites, referred to earlier.

Nominal Composition %				Shear Strength MN/m ² (lbf/in ²) at		Loss in strength (20°→100°C)
Sn	Pb	Sb	Ag	20°C	100°C	
60	40	-	-	20 (2840)	13 (1850)	35%
10	90	-	-	17 (2420)	11 (1560)	35%
62	36	-	2	28 (3980)	12 (1710)	57%
40	58	2	-	24 (3410)	11 (1560)	54%
95	-	5	-	28 (3980)	14 (1990)	50%
5	93.5	-	1.5	18 (2560)	12 (1710)	33%

It will be noted, for example, that the shear strength of the 60/40 tin/lead solder at 20C is appreciably below that given in earlier tables for the same solder at normal testing rates.

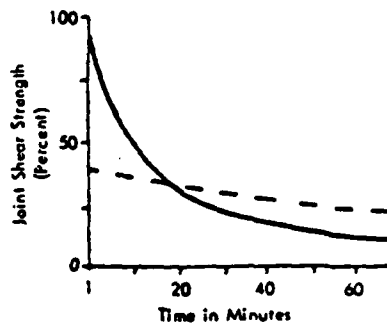
Creep Rupture and Stress Relaxation.- Under a steadily maintained load solder will creep and eventually rupture, especially at higher temperatures. A small amount of data is available on this phenomenon. Some of it is reproduced in the two figures below. The figures are taken from the carrier cited works of Wild and Thwaites, respectively. Both figures are for lap shear joints; the first applies to a 63/37 tin/lead solder, the second to a 95/5 tin/silver solder.





Stress — time to failure curves at various temperatures for overlap joints between brass components soldered with 95% tin-5% silver alloy.

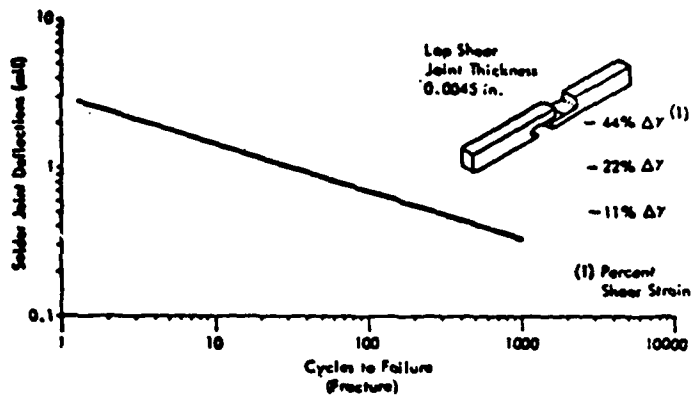
Closely related to creep is the phenomenon of relaxation, that is, the continual reduction in stresses or load while the deformation is held constant. The following figure which is taken from the paper by Wild, pertains to a lap shear joint and shows the relaxation of load (ordinate) with time if the joint is initially loaded to 90% (solid curve) or 40% (dashed curve) of its static strength and the resulting initial deformation is maintained throughout the test.



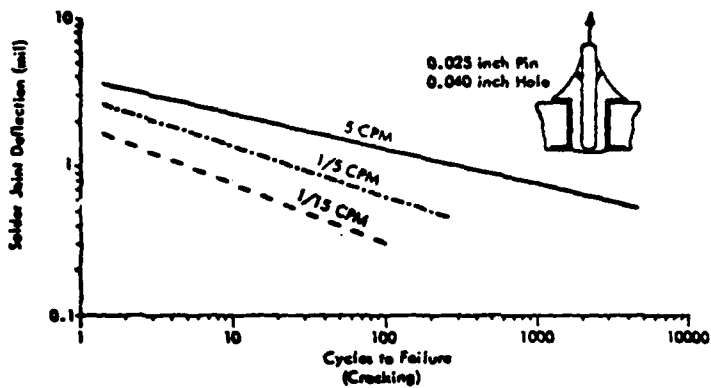
Note Joint Relaxation is Very Rapid, Especially at the Higher Initial Joint Loadings

Stress relaxation properties

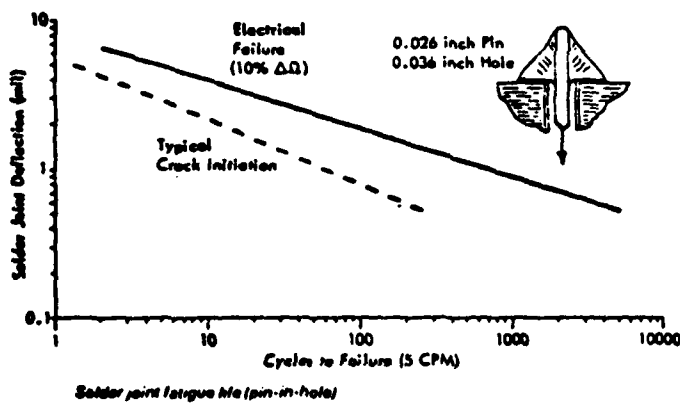
Fatigue.- Solders, like most other metals, are vulnerable to fatigue. The next three figures, from the paper by Wild, provide some data on the fatigue life (cycles to failure) of three types of 63/37 tin/lead solder joints. The first figure pertains to a lap shear joint tested at 5 cycles per minute (CPM). The second figure pertains to a "pin-in-hole" joint loaded so as to produce "tensile shear" in the solder, and the third to a similar joint loaded so as to produce "compressive shear." The effect of loading rate (CPM) is clearly visible in the data of the second figure: the slower the loading rate, the shorter the lifetime (as measured in cycles). A great deal of additional data of the same kind covering additional temperatures and additional solder compositions, can be found in the report "Some Fatigue Properties of Solders and Solder Joints," by R.N. Wild, IBM Report No. 73Z00421, IBM Electronic Systems Center, Owego, NY, January 1973.



Joint Failure was a Distinct Crack Condition at $\times 10$ Magnification
Lap-shear fatigue life (eutectic Sn-Pb solder)



Note Joint Cracking Occurs More Rapidly with Lower Strain Rates
Strain rate effect on fatigue life



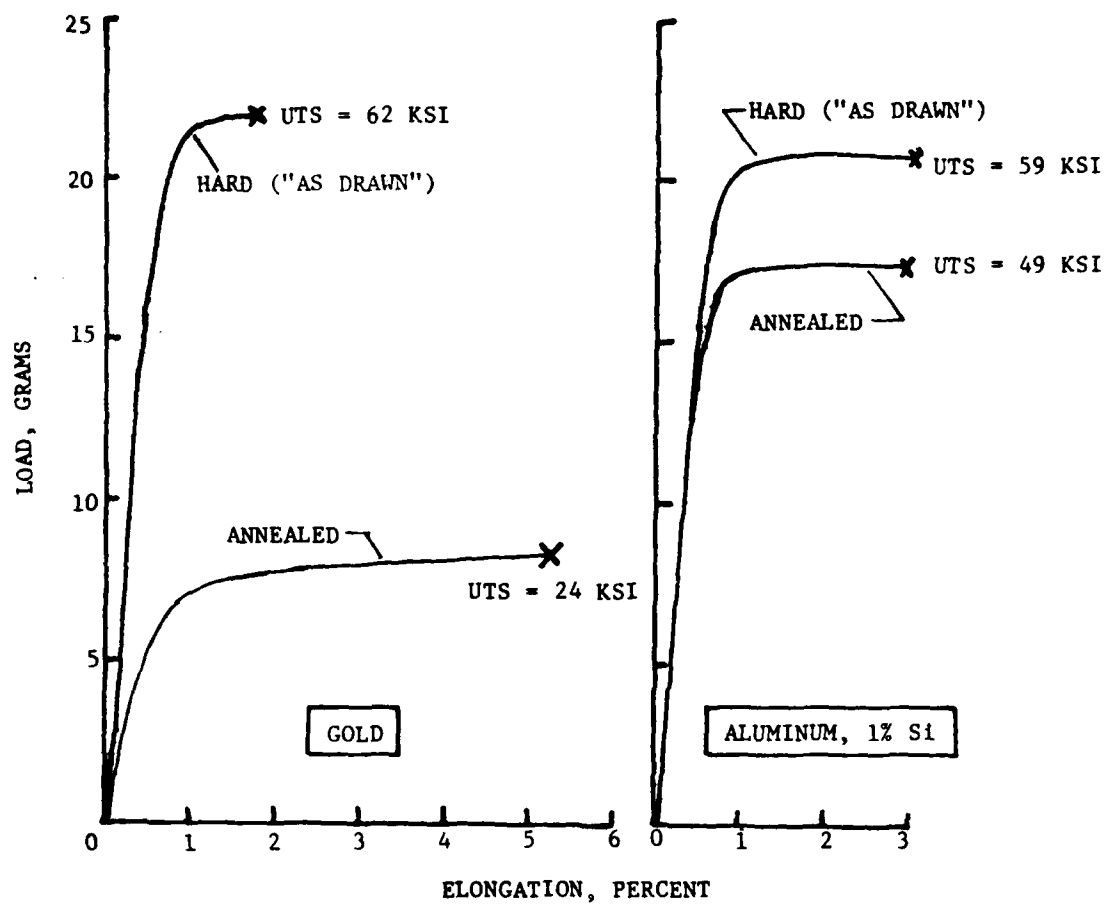
7. Wires

Gold of 99.99% purity and aluminum with 1% silicon or 1% magnesium are materials frequently used for the fine internal wires in microcircuit packages. These wires can be supplied in the hard (or "as drawn") condition or in various annealed states. The annealing reduces the ultimate tensile strength by an amount that depends on the degree of annealing and, in the case of gold, significantly increases the ductility, as measured by the elongation at failure in a tension test with a 10-inch gage length.

The following information from one supplier, the Consolidated Refining Co., Inc. (115 Hoyt Ave., Mamaroneck, NY 10543) will give some idea of the tensile strengths and ductilities obtainable in gold and aluminum fine wires. (Other suppliers include the Sigmund Cohn Corp. of 121 S. Columbus Ave., Mt. Vernon, NY 10553 and the Secon Metals Corp. of 7 Intervale St., White Plains, NY 10606). The range of breaking loads and elongations shown for any given diameter indicates the variations achievable through alteration of the annealing conditions and other manufacturing parameters. The manufacturing parameters can actually be so controlled as to permit the elongations and breaking loads to be specified to within much narrower limits than the table suggests. For example, for 0.001-in. aluminum wire with 1% magnesium, one may specify the breaking load to lie between 15 and 17 grams and the elongation to be between 1 and 3%.

Nominal Diameter, in.	Gold, Hard		Gold, Annealed		Aluminum		
	% Elongation	Min. Breaking Load, grams	% Elongation	Min. Breaking Load, grams	% Elongation	Breaking Loads, grams	
						1% Si	1% Mg
0.0005	0.5-1.5	3	1-3	1	0.5-2.0	1-5	1-5
0.0007	0.5-2.0	6	1-7	2	0.5-2.5	3-12	4-12
0.0008	0.5-2.0	8	1-8	3			
0.0009	0.5-2.0	13	1-8	4			
0.001	0.5-2.5	17	1-12	5	0.5-3.5	12-22	12-24
0.0012					0.5-5.0	14-30	14-30
0.00125					0.5-5.0	15-32	18-36
0.0015	0.5-2.5	35	1-15	12	0.5-5.0	20-50	25-60
0.002	0.5-3.0	70	2-20	20	1-5	40-90	45-100
0.003	0.5-3.0	150	4-25	45			
0.005	0.5-4.0	420	5-25	120			

Typical curves of load vs. elongation for gold and aluminum wires of 0.001-in. diameter are shown in the following graphs. In these graphs, the X's represent the breaking points, and the nominal ultimate tensile strength (UTS) corresponding to each one is marked near the X. The graphs show clearly the significant reduction in strength and increase in elongation produced in gold wires by annealing. The nominal young's moduli of gold and steel are 12,000,000 and 10,000,000 psi, respectively. However, these values are based on the initial slopes of somewhat curving stress-strain curves. A better representation of the load vs. elongation behavior depicted in the graphs for loads up to about 2/3 of the breaking load can be obtained by using reduced moduli of around 10,000,000 and 9,000,000 psi, respectively, for gold and aluminum.



APPENDIX B: FLEXURAL ANALYSIS OF A TWO-COMPONENT COMPOSITE PLATE

Here we consider a composite plate made up of two isotropic elastic plates bonded together, as shown in Figure 1. The two components may have different properties, so we denote by E_1 and ν_1 the Young's modulus and Poisson's ratio of the upper plate, and by E_2 and ν_2 the corresponding quantities for the lower plate. The thicknesses of the two plates are t_1 and t_2 , respectively, and $t = t_1 + t_2$ will denote the combined thickness.

Figure 2 shows a unit segment of the plate acted upon only by bending moments of intensity (e.g., in.-lb/in.) M_x in the x-direction and M_y in the y-direction. These will produce curvatures $K_x \equiv -\partial^2 w / \partial x^2$ and $K_y \equiv -\partial^2 w / \partial y^2$ in the two directions, where $w(x,y)$ represents the deflection surface of the plate. In this appendix equations will be developed showing how the curvatures K_x and K_y are related to the bending moments M_x and M_y . Formulas will also be developed for the extreme-fiber cross-sectional normal stresses in the two components at any location in terms of the bending moments M_x and M_y at that location. Finally, it will be shown how existing information for homogeneous (single component) plates can be used to obtain the bending moments in a two-component plate.

This appendix presents only the basic theory of two-component plates. Application of that theory to flatpack bases consisting of Kovar with a ceramic substrate bonded to it is discussed in Chapter 1, Section V, and demonstrated in Chapter 1, Section VIII.

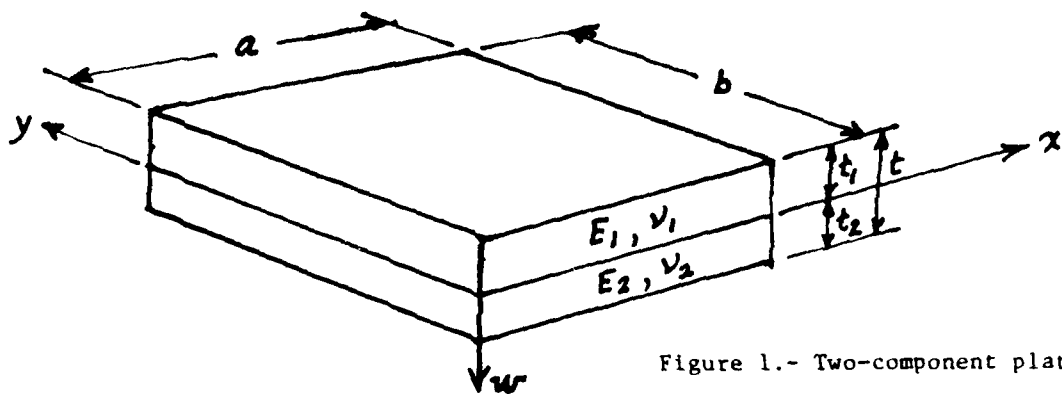


Figure 1.- Two-component plate.

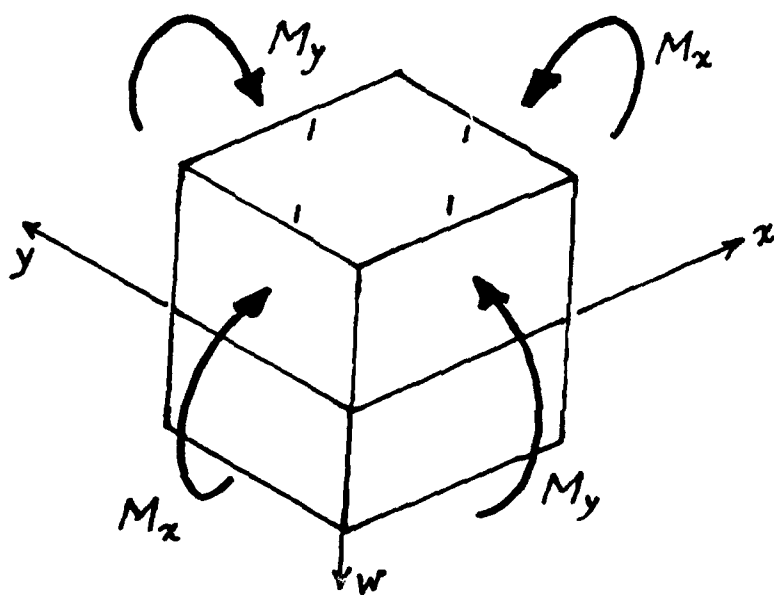


Figure 2.- Bending moments on infinitesimal segment.

1. Notation.- Short-hand symbols will be employed to represent certain parameter combinations that will arise naturally in the course of the derivations. These symbols are shown and defined as follows:

$$D_1 \equiv \frac{E_1 t_1^3}{12(1-\nu_1^2)} \quad D_2 \equiv \frac{E_2 t_2^3}{12(1-\nu_2^2)} \quad (1)$$

$$\bar{S} \equiv \frac{(E_1 t_1)(E_2 t_2)}{(E_1 t_1 + E_2 t_2)} \quad (2)$$

$$\bar{\nu} \equiv \frac{\nu_1 E_2 t_2 + \nu_2 E_1 t_1}{E_2 t_2 + E_1 t_1} \quad (3)$$

$$D_3 \equiv \frac{t^2}{4} \left(\frac{1-\nu_1 \bar{\nu}}{E_1 t_1} + \frac{1-\nu_2 \bar{\nu}}{E_2 t_2} \right)^{-1} \equiv \frac{t^2}{4} \frac{\bar{S}}{1-\bar{\nu}^2} \quad (4)$$

$$D \equiv D_1 + D_2 + D_3 \quad (5)$$

$$D' \equiv \nu_1 D_1 + \nu_2 D_2 + \bar{\nu} D_3 \quad (6)$$

$$\nu \equiv D'/D \quad (7)$$

In addition, we call attention to the notation in Figure 4 that will be used for the extreme-fiber cross-sectional normal stresses (positive for tension) in the individual components. The logic behind the subscripts in the symbols $\sigma_{x_{11}}$, $\sigma_{x_{12}}$, etc. will undoubtedly be obvious to the reader.

2. Moment-Curvature Relations.- Figure 3 shows the bending moments per unit width M_{x_1} , M_{x_2} , M_{y_1} , M_{y_2} , and middle-surface membrane forces per unit width N_x and N_y , in the individual components. It will be noted

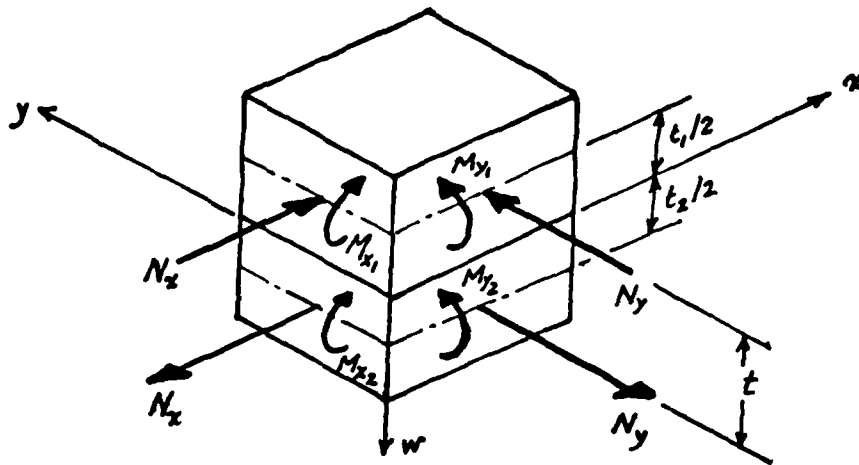


Figure 3.- Bending moments and membrane normal forces in individual components.

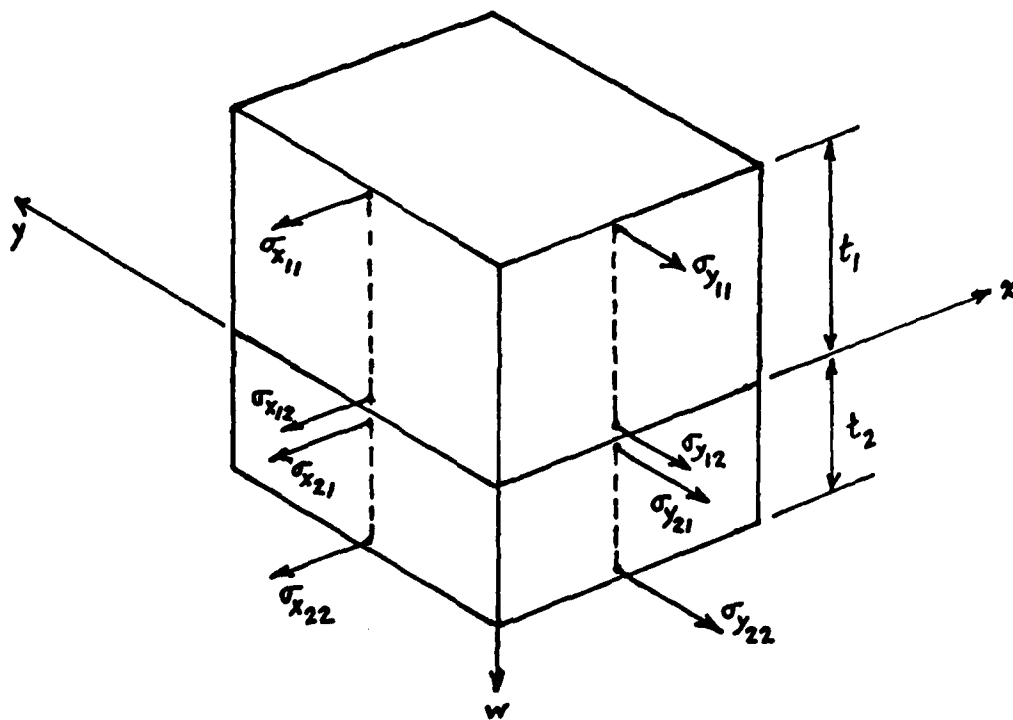


Figure 4.- Notation for extreme-fiber normal stresses in individual components.

that the latter are shown as tension in one component, compression in the other, so that on the cross sections as a whole there are no resultant forces, only resultant couples.

From the static equivalence of Figures 2 and 3, we have the following expressions for those resultant couples:

$$\begin{aligned} M_x &= M_{x_1} + M_{x_2} + N_x \frac{t}{2} \\ M_y &= M_{y_1} + M_{y_2} + N_y \frac{t}{2} \end{aligned} \quad (8)$$

We shall now imagine the curvatures K_x and K_y to be imposed and get expressions for the M_{x_1} , M_{x_2} , M_{y_1} , M_{y_2} , N_x and N_y resulting from that imposition. Substitution of those expressions into Equations (8) will then give the moment-curvature relations for the composite. The details follow:

From the moment-curvature relations for the individual components, we have

$$\begin{aligned} M_{x_1} &= D_1 (K_x + \nu_1 K_y) & M_{y_1} &= D_1 (K_y + \nu_1 K_x) \\ M_{x_2} &= D_2 (K_x + \nu_2 K_y) & M_{y_2} &= D_2 (K_y + \nu_2 K_x) \end{aligned} \quad (9)$$

Continuity of x-wise strain and of y-wise strain at the interface of the two components requires that

$$\begin{aligned} - \frac{N_x - \nu_1 N_y}{E_1 t_1} + K_x \frac{t_1}{2} &= \frac{N_x - \nu_2 N_y}{E_2 t_2} - K_x \frac{t_2}{2} \\ - \frac{N_y - \nu_1 N_x}{E_2 t_2} + K_y \frac{t_1}{2} &= \frac{N_y - \nu_2 N_x}{E_2 t_2} - K_y \frac{t_1}{2} \end{aligned} \quad (10)$$

Solving Equations (10) simultaneously for N_x and N_y gives

$$\begin{aligned} N_x &= \frac{\bar{S}t}{2} \frac{K_x + \bar{\nu}K_y}{1-\bar{\nu}^2} \\ N_y &= \frac{\bar{S}t}{2} \frac{K_y + \bar{\nu}K_x}{1-\bar{\nu}^2} \end{aligned} \quad (11)$$

Substitution of these expressions along with (9) into Equations (8) gives

$$M_x = D(K_x + \nu K_y) \quad M_y = D(K_y + \nu K_x) \quad (12)$$

as the moment-curvature relations for the composite, where D and ν are defined by Equations (5) and (7). It will be noted that Equations (12) are exactly the same as the moment-curvature relations of a homogeneous isotropic elastic plate (p. 81 of Reference 3, allowing for a difference of sign convention on w), except for the new definitions of D and ν . These new definitions reduce to the usual ones when $E_1 = E_2$ and $\nu_1 = \nu_2$, as they should.

Equations (12) can be inverted to give the curvatures in terms of the bending moments:

$$K_x = \frac{M_x - \nu M_y}{D(1-\nu^2)} \quad K_y = \frac{M_y - \nu M_x}{D(1-\nu^2)} \quad (13)$$

From this result we note that where $K_y = 0$, as it is along an x -wise supported edge, M_y and M_x have the following relationship:

$$M_y = \nu M_x \quad (14)$$

3. Stresses.— Any of the extreme-fiber stresses shown in Figure 4 can be obtained by superimposing the stress due to the membrane force and that due to the bending moment for the component in which the stress resides. Thus, referring to Figures 4 and 3 together, for the cross section normal to the x-axis we have

$$\begin{aligned}
 \sigma_{x_{11}} &= - (N_x/t_1) - (6 M_{x_1}/t_1^2) \\
 \sigma_{x_{12}} &= - (N_x/t_1) + (6 M_{x_1}/t_1^2) \\
 \sigma_{x_{21}} &= (N_x/t_2) - (6 M_{x_2}/t_2^2) \\
 \sigma_{x_{22}} &= (N_x/t_2) + (6 M_{x_2}/t_2^2)
 \end{aligned}
 \tag{15}$$

The corresponding equations for the cross section perpendicular to the y-axis are obtained by replacing every x by a y in the above.

Substitution of (9) and (11) into (15) gives the stresses in terms of the curvatures in the following form:

$$\left. \begin{aligned}
 \sigma_{x_{11}} \\
 \sigma_{x_{12}}
 \end{aligned} \right\} = \frac{\bar{S}t}{2t_1} \frac{K_x + \bar{\nu}K_y}{1 - \bar{\nu}^2} + \frac{E_1 t_1}{2} \frac{K_x + \nu_1 K_y}{1 - \nu_1^2}$$

$$\left. \begin{aligned}
 \sigma_{x_{21}} \\
 \sigma_{x_{22}}
 \end{aligned} \right\} = \frac{\bar{S}t}{2t_2} \frac{K_x + \bar{\nu}K_y}{1 - \bar{\nu}^2} + \frac{E_2 t_2}{2} \frac{K_x + \nu_2 K_y}{1 - \nu_2^2}$$

(16)

Replacing every x by a y and every y by an x, we can get the corresponding expressions for $\sigma_{y_{11}}$, $\sigma_{y_{12}}$, $\sigma_{y_{21}}$ and $\sigma_{y_{22}}$

It will usually be more convenient to have the stresses expressed in terms of the bending moments M_x and M_y , rather than in terms of the curvatures K_x and K_y . Therefore we shall use Equations (13) to eliminate K_x and K_y in (16). The resulting stress formulas are

$$\left. \begin{array}{l} \sigma_{x_{11}} \\ \sigma_{x_{12}} \end{array} \right\} = -\frac{\bar{S}t}{2t_1} \frac{M_x(1-\nu\bar{\nu}) + M_y(\bar{\nu}-\nu)}{D(1-\nu^2)(1-\bar{\nu}^2)} + \frac{E_1 t_1}{2} \frac{M_x(1-\nu\nu_1) + M_y(\nu_1-\nu)}{D(1-\nu^2)(1-\nu_1^2)}$$

(17)

$$\left. \begin{array}{l} \sigma_{x_{21}} \\ \sigma_{x_{22}} \end{array} \right\} = \frac{\bar{S}t}{2t_2} \frac{M_x(1-\nu\bar{\nu}) + M_y(\bar{\nu}-\nu)}{D(1-\nu^2)(1-\bar{\nu}^2)} + \frac{E_2 t_2}{2} \frac{M_x(1-\nu\nu_2) + M_y(\nu_2-\nu)}{D(1-\nu^2)(1-\nu_2^2)}$$

and the corresponding formulas for the σ_y stresses are obtained by replacing every x by a y and every y by an x .

If $M_x = M_y$, as it does at the center of a square plate if the boundary conditions and loading are properly symmetric, the stress equations reduce to

$$\left. \begin{array}{l} \sigma_{x_{11}} = \sigma_{y_{11}} \\ \sigma_{x_{12}} = \sigma_{y_{12}} \end{array} \right\} = \frac{M}{D(1+\nu)} \left[-\frac{\bar{S}t}{2t_1(1-\bar{\nu})} + \frac{E_1 t_1}{2(1-\nu_1)} \right]$$

(18)

$$\left. \begin{array}{l} \sigma_{x_{21}} = \sigma_{y_{21}} \\ \sigma_{x_{22}} = \sigma_{y_{22}} \end{array} \right\} = \frac{M}{D(1+\nu)} \left[\frac{\bar{S}t}{2t_2(1-\bar{\nu})} + \frac{E_2 t_2}{2(1-\nu_2)} \right]$$

where M is the common value of M_x and M_y .

4. Use of Existing Data.- The fact that the moment-curvature relations for the two-component plate have the same form as for the homogeneous plate means that any bending moments and deflections known for the latter, and expressed in terms of D and ν , will also be valid for the former, provided that D and ν are evaluated by means of Equations 5 and 7. Thus, much of the existing data for isotropic elastic plates can be taken over bodily and applied to two-component plates. For convenience we are presenting some of this existing data in Tables 1, 2 and 3. These tables give central deflection and bending moments at certain locations for plates with various boundary conditions subjected to a uniform pressure in the downward direction (i.e., in the w -direction of Figure 1). All of the information in these tables is taken from the treatise by Timoshenko and Woinowsky-Krieger, Reference 3, supplemented by Equation (14) of this appendix.*

The deflections given in these tables are valid for all values of ν , but as noted in the tables, the bending moments were computed for $\nu = 0.3$ and therefore, strictly speaking, are valid only for that ν . The error will usually be very small if the bending moments in the tables are assumed to be valid for other values of ν as well. However, if desired, one can readily calculate corrected bending moments, M'_x and M'_y , if ν has a value other than 0.3. The corrected moments at any location can be obtained from the tabulated moments, M_x and M_y , for the same location via the following formulas (from p. 97 of Reference 3):

* Material from Reference 3 is used with the permission of McGraw-Hill Book Company.

$$M'_x = \frac{1}{.91} [(1-.3v)M_x + (v-.3)M_y] \quad (19)$$

$$M'_y = \frac{1}{.91} [(1-.3v)M_y + (v-.3)M_x]$$

If $M_x = M_y = M$, these formulas reduce to

$$M'_x = M'_y = \frac{1+v}{1.3} M \quad (20)$$

If $v = .3$, they reduce to $M'_x = M_x$, $M'_y = M_y$, as they should.

Table 1.- Deflections and Bending Moments in a Uniformly Loaded Rectangular Plate with All Edges Clamped

$\frac{b}{a}$	Central Deflection, δ	Bending Moments (for $\nu = 0.3$)			
		At Center of Plate		At Middle of Longer Edges	
		M_x	M_y	M_x	M_y
1.0	.00126 pa^4/D	.0231 pa^2	.0231 pa^2	-.0513 pa^2	-.0154 pa^2
1.1	.00150 pa^4/D	.0264 pa^2	.0231 pa^2	-.0581 pa^2	-.0174 pa^2
1.2	.00172 pa^4/D	.0299 pa^2	.0228 pa^2	-.0639 pa^2	-.0192 pa^2
1.3	.00191 pa^4/D	.0327 pa^2	.0222 pa^2	-.0687 pa^2	-.0206 pa^2
1.4	.00207 pa^4/D	.0349 pa^2	.0212 pa^2	-.0726 pa^2	-.0218 pa^2
1.5	.00220 pa^4/D	.0368 pa^2	.0203 pa^2	-.0757 pa^2	-.0227 pa^2
1.6	.00230 pa^4/D	.0381 pa^2	.0193 pa^2	-.0780 pa^2	-.0234 pa^2
1.7	.00238 pa^4/D	.0392 pa^2	.0182 pa^2	-.0799 pa^2	-.0240 pa^2
1.8	.00245 pa^4/D	.0401 pa^2	.0174 pa^2	-.0812 pa^2	-.0244 pa^2
1.9	.00249 pa^4/D	.0407 pa^2	.0165 pa^2	-.0822 pa^2	-.0247 pa^2
2.0	.00254 pa^4/D	.0412 pa^2	.0158 pa^2	-.0829 pa^2	-.0249 pa^2
∞	.00260 pa^4/D	.0417 pa^2	.0125 pa^2	-.0833 pa^2	-.0250 pa^2

Table 2.- Deflections and Bending Moments in a Uniformly Loaded Rectangular Plate with All Edges Simply Supported

$\frac{b}{a}$	Central Deflection, δ	Bending Moments at Center of Plate (for $\nu = 0.3$)	
		M_x	M_y
1.0	.00406 pa^4/D	.0479 pa^2	.0479 pa^2
1.1	.00485 pa^4/D	.0554 pa^2	.0493 pa^2
1.2	.00564 pa^4/D	.0627 pa^2	.0501 pa^2
1.3	.00638 pa^4/D	.0694 pa^2	.0503 pa^2
1.4	.00705 pa^4/D	.0755 pa^2	.0502 pa^2
1.5	.00772 pa^4/D	.0812 pa^2	.0498 pa^2
1.6	.00830 pa^4/D	.0862 pa^2	.0492 pa^2
1.7	.00883 pa^4/D	.0908 pa^2	.0486 pa^2
1.8	.00931 pa^4/D	.0948 pa^2	.0479 pa^2
1.9	.00974 pa^4/D	.0985 pa^2	.0471 pa^2
2.0	.01013 pa^4/D	.1017 pa^2	.0464 pa^2
3.0	.01223 pa^4/D	.1189 pa^2	.0406 pa^2
4.0	.01282 pa^4/D	.1235 pa^2	.0384 pa^2
5.0	.01297 pa^4/D	.1246 pa^2	.0375 pa^2
∞	.01302 pa^4/D	.1250 pa^2	.0375 pa^2

Table 3.- Deflections and Bending Moments in a Uniformly Loaded Rectangular Plate with the Long Edges Simply Supported, the Short Edges Clamped

$\frac{b}{a}$	Central Deflection, δ	Bending Moments (for $\nu = 0.3$)			
		At Center of Plate		At Middle of Clamped Edges	
		M_x	M_y	M_x	M_y
1.0	.00192 pa^4/D	.0244 pa^2	.0332 pa^2	-.0204 pa^2	-.0697 pa^2
1.1	.00251 pa^4/D	.0307 pa^2	.0371 pa^2	-.0236 pa^2	-.0787 pa^2
1.2	.00319 pa^4/D	.0376 pa^2	.0400 pa^2	-.0260 pa^2	-.0868 pa^2
1.3	.00388 pa^4/D	.0446 pa^2	.0426 pa^2	-.0281 pa^2	-.0938 pa^2
1.4	.00460 pa^4/D	.0514 pa^2	.0448 pa^2	-.0299 pa^2	-.0998 pa^2
1.5	.00531 pa^4/D	.0585 pa^2	.0460 pa^2	-.0315 pa^2	-.1049 pa^2
1.6	.00603 pa^4/D	.0650 pa^2	.0469 pa^2	-.0327 pa^2	-.1090 pa^2
1.7	.00668 pa^4/D	.0712 pa^2	.0475 pa^2	-.0337 pa^2	-.1122 pa^2
1.8	.00732 pa^4/D	.0768 pa^2	.0477 pa^2	-.0346 pa^2	-.1152 pa^2
1.9	.00790 pa^4/D	.0821 pa^2	.0476 pa^2	-.0352 pa^2	-.1174 pa^2
2.0	.00844 pa^4/D	.0869 pa^2	.0474 pa^2	-.0357 pa^2	-.1191 pa^2
3.0	.01168 pa^4/D	.1144 pa^2	.0419 pa^2	-.0374 pa^2	-.1246 pa^2
∞	.01302 pa^4/D	.1250 pa^2	.0375 pa^2	-.0375 pa^2	-.1250 pa^2

APPENDIX C: APPROXIMATE RESPONSE OF AN ELASTIC FLAT PLATE
TO A PRESCRIBED MOTION OF ITS BOUNDARY

In this appendix a simple approximate "one-term" analysis is presented for the elastic small-deflection flexural response of a flat plate to any prescribed translatory motion of its boundary supports in a direction normal to the plate. The simplicity of the analysis is due to the assumption that at every instant the deflection of the plate, relative to its supports, is that which would be produced by some uniform lateral pressure p . The outcome of the analysis is a differential equation that can be solved for this "equivalent lateral pressure" as a function of time, $p(t)$. For an illustrative application that is relevant to a flatpack in a flatwise impact, the theory is applied to a vertically falling horizontal plate with its boundary brought to rest by a suddenly imposed constant deceleration. Such a plate is an approximate representation of the base in an upside-down flatwise drop test or of the lid in a right-side-up flatwise drop test.

1. Notation.- The symbols E , ν , h , and ρ will denote the Young's modulus, Poisson's ratio, thickness and density of the plate, respectively (with h being used for thickness instead of t , so that t may be used for time); also $m = \rho h$ and $D = Eh^3/[12(1-\nu^2)]$ will denote the mass per unit area and plate flexural stiffness, respectively. If the plate is a two-component composite of the kind treated in Appendix B, with properties E_1 , ν_1 , h_1 , ρ_1 in the upper component and E_2 , ν_2 , h_2 , ρ_2 in the lower component, D and ν must be redefined by Equations (5) and (7) of Appendix B, and m must be evaluated as $\rho_1 h_1 + \rho_2 h_2$. (Note that the symbols h_1 and h_2 are being used here in place of the symbols t_1 and t_2 of Figure 1 of Appendix B.)

The fundamental circular frequency of the plate will be represented by ω_n , and $\tau = \omega_n t$ will be a dimensionless time parameter, with t the real time. In the illustrative application, v_o will denote the velocity of descent of the plate just prior to the onset of the constant deceleration of the supports, and t_s will denote the "stopping time," i.e., the duration of the deceleration. Thus, v_o/t_s will be the magnitude of the deceleration, and $\tau_s = \omega_n t_s$ will be the dimensionless stopping time. The results will be in terms of a dimensionless equivalent lateral pressure Q , defined by $Q(t) = p(t)/m\omega_n v_o$. Other symbols will be introduced and defined as needed.

2. Analysis.- The undeflected middle surface of the plate is imagined to be parallel to the horizontal xy plane of a stationary Cartesian reference frame, and the boundary support translations and elastic deflections of the plate relative to its boundary supports are taken to be positive in the z direction, which is normal to the xy plane and imagined to be downward. The total displacement $w(x,y,t)$ at any point (x,y) of the middle surface at any time t will be approximated by

$$\begin{aligned} w(x,y,t) &= w_o(t) + w_1(x,y,t) \\ &= w_o(t) + p(t)f(x,y) \end{aligned} \quad (1)$$

where $w_o(t)$ is the prescribed translation of the boundary supports; $w_1(x,y,t)$ is the deflection relative to the boundary supports; $f(x,y)$ is the static deflection the plate would experience, relative to its boundary supports, due to a unit uniform downward lateral pressure; and $p(t)$ is an amplitude function. Inasmuch as $f(x,y)$ is the deflection due to a unit lateral pressure, the amplitude function $p(t)$ may be regarded

as an "equivalent lateral pressure," that is, as the lateral pressure which, if applied statically, would give the plate the same deflection (relative to its supports) as it has at time t in its dynamic state.

Using dots to denote differentiation with respect to t , we may write the kinetic energy (KE) as

$$\begin{aligned} \text{KE} &= \frac{1}{2} m \iint \dot{w}^2 dx dy \\ &= \frac{1}{2} m \iint (\dot{w}_0^2 + 2\dot{w}_0 \dot{p}f + \dot{p}^2 f^2) dx dy \end{aligned} \quad (2)$$

Assuming small deflections (no middle-surface stretching) the strain energy (SE) is

$$\begin{aligned} \text{SE} &= \frac{1}{2} D \iint \left(\left(\frac{\partial^2 w_1}{\partial x^2} + \frac{\partial^2 w_1}{\partial y^2} \right)^2 - 2(1-\nu) \left[\frac{\partial^2 w_1}{\partial x^2} \frac{\partial^2 w_1}{\partial y^2} - \left(\frac{\partial^2 w_1}{\partial x \partial y} \right)^2 \right] \right) dx dy \\ &= \frac{1}{2} D p^2 I_1 \end{aligned} \quad (3)$$

where

$$\begin{aligned} I_1 &= \iint \left[(f_{xx} + f_{yy})^2 - 2(1-\nu) (f_{xx} f_{yy} - f_{xy}^2) \right] dx dy \\ &= \iint (f_{xxxx} + 2f_{xxyy} + f_{yyyy}) f dx dy \end{aligned} \quad (4)$$

In Eq. (4) subscript notation has been used for partial derivatives of f , and the second line has been obtained by integrations by parts in the first line, taking into account the fact that f exactly satisfies the boundary conditions (the procedure is described in pp. 88-92 of Ref. 3).

From expressions (2) and (3) the Lagrangian, $L = \text{KE} - \text{SE}$, may be formed, from which the following expressions are obtained:

$$\frac{d}{dt} \left(\frac{\partial L}{\partial \dot{p}} \right) = \frac{d}{dt} \left(\frac{\partial KE}{\partial \dot{p}} \right) = m \iint (\ddot{w}_0 + \ddot{p} f) f \, dx dy \quad (5)$$

$$- \frac{\partial L}{\partial q} = \frac{\partial SE}{\partial q} = D_p I_1 \quad (6)$$

Lagrange's equation,

$$\frac{d}{dt} \left(\frac{\partial L}{\partial \dot{p}} \right) - \frac{\partial L}{\partial p} = 0 \quad (7)$$

then yields the following differential equation governing $p(t)$:

$$\ddot{p} + \omega_n^2 p = - \dot{w}_0 I_2 / I_3 \quad (8)$$

where $I_2 = \iint f \, dx dy$, $I_3 = \iint f^2 \, dx dy$, and

$$\omega_n = \sqrt{D I_1 / m I_3} \quad (9)$$

is the Rayleigh approximation to the fundamental circular frequency of the plate based on the assumed mode $f(x,y)$.

Explicit evaluation of the integrals I_1 , I_2 and I_3 can usually be avoided, and Eq. (8) simplified, through the following expedients:

First, because $f(x,y)$ is the static deflection due to a unit uniform lateral pressure, the conservation of energy principle (external work =

strain energy) may be invoked to write $\frac{1}{2} \iint f(x,y) dx dy = \frac{1}{2} D I_1$,

whence $I_2 = D I_1$, and the differential equation (8) is reduced to

$$\ddot{p} + \omega_n^2 p = - m \omega_n^2 \dot{w}_0 \quad (10)$$

Secondly, if the plate is one whose exact fundamental frequency is already known (e.g., given in Ref. 10), it is suggested that the approximate ω_n , defined by Eq. (9), be replaced by the exact ω_n . (There should be little error in this substitution, inasmuch as the static deflection under uniform pressure is usually a good approximation to the fundamental vibration mode for purposes of the Rayleigh method.) Finally, a reduction in the number of parameters can be effected by putting Eq. (10) into the dimensionless form

$$\frac{d^2Q}{d\tau^2} + Q = - \frac{\ddot{w}_0}{\omega_n v_0} \quad (11)$$

where $\tau = \omega_n t$ is a dimensionless time and $Q = p/m\omega_n v_0$, with v_0 any reference velocity, is a dimensionless "equivalent pressure" parameter.

In the following illustrative application, v_0 will be taken as the velocity of descent of the falling horizontal plate just prior to the onset of the constant deceleration of its boundary supports.

3. Illustrative Application.- We now consider a horizontal plate in a vertical free fall, and assume that at time $t = 0$ a constant deceleration of magnitude v_0/t_s is suddenly imposed on its boundary supports, bringing them to rest in the "stopping time" t_s from the initial velocity v_0 . For this case, with $\tau_s = \omega_n t_s$ denoting the dimensionless stopping time, the right side of Equation (11) reduces to $1/\tau_s$ for $0 \leq \tau \leq \tau_s$ and 0 for $\tau > \tau_s$. The solution of Equation (11), subject to the initial conditions $Q = dQ/d\tau = 0$, is then

$$Q = (1 - \cos \tau) / \tau_s \quad \text{for } 0 \leq \tau \leq \tau_s \quad (12)$$

$$Q = [\cos (\tau - \tau_s) - \cos \tau] / \tau_s \quad \text{for } \tau > \tau_s \quad (13)$$

If the arrest is instantaneous ($\tau_s = 0$), the right side of Eq. (11) is zero for $\tau > 0$, and the jump condition $dQ/d\tau = 1$ at $\tau = 0+$, obtained by integrating Eq. (11) from $\tau = 0-$ to $\tau = 0+$, replaces the initial condition $dQ/d\tau = 0$. The following solution is then obtained:

$$Q = \sin \tau \quad \text{for } \tau \geq 0 \quad (14)$$

Equations (12), (13) and (14) have been used to plot the graphs in Figure 1, which show the elastic response of the plate (as measured by the dimensionless equivalent pressure Q) to the deceleration of its supports for several values of the dimensionless stopping time τ_s . From the positive and negative peaks of such graphs, the curves of Figure 2 were obtained. The solid and dashed curves in this figure give, respectively, the magnitudes of the maximum positive (i.e., downward) response and maximum negative (upward) response, as functions of the dimensionless stopping times τ_s , the response in both cases being expressed in terms of the dimensionless equivalent pressure Q .

Figures 1 and 2 are quite general, in that no assumption has been made as to the planform of the plate or its boundary conditions. We shall now further specialize the present application to the case of a homogeneous square plate with clamped edges and seek information about the maximum flexural stress σ_{\max} (occurring at the midpoints of the edges) and central deflection w_c (relative to the boundary) resulting from any given stopping time t_s . For a square plate with clamped edges it is known,

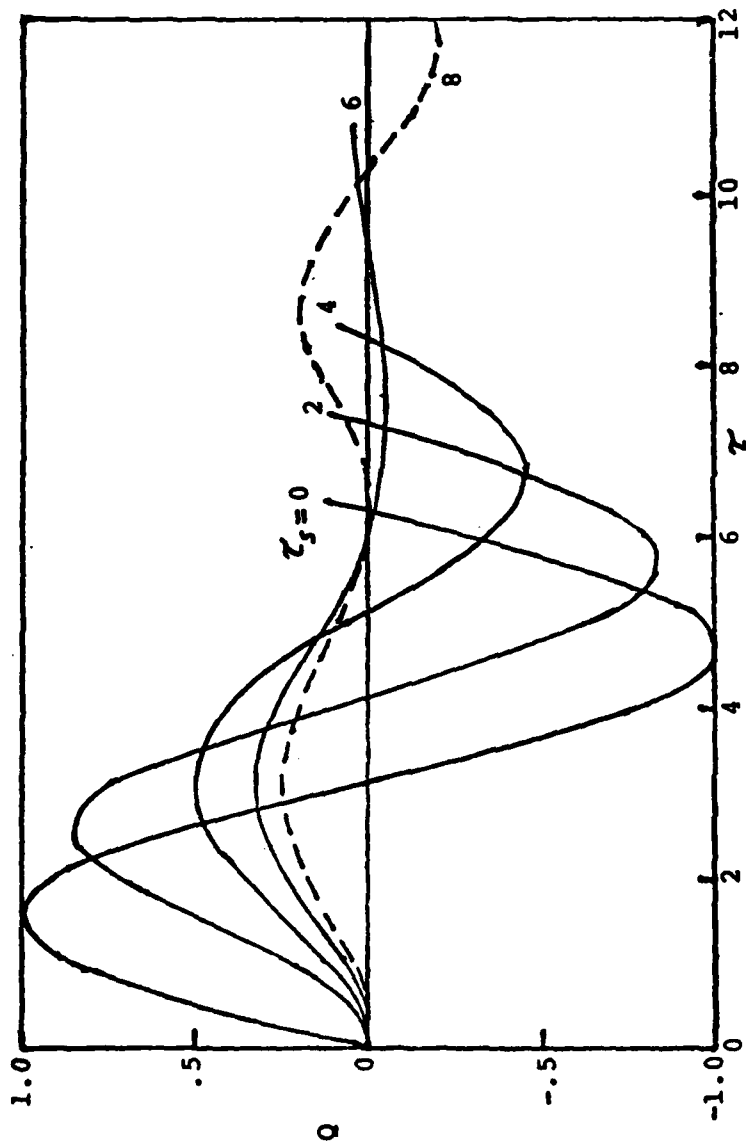


Figure 1.- Elastic response (in terms of dimensionless equivalent downward pressure Q) of a falling horizontal plate to a suddenly imposed constant deceleration of its boundary supports. (τ = dimensionless time; τ_s = dimensionless arresting time.)

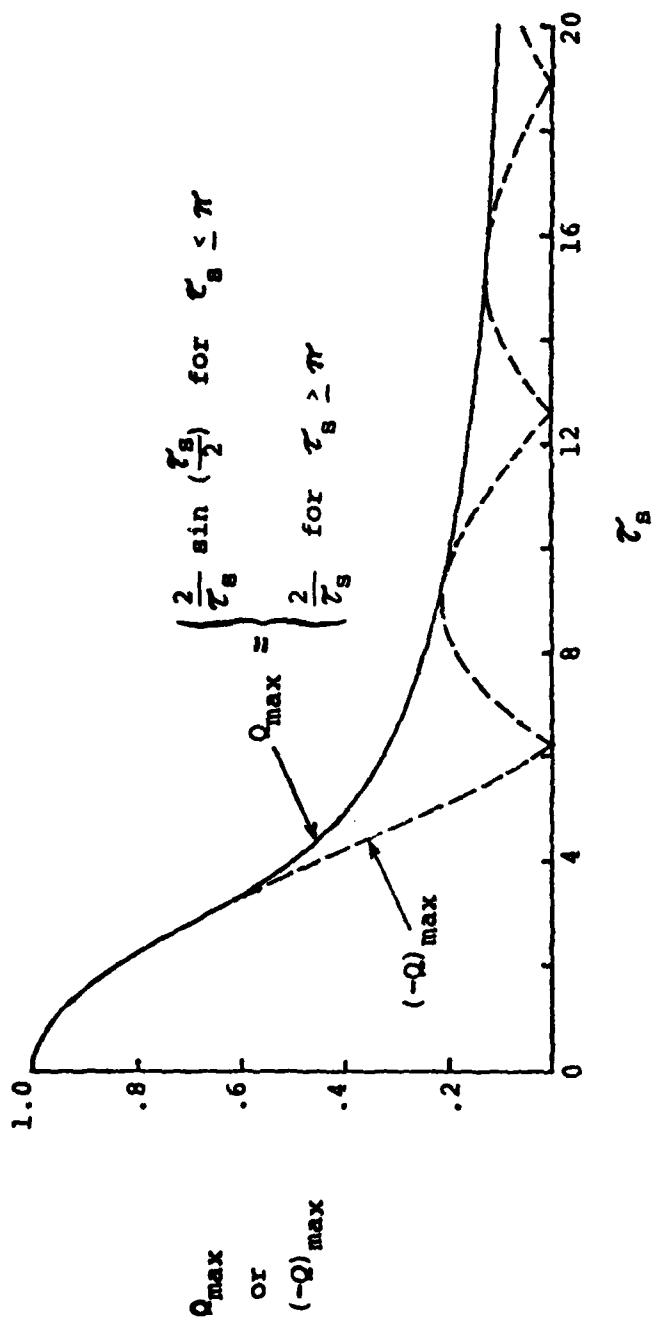


Figure 2.- Peak elastic responses of a falling horizontal plate to suddenly imposed constant deceleration of its boundary supports. (Solid curve: maximum positive (downward) dimensionless equivalent pressure. Dashed curve: maximum negative (upward) dimensionless equivalent pressure.)

from Table 4.30 of Reference 10 that $\omega_n = 35.98\sqrt{D/ma^4}$, where a is the length of a side. For such a plate under uniform lateral pressure p , it is also known from p. 202 of Reference 3, or from Table 1 of Appendix B, that

$\sigma_{\max} h^2/6pa^2 = .0513$ and $w_c D/pa^4 = .00126$, whence
 $p = \sigma_{\max} h^2/6(.0513)a^2 = w_c D/.00126a^4$. Thus the parameter $Q = p/m_n v_o$ can be interpreted as

$$Q = \frac{.3128 \sigma_{\max}}{v_o \sqrt{E'\rho}} = \frac{6.37 w_c h}{v_o a^2} \sqrt{\frac{E'}{\rho}}$$

where $E' = E/(1-\nu^2)$; consequently, σ_{\max} and w_c are given by

$$\sigma_{\max} = 3.20 v_o \sqrt{E'\rho} \cdot Q$$

$$w_c = \frac{.157 v_o a^2}{h} \sqrt{\frac{\rho}{E'}} \cdot Q$$

where Q is read from the solid curve in Fig. 2. We note that σ_{\max} and w_c are both proportional to the initial velocity v_o , and that for instantaneous or near-instantaneous arrest ($Q \approx 1$) σ_{\max} does not depend upon the dimensions of the plate, according to the present analysis.

In order to facilitate such calculations for clamped rectangular plates that are other than square, we present in Figure 3, a graph of $\omega_n \sqrt{ma^4/D}$ as a function of a/b for clamped isotropic rectangular plates of width a and length b (based on the data in Table 4.30 of Reference 10). For simply supported plates, the fundamental circular natural frequency is given by the formula

$$\omega_n = \pi^2 [1 + (a/b)^2] \sqrt{D/ma^4} \quad (15)$$

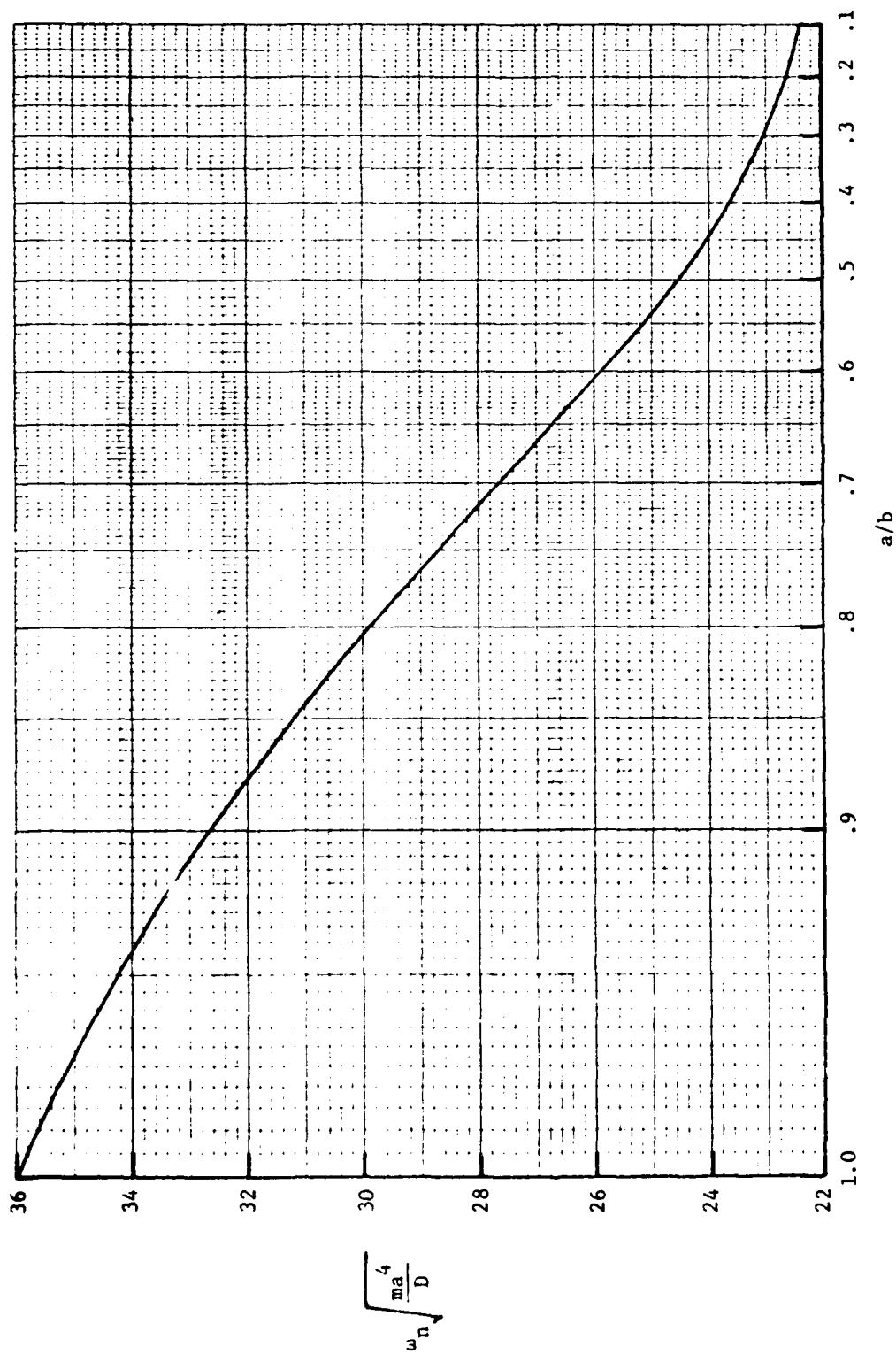


Figure 3.- Graph for determining fundamental circular natural frequency ω_n of clamped rectangular plate (a = width, b = length, m = mass per unit area, D = plate flexural stiffness). (Based on data in Reference 10.)

APPENDIX D: TRANSISTOR THERMAL STRESSES DUE TO INTERNAL HEAT GENERATION

By R.W. Perkins

1. Introduction.- The objective in this appendix is to conduct a preliminary study to obtain an approximate understanding of the thermal stresses that may occur in a transistor device. The problem was proposed by Mark Levi of the Rome Air Development Center. The physical situation is illustrated by Figure 1 which shows a typical part of a transistor device. The silicon transistor is in contact with a copper heat sink at the bottom. Above the silicon is an aluminum conductor and a polyimide film. The aluminum conductor can be described as a cylinder having a diameter and a height of approximately one micron. Above the cylinder is a much larger diameter plate of aluminum with a thickness of about one micron. The total thickness of the polyimide film is approximately two microns. The silicon wafer is approximately 250 microns thick.

The transistor heats up as a result of the current flow and voltage drop that occurs in the p-doped region. The current density is assumed to be approximately 5×10^5 amp/cm², and the voltage drop 0.6 volts. The duty cycle is unknown. The ambient temperature of the heat sink can lie in the range -55°C to 125°C.

Units such as the one described above are assumed to exist in some sort of pattern over the surface of the silicon wafer.

The problem of determining the thermal stresses that are present during the use cycle of the transistor device described above is quite complicated. With the additional specification of a specific geometry and an actual duty cycle, the problem would be amenable to solution by a finite element

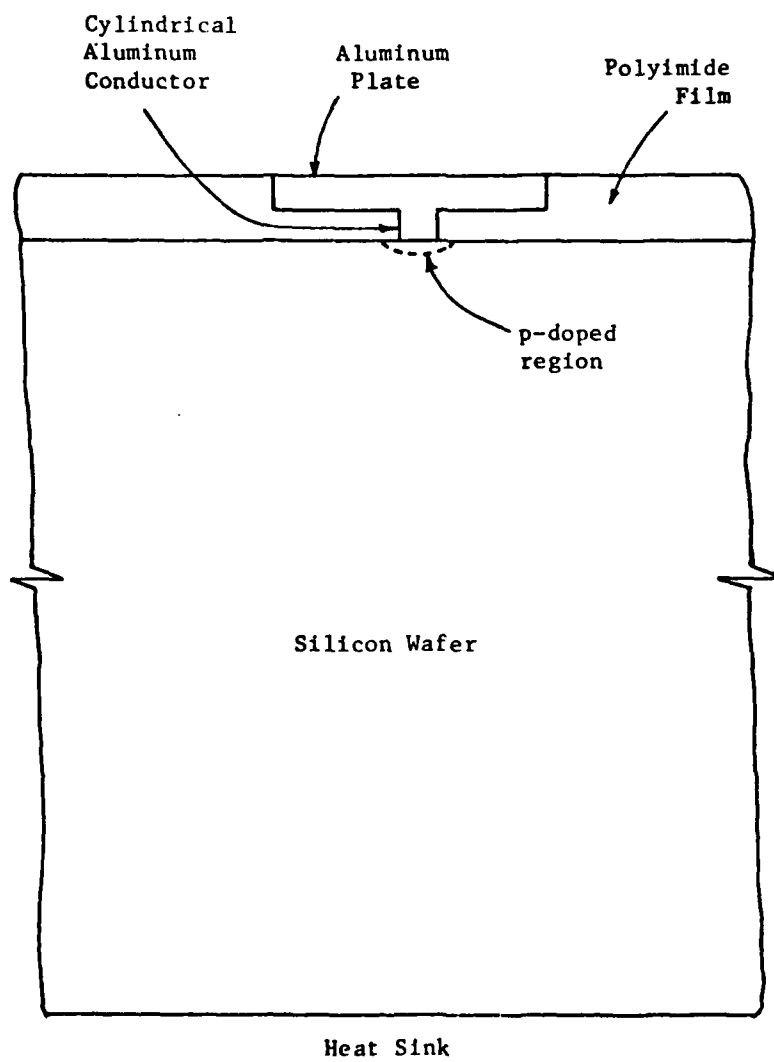


Figure 1. Transistor Device

or a finite difference method. For purposes of making a preliminary analysis a highly simplified one-dimensional problem was formulated and subjected to analysis.

For the purpose of the approximate analysis, the most serious stress problem was assumed to be one that would put the cylindrical aluminum conductor in tension since such a stress might be expected to lead to failure of the conductor and loss of the electrical function of the device. The tensile loading might be expected to cause failure either due to one occurrence of a stress large enough to cause rupture of the aluminum or due to the finite cycling of the aluminum cylinder in tensile strains that occur as a result of thermal cycling of the device.

It is recognized that tensile and shear stresses occur at the polyimide film aluminum and silicon interfaces and that failure may occur at these interfaces. Failures of this type are assumed to be relatively unimportant because they would not result in loss of the electrical function, therefore, stressing of this type is neglected in the analysis.

An initial investigation of the problem suggests that serious tensile stress will occur in the cylindrical aluminum conductor when the temperature of the polyimide film rises because the polyimide has a higher coefficient of thermal expansion than that of the aluminum. Thus, as the temperature of the device rises, the polyimide is restrained from free expansion in the vertical direction by the aluminum plate and the aluminum cylinder. The present report is based on this approximate model. It consists of two parts: (1) Given the temperature of the polyimide film and the aluminum plate and cylinder, estimate the stress in the aluminum cylinder. (2) Approximate analysis of the temperature rise of the polyimide film and aluminum parts.

2. Thermal Stress Analysis.- The model for the thermal stress analysis is shown in Figure 2. The model assumes a one-dimensional problem with uniform temperature rise in the aluminum, T_A , and a possibly different, but uniform, temperature rise in the polyimide, T_P . The coefficients of thermal expansion are designated α_A and α_P for the aluminum and polyimide materials respectively.

The cylinder of aluminum with diameter d and length l is assumed to restrain the free expansion of the polyimide cylinder of diameter D and length l . Within the stressed region, the strain of the aluminum and the polyimide are equal. Taking force equilibrium into account and with the use of the one-dimensional thermoelastic constitutive relations for the aluminum and polyimide, the stress in the aluminum, σ , can be calculated from

$$\frac{\sigma}{E_A} = \frac{\alpha_P T_P - \alpha_A T_A}{1 + \frac{E_A}{E_P(D^2/d^2 - 1)}} \quad (1)$$

Here E_A , E_P represent the Young's moduli of the aluminum and polyimide, respectively. The temperature rise T_A or T_P must be referenced to a temperature for which the assembly is stress-free.

Relation (1) is based on the assumption that $\alpha_P T_P$ is greater than $\alpha_A T_A$ in order that the aluminum stress σ be tensile. If this condition is not met and the stress σ were compressive, then a tensile stress would be transmitted through the polyimide-aluminum interface. Failure associated with this possibility is not considered in the present analysis. It is expected that such a failure would not result in loss of electrical function and is therefore probably less serious than failure in the aluminum cylinder.

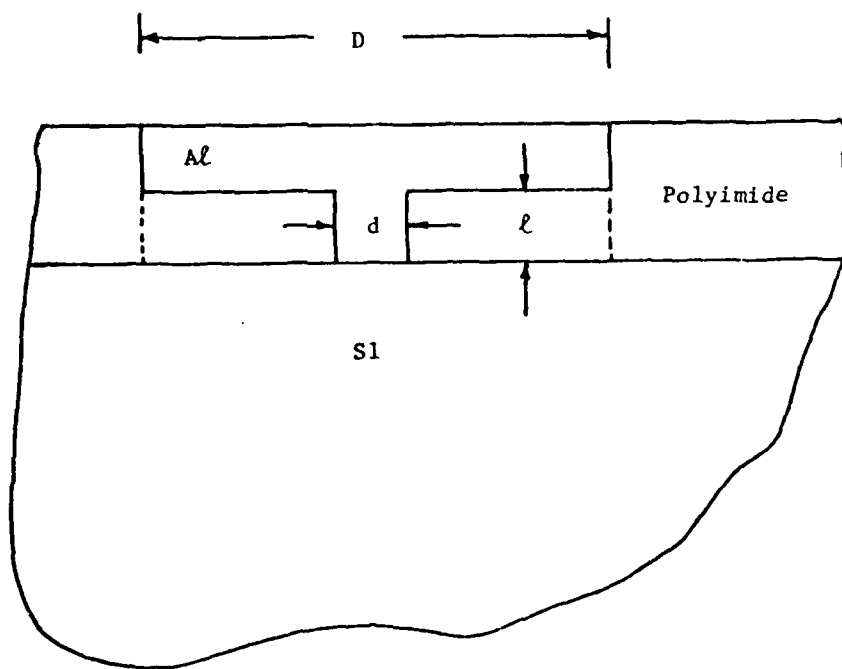


Figure 2. Stress Analysis Model

Relation (1) is also based on the assumptions that E and α are independent of temperature and that the stress in the aluminum is less than the yield point stress. The assumption of constant E and α values restricts the magnitude of the temperature change T. If E is constant over the temperature range of interest, then the average value of α over the temperature range should be used in (1). After the yield point stress is reached in the aluminum, further temperature rise will result in the development of plastic strains in the aluminum.

3. Temperature Analysis.- The model for the temperature analysis is shown in Figure 3. The model assumes that heat is generated at the aluminum-silicon interface. A one-dimensional conduction model is assumed with a linear temperature variation from the upper surface temperature T_p to the temperature T_s of the heat sink. It is assumed that the temperature of the polyimide and the aluminum is uniform and is the same as the upper surface temperature T_p .

Denoting $T = T_p - T_s$, and P the average power generated at the interface, it is found that the maximum temperature T_{max} is

$$T_{max} = \frac{P \cdot H}{k_s w^2} \quad (2)$$

where k_s is the thermal conductivity of silicon. Some of the material properties information is provided in Table 1.

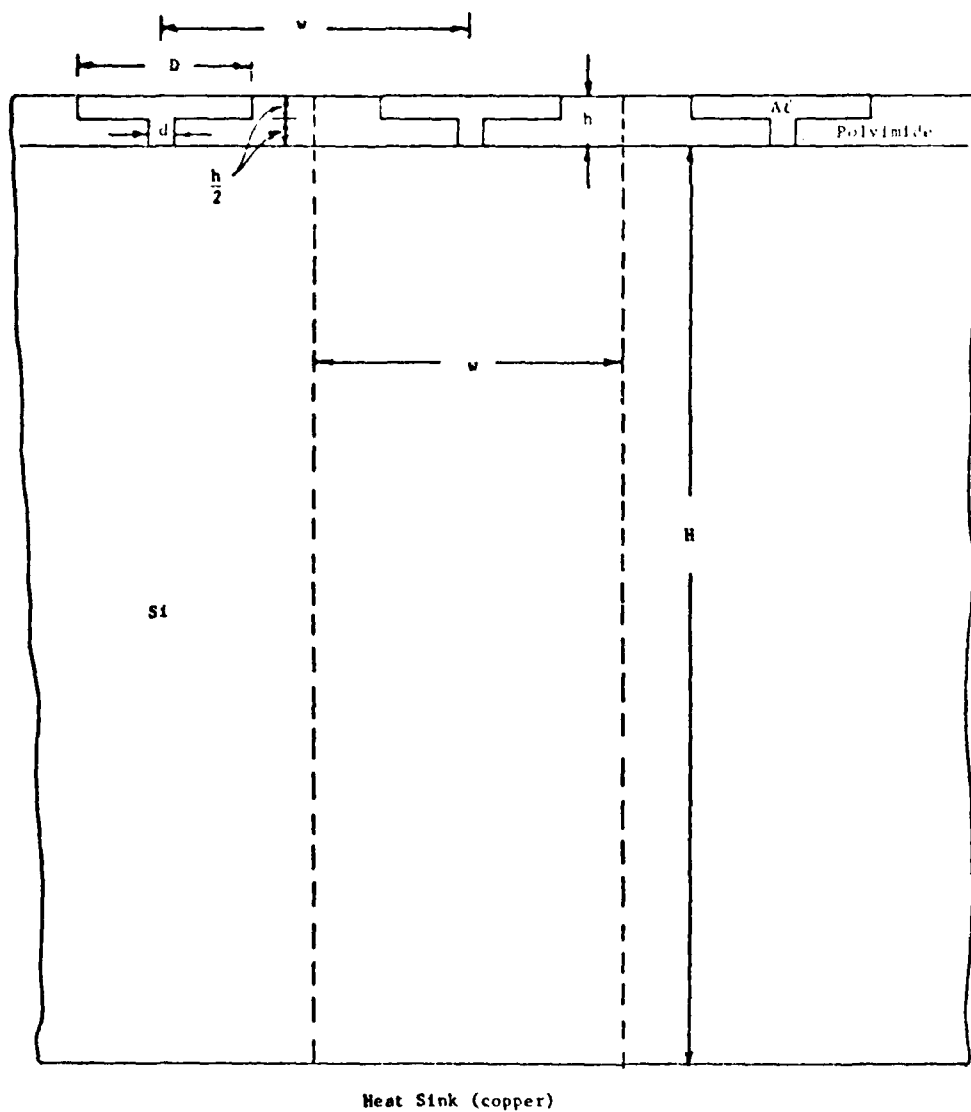


Figure 3. One-Dimensional Temperature Analysis Model

TABLE 1. MATERIALS PROPERTIES INFORMATION

MATERIAL	Density ρ	Thermal Conductivity k	Specific Heat c	Coefficient of Thermal Expansion α	Elastic Modulus E
Al	2685 kg/m ³	225 W/m ² K	900 J/kg ^o K	23 x 10 ⁻⁶ /K	10 x 10 ⁶ psi
Si	2327 kg/m ³	84 W/m ² K	703 J/kg ^o K	(1.1 - 4.1) x 10 ⁻⁶ /K	--
Polyimide	1090 - 1140 kg/m ³	.17 W/m ² K	1675 J/kg ^o K	20 - 180 °C 200 °C 220 °C 240 °C 280 °C	55 x 10 ⁻⁶ /K 70 x 10 ⁻⁶ /K 90 x 10 ⁻⁶ /K 100 x 10 ⁻⁶ /K 110 x 10 ⁻⁶ /K

¹ Reliability Study of Polyimide/glass multilayer, W. Rigling, Martin Marietta Aerospace, AD-777.194, January 1974.

4. Discussion.- In order to obtain some idea of the thermal stresses that may be expected, the results obtained for two specific cases are shown in Table 2. In Case I, a distance of 200 microns is assumed between typical heat generating stations. In this case, the temperature rise is less than one degree centigrade, and therefore, the thermal stress is essentially zero. Case II differs from Case I by closing up the spacing between heat generating stations. In this case, the maximum temperature rise is found to be 22°C.

In order to estimate the thermal stress in the aluminum corresponding to this temperature rise, assume that the temperature of the heat sink is 20°C and that the system is stress-free at that temperature. In accordance with the assumption of the temperature model, the temperature rise of the aluminum and that of the polyimide will be equal. The value of T_A , which is equal to T_p in equation (1) is equal to T_{max} . The corresponding estimate of the thermal stress for this temperature range is found to be 7,040 psi. If, on the other hand, the stress free temperature is lower than the temperature of the heat sink then the value of T_A or T_p would be greater than T_{max} and the corresponding estimate of the thermal stress would also be greater than 7,040 psi. For example, suppose that the temperature of the heat sink is 60°C but the stress-free temperature remains 20°C. With all other conditions the same, the temperature rise T_A would be 62°C and the corresponding thermal stress would be 19,840 psi.

As illustrated by these two examples, one may expect insignificant stresses to exist if the spacing is large while one can expect stresses high enough to cause failure when the spacing is close. Unfortunately, the large spacing case probably greatly underestimates the actual temperature rise because of the assumption of a one-dimensional model. The small spacing example may be taken as a suggestion that serious stressing may occur.

It is recommended on the basis of the results of the small spacing example that a more refined analysis be carried out. It is felt that a finite element or finite difference numerical method applied to an axisymmetric model of essentially one typical station would yield acceptable results. Conclusions regarding the seriousness of the thermal stresses should be postponed until the more refined analysis can be performed.

TABLE 2. CALCULATED RESULTS FOR TWO SPECIFIC CASES

Assumed Data	Case I	Case II
P	3×10^{-3} W	3×10^{-3} W
h	2×10^{-6} m	2×10^{-6} m
H	250×10^{-6} m	250×10^{-6} m
d	1×10^{-6} m	1×10^{-6} m
D	100×10^{-6} m	10×10^{-6} m
w	200×10^{-6} m	20×10^{-6} m

Calculated Quantities

Maximum Temperature Rise ¹	0.22 °C	22°C
Thermal Stress, σ ²	essentially zero	7,040 psi
σ ³	essentially zero	19,840 psi

¹ T_{\max} calculated from equation (2)

² Thermal stress calculated from equation (1) when the temperature of the heat sink is assumed to be 20°C and the assembly is assumed to be stress-free at that temperature.

³ Thermal stress calculated from equation (1) when the temperature of the heat sink is assumed to be 60°C and the assembly is assumed to be stress-free at 20°C.

APPENDIX E: PROPOSED ANALYSIS AND EXPERIMENTS FOR FURTHER
EVALUATION OF THE EFFECTS OF THERMAL SHOCK ON
THE STRESSES AND STRENGTH OF ANNULAR GLASS SEALS

By K. Kokini and C. Libove

1. Introduction.- In Chapter 8 an approximate thermal stress analysis was presented for annular glass lead-through seals in packages subjected to thermal shock. The seal was idealized as consisting of three concentric components: a lead-through wire of circular cross section, a glass annulus surrounding the wire, and a metal annulus surrounding the glass. The temperatures in the latter annulus and the lead were assumed to be uniform (though time-varying) within those two components. Axial (that is, parallel to the lead) heat conduction between the thermal shock test fluid and the glass was neglected, and a state of plane stress was assumed in the glass. As a result, the temperatures and stresses in the glass at any instant of time became functions only of the radial coordinate r , that is, they were independent of the axial coordinate z .

In this appendix improvements in the analysis are proposed, as well as thermal shock experiments on simple models of annular glass seals. The analytical improvements are in the direction of including axial heat flow in the glass and the variation of the glass temperatures and stresses in the axial direction, while retaining all the other aspects of the model analyzed previously. (In particular, the assumption of axial symmetry will be retained, as well as the assumption of uniform temperatures within the lead and the base.) The purpose of the proposed experiments is to correlate any observed thermal shock damage with (a) the geometrical para-

meters of the seal, (b) the depth of oxide produced in the metal in the pre-oxidation step of the sealing process, and (c) the calculated stresses in the glass and the glass-to-metal interfaces.

The details of the proposed work are described more fully in the following sections, in which we shall continue to use the notation of Chapter 8 whenever that notation is still applicable.

2. Improved Temperature Analysis.— The model for temperature analysis, including the effects of axial heat flow in the glass, can still be taken as shown in Figure 2 of Chapter 8 (p. 197), provided that an axial coordinate z , positive upward, is added to the diagram. The origin of the z -coordinates will be taken at the lower (inside) flat surface of the glass annulus, so that $z = 0$ will identify that surface, and $z = l$, where l is the axial thickness of the glass annulus, will identify the upper surface.

The temperature $T(r,z,\tau)$ in the glass is now governed by the field equation

$$\frac{\partial T}{\partial \tau} = a_g \left(\frac{\partial^2 T}{\partial r^2} + \frac{1}{r} \frac{\partial T}{\partial r} + \frac{\partial^2 T}{\partial z^2} \right), \quad (1)$$

the initial condition

$$T(r,z,0) = T_0, \quad (2)$$

the metal-glass interface boundary conditions

$$\rho_k c_k V_l \left(\frac{\partial T}{\partial \tau} \right)_{r=a} = \bar{h} A_o [T_\infty - (T)_{r=a}] + k_g \cdot 2\pi a \int_0^l \left(\frac{\partial T}{\partial r} \right)_{r=a} dz \quad (3)$$

$$\rho_k c_k \frac{V_b}{N} \left(\frac{\partial T}{\partial \tau} \right)_{r=b} = \bar{h} \frac{A_b}{N} [T_\infty - (T)_{r=b}] - k_g \cdot 2\pi b \int_0^l \left(\frac{\partial T}{\partial r} \right)_{r=b} dz, \quad (4)$$

the fluid-glass interface boundary condition

$$k_g \left(\frac{\partial T}{\partial z} \right)_{z=l} = \bar{h} [T - (T)_{z=l}] , \quad (5)$$

and the boundary condition

$$k_g \left(\frac{\partial T}{\partial z} \right)_{z=0} = 0 , \quad (6a)$$

corresponding to the assumption of an adiabatic boundary at the glass surface that is inside the package. Anticipating that calculations will have to be made for test specimens in which both flat surfaces of the glass annulus will be exposed to the thermal shock test fluid, we note that for such specimens Equation (6a) must be replaced by

$$k_g \left(\frac{\partial T}{\partial z} \right)_{z=0} = -\bar{h} [T_\infty - (T)_{z=0}] . \quad (6b)$$

It will be noted that the same \bar{h} is used in Equations (3) and (4) as in Equations (5) and (7); that is, the heat transfer coefficient between fluid and metal is assumed to be the same as that between fluid and glass.

Introducing the dimensionless variables

$$x = r/a \quad Z = z/l \quad (7)$$

$$y = \tau a_g / a^2 = \tau k_g / \rho_g c_g a^2 \quad (8)$$

$$t = \frac{T_\infty - T(r, z, \tau)}{T_\infty - T_0} = t(x, Z, y) \quad (9)$$

$$\begin{aligned}
 A' &= \frac{\bar{h}A_o}{2\pi\ell k_g} & B' &= \frac{\rho_k c_k V \ell}{2\pi\ell\rho_g c_g a^2} \\
 C' &= \frac{\bar{h}A_b}{2\pi\ell k_g N} \cdot \frac{a}{b} & D' &= \frac{\rho_k c_k V b}{2\pi\ell\rho_g c_g abN} \\
 E' &= \bar{h}\ell/k_g & L &= \ell/a
 \end{aligned} \tag{10}$$

we can convert Equations (1) through (6) to the following dimensionless form:

$$\frac{\partial t}{\partial y} = \frac{\partial^2 t}{\partial x^2} + \frac{1}{x} \frac{\partial t}{\partial x} + \frac{1}{L^2} \frac{\partial^2 t}{\partial Z^2} \tag{11}$$

$$t(x, Z, 0) = 1 \tag{12}$$

$$\int_0^1 \left(\frac{\partial t}{\partial x}\right)_{x=1} dZ = A' \cdot (t)_{x=1} + B' \left(\frac{\partial t}{\partial y}\right)_{x=1} \tag{13}$$

$$-\int_0^1 \left(\frac{\partial t}{\partial x}\right)_{x=b/a} dZ = C' \cdot (t)_{x=b/a} + D' \left(\frac{\partial t}{\partial y}\right)_{x=b/a} \tag{14}$$

$$-\left(\frac{\partial t}{\partial Z}\right)_{Z=1} = E' \cdot (t)_{Z=1} \tag{15}$$

$$\left(\frac{\partial t}{\partial Z}\right)_{Z=0} = 0 \tag{16a}$$

$$\left(\frac{\partial t}{\partial Z}\right)_{Z=0} = E' \cdot (t)_{Z=0} \tag{16b}$$

Equations (11) to (16) will be solved by the finite-difference method. Because of the large number of finite difference equations resulting from any reasonably fine grid, it has been found, through trial calculations,

that an iterative solution of the equations is more expedient and economical than a direct solution.

3. Improved Stress Analysis.— Once the temperature distribution is known for any given instant of time the stresses produced by that temperature distribution at that instant of time can be determined. The model to be used for this stress analysis is that shown in Figure 3 of Chapter 8 (p. 200). Again a z-coordinate must be added to the diagram, as was done for the temperature analysis model in Section 2 above.

The most expedient tool for the determination of the stresses is the principle of minimum strain energy, whereby the true distribution of displacements is that which minimizes the strain energy (with proper allowance for the presence of thermal strains). This principle will be implemented with the aid of a finite-difference grid whereby the strains can be expressed in terms of first order finite differences of displacements at the grid points. This energy method avoids the necessity of giving explicit attention to the zero-stress boundary conditions at the top and the bottom surfaces of the model and to the stress-continuity conditions at the two cylindrical interfaces between the glass and the metal. Thus an awkward surfeit of equations at the corners of the metal-glass interfaces is avoided. The method described above is essentially a finite element method except for the fact that an explicit distribution of displacements within the elements (the grid cells) does not have to be postulated.

The finite-difference grid to be used is shown in Figure 1. The grid stations are numbered $i=0, 1, \dots, P$ in the radial direction with $i=0$ corresponding to the axis of the lead ($r=0$) and $i=P$ to the outer boundary

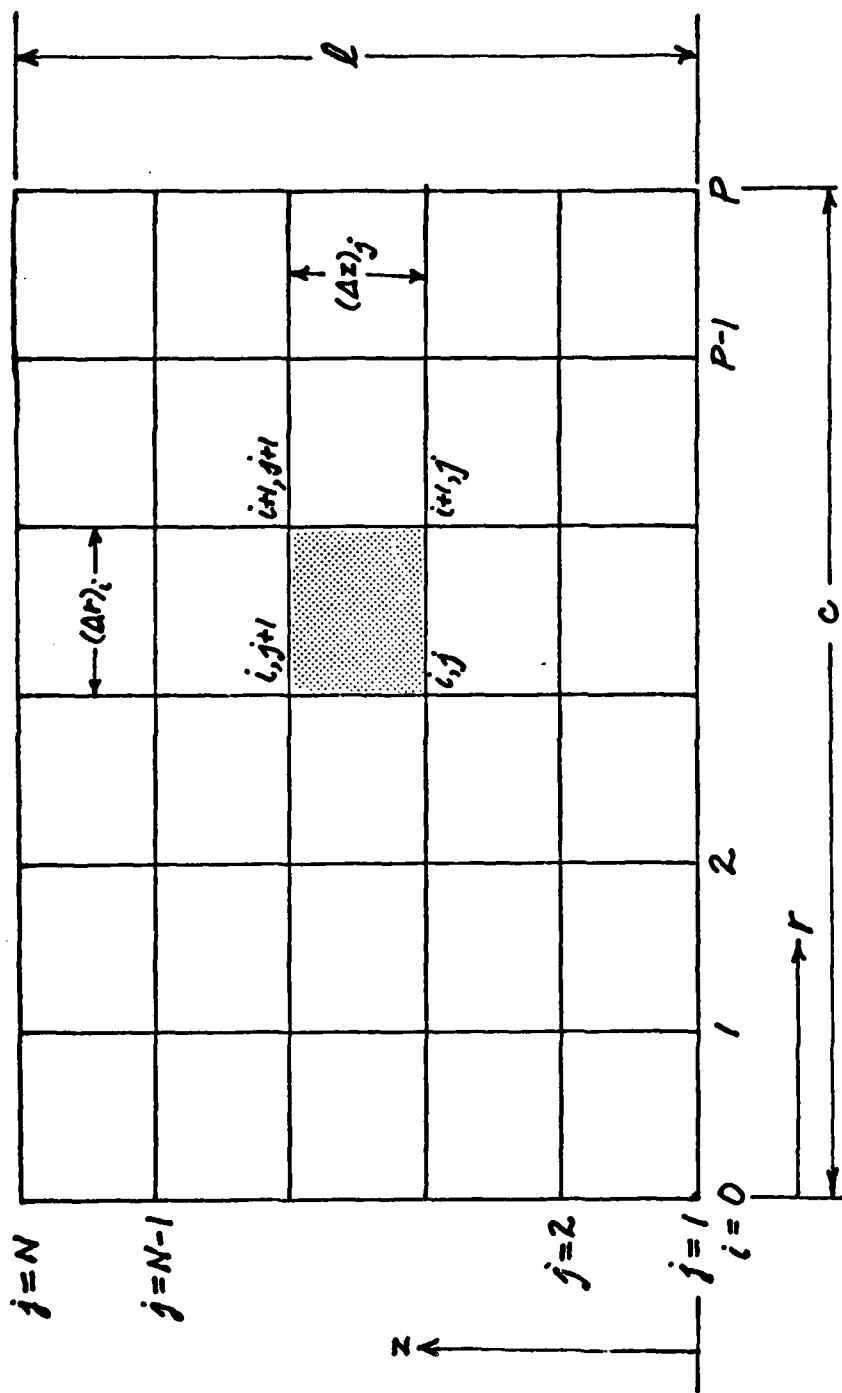


Figure 1.- Finite difference grid to be used for the stress analysis.

($r=c$) of the base. In the axial direction the grid station numbering is $j = 1, 2, \dots, N$, with $j=1$ and N corresponding to the lower and upper boundaries, respectively, of the model. It will be assumed that the grid is laid out in such a way that the metal-glass interfaces ($r=a$ and $r=b$) correspond exactly to certain grid lines. Thus, every cell contains a single material -- either metal or glass, rather than a mixture of materials.

Any grid point will be identified by the pair of numbers (i,j) associated with the two grid lines that intersect at that point, and r_i and z_j will denote the r and z coordinates of that grid point. Any cell, like the one shown shaded in Figure 1, can be identified by the pair of numbers (i,j) associated with the grid point at its lower left corner. The radial and axial dimensions of the cell will be denoted $(\Delta r)_i$ and $(\Delta z)_j$, respectively. $(\Delta r)_i$ may vary in the r -direction and $(\Delta z)_j$ in the z -direction. The shaded cell in Figure 1 is the cross section of a ring of material whose volume is

$$(\Delta V)_{ij} = 2\pi \bar{r}_i (\Delta r)_i (\Delta z)_j \quad (17)$$

where

$$\bar{r}_i = \frac{1}{2} (r_i + r_{i+1}) \quad (18)$$

is the mean radius of the cell. The Young's modulus E , shear modulus G , Poisson's ratio ν and thermal expansion coefficient α for the material in this ring will be denoted E_i , G_i , ν_i and α_i , respectively; and λ_i will denote the value of λ for the cell material, where

$$\lambda \equiv \frac{E\nu}{(1+\nu)(1-2\nu)} \quad (19)$$

It is assumed that some datum configuration exists in which the temperature is uniform at the value T_d and the stress distribution throughout the material is known (e.g., the material may be stress-free if the temperature is uniform at the set point of the glass or uniform at room temperature). The displacement and strains in this datum configuration will be taken as zero. The objective of the stress analysis is to determine the displacements, strains and stress increments produced by any given temperature distribution $T(r,z)$ other than the uniform datum temperature T_d .

The radial (r-wise) and axial (z-wise) displacements will be denoted by $u(r,z)$ and $w(r,z)$, respectively; and the values of u and w at the grid point (i,j) , in particular, will be denoted by u_{ij} and w_{ij} , respectively. The displacements $u(r,z)$ and $w(r,z)$ give rise to the following strains (radial, axial, circumferential, and shear, respectively).

$$\epsilon_r = \frac{\partial u}{\partial r} \quad \epsilon_z = \frac{\partial w}{\partial z} \quad \epsilon_\theta = \frac{u}{r} \quad \gamma_{rz} = \frac{\partial u}{\partial z} + \frac{\partial w}{\partial r} \quad (20)$$

Mean values of these strains for the ring of material represented by the shaded shell of Figure 1 will be denoted by $\epsilon_{r_{ij}}$, $\epsilon_{z_{ij}}$, $\epsilon_{\theta_{ij}}$ and $\gamma_{rz_{ij}}$, respectively, and will be calculated as follows:

$$\epsilon_{r_{ij}} = \frac{1}{2} \left[\frac{u_{i+1,j} - u_{ij}}{(\Delta r)_i} + \frac{u_{i+1,j+1} - u_{i,j+1}}{(\Delta r)_i} \right] \quad (21)$$

$$\epsilon_{z_{ij}} = \frac{1}{2} \left[\frac{w_{i,j+1} - w_{ij}}{(\Delta z)_j} + \frac{w_{i+1,j+1} - w_{i+1,j}}{(\Delta z)_j} \right] \quad (22)$$

$$\epsilon_{\theta_{ij}} = \begin{cases} \frac{1}{4} \left[\frac{u_{ij}}{r_i} + \frac{u_{i+1,j}}{r_{i+1}} + \frac{u_{i,j+1}}{r_i} + \frac{u_{i+1,j+1}}{r_{i+1}} \right] & \text{for } i \neq 0 \\ \frac{1}{2} \left[\frac{u_{i+1,j}}{r_{i+1}} + \frac{u_{i+1,j+1}}{r_{i+1}} \right] & \text{for } i = 0 \end{cases} \quad (23)$$

$$\gamma_{rz_{ij}} = \frac{1}{2} \left[\frac{w_{i+1,j} - w_{ij}}{(\Delta r)_i} + \frac{w_{i+1,j+1} - w_{i,j+1}}{(\Delta r)_i} \right. \\ \left. + \frac{u_{i,j+1} - u_{ij}}{(\Delta z)_j} + \frac{u_{i+1,j+1} - u_{i+1,j}}{(\Delta z)_j} \right] \quad (24)$$

The second of Equations (23) was obtained from the first by imposing the regularity condition

$$\left(\frac{u_{ij}}{r_i} \right)_{i=0} = \left(\frac{u_{ij}}{r_i} \right)_{i=1} \quad (25)$$

The boundary condition of zero radial displacement along the axis of the lead will be satisfied by specifying that

$$u_{ij} = 0 \quad \text{for } i = 0 \quad (26)$$

and rigid-body movement will be eliminated by specifying that

$$w_{ij} = 0 \quad \text{for } (i,j) = (0,1) \quad (27)$$

The mean temperature rise $(\Delta T)_{ij}$, relative to the datum, in the shaded cell of Figure 1 can be estimated as

$$(\Delta T)_{ij} = \frac{1}{4} (T_{ij} + T_{i+1,j} + T_{i,j+1} + T_{i+1,j+1}) - T_d \quad (28)$$

where T_{ij} , $T_{i+1,j}$, etc. are the values of $T(r,z)$ associated with the corners of the cell, as obtained by the temperature analysis of Section 2. The corresponding mean thermal strain is

$$\epsilon_{ij}^t = \alpha_i (\Delta T)_{ij} \quad (29)$$

We now turn to the evaluation of the strain energy of the system of rings represented by the grid rectangles of Figure 1. In the absence of thermal effects, the strain-energy density U^* of an isotropic elastic material in a state of axially symmetric deformation is

$$U^* = \frac{\lambda}{2} (\epsilon_r + \epsilon_z + \epsilon_\theta)^2 + G(\epsilon_r^2 + \epsilon_z^2 + \epsilon_\theta^2) + \frac{1}{2} G_{Y_{rz}}^2 \quad (30)$$

where λ is defined by Equation (19)[†]. If there is a thermal strain ϵ^t , it must be subtracted from each of the normal strains in (30), which results in the following modified expression for the strain-energy density:

$$U^* = \frac{\lambda}{2} (\epsilon'_r + \epsilon'_z + \epsilon'_\theta)^2 + G(\epsilon_r'^2 + \epsilon_z'^2 + \epsilon_\theta'^2) + \frac{1}{2} G_{Y_{rz}}^2 \quad (31)$$

where

$$\epsilon'_r = \epsilon_r - \epsilon^t \quad \epsilon'_z = \epsilon_z - \epsilon^t \quad \epsilon'_\theta = \epsilon_\theta - \epsilon^t \quad (32)$$

Thus, the strain energy density U_{ij}^* in the ring whose cross section is the shaded cell of Figure 1 is

$$U_{ij}^* = \frac{\lambda_i}{2} (\epsilon'_{r_{ij}} + \epsilon'_{z_{ij}} + \epsilon'_{\theta_{ij}})^2 + G_i (\epsilon'_{r_{ij}}{}^2 + \epsilon'_{z_{ij}}{}^2 + \epsilon'_{\theta_{ij}}{}^2) + \frac{1}{2} G_i Y'_{rz_{ij}}{}^2 \quad (33)$$

[†] See S. Timoshenko and J.N. Goodier, "Theory of Elasticity," 2nd ed., McGraw-Hill, NY, 1970, p. 246.

where

$$\begin{aligned}
 \epsilon'_{r_{ij}} &= \epsilon_{r_{ij}} - \epsilon_{ij}^t \\
 \epsilon'_{z_{ij}} &= \epsilon_{z_{ij}} - \epsilon_{ij}^t \\
 \epsilon'_{\theta_{ij}} &= \epsilon_{\theta_{ij}} - \epsilon_{ij}^t \\
 \gamma'_{rz_{ij}} &= \gamma_{rz_{ij}}
 \end{aligned}
 \tag{34}$$

Multiplication of U_{ij}^* by the volume of the ring gives

$$(\Delta U)_{ij} = U_{ij}^* (\Delta V)_{ij}
 \tag{35}$$

for the strain energy of the ring, and summation over all the rings gives

$$U = \sum_{i=0}^{P-1} \sum_{j=1}^{N-1} (\Delta U)_{ij}
 \tag{36}$$

for the total strain energy.

In order to determine the nodal displacements u_{ij} and w_{ij} , U must be minimized with respect to each of those displacements whose value is not already fixed by geometric constants. Thus, the following system of equations must be written:

$$\frac{\partial U}{\partial u_{ij}} = 0 \quad \left(\begin{array}{l} i = 1, 2, \dots, P \\ j = 1, 2, \dots, N \end{array} \right)$$

$$\frac{\partial U}{\partial w_{ij}} = 0 \quad \left(\begin{array}{l} i = 0, 1, 2, \dots, P \\ j = 1, 2, \dots, N \\ \text{with } i=0, j=1 \text{ excluded} \end{array} \right)$$
(37)

Equations (37) will be a system of linear equations in the u_{ij} and w_{ij} to be solved simultaneously for those unknowns. With u_{ij} and w_{ij} determined, the cell strains can be found from Equations (21) to (24), and the strains due to stress alone from Equations (34). The stresses in any cell can then be found by substituting the latter strains into the generalized Hooke's law, using the elastic constants that are appropriate for the material in that cell.

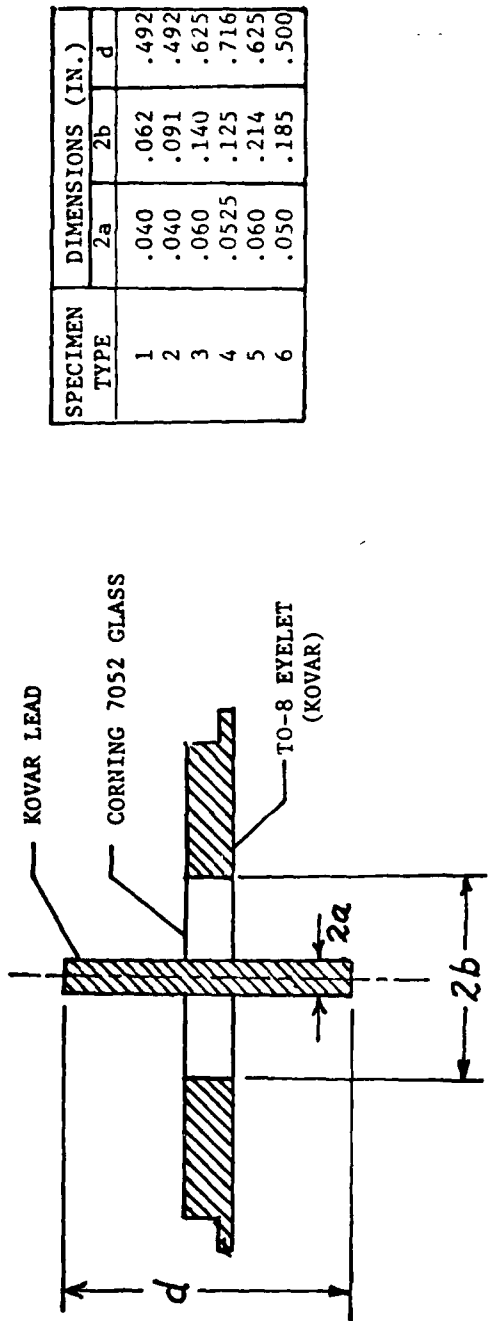
4. Experimental Program.- By the methods discussed in the two preceding sections, one can obtain estimates of the stress distributions in the glass annulus as functions of time. However, the determination of those stresses is not an end in itself. It is equally important for the designer, screener, or stress analyst to be able to draw conclusions as to whether or not those stresses will damage the seal to the extent that hermeticity of the package is compromised during and/or after the thermal shock test. Therefore, besides knowing the stresses, one must also know what the "allowables" are for those stresses.

The determination of allowables is a difficult problem. There is some strength data available for glass, but virtually none of it is directly applicable to the glass in situ in the seal, nor to the interfacial material formed by the glass and the oxide of whatever metal (usually

Kovar) it is bonded to. The direct determination of strengths for the glass and interfacial materials in a seal is virtually impossible for the following reasons: (a) The seals are so small that it would be extremely difficult to handle and test any samples cut from them; (b) even if the small samples could be handled and tested, considerable damage might be done to them in the process of cutting; and (c) even if extreme care were taken to insure no damage due to cutting, the creation of new surfaces by the cutting could have a basic weakening effect. It is true that large scale models of seals could be fabricated that would be physically easier to handle, but then a scale effect would be introduced as another uncertainty along with those produced by the cutting of test specimens from the model.

In view of the difficulties described above, it was decided that allowable stresses for the glass in an annular lead-through seal could best be determined by an indirect method -- that is, by fabricating seals, subjecting them to thermal shock tests of various levels of severity, examining them (visually and by test) for damage, and correlating any observed damage with the theoretical stress histories and distributions computed for them by the methods of Sections 2 and 3.

The test specimens to be used in this study are shown schematically in Figure 2. They consist of commercially available TO-8 Kovar eyelets with a drilled central hole in which a Kovar lead is inserted and sealed with Corning 7052 glass. This combination of materials (Kovar and 7052 glass) is also widely used in the electronics industry, because their matching thermal contractions from the set point to room temperature leads theoretically to a stress-free seal at room temperature. There will



SPECIMEN TYPE	DIMENSIONS (IN.)		
	2a	2b	d
1	.040	.062	.492
2	.040	.091	.492
3	.060	.140	.625
4	.0525	.125	.716
5	.060	.214	.625
6	.050	.185	.500

Figure 2.- Schematic cross section and table of dimensions of the proposed test specimens.

be six different geometries, as indicated by the table in Figure 2 and twenty-five samples of each geometry. The sealing will be performed by the Air Products and Chemicals Co. of Allentown, PA in a furnace with a controlled atmosphere. Prior to the sealing the Kovar parts alone will be subjected to an oxidation process leading to a known and reproducible depth of oxide on the metal surfaces that will later be in contact with the glass.

The testing procedure will consist of the following steps:

- (a) The sample is heated to a known temperature in an oven.
- (b) It is then immediately inserted into a constant-temperature oil bath at a lower temperature and left there long enough for its temperature to become stabilized at that of the bath.
- (c) The sample is removed from the bath, cleaned, and placed in a dye penetrant intended to reveal any cracking. (The sample will have also been subjected to the dye penetrant test before the thermal shock in order to insure the absence of pre-existing cracks.)
- (d) The sample will then be subjected to a "residual torque strength" test, i.e., a test in which the lead is twisted in order to determine what torque (if any) will cause it to rotate in the seal.

The testing procedure just described will first be carried out on one geometry of test specimen but with several samples representing different levels of pre-oxidation, in order to establish an optimum pre-oxidation level. (The findings in this phase of the program will be compared with the recommendations of L. Zakraysek of the General Electric Co. of Syracuse with regard to optimum thickness of the intergranular oxide

layer.) Once the optimum oxide level has been determined, that oxide level will be used in the remaining test specimens, and the main test variable for each geometry will then be the temperature of the specimen prior to its insertion in the oil bath.

In order to try out the experimental procedure and the associated apparatus, six preliminary test specimens of the Type 2 geometry were fabricated and sealed by the Air Products Co., then thermal shock tested at Syracuse University, using water (rather than oil) as the test fluid. Six temperature differences ΔT were employed between oven temperature and water bath temperature, including $\Delta T = 0$ (no thermal shock). The following table of residual torque strengths shows that there was no reduction of strength due to the thermal shock levels employed.

ΔT ($^{\circ}F$)	Residual Torque Strength (lb -in.)
0	82
324	80
524	81
624	95
724	85
924	89

However, for some of the specimens the dye penetrant treatment and visual examination after the thermal shock, but prior to the torque test, did reveal damage. The damage was in the form of a circumferential opening at the lead-glass interface. As the table shows, the subsequent torque strength was not affected by the presence of such cracks, which implies that there was no permanent damage done to the seal by the thermal shock test. However, the possibility of a healing process cannot be ruled

out. That is, there may have been a significant transient separation between lead wire and glass during the thermal shock, followed by virtual closure of the gap when the specimen temperature became once again uniform at room temperature. Methods will be sought for detecting such transient separations.

It is expected that the experiments and the related calculations will show that the severity and damage of a thermal shock test depends not just on the temperature excursion involved, but also on the geometrical parameters of the seal.

REFERENCES

1. "Test Methods and Procedures for Microelectronics." MIL-STD-883B, Rome Air Development Center (AFSC), Griffiss Air Force Base, New York, 31 August 1977.
2. Libove, C.: "Rectangular Flat-Pack Lids under External Pressure: Improved Formulas for Screening and Design (Revised)." RADC-TR-79-138, June 1979. A072421
3. Timoshenko, S.; and Woinowski-Krieger, S.: "Theory of Plates and Shells." McGraw-Hill Book Company, Inc., New York, 1959.
4. Libove, C.: "Rectangular Flat-Pack Lids under External Pressure." RADC-TR-76-118, May 1976. A025625
5. Aalami, B.; and Williams, D.G.: "Thin Plate Design for Transverse Loading." John Wiley & Sons, New York, 1975.
6. Kornishin, M.S.; and Isanbayeva, F.S.: "Flexible Plates and Panels." Report FTD-HC-23-441-69, Air Force Systems Command, Foreign Technology Division, January 21, 1971, AD 722 302. (Translation of Russian book Gibkiye Plastiny i Paneli, 1968).
7. Libove, C.: "Critique of the Centrifuge as a Stressing Device." RADC-TR-78-102, May 1978.
8. Schafft, H.A.: "Methods for Testing Wire-Bond Electrical Connections." U.S. Department of Commerce, National Bureau of Standards, Technical Note 786, November 1973.
9. Moore, Robert: "Reliability Test Program of Ultrasonic Face Down Bonding Technique." RADC-TR-67-128, June 1967, AD 624525.
10. Leissa, A.W.: "Vibration of Plates." NASA SP-160, 1969.
11. Libove, C.: "Impact Stresses in Wires and Wire Bonds: Upper Limit Analysis." RADC-TR-78-103, May 1978. A055270
12. Libove, C.: "Maximum Strain in a Falling Horizontal Wire Due to Instantaneous Arrest of its Ends: Travelling Wave Analysis." Int. J. Non-Linear Mechanics, Vol. 14, No. 3 (1979), pp 175-182.
13. Libove, C.: "Impact Stresses in Flat-Pack Lids and Bases." RADC-TR-78-98, April 1978. A054947
14. Nunziato, J.W.; et al.: "Wave Propagation in Nonlinear Viscoelastic Solids." Encyclopedia of Physics, Spruyer-Verlag, NY, 1970, Vol. VI A/4 - Mechanics of Solids IV, pp. 7-23.

15. Graham, R.A.: "Technique for Measurements of Plane Waves of Uniaxial Strain." Proceedings of Workshop on Nonlinear Waves, sponsored by the National Science Foundation and the University of Illinois, Chicago Circle, March 21-23, 1977. (Author's affiliation: Sandia Laboratories, Albuquerque, NM).
16. Timoshenko, S.P.; and Goodier, J.N.: "Theory of Elasticity," 3rd ed., McGraw-Hill Book Co., Inc., New York, 1970, Chapter 14.
17. Libove, C.; and Stein, M.: "Charts for Critical Combinations of Longitudinal and Transverse Direct Stress for Flat Rectangular Plates." NACA ARR L6A05, March 1946. (Reissued as NACA Wartime Report L-224).
18. Gerard, G.: "Introduction to Structural Stability Theory." McGraw-Hill Book Co., Inc., New York, 1962, pp. 52, 58, 160.
19. Timoshenko, S.P.; and Gere, J.M.: "Theory of Elastic Stability," 2nd ed., McGraw-Hill Book Co., Inc., New York, 1961, Section 9.2.
20. Volterra, E.; and Gaines, J.H.: "Advanced Strength of Materials." Prentice-Hall, Inc., Englewood Cliffs, NJ, 1971.
21. Libove, C.: "Flat-Packs under Thermal Shock: A Simplified Analysis of Flexural Stress in the Lid-to-Wall Seal." RADC-TR-75-308, Dec. 1975.
22. Levy, S.: "Thermal Stresses and Deformations in Beams." Aeronautical Engineering Review, October 1956, pp. 62-70.
23. Rohsenow, W.M.; and Hartnett, J.P. (eds.): "Handbook of Heat Transfer." McGraw-Hill Book Co., Inc., NY, 1973, p. 3-61, eq. (56).
24. Thomas, R.W.: "IC Packages and Hermetically Sealed-In Contaminants." National Bureau of Standards, Special Publication 400-9, Dec. 1974, pp. 4-19.
25. Johnson, G.M.; and Conaway, L.K.: "Reliability Evaluation of Hermetic Dual in Line and Flat Microcircuit Packages." McDonnell-Douglas Unclassified Report on Contract NAS 8-31446 (Oct. 1976-Dec. 1977).
26. Kokini, K.; Perkins, R.W.; Libove, C.: "Thermal Stress Analysis of Glass Seals in Microelectronic Packages under Thermal Shock Conditions." RADC-TR-79-201, July 1979. A073654
27. Carnahan, B.; Luther, H.A.; and Wilkes, J.O.: "Applied Numerical Methods." John Wiley & Sons, Inc., NY, 1969, pp. 440-442.

A decorative border with a repeating floral or scrollwork pattern surrounds the central text.

MISSION
of
Rome Air Development Center

RADC plans and executes research, development, test and selected acquisition programs in support of Command, Control Communications and Intelligence (C³I) activities. Technical and engineering support within areas of technical competence is provided to ESD Program Offices (POs) and other ESD elements. The principal technical mission areas are communications, electromagnetic guidance and control, surveillance of ground and aerospace objects, intelligence data collection and handling, information system technology, ionospheric propagation, solid state sciences, microwave physics and electronic reliability, maintainability and compatibility.

FILMED
5-8